INFORMATION TO USERS

This manuscript has been reproduced from the microfilm master. UMI films the text directly from the original or copy submitted. Thus, some thesis and dissertation copies are in typewriter face, while others may be from any type of computer printer.

The quality of this reproduction is dependent upon the quality of the copy submitted. Broken or indistinct print, colored or poor quality illustrations and photographs, print bleedthrough, substandard margins, and improper alignment can adversely affect reproduction.

In the unlikely event that the author did not send UMI a complete manuscript and there are missing pages, these will be noted. Also, if unauthorized copyright material had to be removed, a note will indicate the deletion.

Oversize materials (e.g., maps, drawings, charts) are reproduced by sectioning the original, beginning at the upper left-hand corner and continuing from left to right in equal sections with small overlaps.

ProQuest Information and Learning
300 North Zeeb Road, Ann Arbor, MI 48106-1346 USA
800-521-0600

Convection of Magma in Volcanic Conduits as a Degassing Mechanism at Active Volcanoes

Jeffrey Bruce Witter

A dissertation submitted in partial fulfillment of the requirements for the degree of

Doctor of Philosophy

University of Washington

2003

Program Authorized to Offer Degree: Earth and Space Sciences

In presenting this dissertation in partial fulfillment of the requirements for the Doctoral degree at the University of Washington, I agree that the Library shall make its copies freely available for inspection. I further agree that extensive copying of the dissertation is allowable only for scholarly purposes, consistent with "fair use" as prescribed in the U.S. Copyright Law. Requests for copying or reproduction of this dissertation may be referred to Proquest Information and Learning, 300 North Zeeb Road, Ann Arbor, MI 48106-1346, to whom the author has granted "the right to reproduce and sell (a) copies of the manuscript in microform and/or (b) printed copies of the manuscript made from microform."

Signature Jeffrey B. Witter

Date 3/11/03

University of Washington
Graduate School

This is to certify that I have examined this copy of a doctoral dissertation by

Jeffrey Bruce Witter

and have found that it is complete and satisfactory in all respects,
and that any and all revisions required by the final
examining committee have been made.

Co-Chairs of Supervisory Committee:

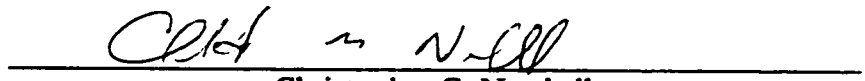

Christopher G. Newhall

Victor C. Kress

Reading Committee:

Christopher G. Newhall

Victor C. Kress

George W. Bergantz

Date: March 11, 2003

University of Washington

Abstract

Convection of Magma in Volcanic Conduits as a Degassing Mechanism at Active Volcanoes

Jeffrey Bruce Witter

Co-Chairs of Supervisory Committee:
Affiliate Professor Christopher G. Newhall
Research Associate Professor Victor C. Kress
Earth and Space Sciences

Convection of magma in the volcanic conduit is a hypothesis that has been proposed to explain long-term, continuous, high rates of gas emission and heat loss at non-explosive, passively degassing volcanoes. I investigate this hypothesis using a geochemical and fluid dynamic approach focusing research at two passively degassing volcanoes, Popocatépetl (Mexico) and Villarrica (Chile) where conduit convection is thought to be the dominant degassing mechanism. Popocatépetl has been the site of voluminous passive degassing accompanied by minor eruptive activity from late-1994 until the time of writing. Villarrica has been characterized by continuous, open-vent, passive degassing from a summit lava lake, with negligible eruption of magmatic material, for the past 17 years. I present a detailed analysis of the chemistry and magnitude of volcanic gas emissions as well as the major and volatile element chemistry of the magma at the two volcanoes. These analyses provide constraints on 1) the magmatic contribution to the emitted volatiles and 2) the physical parameters (i.e. density and viscosity of the magma) that control convection.

These data on the physical parameters of the Popocatépetl and Villarrica magmas combined with analytical fluid dynamic equations for convection of magma in volcanic conduits show that magma convection is a feasible mechanism to provide the observed magnitude of gas emissions considering reasonable conduit sizes and magma ascent velocities at both volcanoes. Further calculations of the Reynolds number and convective velocity scale are presented for magmas having a wide range of viscosity, buoyancy flux, and conduit size, including both cylindrical and dike-shaped conduits. Results indicate that convection of magma in the conduit is likely at Villarrica for conduit radii r = 1 to 5 m. In addition, convection of magma in the conduit is plausible at Popocatépetl for conduit radii r = 2 to 10 m and magma with or without a separate, pre-existing volatile phase. Convection of magma in the volcanic conduit can explain long-term, non-explosive degassing behavior at Popocatépetl, Villarrica, and probably many other volcanoes for which gas emissions far exceed the quantity of gas that could be derived from erupted magma.

TABLE OF CONTENTS

LIST OF FIGURES

LIST OF TABLES

Table number — Page

Acknowledgements

This dissertation was financially supported by a NASA Earth System Science Graduate Student Fellowship as well as NSF Grant# EAR-9980566. I wish to express my appreciation to the Department of Earth and Space Sciences for their support of my graduate work. Departmental funds including the Harry Wheeler Fellowship and the David A. Johnston Award provided needed financial assistance. I am grateful to Servando De la Cruz-Reyna and Jose Luis Macías for supplying rock samples and vital data that made the study of Popocatépetl possible. Special thanks go to Gustavo Fuentealba and the entire staff of the Observatorio Volcanológico de los Andes del Sur for their generous and unfailing support of my research in Chile. Taber Hersum was a great field assistant for the 2001 field season at Villarrica. I want to thank Scott Kuehner for his unending patience with me in the electron microprobe lab. My reading committee Chris Newhall, Victor Kress, and George Bergantz provided valuable manuscript reviews and ideas. I am grateful for thorough reviews of my research on Popocatépetl by Tom Sisson, Michelle Coombs, Jake Lowenstern, and Charlie Bacon. Bob Breidenthal generously provided his expertise in fluid dynamics which made the Reynolds number and velocity scale calculations possible. I have appreciated words of encouragement and scientific advice from: Paul Wallace, Gordon Moore, Tobias Fischer, Pierre Delmelle, John Stix, Fraser Goff, Hugo Delgado, K. Kazahaya, H. Shinohara, Mike McCurry, Tony Irving, Bernard Evans, Mark Ghiorso, Dean Hegg, Nicole Métrich, Lizzette Rodriguez, and Andy Harris. I want to thank Col. Warren Dorlac, M.D. for placing his trust and faith in me as a budding volcano hazards specialist. Working with him at Villarrica was vital to reinvigorating my desire to finish my degree for the sake of pursuing volcano hazard mitigation projects that can make a difference in people's lives. Thanks go to the community of DOEASS grad students for many good times and especially to Nate Chutas, Michele Koppes, and Pete Apostle for friendship and commiseration. Thanks also to Charlie Vos for the use of his basement to build a sea kayak. I occupied his basement for far too long, but the manual labor of building a kayak provided a much needed diversion to my studies and helped preserve my sanity in the last year and a half of my degree. Special thanks to Jo Vos for many, many delicious dinners that kept me nourished and happy. This dissertation would never have been completed without the moral support and encouragement of my family ever since the day I said I wanted to become a volcanologist. Most of all, I would like to thank Amanda for her love, patience, and encouragement, without which I doubt I would have stuck it out through graduate school.

Dedication

To my parents,
Ray and Bunny Witter

INTRODUCTION

Many volcanoes have been observed to continually emit substantial quantities of volcanic gases over time periods ranging from years to millennia, with little to no accompanying eruption of magma. Observations such as these raise two questions. First, if little to no magma is erupted then what is/are the source(s) of such large gas emissions? For most volcanic eruptions, the source of gas emissions is thought to be the *erupted* magma itself. Second, what is the mechanism by which large quantities of volcanic gases can be transported to the earth's surface and emitted to the atmosphere *without* causing an explosive eruption? Sudden expansion of gas bubbles at or near the earth's surface is the driving force behind explosive volcanic eruptions, so the emission of large quantities of volcanic gases at a volcano might lead one to infer that explosive activity is likely. However, at passively degassing volcanoes, the opposite is true: large amounts of volatiles are released in a non-explosive manner.

Convection of magma in the volcanic conduit has been proposed to explain long-term, continuous, high rates of gas emission and heat loss at non-explosive, passively degassing volcanoes (Allard et al., 1994; Kazahaya et al., 1994; Allard, 1997; Harris and Stevenson, 1997; Harris et al., 1999; Simakin and Botcharnikov, 2001; Kazahaya et al., 2002). This hypothesis contends that volatile-rich magma ascends through a volcanic conduit to the surface or to very shallow levels in the volcano where magma-gas separation takes place. The degassed magma is not erupted but descends back down the conduit. A potential candidate for convection of magma in the volcanic conduit would be any volcano that: 1) emits large quantities of volatiles, 2) has no viable alternate sources of volatiles other than magma, 3) does not erupt sufficient quantities of magma to produce the observed gas emission, and for which 4) endogenous growth of the volcanic edifice from intruded magma is minimal. Conduit convection processes have been inferred at volcanoes that cover a wide spectrum of magma compositions from basaltic (e.g. Etna, Izu-Oshima), through andesitic and dacitic (e.g. Sakurajima, Mt. St. Helens), to rhyolitic (e.g. Satsuma-Iwojima). Although conduit convection may be a viable magma transport mechanism

at these and other volcanoes, direct observation of this process is lacking. A specific test for the feasibility of conduit convection at specific volcanoes as well as under a variety of magmatic conditions might provide support for the conduit convection hypothesis.

For this dissertation, I tested the hypothesis of convection of magma in volcanic conduits as a mechanism for long-term, high-flux, non-explosive degassing at two passively degassing subduction zone volcanoes, Popocatépetl (Mexico) and Villarrica (Chile), which span the range of magma compositions from dacite to basaltic andesite. During two field seasons in southern Chile, I measured the sulfur, chlorine, and fluorine flux from the summit crater of Villarrica volcano using a variety of techniques. Volatile flux data from Popocatépetl volcano was obtained from Mexican researchers (CENAPRED, unpubl. data; Delgado-Granados et al., 2001). In the laboratory at UW, I made detailed petrological and chemical analyses of samples of magma recently erupted from the two volcanoes in order to quantify the amounts of volatiles degassed from magma. To do this, I developed new techniques using the electron microprobe that achieve high precision, accuracy, and spatial resolution while maintaining low detection limits for the analysis of sulfur, chlorine, and fluorine in minerals and volcanic glasses. Alternate sources of volatile emissions (other than magma), such as breakdown of sulfur-bearing magmatic phases, degassing from static unerupted magma, fumarolic remobilization of vapor phase precipitates, and assimilation of volatile bearing basement rocks were assessed and quantified where possible. With the chemical data obtained from Popocatépetl and Villarrica magmas, I used current models to calculate physical parameters of the magma such as viscosity and density. These physical parameters were input into previously derived analytical equations for convection of magma in conduits (Stevenson and Blake, 1998) to estimate the size of conduit radii and magma ascent velocities. Lastly, I calculated the Reynolds number and velocity scale for convection of magma in volcanic conduits over a wide range of magma viscosities, buoyancy fluxes, conduit sizes, and conduit geometries. These calculations critically tested the

plausibility of magma convection in the conduit at Popocatépetl and Villarrica and can be employed for other volcanoes as well.

Chapter 1:

Petrology and Intensive Variables of the 1994 – Present Mixed Magmas of Volcán Popocatépetl, Mexico

Introduction

From December 1994 until the time of writing, Volcán Popocatépetl (Mexico) has been characterized by minor eruptive activity and lava dome growth with accompanying high-flux gas emissions (Delgado and Cárdenas-G, 1997; Delgado-Granados et al., 2001; National Center for Disaster Prevention, Mexico City (CENAPRED), unpubl. data). Visual observations suggest that the current eruptive period is similar to other historic periods of unrest. This relatively benign, long-term, low-level volcanic activity, however, is in dramatic contrast to the highly explosive Plinian eruptions that have shaken Popocatépetl on at least three occasions in the Holocene (Siebe *et al.*, 1996a).

The question of why a volcano occasionally erupts explosively while at other times exhibits only minor eruptive activity over an extended time period represents a fundamental issue in volcanology. The dramatic contrast between the explosive and non-explosive eruptive styles exhibited by Popocatépetl makes it a prime candidate for closer study. We focus on pumices and dome rocks from the current eruptive period as examples of non-explosive volcanism at this volcano.

Eruptive products from Popocatépetl commonly show evidence of magma mixing (Cantagrel et al., 1984; Robin, 1984; Boudal and Robin, 1988; Kolisnik, 1990). By magma mixing we refer to both magma hybridization (homogenization of distinct magma batches) and magma mingling (incomplete mechanical mixing of magmas for which chemically and/or visually distinct materials remain). The 1994-present magmas show clear evidence of magma mixing between distinct mafic and silicic end-members in the form of banded and hybridized pumice as well as hybridized lava (Athanasopoulos, 1997; Straub and Martin-Del Pozzo, 2001). This

chapter focuses on the petrology and intensive variables of magmas participating in the recent eruptive activity at Popocatépetl. The goal of this chapter is to quantify the pre-eruptive compositions as well as P, T, f_{O_2}, and f_{S_2} conditions for the two dominant mixing end-members.

Background and Geologic Setting

Popocatépetl (5452 m) is an andesitic stratovolcano that lies ~60 km SE of Mexico City (Figure 1). It is part of the E-W trending Trans-Mexican Volcanic Belt, associated with north-dipping subduction of the Cocos plate beneath the North American plate. Popocatépetl lies at the southern end of the N-S trending Sierra Nevada range that consists of older volcanoes including Iztaccíhuatl (Nixon, 1988a; Nixon, 1988b). Holocene eruptive activity at Popocatépetl included at least three Plinian eruptions, the most recent of which destroyed human settlements in ~800 A.D. (Siebe et al., 1996a; Siebe et al., 1996b; Panfil et al., 1999). Aztec codices record the first historic activity at Popocatépetl in 1354 A.D. (De la Cruz-Reyna *et al.*, 1995). Since that time, Popocatépetl has experienced at least twelve periods of significant unrest, all of which exhibited volcanic activity similar to the 1994-present eruptive period (De la Cruz-Reyna *et al.*, 1995). No Plinian or ignimbrite-forming eruption has occurred at Popocatépetl in historic time.

After nearly 70 years of dormancy, Volcán Popocatépetl began a new period of activity in December 1994 (De la Cruz-Reyna and Siebe, 1997). Elevated levels of degassing, seismicity, and phreatic explosions characterized the initial portion of volcanic unrest at Popocatépetl through early 1996. In March 1996, a dacitic lava dome extruded into the summit crater, (GVN, 1996; De la Cruz-Reyna *et al.*, unpubl. data; Stimac *et al.*, 1997). Since the onset of the current eruptive period, Popocatépetl has continuously degassed at high rates accompanied by relatively minor eruptions. Eruptive activity includes: Vulcanian explosions that eject lithic and juvenile ash and rock debris up to 8 km above the vent; ash-poor "exhalations" of volcanic gas; and

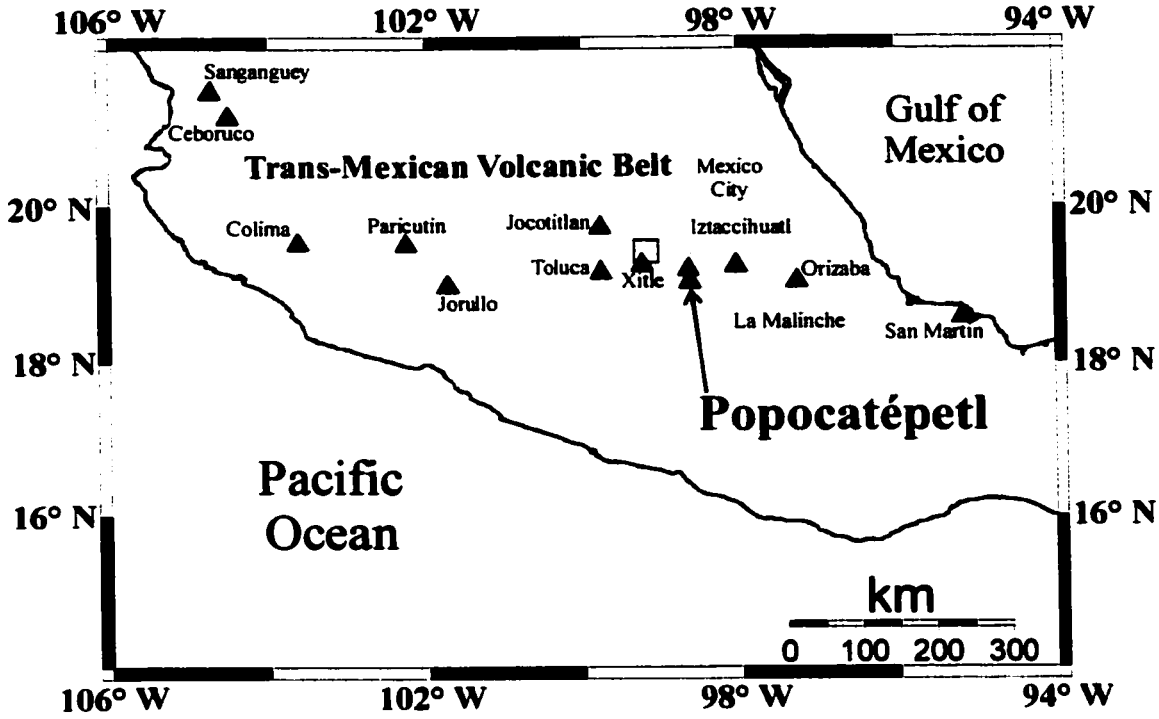

Figure 1. Location map for Popocatépetl. Holocene volcanoes are denoted by *solid triangles* and labeled. Mexico City is shown with an *open square*. Map made with GMT (Wessel & Smith, 1991).

periodic lava dome growth, subsidence, and explosive destruction (De la Cruz-Reyna *et al.*, unpubl. data).

Previous work

Aguilera & Ordoñez (1895) conducted the first geological investigations of Popocatépetl volcano. Their work consisted of surficial mapping of volcanic deposits and a description of the geographical features of the volcano. A series of papers describe Popocatépetl's eruptive period that occurred in the 1920's (Friedlaender, 1921; Waitz, 1921; Camacho, 1925a; Camacho, 1925b; Quintero, 1925; Atl, 1939). Dome explosions and degassing of that period appear to have been similar to the activity occurring at present.

During the 1980's various workers studied the volcanic geology and petrology of Popocatépetl (Cantagrel et al., 1984; Robin, 1984; Robin and Boudal, 1987; Boudal and Robin, 1988; Boudal and Robin, 1989). They pointed out the importance of magma mixing as a petrogenetic process at Popocatépetl, documented giant sector collapse events, and drew renewed attention to the risks associated with future eruptions from the volcano. Kolisnik (1990) studied phenocryst zoning and heterogeneity in Quaternary-to-recent lavas of the Popocatépetl edifice and found ubiquitous evidence for periodic basalt-dacite magma mixing.

Renewal of eruptive activity at Popocatépetl in 1994 stimulated extensive new research on the eruptive history, petrology, and degassing behavior of the volcano (CENAPRED-UNAM, 1995). Martin-Del Pozzo *et al.* (1995) studied ash generated by the phreatic explosions of December 1994 to March 1995. Apart from the typical andesitic mineral assemblage and a rhyolitic glass fraction, they identified gypsum and other sublimates and characterized the ash as non-juvenile material.

Athanasopoulos (1997) conducted a mineralogic and petrologic study of Popocatépetl's March 1996 lava dome, the first magmatic material emitted in the volcano's current period of activity. The March 1996 dome contains a disequilibrium phenocryst assemblage interpreted to reflect magma mixing. The silicic mixing end-

member was inferred to be a dacite magma (900-970 °C, f_{O_2} = ΔNNO=+0.5 to +1.5 log units). The mafic end-member was proposed to be a primitive "sanukitoid" basalt that periodically replenishes the silicic magma chamber. Based on analysis of reaction rims on amphibole grains, Athanasopoulos (1997) concluded that magma took 11-14 days to ascend and erupt in Popocatépetl's summit crater after the mixing event.

Straub & Martin-Del Pozzo (2001) studied the mineralogy and petrology of juvenile tephra samples from eruptions between 1996 and 1998. Their goal was to investigate the causes of magma diversity in thick crusted volcanic arcs. They conclude that the erupted magmas are the result of mixing a magnesian andesite (55-62 wt.% SiO_2, 1085-1170 °C, f_{O_2} ~ QFM, Ni-rich, and several wt.% dissolved H_2O) with a more evolved magma (~950 °C) at depths of ~ 4 to 13 km.

Analytical Methods

Whole Rock Analyses

Major and trace element compositions of four pumice lumps and dome rocks from the current eruptive period were analyzed by X-ray Fluorescence at the WSU Geoanalytical Laboratory or by fusion ICP-MS at Activation Laboratories, Ontario, Canada. To augment our data set of whole rock analyses we flash-melted selected portions of eight more pumice lumps and dome rocks from the same sample suite. The resulting glass beads were analyzed for major elements by EPMA. This method enabled us to obtain a bulk chemical analysis of small, uniform portions of compositionally banded pumice and dome rock. All samples were ground in mortar and pestle then melted in a platinum crucible at 1350 °C for 10 minutes. The resulting glass was reground in mortar and pestle, re-melted at 1350 °C for 10 more minutes, and then quenched in water. EPMA analytical conditions are the same as for glass analyses.

Electron Probe Microanalysis (EPMA)

All EPMA analyses were conducted on a 4-spectrometer JEOL 733 Superprobe at the University of Washington. Mineral analyses were conducted at 15 kV accelerating voltage, ~1-3 μm beam diameter, and 10-25 nA beam current with a maximum count time of 40 seconds for each element. Elements were calibrated using mineral standards, which were also analyzed at the end of each analytical session to check for instrumental drift. Matrix effects were corrected using the ZAF model of Armstrong (1984).

Volatile elements S, Cl, and F were analyzed in apatite and hornblende using an improved analytical method originally developed by T. Thordarson at the University of Hawaii (Thordarson *et al.*, 1996). With this method, we achieved low minimum detection limits while maintaining high analytical precision and accuracy. Analytical conditions were 15 kV accelerating voltage, 100 nA beam current, 5 μm beam diameter, and 400 second total peak count time. To minimize volatile loss, an iterative scheme was employed in which the beam was blanked for ten seconds every ten seconds. This periodic beam blanking reduced sample heating from the electron beam, thus reducing volatile loss. Sulfur and chlorine were analyzed using PET diffraction crystals with the spectrometer aperture window set at its widest setting to maximize the number of X-ray counts. Fluorine was analyzed using an LDE1 diffraction crystal. Fluorine analysis in hornblende proved challenging due to peak overlap problems with the Fe $K\alpha$ line. We created an empirical correction factor for F by analyzing several F-free standards of varying Fe content. We calculated the amount of interference with the F-analysis as a function of Fe and incorporated this correction into the iterative analytical routine (see Appendix A). Since the volatile elements were analyzed in a separate analytical session, we reprocessed the volatile data with the major element data to correct for matrix effects. Prior to each analytical session, volatile elements were calibrated on the following standards: celestite (sulfate sulfur), Scapolite 17120 (chlorine), and Synthetic F-phlogopite (fluorine). Analytical accuracy was checked using basalt glass standards VG-2 and A-99.

Minimum detection limits are calculated to be 24 ppm for sulfur, 16 ppm for chlorine, and 52 ppm for fluorine. Reproducibility of S, Cl, and F analyses was also tested on VG-2 and A-99. The 1σ variations for more than 30 analyses are 1½% at 1500 ppm and 13% at 140 ppm for sulfur, 9% at 200 ppm for chlorine, and 5% at 750 ppm and 12% at 300 ppm for fluorine.

Major element glass analyses were performed at 15 kV accelerating voltage and 10 nA with a 5 μm beam diameter and maximum count time of 40 seconds for each element. Before and after each analytical session, accuracy was checked on glass standards VG-568 (rhyolite) or VG-2 and A-99 (basalts) depending on the composition of the unknown glass. The combination of analyzing sodium first and a defocused beam minimized Na-loss during analysis. Plots of intensity vs. time suggest Na-loss of <0.2 wt.% Na_2O over a 40-second count time using an anhydrous glass standard. Na-loss during analysis of glass inclusions, however, may be significant due to enhanced Na-mobility in hydrous glasses (Devine *et al.*, 1995). No correction was applied for this potential alkali-loss in hydrous inclusions. Matrix effects were corrected using the ZAF model of Armstrong (1984). Mean standard errors as well as errors based on counting statistics for the major element mineral and glass analyses are shown in Tables 1 & 2.

Sulfide/sulfate analyses of glasses were performed by measuring the wavelength shift of the sulfur $K\alpha$ X-ray peak (Carroll and Rutherford, 1988). Analytical conditions were: 7 kV accelerating voltage, 80 nA beam current, and 10 μm beam diameter. We collected x-ray counts simultaneously from two PET diffraction crystals with the spectrometer aperture window set at its narrowest setting to maximize the spatial resolution of the spectrometer's position. The separation between S^{+6} and S^{-2} is 0.00032 sinθ units. We performed wavelength scans across 0.00072 sinθ units in 0.000018 sinθ unit steps counting 30 seconds at each step to fully define the curve of the sulfur peak. The electron beam was blanked for 30 seconds between each step to allow the sample to cool. The low accelerating voltage combined with blanking the beam minimized the effects of element mobility and

Table 1. Mean error associated with analysis of mineral and glass standards (in wt.%)

	Olivine 174			Olivine 197			Sawyer Ilmenite		
	This study[a]	1σ [b]	Accepted[c]	This study[a]	1σ [b]	Accepted[c]	This study[a]	1σ [b]	Accepted[c]
SiO_2	40.79	0.51	40.50	38.45	0.16	38.50	0.08	0.02	n/a
TiO_2	n/a	n/a	n/a	n/a	n/a	n/a	51.17	0.37	51.55
Al_2O_3	n/a	n/a	n/a	n/a	n/a	n/a	0.01	0.01	0.02
Cr_2O_3	n/a	n/a	n/a	n/a	n/a	n/a	0.00	0.00	n/a
FeO^T	9.38	0.11	9.37	18.80	0.16	18.90	46.03	0.20	45.60
MnO	0.14	0.02	0.13	0.19	0.09	0.26	1.61	0.03	1.43
MgO	49.44	0.37	49.20	40.66	0.19	41.65	0.20	0.01	0.26
CaO	0.02	0.01	0.00	0.18	0.02	0.18	0.00	0.01	n/a
NiO	0.38	0.04	0.38	0.03	0.06	0.15	0.01	0.01	n/a
Total	100.15		99.58	98.31		99.64	99.11		98.86
n	6			6			6		

	KH-1 Cpx			Cpx 6927			Alpine Opx		
	This study[a]	1σ [b]	Accepted[c]	This study[a]	1σ [b]	Accepted[c]	This study[a]	1σ [b]	Accepted[c]
SiO_2	49.46	0.45	49.12	51.86	0.37	51.75	50.67	0.51	50.71
TiO_2	0.87	0.04	0.88	0.51	0.01	0.54	0.49	0.02	0.53
Al_2O_3	8.98	0.09	9.11	5.42	0.10	5.14	6.30	0.11	6.05
Cr_2O_3	0.06	0.00	0.06	0.65	0.02	0.61	0.03	0.01	0.03
FeO^t	6.04	0.07	6.05	4.00	0.14	3.80	14.49	0.27	14.60
MnO	0.12	0.02	0.15	0.09	0.01	0.10	0.25	0.02	0.22
NiO	0.02	0.01	n/a	0.05	0.02	n/a	0.03	0.02	n/a
MgO	15.62	0.24	15.74	15.70	0.35	16.08	25.66	0.38	26.15
CaO	17.97	0.36	17.80	21.09	0.24	20.98	1.62	0.03	1.64
Na_2O	1.01	0.05	1.05	0.88	0.04	0.90	0.10	0.02	0.12
Total	100.14		99.96	100.25		99.90	99.64	0.66	100.05
n	7			12			13		

Table 1. continued.

52NL11 Cr-spinel

	This study[a]	1σ [b]	Accepted[c]
SiO_2	0.02	0.02	n/a
TiO_2	0.43	0.04	0.45
Al_2O_3	19.49	0.10	19.40
Cr_2O_3	44.45	0.29	44.55
FeO^T	21.35	0.15	22.12
MnO	0.31	0.01	0.33
MgO	12.10	0.10	12.20
CaO	0.01	0.01	n/a
NiO	0.12	0.02	0.07
Total	98.27		99.12
n	5		

Kakanui Hornblende*

	This study[a]	1σ [b]	Accepted[c]
SiO_2	40.53	0.34	40.37
TiO_2	4.70	0.18	4.77
Al_2O_3	14.47	0.12	14.60
Cr_2O_3	n/a	n/a	n/a
FeO^t	10.49	0.08	10.92
MnO	0.06	0.00	0.09
MgO	12.18	0.33	12.80
CaO	9.82	0.13	10.10
Na_2O	2.43	0.27	2.45
K_2O	2.06	0.03	2.01
P_2O_5	n/a	n/a	n/a
Total	96.73		98.11
n	2		
F	0.18	0.01	0.14

Opx sp-18

	This study[a]	1σ [b]	Accepted[c]
SiO_2	50.50	0.14	51.13
TiO_2	0.08	0.01	0.09
Al_2O_3	3.05	0.07	2.65
Cr_2O_3	0.00	0.00	0.01
FeO^T	24.49	0.28	24.14
MnO	0.72	0.02	0.75
NiO	0.01	0.01	n/a
MgO	20.84	0.19	20.30
CaO	0.26	0.02	0.33
Na_2O	0.03	0.01	n/a
Total	99.99		99.40
n	5		

VG-2 Glass

	This study[a]	1σ [b]	Accepted[c]
SiO_2	50.61	0.45	50.92
TiO_2	1.81	0.13	1.85
Al_2O_3	13.57	0.20	14.09
Cr_2O_3	0.02	0.02	0.00
FeO^T	11.60	0.17	11.86
MnO	0.21	0.03	0.22
MgO	6.84	0.20	6.73
CaO	10.72	0.06	11.14
Na_2O	2.68	0.07	2.63
K_2O	0.20	0.02	0.19
P_2O_5	0.23	0.01	0.20
Total	98.38		99.84
n	9		

Table 1. continued.

	VG-568 Glass			Anorthoclase 2110F			A-99 Glass		
	This study[a]	1σ [b]	Accepted[c]	This study[a]	1σ [b]	Accepted[c]	This study[a]	1σ [b]	Accepted[c]
SiO_2	76.59	0.36	76.75	64.42	0.10	64.38	50.91	0.54	51.04
TiO_2	0.09	0.05	0.12	0.02	0.02	0.02	3.94	0.22	4.07
Al_2O_3	11.96	0.14	12.07	20.56	0.13	20.96	12.29	0.34	12.51
Cr_2O_3	0.02	0.06	0.00	0.00	0.00	0.00	0.01	0.01	0.00
FeO^T	1.20	0.05	1.23	0.12	0.06	0.16	13.31	0.23	13.33
MnO	0.04	0.03	0.03	0.01	0.01	0.00	0.19	0.04	0.15
MgO	0.04	0.01	0.10	0.01	0.01	0.04	5.01	0.15	5.09
CaO	0.44	0.04	0.50	1.22	0.10	1.20	9.12	0.10	9.32
Na_2O	3.63	0.24	3.75	8.57	0.14	8.58	2.65	0.13	2.67
K_2O	4.95	0.11	4.89	3.25	0.15	3.30	0.84	0.04	0.82
P_2O_5	0.01	0.01	0.01	0.02	0.01	0.00	0.44	0.03	0.38
Total	98.96		99.45	98.18		98.64	98.55		99.37
n	14			6			17		

[a] EPMA analysis from this study

[b] Standard deviation of the analyses

[c] Value accepted in the literature

* Kakanui Hornblende inhomogeneous in Fe and Mg

n = number of analyses, n/a = not analyzed, FeO^T = all Fe as FeO

Adequate standards not used in the calibration were not available to check analytical accuracy of plagioclase, apatite, and sulfide

Table 2. Average relative errors based on counting statistics for analyses of minerals and glasses

	Cr-sp	Ilm	Ti-Mgt	Ol	Opx	Cpx	Hbl	Plag	Glass		Sulfide
Si	19.0%	24.0%	7.8%	0.5%	0.4%	0.4%	0.6%	0.6%	0.5%	O	10.9%
Ti	4.7%	1.1%	1.6%	n/a	5.6%	3.5%	3.4%	n/a	8.1%	S	1.4%
Al	0.7%	3.9%	1.3%	n/a	1.5%	1.0%	0.6%	0.8%	0.9%	Fe	0.9%
Cr	0.6%	25.5%	8.0%	n/a	27.9%	36.4%	n/a	n/a	62.5%	Cu	11.6%
Fe	0.6%	0.7%	0.7%	0.9%	1.1%	1.2%	0.9%	7.7%	2.4%	Ni	2.0%
Mn	4.1%	6.0%	4.6%	6.2%	4.3%	6.0%	12.0%	n/a	48.3%	Si	10.8%
Ni	15.1%	67.2%	38.7%	7.6%	56.3%	48.9%	n/a	n/a	n/a		
Mg	0.7%	1.3%	1.3%	0.5%	0.6%	0.7%	0.6%	30.1%	1.7%		
Ca	35.9%	27.7%	14.8%	8.1%	1.6%	0.7%	0.8%	1.2%	1.7%		
Na	n/a	n/a	n/a	n/a	12.9%	2.7%	1.5%	1.4%	2.3%		
K	n/a	n/a	n/a	n/a	n/a	n/a	3.7%	6.3%	4.4%		
P	n/a	n/a	n/a	n/a	n/a	n/a	n/a	n/a	6.5%		

Cr-sp = chromian spinel, Ilm = ilmenite, Ti-mgt = titanomagnetite, Ol = olivine, Opx = orthopyroxene, Cpx = clinopyroxene, Hbl = hornblende, Plag = plagioclase, n/a = not analyzed

oxidation during analysis (Metrich and Clocchiatti, 1996). Analytical accuracy of the method was checked on basalt glass standard VG-2 and NBS soda-lime glass 620. Minimum sulfur content necessary to adequately define the sulfur peak at these analytical conditions is ~500 ppm.

Results

Rock samples used in this study were obtained from small explosive events that occurred in June and December 1997 and January, March, and April 1998. All samples represent juvenile magma and were initially studied under the petrographic microscope. We focused our analytical efforts on pumice lapilli from the eruption of June 30, 1997 and dense blocks of dome material from the eruption of January 1, 1998. The mineralogy of the dome rocks from explosive events in December 1997 and January, March, and April 1998 is identical to the mineralogy of the pumiceous samples of the June 30, 1997 eruption. The rapid quenching of lapilli from the June 30, 1997 eruption made these samples more suitable for our analysis by electron microprobe. Complete sample descriptions can be found in Appendix B.

Petrography and igneous textures

Recent Popocatépetl eruptive products contain phenocrysts and microphenocrysts of olivine, clinopyroxene, orthopyroxene, plagioclase and hornblende. Microphenocrysts of titanomagnetite, ilmenite, and rare apatite are distributed in a microcrystalline groundmass. Chromian spinel commonly occurs as inclusions in olivine. Titanomagnetite and ilmenite occur as inclusions in pyroxene and rarely in plagioclase. Apatite and rare globular sulfide are also found as inclusions, most commonly in pyroxene. Anhedral xenocrysts of quartz are rare. The groundmass varies from light to dark in color. Dark groundmass consists of a dense network of plagioclase and Fe-Ti oxide microlites in brown glass. Light-colored groundmass contains sparse plagioclase microlites in colorless glass.

Olivine (0.1 to 1.5 mm) comes in two types. Larger-sized olivine (>0.5 mm) are the more abundant and are generally subhedral. They contain abundant chromian spinel inclusions (~15 μm diameter) but do not contain glass inclusions. Some of the large-sized, Cr-spinel-rich olivines occur as glomerocrysts of two or more crystals. Some of these glomerocrysts as well as some individual grains of olivine are anhedral and display embayed margins that have reacted extensively with the surrounding silicate liquid. We suggest that these large, Cr-spinel-rich olivines are probably xenocrystic cumulate.

The other type of olivine, microphenocrystic (<0.3 mm), is much less abundant. Some have a skeletal (arrow-shaped) habit suggesting rapid precipitation from the surrounding silicate melt. Olivine microphenocrysts contain few, if any, chromian spinel inclusions but do contain 5-40 μm diameter inclusions of clear brown glass.

Hornblende phenocrysts commonly have an acicular habit and are up to 1 mm in length. More equant hornblende microphenocrysts are generally 0.2 x 0.3 mm in size. All hornblendes have dark "gabbroic-type" (Garcia and Jacobson, 1979) breakdown rims 30-100 μm across made of tiny plagioclase, pyroxene, Fe-Ti oxides, and rare sulfides. Rare hornblende phenocrysts and microphenocrysts possess small plagioclase or pyroxene cores. Some hornblende form partial overgrowths on olivine and pyroxene. Glass inclusions in hornblende are rare.

Whole rock analyses

The March 1996 dome samples (Athanasopoulos, 1997) are silicic andesite to dacite, as are the January 1998 dome samples (Table 3, Figure 2). Brown and white pumice, erupted in June 1997 are compositionally distinct. Brown pumice is andesitic, whereas white pumice is intermediate in composition between brown pumice and the 1996 and 1998 dome rocks. Whole rock data suggest no systematic change in major or trace element composition with time.

Table 3. Whole rock analyses for Popocatépetl

Eruption date	6/30/97		6/30/97		6/30/97		6/30/97	6/30/97		6/30/97		6/30/97
Color Description	Brown Pumice		Brown Pumice		Brown Pumice		Brown Pumice	White Pumice		White Pumice		White Pumice
Label	D		E		F		Dk	G		H		Lgt
Method	EPMA[1]	1σ	EPMA[1]	1σ	EPMA[1]	1σ	ICP[2]	EPMA[1]	1σ	EPMA[1]	1σ	ICP[2]
SiO_2	59.38	0.53	58.46	1.08	57.97	0.36	58.48	61.69	1.77	62.27	1.01	63.28
TiO_2	1.00	0.07	0.91	0.07	0.91	0.12	0.92	0.82	0.61	0.66	0.14	0.73
Al_2O_3	15.80	0.45	14.91	1.12	15.83	0.45	16.14	16.31	1.97	15.29	0.82	16.67
Cr_2O_3	0.02	0.02	0.03	0.02	0.03	0.04	0.14	0.02	0.02	0.03	0.02	0.04
FeO	5.54	0.18	6.13	0.65	5.81	0.17	5.95	4.93	1.42	5.14	0.59	4.57
MgO	5.74	0.36	7.70	1.40	6.43	0.21	7.00	4.51	1.27	5.39	0.79	3.57
MnO	0.12	0.02	0.10	0.02	0.10	0.04	0.10	0.09	0.05	0.09	0.03	0.10
CaO	6.29	0.19	6.36	0.37	6.27	0.10	6.27	5.57	0.67	5.39	0.43	5.08
Na_2O	4.19	0.16	3.84	0.35	4.22	0.27	4.23	4.23	0.33	4.13	0.24	4.59
K_2O	1.34	0.07	1.22	0.17	1.32	0.06	1.35	1.54	0.21	1.48	0.14	1.82
P_2O_5	0.25	0.08	0.26	0.07	0.23	0.03	0.22	0.22	0.08	0.19	0.06	0.17
Total	99.67		99.93		99.09		100.66	99.92		99.97		100.58
n	10		8		8		1	12		9		1
NiO (ppm)	n/a		n/a		n/a		191	n/a		n/a		74

Table 3. Continued

Eruption date	1/1/98		1/1/98		1/1/98		1/1/98	1/1/98
Color	Grey		Grey		Grey		Grey	Grey
Description	Dome rock		Dome rock		Dome rock		Dome rock	Dome rock
Label	A		B		C		BAND	LGT
Method	EPMA[1]	1σ	EPMA[1]	1σ	EPMA[1]	1σ	XRF[3]	XRF[3]
SiO_2	63.77	0.61	63.18	0.45	63.22	0.53	63.47	63.73
TiO_2	0.73	0.08	0.66	0.05	0.70	0.03	0.71	0.69
Al_2O_3	16.50	0.09	16.26	0.17	16.44	0.08	16.40	16.50
Cr_2O_3	0.02	0.02	0.02	0.02	0.01	0.02	0.03	0.03
FeO	4.24	0.13	4.36	0.05	4.44	0.10	3.91	3.91
MgO	3.18	0.05	3.42	0.02	3.46	0.08	3.25	3.04
MnO	0.06	0.04	0.09	0.04	0.07	0.04	0.08	0.08
CaO	4.64	0.11	4.62	0.04	4.88	0.15	4.94	4.80
Na_2O	4.31	0.03	4.39	0.04	4.41	0.32	4.56	4.62
K_2O	1.89	0.03	1.83	0.02	1.78	0.03	1.81	1.85
P_2O_5	0.19	0.08	0.17	0.01	0.15	0.07	0.16	0.16
Total	99.51		99.00		99.55		99.29	99.38
n	5		5		5		1	1
NiO (ppm)	n/a		n/a		n/a		65	61

[1]EPMA analyses conducted on flash-melted whole rock powders

[2]Fusion ICP analyses (J.-L. Macías, unpubl. data)

[3]XRF analyses performed at WSU Geoanalytical Lab

n = number of analyses; 1σ = standard deviation of the EPMA analyses

Figure 2. Compositional variations of SiO_2 versus **a)** MgO, **b)** Al_2O_3, **c)** FeO, **d)** CaO, **e)** NiO, **f)** Na_2O, and **g)** K_2O for whole rocks from the recent eruptions of Popocatépetl. Samples from this study include brown pumice from the June 30, 1997 eruption (*open triangles*), white pumice from the June 30, 1997 eruption (*open circles*), gray dome rock from the January 1, 1998 eruption (*open diamonds*). *Crosses* represent whole rock analyses of the March 1996 dome (Athanasopoulos, 1997). *X's* are whole rock data from various eruptions of Popocatépetl between 1996 and 1998 (Straub & Martin-Del Pozzo, 2001). A least squares linear regression has been fit to the data. R^2 statistics are shown. Open stars are MELTS-derived magmatic end member bulk compositions (see text for explanation). All Fe is reported as FeO.

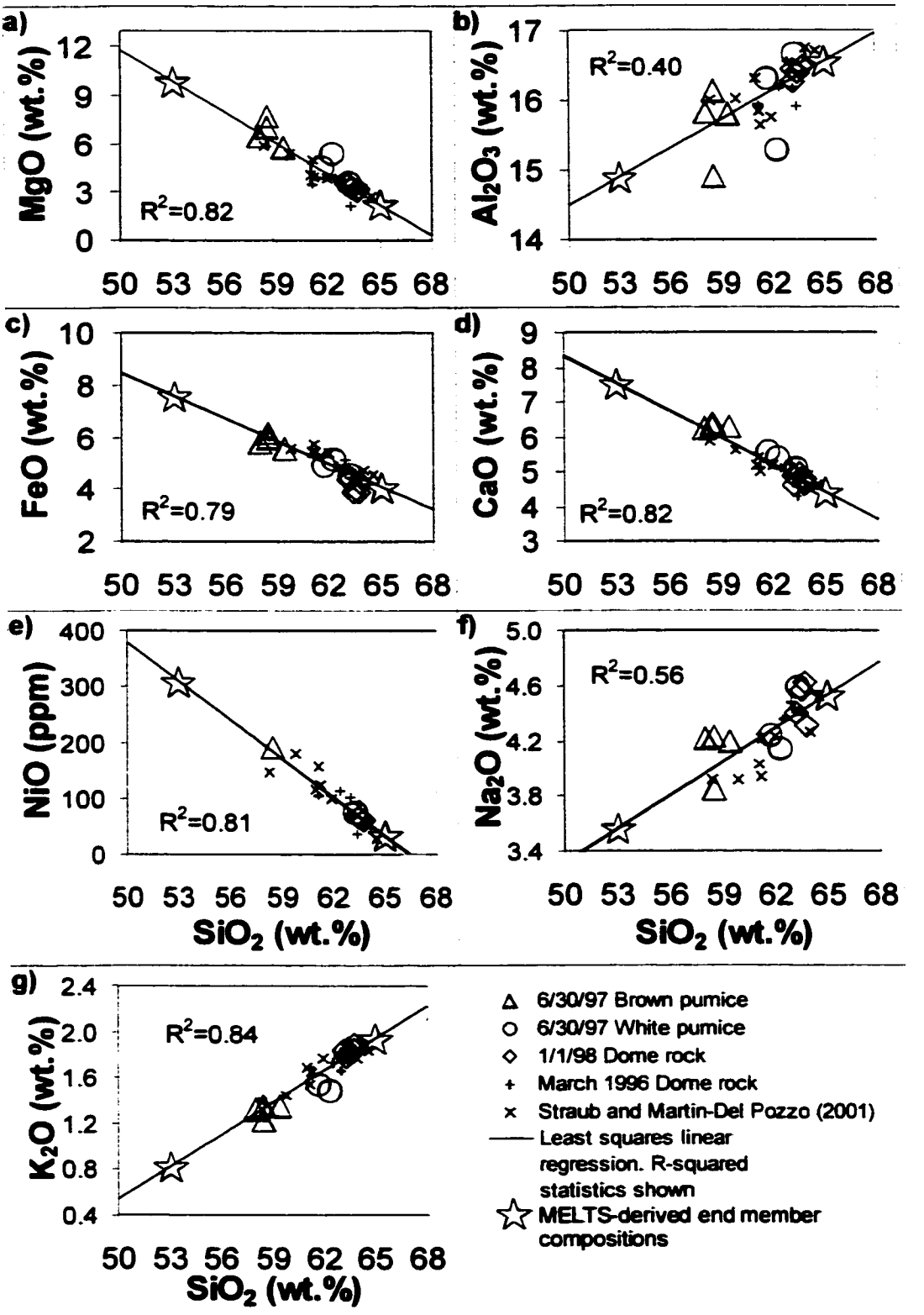
a)
MgO (wt.%)
12
9
6
3
0
R²=0.82
50 53 56 59 62 65 68
b)
Al2O3 (wt.%)
17
16
15
14
R²=0.40
50 53 56 59 62 65 68
c)
FeO (wt.%)
10
8
6
4
2
R²=0.79
50 53 56 59 62 65 68
d)
CaO (wt.%)
9
8
7
6
5
4
3
R²=0.82
50 53 56 59 62 65 68
e)
NiO (ppm)
400
300
200
100
0
R²=0.81
50 53 56 59 62 65 68
SiO2 (wt.%)
f)
Na2O (wt.%)
5.0
4.6
4.2
3.8
3.4
R²=0.56
50 53 56 59 62 65 68
SiO2 (wt.%)
g)
K2O (wt.%)
2.4
2.0
1.6
1.2
0.8
0.4
R²=0.84
50 53 56 59 62 65 68
SiO2 (wt.%)
6/30/97 Brown pumice
6/30/97 White pumice
1/1/98 Dome rock
March 1996 Dome rock
Straub and Martin-Del Pozzo (2001)
Least squares linear regression. R-squared statistics shown
MELTS-derived end member compositions

Modes and mineral chemistry

The relative abundance of mineral phases in Popocatépetl's recent eruptives is: plagioclase > orthopyroxene ≈ clinopyroxene > olivine > ilmenite ≈ titanomagnetite ≈ hornblende > chromian spinel ≈ apatite > sulfide. Modal analyses are shown in Table 4. A short summary of the modal mineralogy and important mineral chemistry data are presented here. A description of the modal analysis procedures and complete analyses of all mineral phases are given in Appendix B.

Olivine

Large, Cr-spinel-rich olivine xenocrysts (Table 5) contain broad, compositionally uniform cores (Fo_{87-91}) with narrow (20-70 μm) normally zoned rims (Fo_{73-88}). Glass inclusion-bearing olivine microphenocrysts also have uniform cores but have a lower Fo-content and more limited compositional range (Fo_{84-86}). High NiO content (= 2300-6700 ppm) varies sympathetically with Fo_{87-91} in the olivine phenocrysts (Figure 3). Glass inclusion-bearing olivine microphenocrysts, however, have much lower NiO (= 1100-1800 ppm) for Fo_{84-86}.

Pyroxene

Pyroxenes from this study are characterized by broad, compositionally uniform cores with or without narrow, zoned rims. Both orthopyroxene and clinopyroxene fall into high-Mg# and low-Mg# groups based on core compositions ($Mg\# = Mg/Mg+Fe^{+2}$; Figure 4; Table 6). A few pyroxene grains do not fit into either grouping. Plots of SiO_2, Al_2O_3, and Cr_2O_3 vs. Mg# further delineate the two groups for both clino- and orthopyroxene (Figure 5).

Hornblende

Popocatépetl hornblende has a restricted compositional range (Table 7) with Mg# = 63-72 ($Mg\# = Mg/Mg+Fe^{T}$), Al_2O_3 = 9-13 wt.%, low concentrations of Cl (~200 ppm) and high F (2100 – 5400 ppm). This contrasts with some subduction zone volcanoes such as Unzen and Montserrat that erupt magmas containing two compositionally distinct amphiboles.

Table 4. Modal analyses by point counting

Sample	Ol	Plag	Opq	Px	Amph	Total Phenos & µphenos	Grndmss[1]	Plag µlite[2]	Total Grndmss	Vesic	# Points
PopoPum 6/30/97 #2 (white pumice)	tr.	23.3	0.4	15.2	0.2	39.1	54.4	6.6	61.0	57.0	1300
PopoPum 6/30/97 d (white pumice)	0.7	19.3	0.2	10.5	0.9	31.6	67.3	1.1	68.4	66.5	1312
PopoPum 6/30/97 c (white pumice)	3.1	32.3	0.5	7.9	tr.	43.8	35.0	21.4	56.4	52.0	1295
Popo 6/30/97 mixa (banded pumice)	1.8	13.3	0.5	4.3	0.5	20.4	40.7	38.9	79.6	31.8	1300
PopoSC 6/30/97 a (brown pumice)	2.9	8.5	tr.	3.7	tr.	15.1	51.3	33.5	84.8	50.2	1300
PopoSC 6/30/97 b (brown pumice)	5.4	7.4	0.1	5.8	0.1	18.8	44.2	37.1	81.3	45.7	1300
PopoPum 1/1/98 e (gray dome rock)	2.0	46.4	1.5	10.7	1.1	61.7	35.6	2.7	38.3	49.2	1300
PopoPum 1/1/98 g (gray dome rock)	1.5	46.3	2.0	10.8	0.5	61.1	35.0	3.8	38.8	48.4	1540
Popo 4/30/96 A2 (1996 dome)[3]	1.6	25.5	n.r.	5.4	4.1	36.6	63.4	n.r.	63.4	n.r.	1466
Popo 4/30/96 B (1996 dome)[3]	1.1	25.7	n.r.	6.5	2.8	36.1	63.9	n.r.	63.9	n.r.	1624

Results are volume percentages of phenocrysts+microphenocrysts in two dimensions calculated vesicle free; tr. = trace amount; n.r. = not reported
Ol=olivine, Plag=plagioclase, Opq=Fe-Ti oxide or sulfide, Px=clino- or orthopyroxene, Amph=amphibole, Vesic=vesicularity, Grndmss=groundmass
Phenos = Phenocrysts > 300 microns; µphenos = microphencrysts = 30-300 microns; µlite = microlites < 30 microns (after Wilcox, 1954)

[1]includes pyroxene and Fe-Ti oxide microlites as well as matrix glass
[2]Plagioclase microlites are the most common mineral phase in the groundmass. They are counted separately as a measure of the crystallinity of the groundmass.

[3]Data from Athanasopoulos (1997)

Table 5. EPMA analyses of olivine (in wt.%)

	Label	SiO_2	MgO	FeO	MnO	CaO	NiO	Total	Fo
Xenocrysts	ol1corets1	40.3	48.3	10.8	0.14	0.13	0.42	100.0	88.9
	ol1rimats1	40.5	47.6	12.1	0.15	0.14	0.34	100.8	87.5
	ol1rimbts1	40.0	47.2	12.6	0.20	0.13	0.30	100.4	87.0
	ol3corets1	40.5	49.1	10.2	0.14	0.12	0.47	100.5	89.6
	ol3rimts1	40.0	45.2	14.1	0.21	0.13	0.24	99.9	85.1
	ol4corets1	40.8	48.7	10.2	0.15	0.12	0.48	100.3	89.5
	ol4rimts1	39.8	45.7	13.8	0.20	0.16	0.17	99.9	85.5
	ol6corets1	40.6	48.7	9.7	0.15	0.11	0.58	99.8	89.9
	ol6rimts1	40.4	44.6	14.7	0.20	0.15	0.19	100.3	84.5
	ol8corets1	40.8	47.3	11.8	0.18	0.13	0.33	100.4	87.7
	ol8rimts1	39.3	43.6	16.4	0.25	0.17	0.15	99.9	82.6
	ol9corets1	41.0	48.2	10.5	0.15	0.12	0.52	100.5	89.1
	ol9rimts1	38.7	39.5	20.9	0.36	0.13	0.11	99.6	77.1
	ol17corets1	40.7	47.2	11.5	0.15	0.15	0.34	100.1	87.9
	ol17rimts1	40.6	45.0	15.1	0.22	0.15	0.20	101.3	84.1
	ol20rimts2	39.3	43.0	17.8	0.29	0.14	0.17	100.6	81.1
	ol20coreats2	40.5	46.7	12.5	0.18	0.14	0.28	100.3	87.0
	ol20rimats2	39.3	41.4	18.5	0.32	0.15	0.14	99.9	80.0
	ol21corets2	41.5	47.4	11.2	0.16	0.13	0.40	100.8	88.3
	ol21rimts2	39.2	42.3	18.9	0.29	0.16	0.28	101.1	80.0
	ol22corets2	40.8	48.8	9.8	0.11	0.14	0.54	100.1	89.9
	ol22rimts2	37.8	38.6	23.3	0.37	0.18	0.19	100.4	74.6
	ol23corets2	41.2	48.6	9.9	0.13	0.13	0.67	100.6	89.7
	ol23rimts2	38.2	40.3	20.5	0.31	0.14	0.18	99.5	77.8
	ol24corets2	41.4	48.7	9.7	0.14	0.12	0.62	100.7	90.0
	ol25corets2	40.6	48.9	9.9	0.13	0.12	0.54	100.2	89.8
	ol26corets2	40.4	46.9	12.4	0.19	0.14	0.23	100.3	87.1
	ol26rimts2	39.0	36.5	23.5	0.41	0.43	0.13	100.0	73.5
	ol30corets5	41.3	47.6	11.4	0.16	0.11	0.34	100.9	88.1
	ol30rimts5	40.1	42.2	17.4	0.27	0.10	0.17	100.3	81.2
	ol30rimats5	40.9	44.4	15.0	0.23	0.14	0.20	100.9	84.1
	ol31corets5	40.9	48.5	10.0	0.12	0.10	0.55	100.3	89.6
	ol31rimats5	40.2	45.1	15.1	0.21	0.13	0.27	101.0	84.2
	ol32corets5	41.1	48.6	10.1	0.13	0.09	0.54	100.6	89.6
	ol32rimts5	41.0	48.1	11.4	0.14	0.11	0.40	101.0	88.3
	ol33corets5	41.4	49.4	9.3	0.16	0.09	0.63	100.9	90.4
	ol33rimts5	40.9	48.4	11.2	0.15	0.14	0.44	101.2	88.5
	ol34corets5	41.6	49.6	9.3	0.14	0.12	0.60	101.4	90.4
	ol34rimts5	40.6	48.8	11.5	0.17	0.12	0.34	101.4	88.3
	ol35corets5	41.6	49.3	8.7	0.12	0.08	0.81	100.5	91.0
	ol35rimts5	40.6	44.4	15.5	0.26	0.12	0.20	101.1	83.6
	ol35rimats5	38.9	38.2	23.3	0.43	0.12	0.14	101.1	74.5
	ol36corets5	41.4	49.4	9.7	0.12	0.10	0.53	101.1	90.1
	ol37corets5	40.9	47.1	12.2	0.16	0.11	0.34	100.8	87.3
	ol37rimts5	39.9	41.8	18.0	0.29	0.13	0.19	100.3	80.5

Table 5. Continued

	Label	SiO_2	MgO	FeO	MnO	CaO	NiO	Total	Fo
Microphenocrysts	ol9aPopoSC63097a	40.5	46.3	13.7	0.22	0.17	0.17	101.1	85.7
	ol9bPopoSC63097a	40.6	46.0	13.9	0.22	0.16	0.17	101.0	85.5
	ol10aPopoSC63097a	40.1	45.1	15.0	0.23	0.16	0.14	100.7	84.3
	ol10bPopoSC63097a	40.6	45.3	14.9	0.22	0.14	0.13	101.4	84.4
	ol17aPopoSC63097a	40.0	46.2	13.9	0.22	0.14	0.16	100.7	85.6
	ol17bPopoSC63097a	40.7	46.0	14.4	0.24	0.13	0.15	101.5	85.1
	ol17cPopoSC63097a	39.8	45.9	14.6	0.20	0.13	0.16	100.7	84.9
	ol25aPopoSC63097a	40.6	45.7	14.8	0.21	0.14	0.17	101.5	84.6
	ol25bPopoSC63097a	39.7	45.6	15.1	0.21	0.16	0.11	100.9	84.3
	ol7aPopoPum1198c	40.5	45.3	15.4	0.22	0.13	0.18	101.7	83.9
	ol7bPopoPum1198c	39.9	46.8	13.2	0.21	0.15	0.17	100.4	86.3

Fo = Mg/(Mg+Fe)

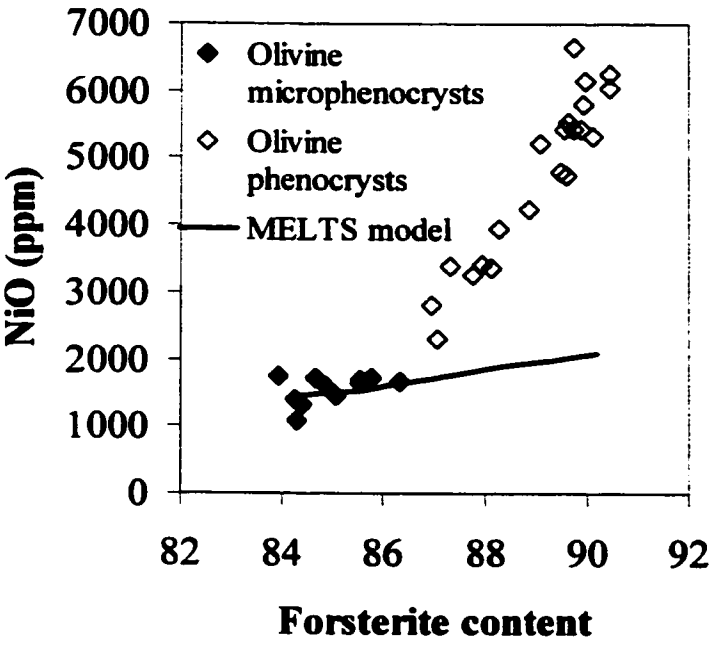

Figure 3. Forsterite content [Mg/(Mg+Fe^{2+})] versus NiO in olivine. The two types of olivine are shown: Cr-spinel and NiO-rich, glass inclusion-free olivine phenocrysts (*open diamonds*) and Cr-spinel and NiO-poor, glass inclusion-bearing olivine microphenocrysts (*filled diamonds*). Results of thermodynamic modeling using the MELTS algorithm (Ghiorso & Sack, 1995) and the inferred bulk composition of the mafic end member (Table 4) are shown (*heavy line*). See text for further explanation.

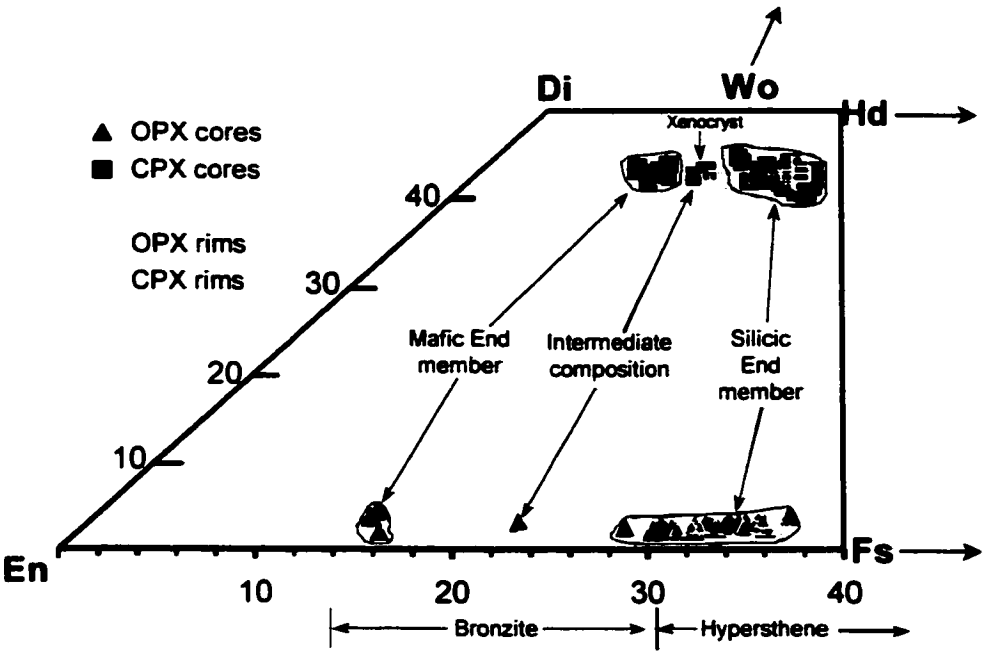

Figure 4. Pyroxene compositions shown on the enstatite-diopside half of the pyroxene quadrilateral. Data shown are orthopyroxene (OPX, *triangles*) and clinopyroxene (CPX, *squares*). Filled symbols are core analyses. Open symbols are rim analyses. Ortho- and clinopyroxenes that are inferred to derive from the mafic and silicic end members are grouped. Pyroxenes of intermediate composition and xenocrysts are labeled. Di=diopside, Hd=hedenbergite, Fs=ferrosillite, En=enstatite, Wo=wollastonite

Table 6. EPMA analyses of clinopyroxene and orthopyroxene (in wt.%)

Clinopyroxene CORE analyses

Label	SiO_2	TiO_2	Al_2O_3	Cr_2O_3	FeO	MnO	MgO	CaO	Na_2O	NiO	Total	Mg#	En	Fs	Wo
cpx20corets1	52.0	0.44	1.74	0.02	9.31	0.28	14.8	20.4	0.44	0.06	99.4	73.9	42.7	15.1	42.3
cpx50corets1	49.8	0.65	3.27	0.40	5.79	0.15	16.4	21.3	0.31	0.05	98.1	83.5	46.9	9.3	43.8
cpx51corets1	50.9	0.63	3.91	0.64	5.61	0.16	16.8	20.1	0.42	0.03	99.1	84.2	48.9	9.2	42.0
cpx25nrMI1ts1	51.7	0.37	1.74	0.06	9.86	0.28	14.3	21.0	0.52	0.04	99.9	72.1	41.0	15.8	43.2
cpx25nrMI2ts1	51.1	0.35	1.25	0.04	9.04	0.30	14.9	21.1	0.38	0.00	98.5	74.6	42.4	14.4	43.1
cpx11corets2	51.6	0.66	3.80	0.53	5.70	0.17	16.6	20.7	0.41	0.05	100.1	83.8	47.8	9.2	43.0
cpx53corets2	50.8	0.62	3.16	0.36	5.64	0.15	16.7	20.7	0.34	0.07	98.5	84.1	48.1	9.1	42.8
cpx10nrMI1ts2	51.2	0.60	2.59	0.20	10.2	0.21	14.3	20.7	0.60	0.03	100.6	71.4	40.9	16.4	42.7
cpx10nrMI2ts2	52.1	0.52	2.69	0.06	9.53	0.25	14.1	21.3	0.54	0.01	101.0	72.5	40.6	15.4	44.0
cpx12nrMI1ts2	53.3	0.29	0.92	0.04	9.09	0.39	14.9	21.5	0.42	0.01	100.8	74.4	42.0	14.4	43.6
cpx39corets5	52.2	0.38	1.52	0.03	9.43	0.30	14.7	20.8	0.42	0.02	99.8	73.5	42.1	15.2	42.8
cpx40corets5	53.1	0.31	0.90	0.01	10.4	0.41	13.7	20.5	0.49	0.01	99.9	70.1	39.9	17.1	43.0
cpx41corets5	51.9	0.68	3.11	0.14	6.97	0.22	15.9	20.4	0.39	0.02	99.8	80.3	46.2	11.3	42.5
cpx55corets5	50.9	0.60	2.35	0.25	10.5	0.32	13.6	19.7	0.59	0.03	98.8	69.8	40.4	17.5	42.1
cpx56nrMI3ts5	52.4	0.44	1.50	0.07	10.2	0.37	13.9	20.3	0.56	0.00	99.7	70.9	40.7	16.7	42.6
cpx56corets5	52.1	0.48	1.45	0.05	10.1	0.28	14.4	19.6	0.50	0.04	98.9	71.7	42.2	16.6	41.2
cpx30corets6	51.2	0.53	2.04	0.09	10.7	0.28	13.9	19.9	0.68	0.04	99.3	69.9	40.7	17.5	41.7
cpx31corets6	52.8	0.36	0.98	0.06	9.05	0.40	14.8	21.2	0.44	0.00	100.0	74.5	42.2	14.5	43.3
cpx34corets6	51.7	0.53	1.92	0.06	10.8	0.27	14.0	19.7	0.61	0.03	99.6	69.7	40.9	17.8	41.4
cpx36corets6	51.8	0.59	2.14	0.15	9.75	0.27	14.4	19.9	0.64	0.03	99.7	72.5	42.2	16.0	41.8
cpx37corets6	52.0	0.50	1.89	0.05	10.0	0.25	14.5	19.8	0.70	0.03	99.8	72.0	42.2	16.4	41.5
cpx38corets6	51.9	0.71	2.31	0.01	10.2	0.29	14.4	20.2	0.50	0.02	100.5	71.5	41.5	16.6	41.9
cpx57corets6	52.7	0.16	0.54	0.02	7.74	0.28	15.0	21.7	0.37	0.02	98.5	77.5	42.9	12.5	44.6
cpx5nrMI1tsSC63097a	52.9	0.34	1.40	0.00	8.22	0.29	15.3	21.9	0.37	0.00	100.7	76.9	43.0	12.9	44.1
cpx5nrMI2tsSC63097a	52.6	0.34	1.31	0.00	9.01	0.36	15.4	20.5	0.31	0.01	99.9	75.3	43.8	14.4	41.9
cpx5coretsSC63097a	52.0	0.51	1.96	0.02	9.57	0.30	15.1	20.6	0.38	0.05	100.4	73.7	42.8	15.2	42.0
cpx2nrMI1tsSC63097b	52.6	0.37	1.19	0.00	9.48	0.37	15.0	21.6	0.40	0.00	101.0	73.8	41.9	14.9	43.3
cpx1nrMI1tsPum63097c	51.5	0.70	3.61	0.70	5.64	0.15	16.5	20.7	0.38	0.02	99.9	83.9	47.7	9.2	43.1
cpx1coretsPum63097c	49.5	1.34	6.21	0.07	6.95	0.15	15.3	20.2	0.38	0.03	100.1	79.7	45.3	11.6	43.1

Table 6. continued

Label	SiO_2	TiO_2	Al_2O_3	Cr_2O_3	FeO	MnO	MgO	CaO	Na_2O	NiO	Total	Mg#	En	Fs	Wo
cpx2nrMI1tsPum63097c	52.7	0.33	1.01	0.00	9.48	0.36	14.8	20.9	0.38	0.03	100.1	73.6	42.1	15.1	42.8
cpx2coreatsPum63097c	51.7	0.46	1.96	0.14	10.9	0.31	14.2	19.1	0.66	0.06	99.6	69.8	41.6	18.0	40.4
cpx3nrMI2tsPum63097c	50.9	0.71	2.92	0.11	10.6	0.29	14.0	19.8	0.62	0.01	99.9	70.1	40.8	17.4	41.7
cpx1nrMI3tsmixa	52.4	0.47	2.92	0.70	4.90	0.13	17.0	21.1	0.36	0.00	99.9	86.1	48.7	7.9	43.4
cpx1nrMI4tsmixa	53.0	0.50	2.73	0.52	5.03	0.13	17.3	21.3	0.34	0.05	100.8	86.0	48.8	8.0	43.2
cpx1nrMI5tsmixa	52.3	0.61	2.60	0.24	6.21	0.17	16.9	20.9	0.33	0.02	100.2	82.9	47.7	9.9	42.4
cpx14nrMI1tsPUM1198c	51.8	0.65	2.43	0.10	10.1	0.25	13.8	20.4	0.54	0.00	100.0	70.9	40.4	16.6	43.0
cpx14coretsPum1198c	52.1	0.49	1.69	0.16	10.2	0.27	14.7	19.9	0.50	0.02	100.0	72.0	42.3	16.5	41.2
cpx17nrMI1tsPUM1198c	52.4	0.39	1.38	0.07	9.95	0.38	14.4	20.7	0.51	0.00	100.2	72.1	41.4	16.0	42.7
cpx17nrMI2tsPUM1198c	52.2	0.47	2.11	0.06	10.7	0.32	14.1	19.4	0.60	0.04	100.0	70.3	41.5	17.6	41.0
cpx17nrMI3tsPUM1198c	51.7	0.41	1.89	0.05	10.1	0.32	14.3	20.4	0.52	0.04	99.7	71.6	41.2	16.3	42.5
cpx17coretsPum1198c	51.7	0.49	2.09	0.12	10.7	0.29	14.5	19.5	0.58	0.03	100.0	70.7	41.9	17.3	40.7
cpx10nrMI1tsPUM1198d	51.5	0.50	2.12	0.15	10.3	0.26	13.8	20.3	0.61	0.03	99.5	70.5	40.4	16.9	42.7
cpx10coretsPum1198d	51.5	0.50	1.94	0.10	10.4	0.28	14.6	19.9	0.61	0.00	99.9	71.4	41.9	16.8	41.3

Clinopyroxene RIM analyses

Label	SiO_2	TiO_2	Al_2O_3	Cr_2O_3	FeO	MnO	MgO	CaO	Na_2O	NiO	Total	Mg#	En	Fs	Wo	ΔEn
cpx20rimts1	51.2	0.95	2.82	0.01	8.26	0.20	15.7	20.3	0.34	0.02	99.8	77.2	45.0	13.3	41.8	-2.3
cpx20nrMI1ts1	51.7	0.64	2.05	0.01	8.32	0.24	15.9	19.9	0.34	0.00	99.0	77.3	45.6	13.4	41.0	
cpx20nrMI2ts1	50.7	1.09	3.30	0.03	8.15	0.20	15.7	20.3	0.37	0.02	99.8	77.4	45.0	13.1	41.9	
cpx25nrMI3ts1	50.9	0.78	2.68	0.04	7.99	0.23	15.6	20.1	0.36	0.01	98.7	77.7	45.3	13.0	41.7	
cpx11rimts2	50.5	0.94	3.32	0.22	7.90	0.20	15.9	20.6	0.33	0.01	99.9	78.2	45.3	12.6	42.1	2.5
cpx10rimts2	50.9	0.54	2.70	0.22	5.92	0.19	17.2	20.3	0.29	0.02	98.3	83.9	49.0	9.4	41.6	-8.5
cpx39rimts5	52.1	0.31	1.13	0.01	9.54	0.40	14.4	21.6	0.38	0.03	99.9	72.9	40.9	15.2	43.9	1.2
cpx40rimts5	52.6	0.27	0.98	0.00	10.3	0.45	14.0	20.6	0.50	0.00	99.7	70.9	40.6	16.6	42.8	-0.7
cpx41rimts5	51.7	0.82	2.05	0.02	8.87	0.25	14.8	20.3	0.36	0.00	99.2	74.9	43.1	14.5	42.4	3.1
cpx55rimts5	52.0	0.40	1.25	0.00	9.75	0.39	14.6	20.1	0.43	0.00	98.9	72.7	42.3	15.9	41.8	-1.9
cpx56rimts5	52.7	0.44	1.47	0.08	10.1	0.39	14.0	20.3	0.53	0.01	100.0	71.1	40.8	16.6	42.6	1.4
cpx30rimts6	52.5	0.57	1.71	0.04	8.07	0.24	16.0	20.4	0.34	0.00	99.9	77.9	45.4	12.9	41.7	-4.7
cpx31rimts6	52.7	0.27	0.91	0.01	10.3	0.38	14.0	20.6	0.51	0.00	99.7	70.9	40.6	16.7	42.8	1.6
cpx34rimts6	51.4	0.51	2.20	0.14	9.80	0.29	14.4	19.9	0.58	0.02	99.1	72.3	42.1	16.1	41.8	-1.2

Table 6. continued

Label	SiO_2	TiO_2	Al_2O_3	Cr_2O_3	FeO	MnO	MgO	CaO	Na_2O	NiO	Total	Mg#	En	Fs	Wo	ΔEn
cpx36rimts6	52.2	0.34	1.04	0.01	9.92	0.42	14.0	21.2	0.49	0.01	99.6	71.6	40.3	16.0	43.7	1.9
cpx37rimts6	52.5	0.33	1.47	0.09	8.86	0.34	14.9	21.1	0.40	0.01	99.9	74.9	42.5	14.2	43.3	-0.3
cpx38rimts6	52.3	0.50	1.61	0.08	10.8	0.32	14.3	19.8	0.49	0.04	100.2	70.2	41.3	17.5	41.2	0.2
cpx57rimts6	51.7	0.29	0.83	0.02	9.87	0.37	14.3	20.6	0.46	0.00	98.5	72.0	41.2	16.0	42.8	1.7
cpx5rimSC63097a	50.7	0.82	2.85	0.06	7.78	0.21	16.2	20.9	0.34	0.06	99.8	78.8	45.5	12.3	42.2	-2.7
cpx1rimaPum63097c	51.7	0.72	3.82	0.36	6.22	0.15	17.1	19.7	0.38	0.00	100.1	83.1	49.2	10.0	40.7	-3.9
cpx2rimPum63097c	52.8	0.52	1.36	0.00	9.28	0.27	16.3	19.6	0.32	0.03	100.5	75.8	45.8	14.6	39.6	-4.2
cpx14rimPum1198c	51.4	0.78	3.08	0.09	7.25	0.21	16.4	20.5	0.34	0.04	100.0	80.1	46.6	11.6	41.8	-4.3
cpx17rimPum1198c	52.8	0.29	1.04	0.02	10.0	0.39	14.5	20.6	0.50	0.04	100.2	72.1	41.5	16.1	42.4	0.4
cpx10rimPum1198d	52.9	0.31	1.11	0.02	10.6	0.34	14.3	20.3	0.49	0.05	100.4	70.7	41.1	17.1	41.8	0.8

Orthopyroxene CORE analyses

Label	SiO_2	TiO_2	Al_2O_3	Cr_2O_3	FeO	MnO	MgO	CaO	Na_2O	NiO	Total	Mg#	En	Fs	Wo
opx7corets1	53.4	0.27	0.89	0.02	14.3	0.35	27.5	1.55	0.01	0.05	98.3	77.4	75.1	21.9	3.0
opx19corets1	53.3	0.21	1.02	0.08	18.9	0.45	25.0	1.13	0.04	0.05	100.2	70.2	68.6	29.1	2.2
opx50corets1	52.3	0.21	0.80	0.03	19.3	0.49	24.3	1.14	0.04	0.01	98.5	69.2	67.6	30.1	2.3
opx51corets1	55.3	0.16	1.25	0.22	9.38	0.22	30.4	2.20	0.03	0.06	99.3	85.3	81.6	14.1	4.2
opx8corets2	52.3	0.25	0.69	0.05	22.1	0.74	22.3	1.18	0.01	0.00	99.6	64.3	62.8	34.8	2.4
opx11corets2	56.3	0.22	1.43	0.10	9.31	0.21	30.6	1.88	0.07	0.13	100.2	85.4	82.3	14.1	3.6
opx14nrMI1ts2	53.6	0.23	0.80	0.01	18.2	0.64	25.8	1.27	0.01	0.02	100.6	71.7	69.9	27.6	2.5
opx14corets2	51.9	0.24	0.89	0.03	20.3	0.54	22.9	1.16	0.03	0.03	98.1	66.9	65.3	32.3	2.4
opx53corets2	52.8	0.24	0.39	0.00	18.6	0.67	24.1	1.40	0.02	0.01	98.2	69.9	67.9	29.3	2.8
opx39corets5	52.9	0.25	1.16	0.09	21.7	0.50	22.4	1.48	0.06	0.02	100.6	64.7	62.8	34.2	3.0
opx40corets5	52.9	0.26	0.73	0.01	22.2	0.54	22.8	1.46	0.05	0.04	100.9	64.6	62.8	34.4	2.9
opx55corets5	52.2	0.31	1.14	0.05	20.9	0.44	22.2	1.43	0.05	0.04	98.7	65.4	63.5	33.6	2.9
opx56nrMI1ts5	53.2	0.27	0.91	0.03	21.1	0.46	22.7	1.43	0.10	0.01	100.2	65.8	63.9	33.2	2.9
opx30corets6	51.8	0.22	1.23	0.03	21.3	0.55	22.6	1.33	0.07	0.02	99.2	65.4	63.7	33.6	2.7
opx31corets6	54.9	0.12	1.61	0.43	10.2	0.22	30.9	0.98	0.04	0.12	99.5	84.3	82.7	15.4	1.9
opx32corets6	52.6	0.29	1.45	0.01	20.7	0.51	22.9	1.48	0.07	0.02	100.0	66.3	64.3	32.7	3.0
opx33corets6	52.0	0.27	0.92	0.06	22.0	0.52	22.4	1.48	0.05	0.03	99.7	64.5	62.6	34.5	3.0
opx35corets6	53.3	0.19	0.96	0.13	20.7	0.42	23.6	1.25	0.05	0.05	100.6	67.1	65.4	32.1	2.5

Table 6. continued

Label	SiO_2	TiO_2	Al_2O_3	Cr_2O_3	FeO	MnO	MgO	CaO	Na_2O	NiO	Total	Mg#	En	Fs	Wo
opx36corets6	52.0	0.20	0.41	0.01	22.1	0.77	21.3	1.85	0.06	0.01	98.7	63.2	60.8	35.4	3.8
opx37corets6	52.7	0.23	1.13	0.03	20.5	0.41	23.5	1.25	0.06	0.04	99.9	67.2	65.5	32.0	2.5
opx38corets6	52.7	0.25	0.81	0.04	22.1	0.53	22.5	1.31	0.06	0.02	100.2	64.5	62.8	34.6	2.6
opx57corets6	52.6	0.22	0.86	0.03	18.9	0.49	24.1	1.00	0.03	0.05	98.3	69.4	68.0	29.9	2.0
opx8nrMI1tsSC63097a	53.0	0.28	1.18	0.11	20.6	0.44	23.8	1.31	0.04	0.01	100.8	67.3	65.6	31.8	2.6
opx8nrMI2tsSC63097a	53.6	0.17	0.59	0.06	20.5	0.67	24.3	1.04	0.03	0.01	101.0	67.9	66.5	31.4	2.1
opx8nrMI3tsSC63097a	53.5	0.27	0.91	0.07	20.1	0.48	23.9	1.40	0.04	0.02	100.6	67.9	66.0	31.2	2.8
opx8nrMI4tsSC63097a	53.4	0.20	0.85	0.02	20.3	0.47	24.0	1.22	0.03	0.04	100.5	67.8	66.2	31.4	2.4
opx8coretsSC63097a	52.3	0.25	1.08	0.11	20.4	0.45	23.8	1.39	0.05	0.04	99.8	67.5	65.6	31.6	2.8
opx1nrMI2tsPum63097c	51.8	0.24	1.11	0.03	21.5	0.49	22.9	1.37	0.05	0.03	99.6	65.5	63.8	33.5	2.7
opx1coretsPum63097c	52.6	0.22	0.83	0.00	20.0	0.48	23.9	1.37	0.04	0.03	99.5	68.0	66.2	31.1	2.7
opx1nrMI1atsmixb	52.0	0.26	1.01	0.07	21.0	0.52	23.8	1.27	0.06	0.03	99.9	66.9	65.2	32.3	2.5
opx1nrMI1btsmixb	52.3	0.24	0.91	0.04	21.0	0.51	23.3	1.29	0.06	0.00	99.7	66.4	64.7	32.7	2.6
opx4coretsPum1198c	52.3	0.18	1.84	0.44	18.9	0.46	25.0	0.99	0.05	0.05	100.2	70.1	68.8	29.3	2.0
opx12nrMI1tsPUM1198d	53.1	0.14	0.96	0.01	21.8	0.58	22.5	1.21	0.05	0.05	100.3	64.8	63.2	34.3	2.4
opx12nrMI2tsPUM1198d	52.2	0.32	1.11	0.04	21.1	0.50	23.0	1.26	0.04	0.07	99.6	66.0	64.4	33.1	2.5
opx12coreatsPum1198d	52.1	0.20	1.16	0.01	19.9	0.49	24.7	1.07	0.04	0.05	99.8	68.9	67.5	30.4	2.1
opx1anrsulf1ts1198e	54.7	0.24	2.45	0.21	10.6	0.21	30.5	1.77	0.03	n/a	100.7	83.7	80.9	15.7	3.4
opx1bnrsulf1ts1198e	53.9	0.27	2.54	0.09	11.3	0.23	30.1	1.76	0.04	n/a	100.2	82.6	79.8	16.8	3.4
opx1cnrsulf1ts1198e	54.8	0.26	2.36	0.15	11.0	0.22	30.2	1.79	0.03	n/a	100.8	83.1	80.3	16.3	3.4

Orthopyroxene RIM analyses

Label	SiO_2	TiO_2	Al_2O_3	Cr_2O_3	FeO	MnO	MgO	CaO	Na_2O	NiO	Total	Mg#	En	Fs	Wo	ΔEn
opx19rimts1	54.7	0.25	0.81	0.00	14.4	0.35	27.2	1.58	0.01	0.07	99.3	77.1	74.7	22.2	3.1	-6.0
opx50rimts1	52.4	0.32	0.67	0.01	18.4	0.55	24.3	1.57	0.03	0.00	98.2	70.2	68.0	28.8	3.1	-0.4
opx8rimts2	52.7	0.25	1.01	0.00	19.5	0.58	23.5	1.29	0.03	0.04	98.8	68.3	66.5	30.9	2.6	-3.7
opx11rimts2	55.3	0.28	2.42	0.26	10.0	0.19	29.9	1.59	0.06	0.05	100.0	84.3	81.6	15.3	3.1	0.7
opx14rimts2	54.1	0.24	1.92	0.20	10.4	0.22	29.6	1.78	0.04	0.06	98.5	83.6	80.7	15.9	3.5	-15.4
opx39rimts5	52.9	0.31	1.11	0.03	22.0	0.57	21.4	1.63	0.06	0.04	100.1	63.5	61.4	35.3	3.3	1.4
opx40rimts5	53.6	0.14	0.35	0.00	22.4	0.79	22.0	1.23	0.03	0.00	100.5	63.7	62.1	35.4	2.5	0.7

Table 6. continued

Label	SiO_2	TiO_2	Al_2O_3	Cr_2O_3	FeO	MnO	MgO	CaO	Na_2O	NiO	Total	Mg#	En	Fs	Wo	ΔEn
opx41rimts5	55.0	0.34	1.31	0.04	14.8	0.35	26.8	1.66	0.04	0.01	100.4	76.3	73.8	22.9	3.3	
opx55rimts5	52.7	0.19	0.95	0.05	20.4	0.52	22.6	1.23	0.09	0.05	98.8	66.4	64.7	32.8	2.5	-1.2
opx56rimts5	52.0	0.23	0.90	0.02	21.5	0.65	22.0	1.62	0.05	0.01	99.0	64.6	62.5	34.2	3.3	1.4
opx30rimts6	52.0	0.25	1.18	0.03	21.4	0.50	22.8	1.35	0.07	0.04	99.5	65.5	63.7	33.6	2.7	-0.1
opx31rimts6	52.2	0.21	0.71	0.00	22.3	0.71	21.9	1.36	0.05	0.03	99.5	63.6	61.8	35.4	2.8	20.9
opx32rimts6	53.0	0.18	0.43	0.00	21.9	0.76	22.0	1.59	0.05	0.02	99.9	64.1	62.1	34.7	3.2	2.3
opx33rimts6	52.3	0.22	0.69	0.00	21.6	0.71	22.5	1.40	0.05	0.01	99.4	65.0	63.2	34.0	2.8	-0.6
opx35rimts6	52.4	0.30	1.33	0.08	20.5	0.46	23.3	1.33	0.06	0.03	99.7	67.0	65.2	32.1	2.7	0.2
opx37rimts6	53.5	0.16	0.89	0.08	19.4	0.63	24.2	1.17	0.05	0.04	100.2	69.0	67.4	30.3	2.3	-1.8
opx38rimts6	52.8	0.24	1.31	0.12	19.8	0.64	23.6	1.40	0.06	0.03	100.0	68.0	66.1	31.1	2.8	-3.3
opx57rimts6	52.9	0.11	0.41	0.02	20.0	0.66	23.5	0.92	0.03	0.06	98.5	67.8	66.5	31.6	1.9	1.6
opx8rimtsSC63097a	51.7	0.23	0.88	0.07	20.4	0.47	24.1	1.33	0.03	0.01	99.3	67.8	66.0	31.4	2.6	-0.4
opx1rimtsPum63097c	52.4	0.17	0.43	0.03	19.8	0.68	24.5	1.20	0.04	0.02	99.3	68.8	67.2	30.4	2.4	-1.0
opx4rimtsPum1198c	52.3	0.18	0.41	0.00	21.5	0.70	22.9	1.23	0.03	0.02	99.2	65.4	63.8	33.7	2.5	4.9
opx4rimatsPum1198c	52.5	0.18	0.46	0.02	22.2	0.81	22.7	1.26	0.05	0.02	100.2	64.7	63.0	34.4	2.5	
opx12rimtsPum1198d	52.8	0.20	0.73	0.02	20.1	0.66	24.2	1.18	0.03	0.03	100.0	68.2	66.6	31.1	2.3	0.9

ΔEn < 1.0 defined as "unzoned"
Negative ΔEn = reverse zonation
Positive ΔEn = normal zonation
n/a = not analyzed

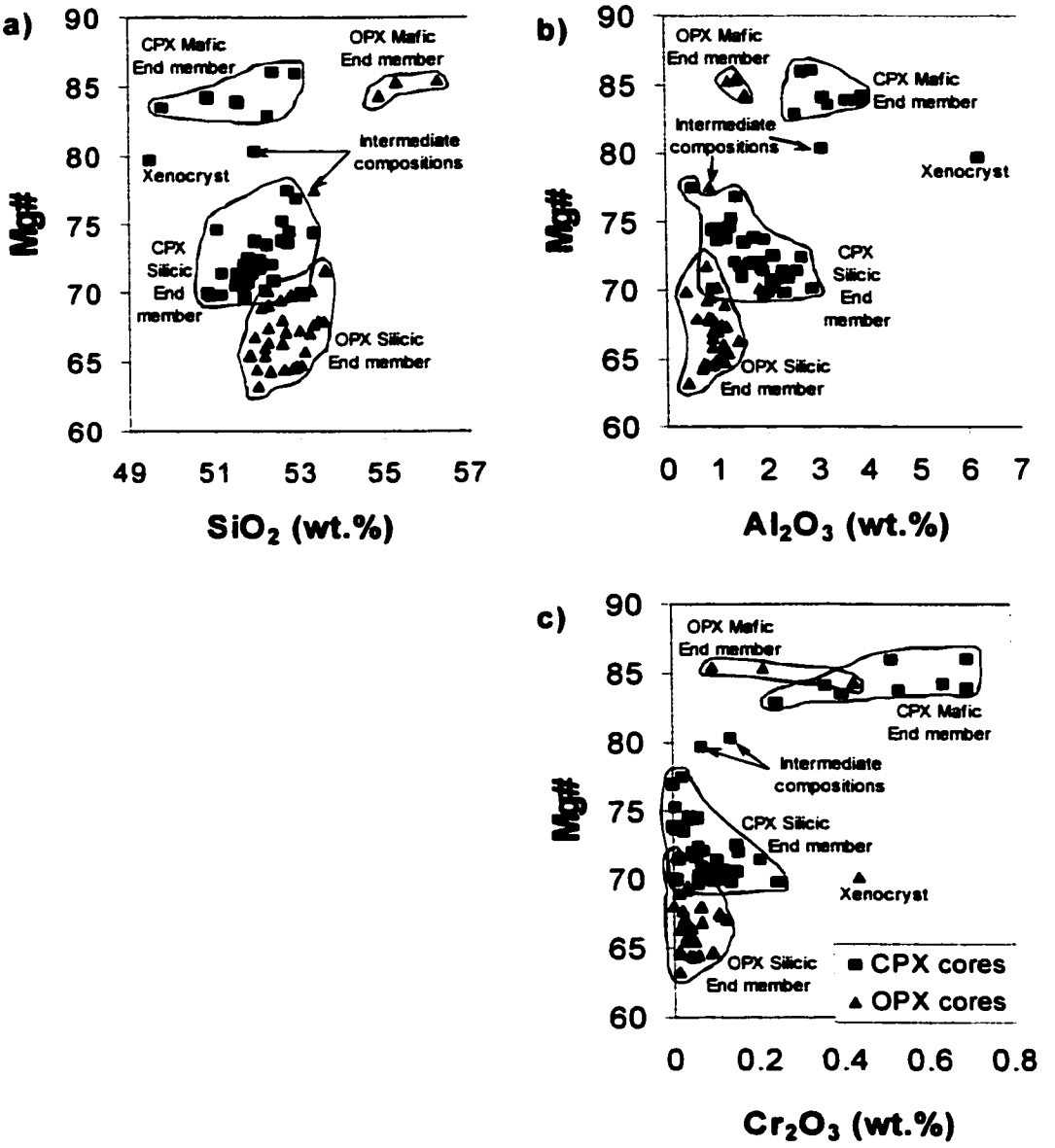

Figure 5. Pyroxene core compositions shown on plots of **a)** SiO_2, **b)** Al_2O_3, and **c)** Cr_2O_3 versus Mg# [=Mg/(Mg+Fe^{2+})]. Ortho- and clinopyroxenes that are inferred to derive from the mafic and silicic end members are grouped. Pyroxenes of intermediate composition and xenocrysts are labeled. Pyroxene rim compositions not shown for clarity.

Table 7. EPMA analyses of hornblende (in wt.% except where noted)

Label	SiO_2	TiO_2	Al_2O_3	FeO	MnO	MgO	CaO	Na_2O	K_2O	S (ppm)	Cl (ppm)	F (ppm)	Subtotal	-O=F,Cl	Total
hbl14coreats1	43.1	2.37	11.9	12.3	0.14	13.2	10.9	2.41	0.47	74	154	5267	97.4	0.23	97.2
hbl14corebts1	42.9	2.25	11.9	12.9	0.14	13.6	10.4	2.69	0.41	n/a	n/a	n/a	97.2	n/a	97.2
hbl2coreats2	43.5	2.40	12.0	11.5	0.16	14.7	10.4	2.45	0.45	n/a	n/a	n/a	97.5	n/a	97.5
hbl2corebts2	43.2	1.99	12.6	12.6	0.15	13.8	10.4	2.45	0.44	78	109	2713	98.0	0.12	97.9
hbl20coreats6	44.5	2.20	11.3	10.9	0.19	14.9	10.6	2.42	0.45	65	111	3331	97.8	0.14	97.6
hbl21coreats6	45.2	2.05	9.9	10.8	0.13	14.8	11.0	2.47	0.43	0	146	5445	97.3	0.23	97.1
hbl21corebts6	45.2	1.87	10.1	11.0	0.14	15.4	11.0	2.30	0.39	n/a	n/a	n/a	97.3	n/a	97.3
hbl21midts6	45.4	2.11	10.0	10.6	0.14	15.4	11.1	2.38	0.36	n/a	n/a	n/a	97.5	n/a	97.5
hbl22coreats6	43.1	2.45	11.3	12.0	0.18	13.6	11.1	2.40	0.38	n/a	n/a	n/a	96.5	n/a	96.5
hbl22corebts6	42.2	2.94	11.3	12.4	0.19	13.3	10.7	2.58	0.41	n/a	n/a	n/a	96.0	n/a	96.0
hbl25coreats5	44.1	1.98	10.6	13.7	0.22	13.1	10.5	2.31	0.46	80	437	2134	97.1	0.10	97.0
hbl25midts5	45.6	2.01	9.2	11.3	0.15	15.3	10.8	2.54	0.34	n/a	n/a	n/a	97.2	n/a	97.2
hbl26coreats5	42.9	2.11	12.0	12.4	0.18	13.4	10.3	2.54	0.48	89	201	4935	96.7	0.21	96.5
hbl26midts5	42.6	2.20	12.6	13.1	0.24	13.1	10.4	2.57	0.51	n/a	n/a	n/a	97.2	n/a	97.2
hbl26midats5	42.8	2.21	11.9	12.5	0.16	13.6	10.4	2.68	0.47	n/a	n/a	n/a	96.6	n/a	96.6
hbl27corets5	42.4	2.15	13.0	12.7	0.18	12.8	10.5	2.60	0.54	80	217	4593	97.3	0.20	97.1
hbl27midts5	42.8	2.25	12.3	12.8	0.19	13.6	10.4	2.34	0.47	n/a	n/a	n/a	97.1	n/a	97.1

n/a = not analyzed

Popocatépetl hornblende compositions (Figure 6) are similar to groundmass amphibole (magnesiohastingsite) in mafic inclusions in Montserrat andesite (Murphy *et al.*, 2000) and groundmass amphibole (pargasite) from Unzen volcano (Sato *et al.*, 1999). They plot well outside of the field for amphibole phenocrysts (magnesiohornblende) in Montserrat andesite and Unzen dacite.

Sulfide

Sulfide globules (Table 8) contain 33-40 wt.% S and are rich in Fe (30-58 wt.%). Sulfide inclusions in pyroxene are the most Fe-rich. Other sulfide globules found in contact with silicate melt, between two differing minerals, or in hornblende reaction rims have variable concentrations of Cu (up to 27 wt.%) and Ni (up to 33 wt.%).

Glass inclusions

Glass inclusions (GI's) occur in all phenocryst phases. We focused analytical efforts on glass inclusions in olivine microphenocrysts and pyroxene phenocrysts in thin section with the aim of obtaining chemical data on the pre-eruptive magmatic end-members. Glass inclusions ≥10 μm in diameter, without visible intersecting cracks or evidence for post-entrapment crystallization were chosen for analysis. Despite taking care in choosing glass inclusions, some analyses displayed anomalous elevated Ca and Al contents. These anomalous analyses were interpreted to result from microscopic post-entrapment plagioclase crystallization and/or inhomogeneity of the quench products contained in the glass inclusion. Such analyses were excluded from further consideration.

Forty-two glass inclusions in olivine were analyzed for major elements (Table 9; Figure 7). Twenty of these were recalculated for post-entrapment crystallization using the thermodynamics-based correction scheme of Kress & Ghiorso (2001). This algorithm incrementally adds small quantities of instantaneous equilibrium liquidus olivine back into the inclusion composition until the instantaneous liquidus olivine composition most closely matches that of the host. The program tracks changes in

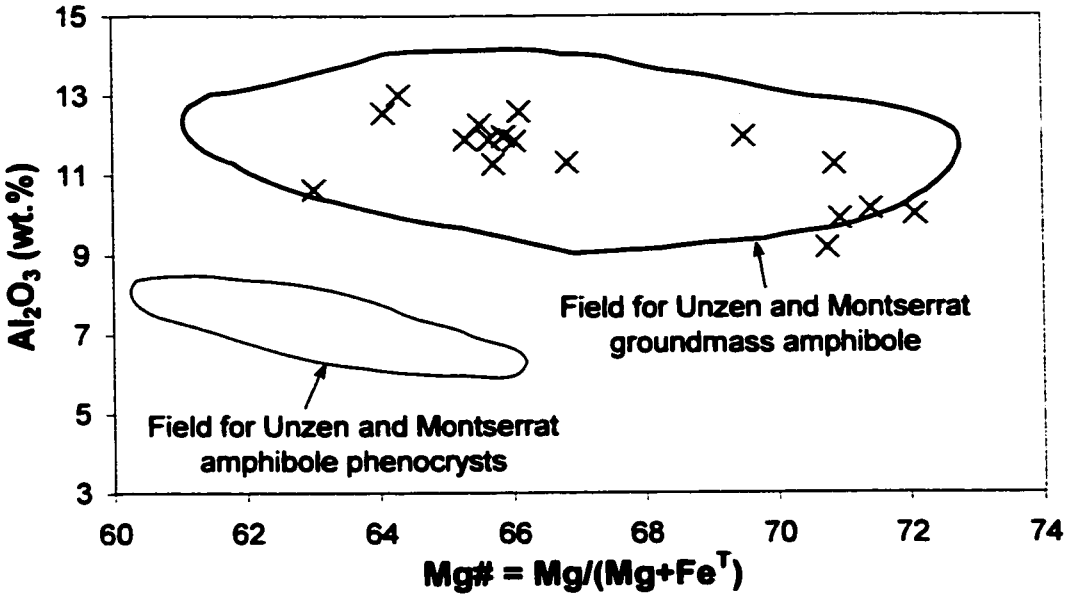

Figure 6. Hornblende compositions shown on a plot of Mg# [=Mg/(Mg+Fe^T)] versus Al_2O_3. Fe^T = total iron. Hornblende data from this study (*X's*) fall within the field for groundmass pargasite in dacite from the 1991-95 eruption of Unzen volcano, Japan (Sato *et al.*, 1999) and the field for groundmass magnesiohastingsite in andesite from the ongoing eruption of Soufriere Hills volcano, Montserrat (Murphy *et al.*, 2000). Hornblende from this study fall outside the field for amphibole (magnesiohornblende) phenocrysts found in rocks from both the 1991-95 eruption of Unzen and the ongoing eruption of Sourfriere Hills (Sato *et al.*, 1999; Murphy *et al.*, 2000).

Table 8. EPMA analyses of sulfide globules (in element wt.%)

Label	O	S	Fe	Cu	Ni	Si	Total	Comments
sulf1acpx56ts5	0.41	39.3	58.2	0.42	2.41	n/a	100.8	Inclusion in clinopyroxene
sulf1bcpx56ts5	0.47	39.3	57.9	0.32	2.15	n/a	100.2	Inclusion in clinopyroxene
sulf1opx1tsSC63097b	0.87	33.5	35.3	27.39	2.42	n/a	99.5	Inclusion in orthopyroxene in contact with melt (re-entrant?)
sulf1nrol1tsSC63097b	2.26	35.4	49.9	1.01	11.7	n/a	100.3	Between olivine, orthopyroxene, and vesicle
sulf2nrol1tsSC63097b	1.16	36.2	40.3	10.35	11.4	n/a	99.5	Between orthopyroxene and olivine
sulf3nrol1tsSC63097b	0.34	35.1	35.7	0.00	26.7	n/a	97.9	Between orthopyroxene and melt
sulf4nrol1tsSC63097b	1.42	36.5	35.8	12.43	15.1	n/a	101.2	Between olivine and vesicle
sulf5nrol1tsSC63097b	0.72	37.1	50.9	0.23	10.7	n/a	99.7	Between olivine and vesicle
sulfide1tsPum1198e	0.79	40.1	56.9	0.01	2.88	0.05	100.8	Inclusion in orthopyroxene
sulfide2tsPum1198e	0.72	37.0	34.6	0.00	25.6	0.40	98.4	In hornblende reaction rim
sulfide2newtsPum1198e	0.55	34.1	31.6	0.00	32.7	0.13	99.0	In hornblende reaction rim
sulfide1tsPum1198f	0.98	33.6	39.8	24.26	0.57	0.29	99.5	Wetted to ilmenite grain and in contact with matrix glass
sulfide1atsPum1198g	0.44	39.3	57.8	0.30	1.78	0.05	99.7	Inclusion in plagioclase
sulfide1btsPum1198g	0.38	39.0	58.0	0.36	1.81	0.02	99.5	Inclusion in plagioclase

Table 9. EPMA analyses of glass inlcusions (in wt.%)

Glass inclusions in olivine: Eruption of June 30, 1997 -- Brown Andesite pumice

Label	SiO_2	TiO_2	Al_2O_3	Cr_2O_3	FeO	MnO	MgO	CaO	Na_2O	K_2O	P_2O_5	Total	H_2O*
MI1ol20ts1	56.0	1.30	18.3	0.00	4.78	0.04	2.19	7.49	4.20	1.31	0.28	95.9	4.1
MI1aol20ts1	57.1	1.13	18.8	0.03	3.67	0.09	2.29	7.34	4.14	1.27	0.28	96.1	3.9
MI1bol20ts1	56.9	0.87	18.5	0.06	5.11	0.05	2.55	7.25	3.70	1.25	0.30	96.5	3.5
MI1ol22ts1'	57.9	1.05	17.0	0.00	6.29	0.13	4.84	6.46	4.45	1.39	0.24	99.8	0.2
MI2aol22ts1	59.8	0.98	18.2	0.04	5.58	0.10	2.82	6.65	4.89	1.61	0.23	100.9	-0.9
MI2bol22ts1	59.7	1.16	18.1	0.00	5.84	0.10	2.78	6.68	4.75	1.79	0.25	101.2	-1.2
MI3ol22ts1'	57.2	0.91	17.0	0.00	6.42	0.09	4.66	6.76	3.63	1.18	0.25	98.1	1.9
MI4ol22ts1'	57.6	1.09	16.9	0.00	6.20	0.11	4.50	6.33	3.97	1.25	0.23	98.1	1.9
MI5ol22ts1'	57.8	1.01	17.3	0.01	5.74	0.06	3.97	6.30	4.33	1.43	0.25	98.2	1.8
MI1aol7tsSC63097a	56.9	1.20	18.1	0.02	4.83	0.10	3.51	7.27	3.99	1.24	0.33	97.5	2.5
MI1ol7tsSC63097a'	55.6	1.19	17.3	0.00	5.33	0.11	5.61	6.86	3.79	1.14	0.30	97.2	2.8
MI1col7tsSC63097a	56.5	1.17	18.3	0.00	4.46	0.05	3.74	7.32	4.06	1.21	0.24	97.0	3.0
MI1ol8tsSC63097a	58.0	1.18	18.6	0.01	6.16	0.03	3.06	6.53	4.65	1.75	0.27	100.2	-0.2
MI1ol9tsSC63097a	54.1	1.17	17.9	0.04	4.90	0.06	2.48	8.19	4.20	1.11	0.25	94.4	5.6
MI2ol9tsSC63097a	54.1	1.23	17.6	0.04	5.21	0.09	4.26	7.93	4.01	1.18	0.33	96.0	4.0
MI3ol9tsSC63097a	54.8	1.15	17.8	0.11	4.52	0.06	4.68	7.81	4.34	1.12	0.35	96.8	3.2
MI1ol10tsSC63097a'	56.2	0.95	17.9	0.05	5.09	0.09	3.85	7.29	3.96	1.11	0.29	96.8	3.2
MI1ol13tsSC63097a	63.3	1.32	15.5	0.00	5.55	0.05	2.13	3.94	4.81	2.39	0.42	99.4	0.6
MI1ol16tsSC63097a	58.7	1.06	18.6	0.02	5.47	0.13	2.70	6.72	4.80	1.94	0.27	100.4	-0.4
MI1ol17tsSC63097a'	54.2	1.06	17.3	0.00	6.18	0.10	4.91	7.69	3.82	1.02	0.27	96.5	3.5
MI2ol17tsSC63097a'	56.0	1.10	16.9	0.01	6.37	0.13	5.06	7.12	4.11	1.38	0.25	98.4	1.6
MI3ol17tsSC63097a'	56.0	1.01	17.3	0.02	6.52	0.14	5.15	6.78	4.49	1.64	0.26	99.4	0.6
MI1ol25tsSC63097a'	54.0	1.34	16.3	0.02	6.33	0.14	4.43	8.00	4.18	1.00	0.28	96.0	4.0
MI1ol1tsSC63097b	59.1	0.92	18.0	0.00	5.35	0.10	2.73	5.41	5.07	1.59	0.26	98.6	1.4
MI1aol9tsSC63097b'	55.6	1.18	16.8	0.01	6.58	0.13	5.79	6.91	4.02	1.05	0.23	98.3	1.7
MI2ol9tsSC63097b'	55.4	0.83	16.7	0.03	6.84	0.09	5.86	7.14	4.27	1.17	0.24	98.5	1.5

Table 9. continued

Label	SiO_2	TiO_2	Al_2O_3	Cr_2O_3	FeO	MnO	MgO	CaO	Na_2O	K_2O	P_2O_5	Total	H_2O*
MI1ol10tsSC63097b	59.7	1.19	19.0	0.02	4.90	0.03	2.81	7.09	4.46	1.40	0.23	100.9	-0.9
GI1OL2ts63097A'	53.3	1.25	18.9	0.00	4.63	0.07	4.71	8.89	3.76	1.05	0.31	96.8	3.2
GI2OL4ts63097A'	54.7	1.03	17.4	0.02	6.82	0.11	5.94	7.11	3.84	1.39	0.26	98.7	1.3
GI1OL6ts63097B'	52.8	1.19	18.5	0.01	5.75	0.11	4.52	8.10	4.10	0.97	0.28	96.3	3.7
GI1OL4ts63097E'	55.6	0.92	18.0	0.00	6.67	0.11	3.99	7.06	4.63	1.45	0.29	98.7	1.3
GI3OL4ts63097E'	55.8	1.02	18.1	0.01	6.51	0.07	3.95	7.20	4.85	1.56	0.26	99.3	0.7
GI1OL4ts63097A'	54.7	1.07	17.1	0.01	6.57	0.11	6.03	7.21	4.31	1.45	0.22	98.7	1.3
Glass inclusions in olivine: Eruption of June 30, 1997 -- Mingled pumice													
MI1ol1TSmixa	62.7	0.96	18.6	0.07	3.44	0.05	1.65	4.92	4.59	1.86	0.26	99.1	0.9
MI1ol4TSmixa	57.4	1.20	18.5	0.01	4.68	0.10	1.75	7.01	4.48	1.37	0.28	96.7	3.3
MI1aol1TSmixb	55.2	0.89	17.0	0.02	5.25	0.11	3.42	6.81	4.29	1.30	0.20	94.5	5.5
MI1bol1TSmixb	54.8	0.95	17.0	0.00	5.44	0.11	3.05	6.68	4.31	1.29	0.25	93.9	6.1
MI1col1TSmixb	55.0	1.12	16.9	0.06	5.49	0.06	3.32	6.93	4.25	1.22	0.21	94.5	5.5
Glass inclusions in olivine: Eruption of January 1, 1998 -- Dacite Dome rock													
MI1ol3tsPUM1198c	64.5	0.22	21.0	0.00	1.67	0.00	1.20	3.42	7.22	2.02	0.49	101.8	-1.8
MI1ol7tsPUM1198c	68.8	0.95	18.6	0.00	0.99	0.02	0.31	4.03	5.25	1.96	0.34	101.2	-1.2
MI2ol7tsPUM1198c'	61.8	1.20	18.4	0.01	3.34	0.09	3.49	2.97	4.98	3.32	0.28	99.8	0.2
MI1ol8tsPUM1198c	66.7	0.38	17.5	0.00	1.96	0.00	2.20	3.43	5.44	2.03	0.31	99.9	0.1
Glass inclusions in clinopyroxene: Eruption of June 30, 1997 -- Brown Andesite pumice													
MI1cpx20ts1	63.8	1.03	13.6	0.00	5.43	0.13	2.86	4.76	2.89	2.25	0.27	97.1	2.9
MI2cpx20ts1	62.6	0.83	13.6	0.00	5.83	0.14	3.37	5.64	2.52	2.20	0.27	97.0	3.0
MI3cpx20ts1	68.4	0.26	10.5	0.03	3.46	0.02	2.71	4.59	2.10	3.56	0.11	95.7	4.3
MI4cpx20ts1	60.5	0.74	14.1	0.00	6.17	0.09	3.25	5.82	3.72	2.11	0.31	96.7	3.3
MI1cpx25ts1	70.7	0.10	12.1	0.01	3.28	0.04	0.95	2.07	3.48	3.63	0.06	96.4	3.6
MI2cpx25ts1	72.1	0.87	11.1	0.00	3.16	0.02	0.64	1.95	2.88	3.21	0.09	96.0	4.0
MI3cpx25ts1	58.8	0.85	13.1	0.06	5.58	0.01	4.23	6.42	3.14	1.76	0.41	94.3	5.7
MI4cpx25ts1	63.6	1.30	15.1	0.00	4.42	0.09	1.66	3.18	3.92	2.30	0.35	95.8	4.2
MI1cpx27ts1	64.8	1.22	15.5	0.02	5.40	0.10	1.99	3.78	4.75	2.24	0.42	100.2	-0.2

Table 9. continued

Label	SiO_2	TiO_2	Al_2O_3	Cr_2O_3	FeO	MnO	MgO	CaO	Na_2O	K_2O	P_2O_5	Total	H_2O^*
MI1cpx5tsSC63097a	64.3	0.94	15.2	0.04	5.40	0.10	1.51	3.30	4.24	2.33	0.36	97.7	2.3
MI2cpx5tsSC63097a	61.0	1.64	15.6	0.00	5.44	0.08	1.93	3.70	4.91	2.12	0.27	96.7	3.3
Glass inclusions in clinopyroxene: Eruption of June 30, 1997 -- White Dacite pumice													
MI2bcpx10ts2	66.6	0.88	13.3	0.02	4.04	0.09	2.19	4.81	1.62	1.97	0.28	95.8	4.2
MI1cpx12ts2	73.8	0.76	12.4	0.01	3.47	0.09	0.53	1.56	1.51	3.23	0.06	97.4	2.6
MI1acpx12ts2	72.3	0.71	11.5	0.00	3.88	0.05	1.54	2.93	1.38	3.02	0.02	97.3	2.7
MI3cpx12ts2	70.0	0.40	11.3	0.00	3.19	0.05	1.25	2.66	4.04	3.18	0.02	96.0	4.0
MI4cpx12ts2	73.4	0.39	11.8	0.00	2.64	0.06	0.44	1.11	4.70	3.52	0.01	98.0	2.0
MI1cpx1tsPum63097c	70.3	0.93	13.1	0.02	2.77	0.05	0.56	1.89	4.26	3.37	0.34	97.5	2.5
MI1cpx2tsPum63097c	73.8	0.88	11.5	0.01	2.40	0.08	0.64	1.45	3.59	3.72	0.09	98.2	1.8
Glass inclusions in clinopyroxene: Eruption of June 30, 1997 -- Mingled pumice													
MI2cpx1TSmixa	56.8	1.14	18.3	0.01	5.99	0.13	3.21	6.26	4.11	1.34	0.25	97.5	2.5
MI3cpx1TSmixa	56.7	0.94	19.5	0.00	4.73	0.11	1.51	3.67	6.08	1.54	0.25	94.9	5.1
MI4cpx1TSmixa	55.9	1.02	17.5	0.03	5.17	0.08	3.89	7.04	4.73	1.37	0.26	97.0	3.0
MI5cpx1TSmixa	56.8	1.14	18.6	0.01	5.05	0.10	2.16	4.39	5.77	1.58	0.24	95.8	4.2
MI1cpx1Tsmixb	61.4	1.13	13.3	0.04	6.18	0.15	4.40	7.26	4.72	1.98	0.33	100.9	-0.9
Glass inclusions in clinopyroxene: Eruption of January 1, 1998 -- Dacite Dome rock													
MI2cpx56ts5	74.4	0.15	11.8	0.00	1.84	0.02	0.56	1.44	3.43	3.77	0.06	97.4	2.6
MI3cpx56ts5	74.0	0.28	12.1	0.00	1.78	0.07	0.51	1.38	3.68	4.02	0.06	97.9	2.1
MI1cpx14tsPum1198c	71.2	0.59	13.6	0.00	1.88	0.03	0.57	1.91	3.90	3.34	0.07	97.0	3.0
MI1cpx17tsPum1198c	76.2	0.34	11.8	0.03	1.92	0.09	0.36	1.19	4.14	3.23	0.02	99.3	0.7
MI2cpx17tsPum1198c	73.8	0.39	12.6	0.00	1.69	0.05	0.44	1.30	3.74	4.10	0.10	98.2	1.8
MI3cpx17tsPum1198c	73.9	0.40	12.8	0.00	1.80	0.06	0.42	1.60	3.90	3.90	0.07	98.8	1.2
MI1cpx10tsPum1198d	74.5	0.46	12.4	0.01	1.83	0.03	0.66	1.37	3.93	3.18	0.03	98.4	1.6
Glass inclusions in orthopyroxene: Eruption of June 30, 1997 -- Brown Andesite pumice													
MI1opx8tsSC63097a'	70.7	0.40	12.0	0.00	4.02	0.07	1.42	2.20	3.62	2.40	0.30	97.1	2.9
MI2opx8tsSC63097a'	72.8	0.36	11.8	0.01	3.14	0.08	1.21	0.98	3.35	3.40	0.02	97.1	2.9
MI3opx8tsSC63097a'	71.3	0.32	12.1	0.00	3.68	0.08	1.23	2.04	3.39	2.25	0.09	96.5	3.5
MI4opx8tsSC63097a'	70.5	0.51	12.4	0.00	3.67	0.07	1.29	1.68	3.59	3.09	0.08	96.8	3.2

Table 9. continued

Label	SiO_2	TiO_2	Al_2O_3	Cr_2O_3	FeO	MnO	MgO	CaO	Na_2O	K_2O	P_2O_5	Total	H_2O*
MI1opx2tsSC63097b	67.3	1.09	13.8	0.00	5.45	0.05	1.16	2.81	5.40	2.39	0.31	99.8	0.2
MI2opx2tsSC63097b	67.6	0.43	12.2	0.00	6.38	0.02	2.62	2.70	3.98	1.69	0.18	97.7	2.3
GI1opx4ts63097D[r]	56.2	1.07	17.0	0.01	6.52	0.11	4.21	6.82	4.89	1.63	0.25	98.6	1.4
GI1opx1ts63097E[r]	71.5	0.32	12.2	0.00	4.05	0.07	1.39	1.15	3.79	3.91	0.07	98.4	1.6
GI1opx3ts63097E[r]	71.2	0.34	12.1	0.01	4.63	0.08	1.73	1.27	3.46	3.37	0.26	98.4	1.6
GI3opx3ts63097E[r]	70.7	0.51	12.2	0.02	4.98	0.08	1.71	1.66	3.95	2.77	0.04	98.6	1.4
Glass inclusions in orthopyroxene: Eruption of June 30, 1997 -- White Dacite pumice													
Label	SiO_2	TiO_2	Al_2O_3	Cr_2O_3	FeO	MnO	MgO	CaO	Na_2O	K_2O	P_2O_5	Total	H_2O*
MI2opx8ts2	69.6	0.91	14.4	0.01	3.35	0.03	0.44	2.10	4.99	2.80	0.13	98.8	1.2
MI1opx14ts2	64.4	0.83	14.0	0.00	5.81	0.17	3.76	4.24	1.55	1.27	0.48	96.5	3.5
MI1opx1tsPum63097c	64.6	0.36	12.4	0.00	6.15	0.13	4.41	2.04	4.13	2.72	0.21	97.2	2.8
MI2opx1tsPum63097c[r]	70.5	0.35	11.9	0.00	4.52	0.04	1.39	1.47	3.40	3.28	0.12	97.0	3.0
MI1opx4TSPum63097d	73.0	0.85	13.5	0.00	3.80	0.06	0.60	1.48	4.39	3.35	0.13	101.1	-1.1
MI2opx4TSPum63097d	72.1	0.82	13.9	0.00	3.74	0.10	0.60	1.52	4.49	3.38	0.13	100.8	-0.8
Glass inclusions in orthopyroxene: Eruption of June 30, 1997 -- Mingled pumice													
MI1aopx1TSmixb[r]	69.0	0.59	13.2	0.01	4.36	0.03	1.42	2.03	4.55	2.88	0.12	98.2	1.8
MI1bopx1TSmixb[r]	67.9	0.67	13.8	0.00	3.81	0.10	1.24	2.24	4.59	2.87	0.15	97.4	2.6
MI1copx1TSmixb	68.7	0.66	13.1	0.03	4.21	0.10	1.27	2.03	4.50	2.97	0.12	97.7	2.3
Glass inclusions in orthopyroxene: Eruption of January 1, 1998 -- Dacite Dome rock													
MI1opx56ts5[r]	74.2	0.39	12.0	0.02	3.32	0.04	1.19	1.16	3.47	3.37	0.08	99.2	0.8
MI1opx12tsPum1198d[r]	74.1	0.62	12.3	0.00	3.08	0.02	1.07	0.76	3.82	3.98	0.06	99.7	0.3
Glass inclusions in hornblende													
MI2hbl1tsPum1198c	66.1	0.25	16.9	0.03	0.01	0.06	1.25	2.14	5.25	3.70	0.01	95.6	4.4

*H_2O determined using the difference technique

[r] recalculated for post-entrapment crystallization using the correction algorithm of Kress and Ghiorso (2001)

Figure 7. Compositional variations of SiO_2 versus **a)** MgO, **b)** CaO, **c)** FeO, **d)** Na_2O, **e)** Al_2O_3, **f)** K_2O, and **g)** Na_2O+K_2O for glass inclusions and matrix glasses from the recent eruptions of Popocatépetl. All Fe is reported as FeO. Divisions in **g)** are according to the classification scheme of LeBas *et al.* (1986). Glass inclusions are hosted by olivine microphenocrysts corrected for post-entrapment crystallization (OL, *open diamonds*), clinopyroxene (CPX, *open squares*), orthopyroxene corrected for post-entrapment crystallization (OPX, *open triangles*), and hornblende (HBL, *X's*). Matrix glasses are denoted by *crosses*. Also plotted are silicate liquid compositions of the mafic (*large filled circles*) and silicic (*large open circles*) end member magmas derived from thermodynamic modeling using MELTS (Ghiorso & Sack, 1995) and the inferred magmatic end member bulk compositions. The MELTS-derived mafic liquid is in equilibrium with olivine Fo_{84-86} at f_{O_2} = ΔNNO +1. The MELTS-derived silicic liquid data points cover the range of conditions 900-1000 °C, 0.5-1.5 wt.% H_2O, 500-1000 bar, and f_{O_2} = ΔNNO +0.3. See text for further explanation.

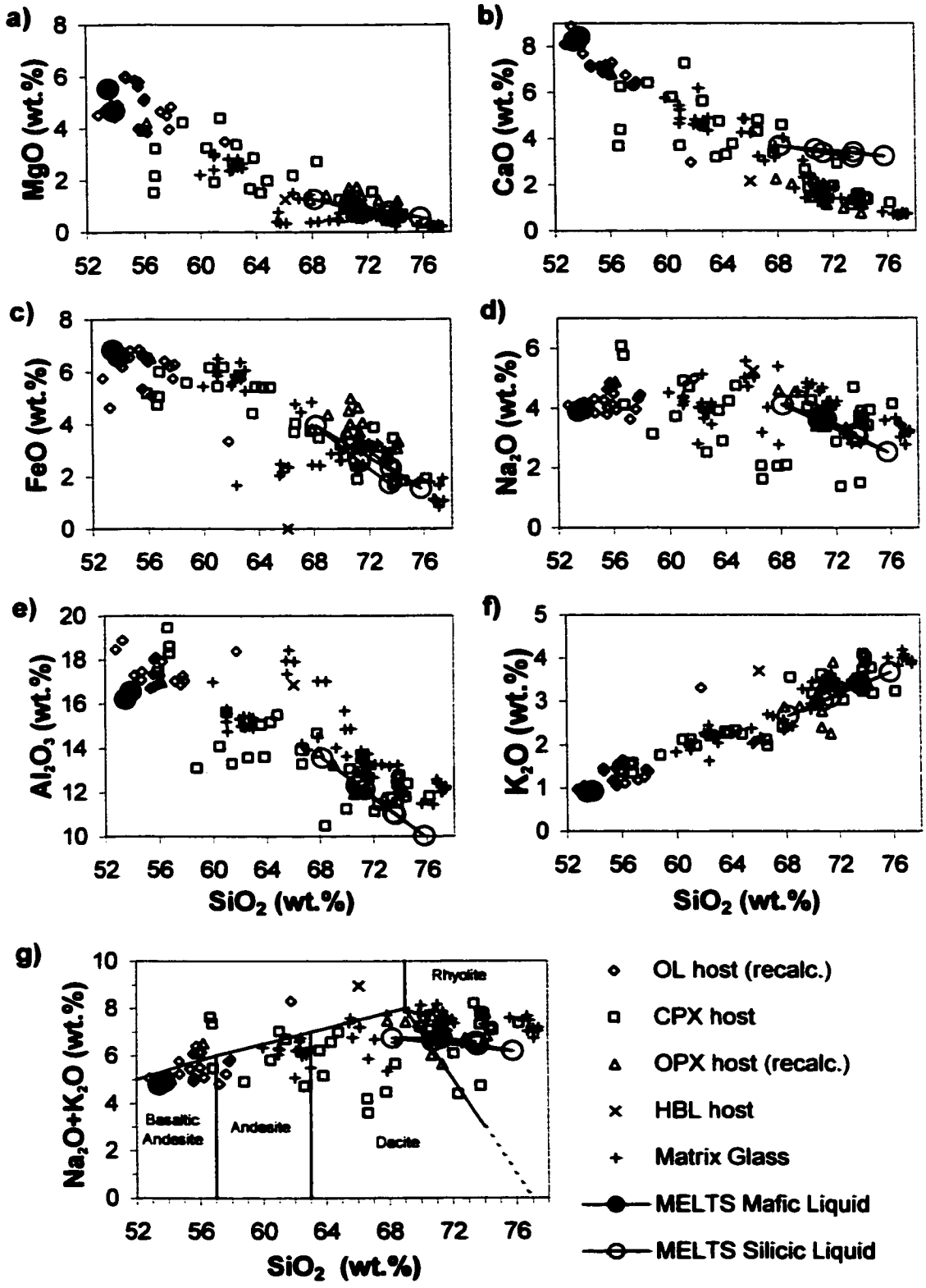
a)
MgO (wt.%)
b)
CaO (wt.%)
c)
FeO (wt.%)
d)
Na2O (wt.%)
e)
Al2O3 (wt.%)
SiO2 (wt.%)
f)
K2O (wt.%)
SiO2 (wt.%)
g)
Na2O+K2O (wt.%)
Rhyolite
Basaltic Andesite
Andesite
Dacite
SiO2 (wt.%)
OL host (recalc.)
CPX host
OPX host (recalc.)
HBL host
Matrix Glass
MELTS Mafic Liquid
MELTS Silicic Liquid

pressure, temperature, inclusion volume and redox, maintaining thermodynamic equilibrium as it backtracks the post-entrapment crystallization path. The method assumes that the inclusions were sealed throughout the crystallization process and that the effect of diffusion is negligible on the time scale of crystallization. The magnitude of post-entrapment crystallization of olivine varies between 1 and 10 wt.%.

Twenty-one glass inclusions in orthopyroxene and thirty glass inclusions in clinopyroxene were analyzed for major elements (Table 9; Figure 7). Post-entrapment crystallization correction calculations were performed on thirteen orthopyroxene-hosted glass inclusions (Kress and Ghiorso, 2001). Post-entrapment crystallization in orthopyroxene-hosted glass inclusions varied from 0 to 5 wt.%. Post-entrapment crystallization correction calculations for clinopyroxene-hosted glass inclusions were not possible because of apparent problems with the MELTS algorithm forming the basis for the entrapment correction program (Ghiorso and Sack, 1995). We expect a low degree of post-entrapment crystallization in the clinopyroxene-hosted glass inclusions, similar to that for orthopyroxene-hosted glass inclusions.

According to the classification scheme of LeBas *et al.* (1986), post-entrapment crystallization corrected GI's in olivine are mostly basaltic andesite. GI's in clinopyroxene span the range basaltic andesite to rhyolite. GI's in orthopyroxene are dacite to rhyolite (Figure 7, Table 9). With increasing silica, Al_2O_3, TiO_2, MgO, FeO, CaO, and P_2O_5 decrease. For K_2O, the opposite is true. There are no obvious trends for MnO, Cr_2O_3, and Na_2O.

We estimated the concentration of H_2O in glass inclusions using the difference technique (100 wt.% - analytical total of major elements; Anderson, 1974). The detection limit using this method is ~1 wt.% H_2O. Glass inclusions hosted by olivine, with H_2O contents that exceed the detection limit, contain 1.3 – 6.1 wt.% H_2O (average 3.1 wt.% H_2O). Dacite-to-rhyolite glass inclusions hosted by pyroxene with H_2O contents that exceed the detection limit have 1.2 – 4.3 wt.% H_2O (average 2.7 wt.% H_2O).

Matrix glasses

Fifty-seven major element analyses of matrix glasses were performed by EPMA (Table 10). Each analysis represents a single point in the matrix glass. Care was taken to avoid the solid phases in microlite-rich glass by inspecting the region of interest with high magnification BSE imaging. Analyses with unusually high Ca, Al, or Fe contents were presumed to be due to subsurface plagioclase and/or magnetite microlites and were excluded. Our major element data are similar to the data on light and dark matrix glasses found in the March 1996 dome rocks of Popocatépetl reported in Athanasopoulos (1997).

According to the classification scheme of LeBas *et al.* (1986), matrix glasses have compositions ranging from andesite to rhyolite (Figure 7, Table 10). Brown, microlite-rich matrix glasses are less evolved than colorless, microlite-poor matrix glasses. The matrix glass compositional variations mimic that of the glass inclusions: with increasing silica, Al_2O_3, TiO_2, MgO, FeO, CaO, and P_2O_5 decrease while K_2O increases. Within error, no trend exists for MnO, Cr_2O_3, and Na_2O. Matrix glasses from the brown andesite and white dacite pumices of the June 30, 1997 eruption contain 60-68 wt.% SiO_2 and 70-72 wt.% SiO_2, respectively. Matrix glass in the dacite dome rock erupted January 1, 1998 is the most evolved with 76-77 wt.% SiO_2.

Discussion

Estimation of intensive variables: T, P, and f_{O_2}

Two-Pyroxene geothermometry

Magmatic temperatures were calculated using orthopyroxene/clinopyroxene pair compositions and the QUILF program (Andersen *et al.*, 1993). Results are listed in Table 11. Most pyroxene pairs used in the geothermometry calculation were in direct contact; however, a few pyroxene pairs were separated by up to a few millimeters of groundmass.

Table 10. EPMA analyses of matrix glasses (in wt.%)

Eruption of June 30, 1997 -- Brown Andesite pumice

Label	SiO_2	TiO_2	Al_2O_3	Cr_2O_3	FeO	MnO	MgO	CaO	Na_2O	K_2O	P_2O_5	Total	H_2O*
matrix100ts1	62.7	1.46	15.4	0.02	5.74	0.09	2.81	4.66	3.86	2.18	0.36	99.3	0.7
matrix100ats1	61.0	1.21	15.6	0.00	5.99	0.13	2.92	5.44	4.10	1.94	0.29	98.5	1.5
matrix100bts1	62.0	1.49	15.3	0.00	5.47	0.10	2.82	4.62	2.81	2.27	0.31	97.2	2.8
matrix101ts1	60.0	1.24	17.0	0.00	5.45	0.06	2.20	5.77	4.52	1.82	0.34	98.4	1.6
matrix102ts1	61.0	1.38	15.8	0.00	5.85	0.14	2.98	5.26	4.38	1.87	0.30	98.9	1.1
matrix103ts1	62.3	1.21	15.4	0.00	5.89	0.08	2.56	4.63	4.01	2.29	0.33	98.7	1.3
matrix104ts1	62.1	0.98	15.0	0.06	5.60	0.08	2.37	4.83	4.02	2.20	0.29	97.5	2.5
matrix105ts1	62.7	1.49	15.0	0.02	6.37	0.06	2.53	4.79	3.93	2.21	0.34	99.4	0.6
matrix1cpx20ts1	63.0	1.06	15.4	0.00	6.06	0.18	2.64	4.91	3.45	2.04	0.34	99.0	1.0
matrix2cpx20ts1	61.0	1.14	15.2	0.00	6.03	0.09	2.39	4.65	4.34	1.97	0.33	97.1	2.9
matrix3cpx20ts1	63.0	1.08	14.9	0.00	5.27	0.09	2.46	4.37	4.17	2.17	0.31	97.8	2.2
matrix1cpx25ts1	67.8	0.80	14.5	0.00	4.84	0.08	1.44	3.18	2.78	2.57	0.27	98.3	1.7
matrix2cpx25ts1	66.6	1.13	14.2	0.00	4.78	0.04	1.52	3.23	3.19	2.69	0.33	97.7	2.3
matrix3cpx25ts1	67.1	0.93	13.9	0.00	4.46	0.08	1.29	3.04	4.02	2.66	0.29	97.8	2.2
matrix1opx8tsSC63097a	72.1	0.68	13.3	0.01	2.98	0.07	0.70	1.90	4.23	3.14	0.12	99.2	0.8
matrix2opx8tsSC63097a	71.2	0.76	13.6	0.00	3.23	0.09	0.74	1.88	3.82	3.33	0.15	98.7	1.3
matrix1ol25tsSC63097a	62.3	1.53	15.0	0.02	5.80	0.05	2.41	4.62	4.17	2.44	0.37	98.7	1.3
matrix2ol25tsSC63097a	62.4	1.46	15.0	0.01	5.88	0.06	2.58	4.55	3.67	2.32	0.33	98.2	1.8
Eruption of June 30, 1997 -- White Dacite pumice													
matrix1ts2	71.0	1.16	13.5	0.00	2.30	0.05	0.68	1.36	4.68	3.49	0.30	98.6	1.4
matrix2ts2	71.6	1.16	13.8	0.00	2.47	0.00	0.63	1.33	3.64	3.45	0.21	98.2	1.8
matrix2ts2	70.0	1.15	13.6	0.00	2.60	0.01	0.73	1.43	4.69	3.45	0.41	98.1	1.9
matrix3ts2	71.1	1.21	13.9	0.00	2.49	0.04	0.68	1.40	3.70	3.59	0.24	98.3	1.7
matrix4ts2	71.1	1.26	13.4	0.00	2.24	0.07	0.64	1.28	4.04	3.44	0.28	97.7	2.3
matrix5ts2	71.4	1.17	13.7	0.05	2.27	0.04	0.68	1.30	3.73	3.59	0.23	98.2	1.8
matrix6ts2	71.1	1.00	13.8	0.02	2.36	0.05	0.66	1.70	3.58	3.60	0.43	98.2	1.8
matrix7ts2	65.5	0.62	17.9	0.01	2.05	0.05	0.41	4.27	5.02	2.37	0.16	98.3	1.7
matrix9ts2	70.8	1.08	13.0	0.00	3.08	0.07	0.58	1.52	4.57	3.33	0.17	98.2	1.8
matrix11ts2	71.5	1.13	13.4	0.01	3.35	0.04	0.55	1.48	3.41	3.41	0.15	98.4	1.6

Table 10. continued

Label	SiO_2	TiO_2	Al_2O_3	Cr_2O_3	FeO	MnO	MgO	CaO	Na_2O	K_2O	P_2O_5	Total	H_2O^*
matrix14ts2	71.7	1.07	13.2	0.00	3.13	0.07	0.61	1.55	3.74	3.32	0.22	98.6	1.4
matrix17ts2	71.6	1.08	13.4	0.00	3.04	0.04	0.58	1.47	3.43	3.37	0.18	98.1	1.9
matrix200ts2	73.8	1.11	13.2	0.00	3.07	0.01	0.57	1.36	2.83	3.54	0.10	99.6	0.4
matrix201ts2	72.6	0.88	13.3	0.00	3.24	0.04	0.59	1.41	3.14	3.39	0.22	98.8	1.2
matrix2opx8ts2	71.6	0.92	13.1	0.02	3.11	0.03	0.50	1.52	4.23	3.36	0.27	98.7	1.3
matrix3opx8ts2	67.9	0.67	17.0	0.00	2.43	0.05	0.37	3.68	5.40	2.34	0.11	99.9	0.1
matrix1opx14ts2	69.9	0.79	14.9	0.00	2.60	0.04	0.43	2.32	4.85	2.94	0.10	98.8	1.2
matrix3opx14ts2	65.6	0.60	17.4	0.00	2.47	0.01	0.76	4.87	5.57	2.01	0.22	99.4	0.6
matrix1cpx12ts2	71.2	0.87	12.9	0.00	3.21	0.10	0.52	1.35	4.03	3.59	0.11	97.9	2.1
matrix2cpx12ts2	68.5	0.56	17.0	0.01	2.43	0.05	0.40	4.03	4.13	2.42	0.14	99.7	0.4
matrix3cpx12ts2	73.2	0.69	13.2	0.00	2.95	0.13	0.49	1.32	2.81	3.50	0.10	98.4	1.6
matrix1cpx10ts2	65.7	0.65	18.4	0.00	2.16	0.02	0.33	4.85	4.72	2.06	0.07	99.0	1.0
matrix2cpx10ts2	69.9	0.71	15.7	0.00	2.88	0.06	0.52	3.06	4.42	2.81	0.16	100.1	-0.1
matrix3cpx10ts2	66.1	0.75	17.9	0.00	2.36	0.06	0.33	4.25	5.03	2.17	0.11	99.1	0.9
matrix1cpx1tsPum63097c	71.4	0.75	12.9	0.00	2.97	0.02	0.55	1.44	4.22	3.64	0.15	98.0	2.0
matrix3cpx1tsPum63097c	69.2	0.79	14.0	0.00	2.87	0.09	0.45	1.85	4.56	3.29	0.14	97.3	2.7
matrix1cpx2tsPum63097c	71.7	0.82	12.8	0.00	3.04	0.03	0.53	1.46	3.98	3.51	0.13	97.9	2.1
matrix1newopx3tsPum63097c	72.0	0.89	12.7	0.02	3.26	0.08	0.56	1.41	4.10	3.43	0.15	98.5	1.5
Eruption of June 30, 1997 -- Mingled pumice													
matrix1ol1TSmixb	61.0	1.57	14.7	0.06	6.51	0.14	3.01	4.87	4.22	2.03	0.31	98.5	1.5
Eruption of January 1, 1998 -- Dacite Dome rock													
Label	SiO_2	TiO_2	Al_2O_3	Cr_2O_3	FeO	MnO	MgO	CaO	Na_2O	K_2O	P_2O_5	Total	H_2O^*
matrix501ts5	76.7	0.22	12.6	0.02	1.11	0.00	0.20	0.68	3.49	4.19	0.11	99.3	0.7
matrix502ts5	76.8	0.18	12.4	0.00	1.06	0.02	0.22	0.69	3.43	4.07	0.05	99.0	1.0
matrix503ts5	76.7	0.13	12.4	0.01	1.13	0.00	0.19	0.69	3.04	4.00	0.03	98.4	1.6
matrix1cpx56ts5	77.1	0.76	12.0	0.00	1.66	0.05	0.25	0.79	2.78	3.96	0.06	99.4	0.6
matrix2opx56ts5	77.4	0.41	12.1	0.01	1.92	0.09	0.22	0.71	3.18	3.87	0.07	100.0	0.0
matrix3opx56ts5	76.4	0.52	11.4	0.03	1.79	0.01	0.23	0.71	3.67	3.83	0.01	98.7	1.3
matrix601ts6	77.1	0.11	12.0	0.00	0.84	0.01	0.21	0.71	3.19	3.96	0.00	98.1	1.9
matrix602ts6	77.4	0.17	12.2	0.02	1.07	0.01	0.21	0.72	3.25	3.93	0.03	99.0	1.0

Table 10. continued

Label	SiO_2	TiO_2	Al_2O_3	Cr_2O_3	FeO	MnO	MgO	CaO	Na_2O	K_2O	P_2O_5	Total	H_2O*
matrix1hbl1tsPum1198c	75.6	0.53	11.5	0.01	1.77	0.00	0.25	0.81	3.59	4.01	0.07	98.1	1.9
matrix1cpx17tsPum1198c	74.0	0.84	12.2	0.00	1.85	0.00	0.22	1.10	3.64	3.67	0.16	97.7	2.3

* H_2O determined using the difference technique

Table 11. Pyroxene geothermometry

Temperatures obtained with QUILF (Andersen et al., 1993)

"Cool" cores	Temp in deg. C	QUILF err.
opx19corets1-cpx20corets1	949	8
opx55corets5-cpx55corets5	976	27
opx40cpx40corets5	969	19
opx30cpx30corets6	967	42
opx35cpx34corets6	961	5
opx33cpx34corets6	977	32
opx37cpx37corets6	956	33
opx38cpx38corets6	945	45
opx1core-cpx2coreaPopoPum63097c	989	4
opx4core-cpx14corePopoPum1198c	941	27
opx4core-cpx17corePopoPum1198c	945	28
opx12corea-cpx10corePopoPum1198d	936	29
Average of "Cool" cores	**959**	
Std. Dev. (1-sigma)	17	
n=	12	
"Cool" rims		
cpx40opx40rimts5	907	23
opx55rimts5-cpx55rimts5	935	29
opx56rimts5-cpx56rimts5	1002	23
cpx31opx31rimts6	935	26
cpx31opx32rimts6	965	37
cpx34opx35rimts6	974	39
cpx37opx37rimts6	937	28
cpx38opx38rimts6	1000	19
opx4rima-cpx17rim PopoPum1198c	920	38
opx4rim-cpx17rim PopoPum1198c	921	32
opx12rim-cpx10rim PopoPum1198d	943	22
Average of "Cool" rims	**949**	
Std. Dev. (1-sigma)	32	
n=	11	
"Hot" rims		
opx19rimts1-cpx20rimts1	1053	38
opx19rimts1-cpx50rimts1	1048	41
cpx41opx41rimts5	1065	46
Average of "Hot" rims	**1055**	
Std. Dev. (1-sigma)	9	
n=	3	
Xenocrystic "Cold" core and rim		
cpx57corets6-opx57corets6	882	29
cpx57rimts6-opx57rimts6	881	7
cpx57rim2ts6-opx57rim2ts6	860	14

Low-Mg# pyroxene core pairs yield temperatures of 959±17 °C (n=12). High-Mg# pyroxene core pairs are out of equilibrium and do not yield reliable temperature estimates. Temperatures derived from pyroxene rims come in low and high temperature groups. The low temperature rims yield 949±32 °C (n=11) and involve unzoned to weakly zoned low-Mg# pyroxenes or high-Mg# pyroxenes with strong normal zonation. The temperatures derived from the pyroxene cores and low-Mg# pyroxene rims are in good agreement. The high temperature pyroxene rims yield 1055±9 °C (n=3) and involve either low-Mg# pyroxene with reversely zoned rims or high-Mg# pyroxenes with weak normally zoned rims.

One pyroxene pair yields temperatures of ~870 °C for both core and rim. This pyroxene pair is possibly derived from the cooler margins of the magma body. Straub and Martin-Del Pozzo (2001) found one pair of low-Mg# pyroxenes and determined a temperature of 930-950 °C using the geothermometer of Lindsley and Andersen (1983).

Hornblende-plagioclase geothermometry

The composition of Popocatépetl hornblende allows use of the hornblende-plagioclase (Hbl-Plag) geothermometer of Holland and Blundy (1994). However, accurate application of the Hbl-Plag geothermometer is difficult, since the composition of plagioclase in equilibrium with hornblende at the time of crystallization is unknown. Taking a conservative approach, we assume that at hornblende saturation, the coexisting plagioclase had a composition that lies in the range of the measured plagioclase compositions (An_{28-61}). Utilizing the edenite-tremolite geothermometer (for mineral assemblages lacking quartz) over a pressure range of 0-5 kbar, the entire measured plagioclase and hornblende compositional range yields temperatures from ~775 to 900°C.

Apatite saturation temperature

Apatite saturation temperatures were calculated using the model equation from Piccoli & Candela (1994):

$$T = \frac{\left[26{,}400 \cdot C^{l}_{SiO_2} - 4{,}800\right]}{12.4 \cdot C^{l}_{SiO_2} - \ln\left(\frac{C^{l,o}_{P_2O_5}}{1 - X/100}\right) - 3.97}, \qquad (1)$$

where T is the apatite saturation temperature (in Kelvin), $C^{l,o}_{P_2O_5}$ is the P_2O_5 concentration in the initial melt (whole rock P_2O_5 content), $C^{l}_{SiO_2}$ is the SiO_2 concentration in the melt at apatite saturation (whole rock SiO_2 content), and X is the crystallinity (in wt.%). Using whole rock compositions of the most silicic clasts, and ~35 vol.% (~40 wt.%) crystallinity (from modal analysis of June 30, 1997 white pumice samples), these calculations suggest apatite saturation at between 945 °C and 959 °C (n=4). This is in good agreement with temperatures derived from cores of low-Mg# pyroxene.

Fe-Ti oxide geothermometry and oxygen barometry

The thermodynamic formulation of Ghiorso & Sack (1991) and QUILF (Andersen *et al.*, 1993) were both used to estimate temperature and f_{O_2} from Fe-Ti oxide pairs (Table 12). Oxide pairs that did not pass the Mg/Mn partition test of Bacon & Hirschmann (1988) were not used. Most of the oxide pairs used in the T-f_{O_2} calculation were in contact; pairs not in contact were less than 100 μm apart.

Fe-Ti oxide compositions cover a wide range (X_{Ilm} = 0.63-0.79 and X_{Usp} = 0.30-0.47). Similarly, temperature estimates from both geothermometers cover a broad range (910-1030 °C using QUILF and 1040-1190 °C using Ghiorso & Sack (1991); n=27 pairs). Oxygen fugacity results are comparable using both methods and have the range ΔNNO +0.5 to ΔNNO +1.5. Athanasopoulos (1997) analyzed several Fe-Ti oxide pairs from the March 1996 lava dome that have a very similar compositional range. Variable degrees of magma mixing and/or incomplete thermal re-equilibration are possible explanations for the wide variation in T and f_{O_2} obtained using each method.

Table 12. Oxygen thermobarometry results from Fe-Ti oxide pairs and the formulations of Ghiorso and Sack (1991) and QUILF (Andersen et al., 1993)

	Ghiorso and Sack			QUILF		
	Temp. °C	log fO_2	ΔNNO	Temp. °C	log fO_2	ΔNNO
June 30, 1997 Brown Andesite Pumice						
mgt5/ilm5ts1	1066	-7.98	1.2	933	-10.10	1.2
mgt6/ilm6ts1	1116	-7.18	1.4	988	-9.06	1.3
mgt6a/ilm6ts1	1081	-7.54	1.5	964	-9.35	1.4
mgt7/ilm7ts1	1075	-7.56	1.5	952	-9.48	1.5
mgt6/ilm6(r)ts1	1107	-7.32	1.3	974	-9.31	1.3
mgt6a/ilm6(r)ts1	1073	-7.68	1.4	951	-9.60	1.4
mgt21/ilm21ts1	1107	-7.36	1.3	945	-9.90	1.2
mgt21a/ilm21ts1	1124	-7.19	1.2	960	-9.70	1.1
mgt22/ilm22ts1	1108	-7.76	0.9	957	-10.14	0.7
mgt22a/ilm22ts1	1055	-8.31	1.0	909	-10.76	0.9
June 30, 1997 White Dacite Pumice						
mgt1/ilm1ts2	1060	-8.65	0.6	952	-10.39	0.6
mgt2/ilm2ts2	1074	-8.48	0.6	954	-10.44	0.5
mgt3/ilm2ts2	1078	-8.44	0.6	957	-10.40	0.5
mgt8/ilm8ts2	1085	-8.28	0.7	960	-10.24	0.6
mgt23/ilm23ts2	1186	-6.58	1.1	1033	-8.69	1.0
mgt23b/ilm23ts2	1179	-6.65	1.1	1029	-8.75	1.0
mgt24/ilm24ts2	1069	-8.50	0.7	949	-10.40	0.6
mgt24a/ilm24ts2	1085	-8.32	0.6	962	-10.24	0.6
January 1, 1998 Dacite Dome Rock						
mgt10/ilm10ts5	1186	-7.03	0.6	1029	-9.14	0.6
mgt11/ilm11ts5	1093	-7.59	1.2	961	-9.61	1.2
mgt14/ilm14ts5	1132	-7.51	0.8	1001	-9.44	0.7
mgt25/ilm25ts5	1057	-8.25	1.1	939	-10.16	1.0
mgt26/ilm26ts5	1064	-8.32	0.9	941	-10.29	0.9
mgt26a/ilm26ts5	1058	-8.38	0.9	934	-10.36	0.9
mgt12/ilm12ts6	1040	-8.88	0.7	915	-10.98	0.6
mgt13/ilm13ts6	1091	-7.51	1.4	963	-9.44	1.3
mgt29/ilm29ts6	1114	-7.48	1.1	972	-9.62	1.0
Average	1095	-7.80	1.0	962	-9.85	0.9
1σ std. dev.	39	0.62	0.3	31	0.60	0.3

All oxide pairs passed Mg/Mn Partition test of Bacon and Hirschmann (1988)
ΔNNO calculated using buffer equation from Frost (1991)
Assume P=1000 bar

The differing results from the two methods, however, must be reconciled. We suggest that the values presented here using the thermodynamic formulation of Ghiorso & Sack (1991) may significantly overestimate the temperature of Popocatépetl magma. Evans *et al.* (2001a) found that for hydrous, silicic and intermediate volcanic rocks at high oxygen fugacity (>ΔNNO +1) and 700-900 °C, the model of Ghiorso & Sack (1991) overestimates T and f_{O_2}. This error may be associated with inadequate characterization of the $R\bar{3}$ - $R\bar{3}\frac{2}{c}$ transition in the rhombohedral phase (B. W. Evans & M. S. Ghiorso, pers. comm., 2001). New experimental results for the Fe-Ti-O system at 1 bar and 1000-1300 °C are consistent with this hypothesis (Lattard *et al.*, 2001). The new data suggest that Popocatépetl Fe-Ti oxides equilibrated at temperatures ≤1000 °C at an oxygen fugacity between NNO to ΔNNO +1. This temperature and fugacity estimate is consistent with QUILF calculations. We conclude from this that Fe-Ti oxides record temperatures that probably span the range ~900-1000 °C and f_{O_2} = NNO to ΔNNO +1.

Sulfide/Sulfate wavelength shift analysis

As another measure of oxygen fugacity, two glass inclusions in olivine were analyzed for sulfide/sulfate using the wavelength shift of sulfur $K\alpha$ X-rays (Carroll and Rutherford, 1988). The results were converted to oxygen fugacity using the method of Wallace & Carmichael (1994). This method assumes that sulfur is dissolved as S^{+6} and S^{-2} in the glass inclusion and that there is a linear relationship between the S^{+6}/S_{total} ratio and the wavelength shift. Recent X-ray absorption spectroscopy measurements (Paris *et al.*, 2001) support the validity of these assumptions. Measurements suggest that the silicate melt in olivine-hosted glass inclusions has an oxygen fugacity of ΔNNO +1.2 log units and the sulfur dissolved in the melt is dominated by sulfate (87 mol%). Metrich & Clocchiatti (1996) comment that oxidation of sulfur in glasses can be caused by post-entrapment changes in the Fe^{+2}/Fe^{+3} ratio of the melt, H_2 loss (by diffusion), and heating due to long time

periods under the electron beam. In our case, limited post-entrapment crystallization of the host olivine probably minimizes the Fe^{+2}/Fe^{+3} evolution of the melt. Furthermore, redox calculations using the scheme of Kress & Ghiorso (2001) suggest that the ferric-ferrous ratio of the melt will not change substantially during limited post-entrapment crystallization. Hydrogen loss is difficult to assess but may be significant considering the high beam currents, long count times, and hydrous nature of the glass inclusions compared to the nominally anhydrous standard glasses. We would expect that if electron beam-induced H-loss is occurring, it would result in higher inferred melt oxygen fugacities. Though not quantified, we reduced the amount of heating due to the electron beam, which may cause H-loss, by reducing the accelerating voltage. A more detailed analysis of potential H-loss and oxidation due to electron bombardment is necessary to resolve this issue.

Evidence for magma mixing

Evidence for magma mixing is ubiquitous in the pumice and dome rocks from Popocatépetl on the macroscopic, petrographic, and chemical level. Hand samples of pumice and dome rocks contain bands and lenses of light and dark material suggesting the mechanical mingling of magmas of differing composition. Disequilibrium textures and mineralogy include olivine (Fo_{90}) in a dacitic to rhyolitic matrix glass (some with orthopyroxene reaction rims), sieve-textured and resorbed plagioclase, reverse zonation in the rims of low-Mg# pyroxene, and normal zonation in the rims of olivine and high-Mg# pyroxene. Our observations are consistent with other studies of Popocatépetl that suggest magma mixing is a common process during the 40,000 year history of the modern Popocatépetl cone (Cantagrel et al., 1984; Robin, 1984; Boudal and Robin, 1988; Kolisnik, 1990; Athanasopoulos, 1997).

Definition of the end-member magmas: MELTS modeling

It is likely that one or both of the presumed magmatic end-members may themselves be the product of mixing processes. Nevertheless, variation in the most

recent eruption products can be well described by mixing of two distinct and relatively homogeneous compositions immediately prior to eruption, and this final mixing event is likely the most relevant in terms of unraveling details of the eruption process. We used the MELTS algorithm (Ghiorso and Sack, 1995) to help define the compositions and intensive parameters of the mixing end-members in the following manner.

We first assume that end-member compositions lie along the linearly regressed mixing line (Figure 2). Compositions along extrapolations of this mixing line were explored to find potential end-member compositions that could have been in equilibrium with phenocryst phases. The chosen bulk compositions must saturate a mineral assemblage consistent with the proportions present in the rock samples. The mineral compositions determined by MELTS must be consistent with phase compositions determined by EPMA. Reasonable pressure conditions were iteratively tested using MELTS. The magmatic conditions were constrained with temperatures, H_2O contents, and f_{O_2} determined from methods described previously. This approach allows simultaneous application of a large number of thermodynamic constraints on potential conditions and compositions. In practice, this places tight constraints on permissible end-member compositions. Our inferences of the bulk compositions and magmatic conditions of the silicic and mafic end-members are shown in Table 13.

The MELTS-modeled silicic end-member is a dacite (65 wt.% SiO_2) that crystallized predominantly at low pressures (< 1.5 kbar or < 6 km) with 0.5-1.5 wt.% H_2O and f_{O_2} = ΔNNO +0.3 log units. A crystallization interval of 1000-900 °C produces a phase assemblage of plagioclase + clinopyroxene + orthopyroxene + titanomagnetite ± ilmenite. The plagioclase and pyroxene compositions computed by MELTS match EPMA results quite well (Figures 8 & 9). In addition, MELTS predicts ~30-40 wt.% feldspar, ~6-8 wt.% pyroxene, and ~0.5-1 wt.% titanomagnetite (at 0.5-1.5 wt.% H_2O, 0.1 – 1 kbar, 950 °C, and f_{O_2} = ΔNNO +0.3 log units) which is consistent with modal observations (Table 4). The MELTS-predicted silicate liquid

Table 13. Popocatépetl Mixing End Members

End member bulk compositions derived using the MELTS algorithm (Ghiorso and Sack, 1995)

Silicic End Member (ox. wt.%)	
SiO_2	65
TiO_2	0.63
Al_2O_3	16.57
FeO	4.12
MgO	2.19
MnO	0.08
CaO	4.91
Na_2O	4.53
K_2O	1.95
P_2O_5	0.14
Total	99.6
H_2O	0.5-1.0
NiO	33 ppm
fO_2	ΔNNO +0.3
P (kbar)	0.5 - 1.5

Equilibrium crystallization

900-1000 deg. C crystallization interval

Mineralogy

Plagioclase

Low-Mg# Pyroxene

Titanomagnetite

Ilmenite

Mafic End Member (ox. wt.%)	
SiO_2	53
TiO_2	1.10
Al_2O_3	14.9
FeO	7.57
MgO	9.94
MnO	0.12
CaO	7.55
Na_2O	3.56
K_2O	0.82
P_2O_5	0.27
Total	98.8
H_2O	3
NiO	308 ppm
fO_2	ΔNNO +1
P (kbar)	1 - 4

Fractional crystallization

T_{min} prior to mixing = 1050 deg. C

Mineralogy

Olivine

High-Mg# Pyroxene

	Mixture 1 45 wt.% Mafic 55 wt.% Silicic	Mixture 2 15 wt.% Mafic 85 wt.% Silicic
SiO_2	58.4	63.2
TiO_2	0.89	0.70
Al_2O_3	15.7	16.3
FeO	6.02	4.64
MgO	6.45	3.35
MnO	0.10	0.09
CaO	6.36	5.31
Na_2O	4.00	4.38
K_2O	1.33	1.78
P_2O_5	0.21	0.16
Total	99.2	99.5
Represents	Brown Andesite Pumice 6/30/1997	White Dacite Pumice 6/30/1997 and Dome Rocks 1/1/1998

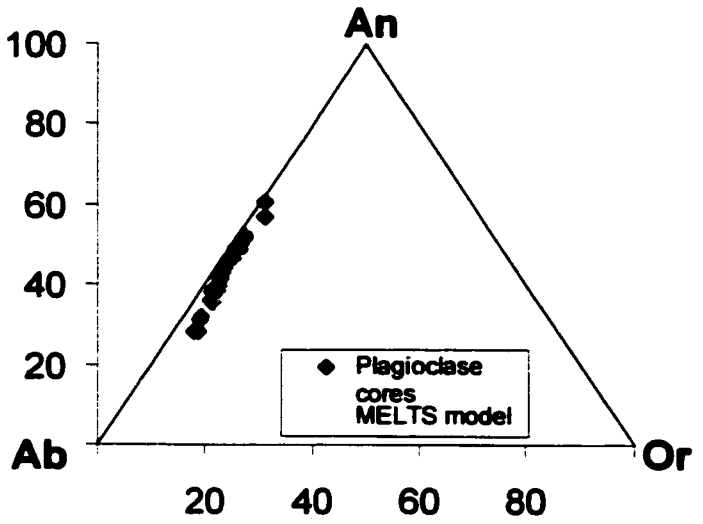

Figure 8. Feldspar ternary diagram showing the compositions of plagioclase cores (*solid diamonds*). Also shown are plagioclase compositions derived from thermodynamic modeling using MELTS (Ghiorso & Sack, 1995) and the inferred bulk composition of the silicic end member magma (*open circles*). The MELTS-derived plagioclase data points cover the range of conditions 900-1000 °C, 0.5-1.5 wt.% H_2O, 500-1000 bar, and f_{O_2} = ΔNNO +0.3. See text for further explanation.

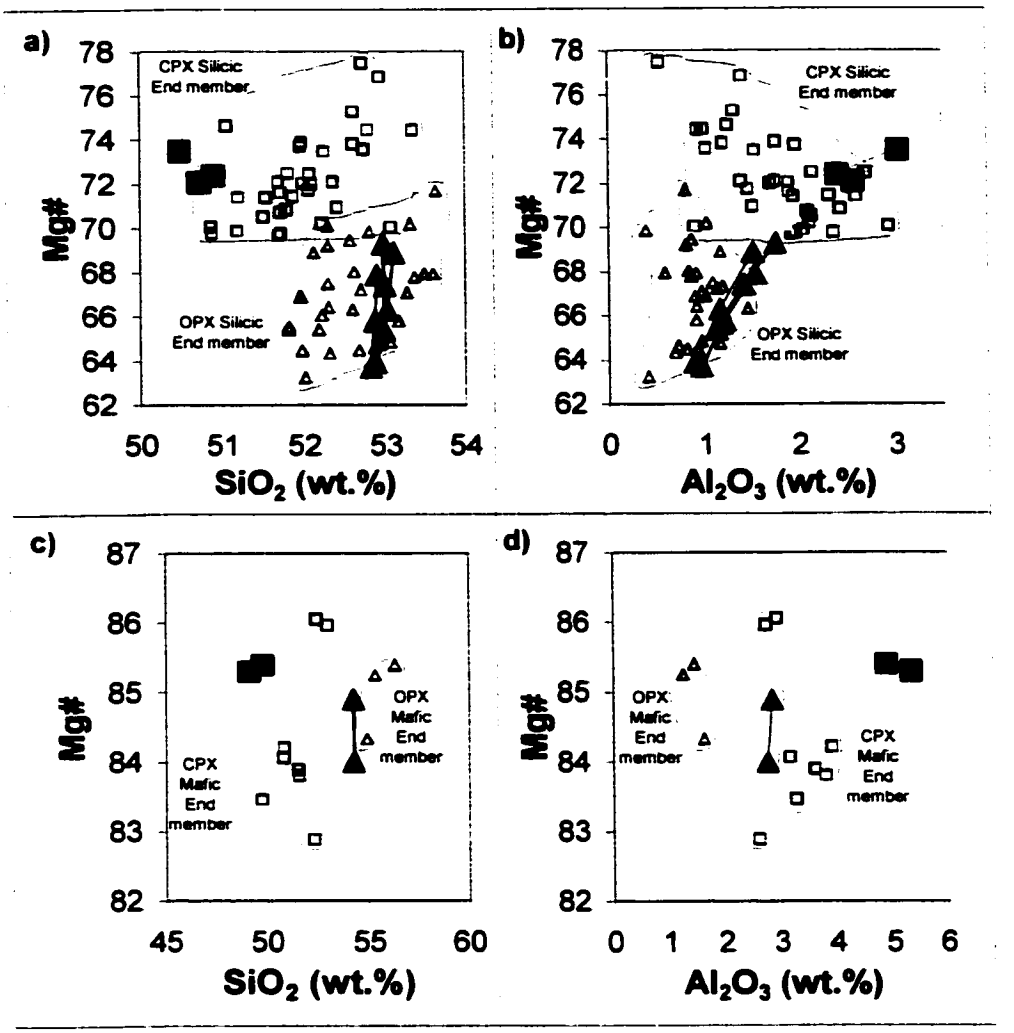

Figure 9. Comparison of pyroxene core compositions from EPMA analyses and pyroxene compositions calculated by MELTS thermodynamic modeling (Ghiorso & Sack, 1995). Orthopyroxene (*triangles*) and clinopyroxene (*squares*) compositions from the silicic end member are shown in **a)** SiO_2 and **b)** Al_2O_3 versus Mg# and those from the mafic end member are shown in **c)** SiO_2 and **d)** Al_2O_3 versus Mg#. *Open symbols* are pyroxene core compositions measured by EPMA. *Solid symbols* are pyroxene compositions derived from MELTS thermodynamic modeling of the mafic and silicic end members. The MELTS-derived silicic pyroxene data covers the range of conditions 900-1000 °C, 0.5-1.5 wt.% H_2O, 100-1000 bar, and f_{O_2} = ΔNNO +0.3. The MELTS-derived mafic pyroxene data covers the range of conditions 1050-1150 °C, 3 wt.% H_2O, 1000-2000 bar, and f_{O_2} = ΔNNO +1. See text for further explanation.

compositions at these conditions also match the EPMA analyses of matrix glasses in the samples of June 30, 1997 white dacite pumice (Figure 7). Bulk compositions with higher SiO_2 are too poor in CaO, which results in insufficient feldspar crystallization. Conditions of higher f_{O_2} increases the Mg# in orthopyroxene to unsuitable levels. Pressures greater than 1.5 kbar forces too much Al_2O_3 into pyroxene. MELTS modeling of the silicic end-member employed initial H_2O contents (0.5 – 1.5 wt.% H_2O) that are lower than those inferred from glass inclusions in low-Mg# pyroxenes (1.2 – 4.3 wt.% H_2O). This was done in order to increase liquidus temperatures and promote crystallization so as to match the modeled mass of crystallization with modal amounts observed in white dacite pumice (Table 4). Higher H_2O contents suppress the liquidus and decrease the total amount of crystallization. The CaO content of the starting bulk composition was artificially increased by 0.5 wt.% CaO for the MELTS modeling. This step was necessary in order to increase stability of clinopyroxene. The increase is within error of the linear least squares-derived end-member bulk composition.

The MELTS-modeled mafic end-member is a basaltic andesite (53 wt.% SiO_2) with ~3 wt.% H_2O and f_{O_2} = ΔNNO +1 log units (Table 13). Magmas of this composition are not known to have erupted from Popocatépetl. Larocque *et al.* (1998) report a basaltic andesite (54.4 wt.% SiO_2) erupted from Cerro Tecajete in the nearby Valley of Mexico, however, it is more alkalic and less magnesian than the calculated mafic end-member for Popocatépetl. The pressure-temperature evolution of the mafic end-member consists of olivine fractionation at moderate pressures (2-4 kbar, 1150-1300 °C) followed by low-pressure (1-2 kbar, 1050-1150 °C) pyroxene fractionation. This P-T evolution was chosen to avoid high-pressure orthopyroxene saturation and low-pressure feldspar saturation. Lower silica bulk compositions (e.g. 50 wt.% SiO_2) are unsatisfactory due to insufficient melt evolution with crystallization. Water content of at least 1 wt.% is necessary to suppress high-pressure orthopyroxene saturation. H_2O contents higher than 3 wt.% suppress olivine crystallization

excessively. High oxygen fugacity is desirable to decrease ferrous iron content, which increases Fo content in olivine. Lower oxygen fugacities allow for too much olivine crystallization and suppresses low-pressure orthopyroxene saturation.

MELTS modeling supports a xenocrystic origin of the large, Fo_{87-91}, Ni-rich and Cr-spinel-bearing olivine (Figure 3). The high Ni-content could not have been derived from the permissible silicate melt compositions for the mafic end-member. In contrast, the low-Ni, Fo_{84-86} olivines that contain melt inclusions likely did crystallize from the mafic end-member. We speculate that the xenocrystic Fo_{87-91}, Ni-rich olivines and their included Cr-spinel were plucked from the mantle and/or crystallized from a primitive Mg-, Ni-, and Cr-rich mantle melt (Clynne and Borg, 1997) which were subsequently incorporated into Popocatépetl's mafic end-member magma.

MELTS-derived pyroxene compositions for the mafic end-member match EPMA analyses fairly well (Figure 9) although they are generally higher in Al_2O_3 than EPMA analyses. The CaO content of the starting bulk composition was artificially decreased by 0.5 wt.% CaO for MELTS modeling. This step was necessary in order to increase the relative stability of orthopyroxene. This decrease is within error of the linear least squares-derived end-member bulk composition. MELTS-calculated silicate liquids for the mafic end-member match olivine-hosted melt inclusion compositions very well (Figure 7). MELTS modeling suggests the mafic end-member crystallized ~10 wt.% modal olivine prior to mixing.

Proportions and depth of magma mixing

With the compositions of the mixing end-members identified, we can calculate the proportions of mixing needed to derive the compositions of individual pumice or lava clasts (Table 13). Compositions of the most mafic samples (~58 wt.% SiO_2), represented by brown andesite pumice erupted on June 30, 1997, are consistent with mixing of ~55 wt.% mafic end-member and ~45 wt.% silicic end-member. The most silicic clasts (~63 wt.% SiO_2) are represented by white dacite pumice erupted on

June 30, 1997 and gray dacite dome rocks erupted January 1, 1998. These are inferred to be made up of ~85 wt.% silicic end-member and ~15 wt.% mafic end-member.

Based on the minimum pressure estimates for the mafic end-member (1 kbar) and the maximum pressure estimate for the silicic end-member (1.5 kbar) derived from the MELTS simulations presented above, we infer that magma mixing occurred at pressures between ~1 and 1.5 kbar (~4-6 km depth). This result is toward the shallow end of the ~4-13 km range of mixing depths proposed by Straub & Martin-Del Pozzo (2001) for the recent eruptives of Popocatépetl.

Sulfide liquid stability constraints on f_{O_2} and f_{S_2}

Sulfide inclusions in phenocryst phases may provide additional clues as to the original oxygen fugacity of the magma as well as an estimate of sulfur fugacity. We analyzed by EPMA one high-iron sulfide inclusion (sulfide1tsPum1198e, Table 8) as well as its high-Mg# orthopyroxene host (opx1ab&cnrsulf1ts1198e, Table 6) that is thought to have crystallized from the mafic end-member. The Cu content of this sulfide is nearly zero, suggesting that the thermochemical model of Kress (2002) for O-S-Fe-Ni liquids can be applied without extrapolation. However, this yields an oxygen fugacity estimate 0.9 log units below fayalite-magnetite-quartz (ΔNNO -1.6 log units) and an unrealistically high estimated sulfur fugacity. This calculation is extremely sensitive to analytical error and the anion contents of sulfide liquids are known to be subject to extremely rapid resetting (Kress, 1997).

We can impose more robust bounds on initial oxidation state and sulfur fugacity considering cation reactions with coexisting phases. If we assume that the sulfide was originally in equilibrium with the calculated composition of the host basaltic andesite end-member (Table 13), we can use the reaction:

$$Fe^{sulfliq} + O^{sulfliq} = FeO^{sulliq} \qquad (2)$$

A similar reaction can be considered relative to the orthopyroxene host, but the resulting constraint on oxygen fugacity will be less stringent because the activity

of FeO in the orthopyroxene is only weakly dependent on f_{O_2}. Reaction 2 implies that increasing either iron activity or oxygen fugacity will drive iron into the silicate liquid. High-iron sulfide liquids will have lower maximum oxygen fugacity stability limits than low-iron sulfide liquids at a given sulfur fugacity. Increasing sulfur fugacity increases sulfur content of the sulfide, lowering both Fe and O activities, and thus stabilizing the sulfide liquid to higher oxygen fugacity. In order to place a bound on this additional degree of freedom, we must consider another reaction involving sulfur. One obvious candidate is the formation of anhydrite:

$$S^{sulfliq} + 3O^{sulfliq} + CaO^{silliq} = CaSO_4^{anhydrite} \qquad (3)$$

The sulfide liquid model of Kress (2002) is not yet calibrated for elevated pressure. It has long been recognized that a magma's redox state relative to solid buffers such as fayalite-magnetite-quartz (FMQ) or NNO represents a roughly temperature- (Sato, 1978; Carmichael and Ghiorso, 1986) and pressure- (Kress and Carmichael, 1991) independent coordinate of silicate liquid oxidation state. Kress (2002) observed that expressing sulfur fugacity relative to buffers such as Pt-PtS and Fayalite-Magnetite-Quartz-Pyrrhotite (FMQP) represents an approximately temperature-independent coordinate of sulfur-fugacity as well. Unpublished sulfide volume data from our laboratory suggests that FMQP may also be a pressure-independent coordinate of sulfur fugacity. This gives us a useful, if yet unproven, tool for exploring the stability limits of sulfide liquids at elevated pressure.

Calculations were performed using the sulfide liquid model of Kress (2002), the silicate liquid model of Ghiorso & Sack (1995) and thermodynamic data for anhydrite from Robie & Hemingway (1995). Results suggest that anhydrite can coexist with the calculated silicate liquid and observed sulfide liquid at an oxygen fugacity of about ΔNNO +0.4 log units and a sulfur fugacity approximately 2.1 log units above FMQP. As anhydrite was not stable in any Popocatépetl magmas, these estimates are maximum bounding values for both oxygen and sulfur fugacities of the mafic end-member.

Summary of the mineralogy and pre-eruptive conditions of the magmatic end-members

Mafic End-member

The mineralogy of the mafic end-member includes olivine (Fo_{84-86}), minor high-Mg# clinopyroxene and orthopyroxene, and xenocrystic Ni-rich and Cr-spinel-bearing olivine (Fo_{87-91}). None of the available geothermometers can be used to estimate the temperature of the mafic end-member immediately prior to mixing. We can infer, however, that the mafic end-member was probably at least as hot as the highest temperature recorded in high-Mg# pyroxene rims (~1050 °C).

Mafic volcanics in Central and Western Mexico are typically relatively oxidized. The basalt to basaltic andesite eruptives of Jorullo volcano have compositions and mineralogy very similar to Popocatépetl's mafic end-member (Luhr and Carmichael, 1985). Luhr & Carmichael (1985) suggest that pre-eruptive oxygen fugacity for these volcanics fall in the range ΔNNO +0.6 to ΔNNO +2.5. Basaltic andesites of Western Mexico in general have oxygen fugacities in the range NNO to ΔNNO +1 (Carmichael, 1991). Wallace & Carmichael (1999) found calc-alkaline basaltic andesites from the Chichinautzin Volcanic Field (located immediately west of Popocatépetl) to have oxygen fugacities in the range ΔNNO –0.5 to ΔNNO +0.9 log units.

Sulfide/sulfate measurements in olivine-hosted glass inclusions from this study indicate ΔNNO = +1.2 log units. Unfortunately, this f_{O_2} estimate may be corrupted by oxidation effects caused by the electron beam during analysis. Thermodynamic modeling of a single sulfide inclusion in high-Mg# orthopyroxene gives a maximum f_{O_2} = ΔNNO+0.4. We cannot rule out the possibility that the single sulfide inclusion and its orthopyroxene host are xenocrysts and thus irrelevant to pre-mixing conditions in the mafic end-member. MELTS modeling of the bulk composition of the calculated mafic end-member constrained oxygen fugacity to ΔNNO+1. Lastly, thermodynamic modeling of post-entrapment crystallization in

olivine-hosted glass inclusions suggest f_{O_2} < NNO. Considering analogous mafic magmas of the Chichinautzin Volcanic Field together with our results suggests that the redox-state of Popocatépetl's mafic end-member magma was probably between QFM and ΔNNO+1, but the exact value is poorly constrained.

The pressure at which the mafic end-member crystallized is constrained using two methods. We can use the H_2O solubility model of Moore *et al.* (1998) to estimate the minimum pressure at which glass inclusions were trapped in olivine. The estimated 1.3 – 6.1 wt.% H_2O determined using the difference technique corresponds to 0.2 – 2.6 kbar saturation pressure. MELTS modeling of the inferred mafic assemblage indicates pressures of 1 – 4 kbar.

Silicic End-member

Inclusions of sulfide in low-Mg# phenocrysts suggest that sulfide liquid saturation probably occurred early in the silicic end-member's history. Magnetite, ilmenite, and apatite crystallization occurred concurrently. This was followed in turn by large quantities of plagioclase and low-Mg# pyroxene crystallization.

Low-Mg# pyroxene cores, low-temperature pyroxene rims, and apatite saturation suggest that these phases all equilibrated near 950 °C. We interpret these to record the temperature of the silicic end-member prior to the mixing event. MELTS modeling of the silicic mineral assemblage implies crystallization temperatures that are consistent with this interpretation (900 – 1000 °C).

A single Fe-rich sulfide inclusion in low-Mg# pyroxene suggests an oxygen fugacity below NNO early in the silicic end-member's history. From MELTS modeling we infer that the silicic mineral assemblage crystallized at f_{O_2} = ΔNNO +0.3 log units. Fe-Ti oxides disseminated in matrix of hybridized silicate melt record an oxygen fugacity between NNO and NNO+1. This is a typical value for silicic subduction-zone magmas (Rutherford et al., 1985; Druitt and Bacon, 1989; Mandeville et al., 1996). We do not know if the Fe-Ti oxides record the oxygen fugacity of the silicic end-member magma or the mixed magma since resetting of the

Fe-Ti oxides may have occurred during magma mixing. A more detailed study of chemical zonation in Fe-Ti oxides and the inferred variations in temperature and f_{O_2} would be useful in this regard.

Regardless of the history of the Fe-Ti oxides, the mechanism for the increase in f_{O_2} is unknown. It is possible that the rare sulfide inclusion-bearing, low-Mg# pyroxene derives from a separate, low-f_{O_2} magma which is not related to the high-f_{O_2} silicic magma body resident beneath Popocatépetl. These phenocrysts may represent the remnants of a reduced magma injected previously.

The storage pressure of the silicic end-member is unconstrained, as there are no applicable geobarometers. According to the H_2O solubility model of Moore *et al.* (1998) the minimum pressure at which glass inclusions (with 1.2 – 4.3 wt.% H_2O determined by difference) were trapped in pyroxene has the range 0.2 – 1.3 kbar. MELTS modeling of the inferred silicic assemblage indicates crystallization pressures $\leq$ 1.5 kbar.

Hornblende: a product of mixing?

Hornblende phenocrysts and microphenocrysts are found evenly disseminated, surrounded by both the dark and light matrix glasses, in all pumices and lava blocks. No hornblende, or amphibole phases of any kind, have been identified in dacite pumices from the ~800 A.D. large magnitude, explosive eruption of Popocatépetl (J. Witter, 2001, unpubl. data). If we assume that the ~800 A.D. dacite pumices are representative of a resident silicic magma body beneath the volcano, this suggests that the hornblende found in the recent products is not derived from the silicic end-member. A single glass inclusion in hornblende that contained no visual evidence (using BSE imaging) for post-entrapment crystallization was analyzed by EPMA and is dacite in composition. If no post-entrapment crystallization occurred, this suggests that hornblende was probably not derived from the mafic end-member. Petrographic observations are inconsistent with hornblende originating from only the silicic or

mafic end-members because hornblende is found as partial overgrowths on both low-Mg# pyroxene and olivine.

If Popocatépetl hornblende is derived neither from the mafic or silicic end-members, the possibility remains that the hornblende crystallized during mixing. Plagioclase and pyroxene microphenocrysts form cores of some hornblende suggesting that hornblende saturated very late in the crystallization sequence. In addition, the acicular habit of hornblende suggests that crystallization was rapid. Compositionally, Popocatépetl hornblende is very similar to groundmass pargasite in Unzen dacite (Sato *et al.*, 1999) and groundmass amphibole (magnesiohastingsite) found in mafic inclusions in Montserrat andesite (Murphy *et al.*, 2000; Figure 6).

The concentration of Cl in Popocatépetl hornblende is consistent with a low-pressure origin. Sato *et al.* (1999) found magnesiohornblende phenocrysts in Unzen lavas contained much higher concentrations of Cl than did the groundmass pargasite. They concluded that the low Cl content of the Unzen groundmass pargasite (100-300 ppm Cl) is a result of crystallization from a partially degassed magma. Popocatépetl hornblende also contains low Cl contents (< 300 ppm Cl). We infer that Popocatépetl hornblende also crystallized from a partially degassed magma. Partial degassing may have served to enhance hornblende saturation (Ghiorso, 1999).

Magmatic temperatures of 775-900 °C derived from the Hbl-Plag geothermometer of Holland & Blundy (1994) are significantly lower than the temperatures derived from pyroxene and Fe-Ti oxide geothermometry. Sato *et al.* (1999) conducted experiments on groundmass pargasite from Unzen volcano that are compositionally very similar to Popocatépetl hornblende. Their work shows that the maximum temperature of amphibole crystallization is 930 °C at 2 kbar, 900 °C at 1 kbar, and 820 °C at 0.5 kbar. Therefore, the temperature range derived from the amphibole-plagioclase geothermometer (~775 to 900 °C) suggests a minimum pressure for hornblende crystallization between ~0.4 and 1 kbar. The hornblende reaction rims probably formed during magma ascent at even lower pressures that were outside the hornblende stability range.

Other experiments have been conducted to define the stability limits of amphibole in subduction-related andesites and dacites. The starting bulk composition and the composition of the amphibole in Mount St. Helens dacite (Rutherford et al., 1985; Rutherford and Devine, 1988) are different enough from those of Popocatépetl that they are an imprecise analogue. Experiments on lavas from the Trans-Mexican Volcanic Belt with compositions similar to Popocatépetl (Blatter and Carmichael, 1998; Moore and Carmichael, 1998) were run at an average oxygen fugacity of ΔNNO+2. This is much higher than the f_{O_2} inferred for Popocatépetl and thus the results of these experiments are not directly applicable. The Al-in-hornblende geobarometer of Johnson & Rutherford (1989) is based on the phase assemblage melt + fluid + quartz + sanidine + plagioclase (An_{30}) + hornblende + biotite + sphene + ilmenite or magnetite. Recent Popocatépetl eruption products do not contain quartz, sanidine, biotite, or sphene, and therefore this barometer is not applicable.

Comparison with previous models

Straub & Martin-Del Pozzo (2001) propose that the mafic end-member consisted of a near-primary magnesian andesite (55-62 wt.% SiO_2) at f_{O_2} = QFM, high $Mg\#_{melt}$ = 72-75, high Ni-content, and several wt.% H_2O that crystallized olivine and clinopyroxene at temperatures of 1170-1085 °C at lower crustal levels. This mafic magma mixed with a more evolved magma ($Mg\#_{melt}$ = 35-40) containing low-Mg# clino- and orthopyroxene and plagioclase at ~950 °C. Although the broad conclusions of both studies regarding magma mixing of mafic and silicic end-members are similar, this study differs from the study of Straub & Martin-Del Pozzo (2001) in several important aspects.

First, in this study, complete major and minor element compositions of the magmatic end-members have been defined (Table 13). These calculated bulk compositions are consistent with observed bulk rock chemical variations as well as the phase compositions and modal proportions of the observed mineral assemblages.

We have attempted to place tight constraints on the intensive parameters of the end-member magmas using a wide array of geothermobarometers and thermodynamic models. In contrast, Straub & Martin-Del Pozzo (2001) allow a variable composition of the mafic end-member (55-62 wt.% SiO_2). Although, we accept that the end-member magmas may themselves be the product of magma mixing, we conclude that the mafic end-member must have a more mafic average composition of ~53 wt.% SiO_2. This is necessary to explain olivine microphenocrysts that crystallized from the mafic end-member and trapped melt with < 55 wt.% SiO_2.

Second, we determine that the high Fo-content, Ni-rich, Cr-spinel bearing olivines found in the recent Popocatépetl erupted products did not crystallize from the mafic end-member and are xenocrystic, based on petrographic evidence as well as thermodynamic modeling of Ni-in-olivine. Straub & Martin-Del Pozzo (2001) assumed that these Fo-rich olivines crystallized from a near-primary mantle melt and inferred that this mantle melt is the parental arc magma underneath Popocatépetl. In order to explain the high Ni-contents of these Cr-spinel bearing olivine they proposed unusually high olivine-silicate liquid partition coefficients for Ni ($K_{DNi}^{ol/liq} = 18$). Our thermodynamic analysis using MELTS indicates lower values ($K_{DNi}^{ol/liq} = 10$). The assumption that these Cr-spinel bearing olivines crystallized from the mafic end-member led Straub & Martin-Del Pozzo (2001) to derive an oxygen fugacity of QFM for the mafic end-member using the $Fe^{3+}/\Sigma Fe$ ratio of Cr-spinel in olivine (Fo_{89-90}). Our interpretation that these olivines are xenocrystic implies that this f_{O_2} estimate is not applicable to the mafic end-member.

Conclusions

The current manifestation of unrest at Popocatépetl involves the ascent of a basaltic andesite magma with 53 wt.% SiO_2 and ~3 wt.% H_2O from depths greater than 16 km. The oxygen fugacity of the mafic magma is uncertain but it probably lies in the range QFM to ΔNNO +1 log units. Olivine (Fo_{84-86}) and high-Mg# pyroxene

crystallized in the basaltic andesite over a pressure range of 1-4 kbar (~4-16 km). Abundant xenocrysts of high Fo-content, Ni-rich, Cr-spinel bearing olivine may have been entrained from the mantle. The mafic end-member mixed with silicic magma at a depth of ~4-6 km. Magma mixing and entrainment processes may have involved tunneling of mafic magma through the silicic magma (Bergantz and Breidenthal, 2001) to produce banded pumice. More extensive mixing produced the hybridized pumice and lava, possibly during magma ascent in the volcanic conduit. The silicic end-member magma, presumed to currently reside beneath Popocatépetl, is a dacite with 65 wt.% SiO_2 containing ~3 wt.% H_2O at an oxygen fugacity of ~ΔNNO +0.5. The mineralogy of the silicic end-member is two-pyroxene + plagioclase + Fe-Ti oxides + apatite with mineral inclusions of Fe-Ti oxides, apatite, and sulfide. These mineral phases likely crystallized at pressures of ~1.5 kbar. However, further crystallization of these phases probably occurred during magma ascent. Hornblende precipitated during or after magma mixing. Hornblende saturation was short-lived followed by formation of breakdown reaction rims as the mixed magma ascended to shallower levels. The silicic and mafic end-member magmas mixed in proportions having the range 45:55 wt.% to 85:15 wt.% silicic: mafic magma to produce the erupted clasts.

Chapter 2:

Immediate Sources of Volatiles for the 1994 – Present Eruption of Popocatépetl, Mexico

Introduction

From December 1994 until the time of writing, Volcán Popocatépetl (Mexico) has non-explosively degassed an average of 7000 tons/day SO_2 into the troposphere (Delgado and Cárdenas-G, 1997; Delgado-Granados et al., 2001; National Center for Disaster Prevention, Mexico City (CENAPRED), unpubl. data). The current eruptive period is similar to other eruptions that have occurred in historic time. This is the first time, however, that such massive degassing could be measured quantitatively. Popocatépetl degassed a total of ~20 Mt SO_2 since 1994, accompanied by relatively minor eruptive activity. This value compares with the ~17 Mt SO_2 (Gerlach *et al.*, 1996) injected into the stratosphere in a single day during the climactic, highly explosive eruption of Pinatubo (Philippines) on June 15, 1991.

The focus of this chapter is to quantify the immediate source(s) of sulfur and other gases (H_2O, CO_2, HCl, and HF) in Popocatépetl magma, develop a volatile budget, and investigate the physical processes involved in passive degassing at this volcano. We consider a number of potential explanations for the high observed ratio of volatiles:erupted magma. Most of these scenarios prove to be either not feasible or improbable. We present a range of plausible scenarios to explain the observed phenomena.

Geologic Setting

Popocatépetl (5452 m) is an andesitic stratovolcano that lies ~60 km SE of Mexico City (Figure 1). Eruptions at Popocatépetl are commonly characterized by magma mixing between mafic and silicic end-members (Cantagrel et al., 1984; Robin, 1984; Boudal and Robin, 1988; Kolisnik, 1990). This includes the most recent

active phase extending from 1994 to the present (Athanasopoulos, 1997; Straub and Martin-Del Pozzo, 2001).

From March 1996, when dome growth commenced, until December 2000, 3.1 x 10^7 m^3 of magma was extruded, based on aerial photogrammetry (De la Cruz-Reyna *et al.*, unpubl. data). During this same time period the average SO_2 flux was 8400 tons/day, yielding a total of 14.8 Mt SO_2. Assuming ~20 vol.% crystals with melt density of 2300 kg/m^3, about 5.7 x 10^{10} kg silicate melt has been erupted during the March 1996 to December 2000 period of activity. For this mass of silicate melt alone to supply the 14.8 Mt observed SO_2 emission, the silicate melt phase, must have initially contained ~13 wt.% S. This exceeds the experimentally-derived sulfur solubility limits in silicic and intermediate magmas by two or more orders of magnitude (Wendlandt, 1982; Carroll and Rutherford, 1985; Luhr, 1990; Scaillet et al., 1998). This apparent paradox has been encountered by other workers and is commonly referred to as the "excess sulfur" problem (Luhr et al., 1984; Sigurdsson et al., 1990; Andres et al., 1991; Westrich and Gerlach, 1992; Gerlach and McGee, 1994; Gerlach et al., 1994; Kazahaya et al., 1994; Wallace and Gerlach, 1994; Gerlach et al., 1996; Mandeville et al., 1996; Witter, 1997; Wallace, 2001; Kazahaya et al., 2002).

Petrology

Several recent papers have described magma mixing at Popocatépetl (Cantagrel et al., 1984; Robin, 1984; Boudal and Robin, 1988; Kolisnik, 1990; Athanasopoulos, 1997; Straub and Martin-Del Pozzo, 2001). Chapter 1 of this dissertation presents a detailed petrologic re-analysis of recent mixed magmas from Popocatépetl. The silicic end-member of recent magma mixing at Popocatépetl is a dacite with 65 wt.% SiO_2 containing ~3 wt.% H_2O that crystallized at pressures $\leq$ 1.5 kbar and at an oxygen fugacity of ~ΔNNO +0.5. The mineralogy of the silicic end-member is two-pyroxenes + plagioclase + Fe-Ti oxides + apatite with mineral inclusions of Fe-Ti oxides, apatite, and sulfide. The mafic end-member is a basaltic

andesite with 53 wt.% SiO_2 and ~3 wt.% H_2O that crystallized olivine (Fo_{84-86}) and high-Mg# pyroxene at moderate pressures (1-4 kbar). Oxygen fugacity of the mafic end-member is uncertain but it probably lies in the range QFM to ΔNNO +1 log units. The mafic end-member also contains abundant xenocrysts of high Fo-content, Ni-rich, Cr-spinel bearing olivine. Hornblende likely precipitated either during or shortly after magma mixing. Hornblende saturation was short-lived followed by formation of breakdown reaction rims during final magma ascent. The silicic and mafic end-member magmas mixed in proportions ranging from 45:55 wt.% to 85:15 wt.% silicic:mafic magma to produce the erupted clasts considered in this study.

Gas Measurements

Gas measurements at Popocatépetl have focused on SO_2, using correlation spectrometry (COSPEC). Carbon dioxide emissions have also been measured using LI-COR and passive infrared spectroscopy (FTIR). COSPEC measurements began in January 1994 and showed emission rates of ~1500 to ~12,500 tons/day SO_2 (Delgado and Cárdenas-G, 1997; Delgado-Granados et al., 2001). On rare occasions, SO_2 emissions have reached 30,000-50,000 tons/day SO_2 (Goff *et al.*, 1998). For comparison, Mount St. Helens (USA) emitted 100-2500 tons/day SO_2 during the dome growth period of 1980-86 (Gerlach and McGee, 1994) and Galeras (Colombia) emitted 20-880 tons/day SO_2 during an explosive and passive degassing phase from December 1992 to March 1993 (Fischer *et al.*, 1994).

LI-COR measurements of CO_2 in June 1995 varied between 6400 and 9000 tons/day CO_2 (Gerlach *et al.*, 1997) Using the same methodology, Delgado *et al.* (1998) reported average fluxes of >40,000 tons/day CO_2 between 1996 and 1998. In February 1998, passive FTIR measured 38,000 tons/day CO_2 with excursions that exceeded 100,000 tons/day CO_2 (Goff *et al.*, 2001). These measurements establish Popocatépetl as one of the greatest known natural producers of SO_2 and CO_2.

Relative HCl and HF emission rates have been measured using volatile traps and passive FTIR. Volatile trap studies, combined with SO_2 flux measurements,

suggest that between the onset of activity and November 1996, Popocatépetl had emitted 0.75 Mt HCl and 0.075 Mt HF (Goff *et al.*, 1998).This represents an average emission rate of 740 tons/day HCl and 74 tons/day HF, respectively. Emission rates measured by passive FTIR in 1997 and 1998 have the range 190-1700 tons/day HCl and 35-250 tons/day HF (Goff *et al.*, 2001).

Analytical Methods

Electron Probe Microanalysis (EPMA)

All EPMA analyses were conducted on a 4-spectrometer JEOL 733 Superprobe at the University of Washington. Methods for the EPMA analysis of major elements in glass inclusions, matrix glasses, olivine, and pyroxene are presented in Chapter 1. Volatile elements S, Cl, and F were analyzed in glasses using an improved analytical method originally developed by T. Thordarson at the University of Hawaii (Thordarson *et al.*, 1996). With this method, we achieved very low minimum detection limits while maintaining high analytical precision and accuracy. Analytical conditions were 15 kV accelerating voltage, 100 nA beam current, 5 μm beam diameter, and 400 second total peak count time. To minimize volatile loss, an iterative scheme was employed in which the beam was blanked for ten seconds after every ten seconds of counting. This procedure minimized heating of the sample and consequent volatile loss. We conducted a test for volatile mobility under the electron beam and found X-ray count rates for S, Cl, and F remain stable during the entire period of analysis. Sulfur and chlorine were analyzed using PET diffraction crystals with the spectrometer aperture window set at its widest setting to maximize the number of X-ray counts. Fluorine was analyzed using an LDE1 diffraction crystal. Fluorine analysis proved challenging due to peak overlap problems with the Fe $K\alpha$ line. We created an empirical correction factor for F by analyzing several F-free standards of varying Fe content. We calculated the amount of interference with the F-analysis as a function of Fe and incorporated this correction into the iterative analytical routine (see Appendix A). Since the volatile elements

were analyzed in a separate analytical session, we reprocessed the volatile data with major element data (collected previously; see Chapter 1) to correct for matrix effects using the ZAF model of Armstrong (1984). Prior to each analytical session, volatile elements were calibrated on the following standards: NiS (sulfide sulfur), celestite (sulfate sulfur), Scapolite 17120 (chlorine), and Synthetic F-phlogopite (fluorine). Analytical accuracy was checked using basalt glass standards VG-2 and A-99 (for S, Cl, and F) and NBS soda-lime glasses 620 & 621 (for S and Cl). Minimum detection limits are calculated to be 24 ppm for sulfur, 16 ppm for chlorine, and 52 ppm for fluorine. Reproducibility of S, Cl, and F analyses was also tested on VG-2 and A-99. The 1σ variations for more than 30 analyses are 1½% at 1500 ppm and 13% at 140 ppm for sulfur, 9% at 200 ppm for chlorine, and 5% at 750 ppm and 12% at 300 ppm for fluorine (Table 14).

SIMS Analyses

H_2O, CO_2, S, Cl, and F in glass inclusions were analyzed using secondary ion mass spectrometry (SIMS) at the Department of Terrestrial Magnetism, Carnegie Institution of Washington. The analytical methods for this technique are described in Hauri *et al.* (2002). SIMS analysis could only be performed on inclusions that were greater than about 40 microns in smallest dimension. A comparison of EPMA and SIMS analyses of S, Cl, F, and H_2O in glass inclusions is shown in Figure 10.

Results

Glass inclusions

Glass inclusions occur in all phenocryst phases. We focused analytical efforts on glass inclusions in olivine and pyroxene with the aim of obtaining chemical data on the volatile contents of the pre-eruptive magmatic end members. We concentrated our analytical efforts on glass inclusions that were ≥10 μm in diameter and without intersecting cracks or visual evidence for post-entrapment crystallization. The

Table 14. Comparison of analyses of S, Cl, and F in various glass standards by EPMA and wet chemistry

	VG-2					A-99				
Reference:	this study	D & G	Th (CSIRO)	Th (Cameca)	Dixon	this study	D & G	Th (CSIRO)	Th (Cameca)	Dixon
S conc.	**1429(20)**	**1495(11)**	**1365(29)**	**1348(62)**	**1340(80)**	**138(18)**	**153(3)**	**220(29)**	**135(62)**	**170(80)**
S MDL	24	30	n.r.	n.r.	n.r.	23	30	n.r.	n.r.	n.r.
S err	20	13	n.r.	n.r.	n.r.	12	13	n.r.	n.r.	n.r.
n	42	25	139	134	19	36	10	139	134	19
Cl conc.	**293(9)**	**313(8)**	**316(19)**	**291(52)**	**n.a.**	**207(18)**	**218(7)**	**227(19)**	**229(52)**	**n.a.**
Cl MDL	16	30	n.r.	n.r.	n.a.	16	30	n.r.	n.r.	n.a.
Cl err	9	12	n.r.	n.r.	n.a.	8	12	n.r.	n.r.	n.a.
n	42	25	139	134	n.a.	36	10	139	134	n.a.
F conc.	**289(34)**	**275(28)**	**300(72)**	**n.a.**	**n.a.**	**745(35)**	**745(11)**	**765(72)**	**n.a.**	**n.a.**
F MDL	52	80	n.r.	n.a.	n.a.	54	80	n.r.	n.a.	n.a.
F err	29	20	n.r.	n.a.	n.a.	29	20	n.r.	n.a.	n.a.
n	32	25	139	n.a.	n.a.	36	10	139	n.a.	n.a.

	NBS 620			NBS 621		
Reference:	this study	Saito EPMA	Saito W.C.	this study	Saito EPMA	Saito W.C.
S conc.	**1139(15)**	**1080(80)**	**1160**	**454(24)**	**460(20)**	**450**
S MDL	22	n.r.	n.r.	22	n.r.	n.r.
S err	18	n.r.	n.r.	7	n.r.	n.r.
n	6	n.r.	n.r.	4	n.r.	n.r.
Cl conc.	**201(11)**	**180(20)**	**170**	**171(11)**	**160(20)**	**140**
Cl MDL	15	n.r.	n.r.	15	n.r.	n.r.
Cl err	7	n.r.	n.r.	6	n.r.	n.r.
n	7	n.r.	n.r.	4	n.r.	n.r.

All data reported in ppm, All analyses by EPMA except where noted, Standard deviation (1-sigma) shown in parentheses
n.r. = not reported, n.a. = not analyzed
conc. = concentration, MDL = minimum detection limit, err = error based on counting statistics (1-sigma)
D & G = M. Davis and M. Garcia, unpubl. data, University of Hawaii, 2000.
Th (CSIRO) = Thordarson et al. (1996) CSIRO trace routine, Th (Cameca) = Thordarson et al. (1996) Cameca trace routine,
Dixon = Dixon (1991), Saito EPMA = Saito et al. (2001) EPMA analysis, Saito W.C. = Saito et al. (2001) wet chemistry analysis

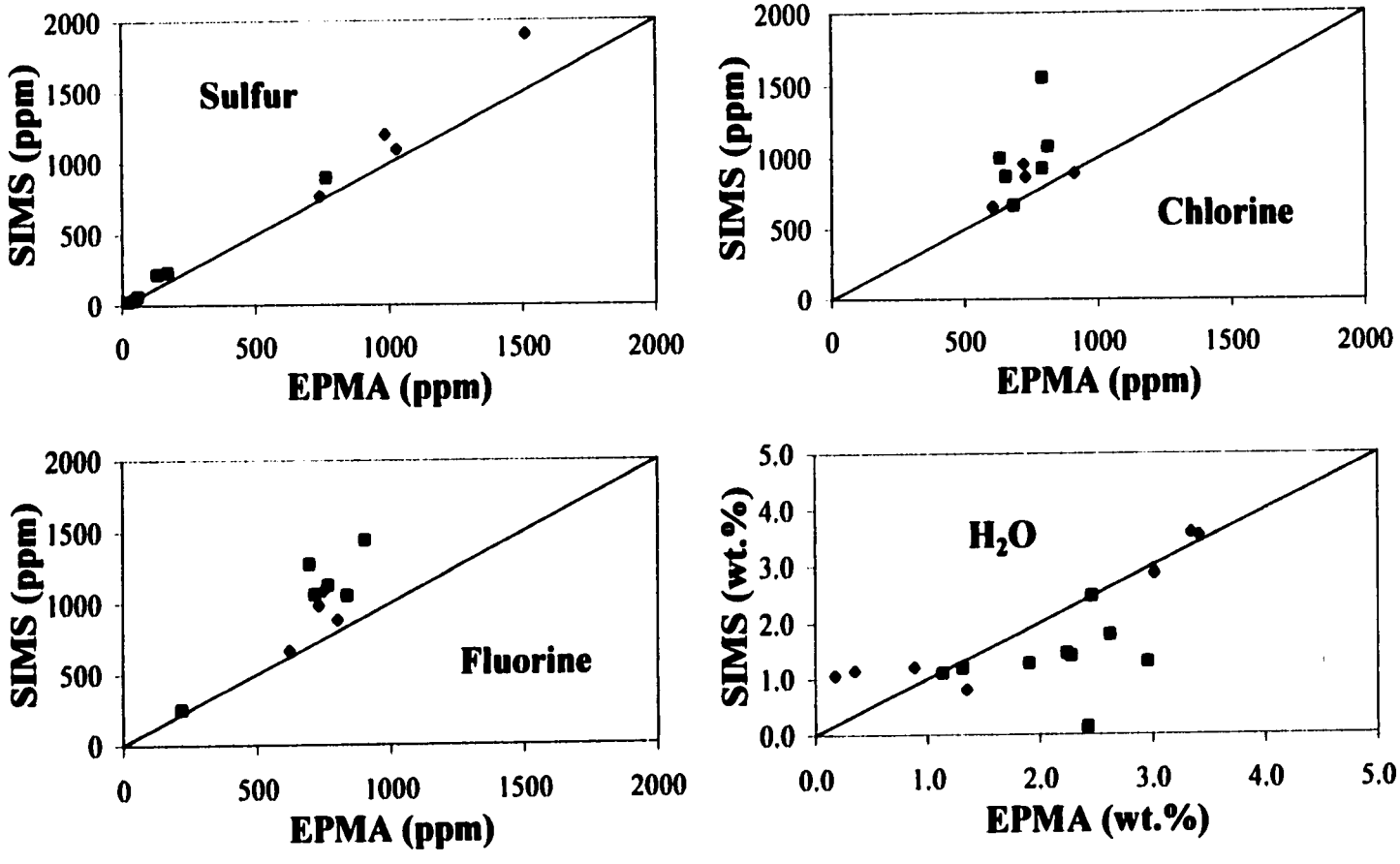

Figure 10. Comparison of glass inclusion analyses of S, Cl, F, and H_2O by EPMA and SIMS. Glass inclusions are hosted by olivine (*filled diamonds*) and pyroxene (*filled squares*). Errors for both techniques are similar in size or smaller than the symbols for S, Cl, F, and H_2O (SIMS only). Errors associated with calculating H_2O by difference from EPMA analyses are estimated at ±0.5 wt. %.

concentration of H_2O in glass inclusions was estimated using SIMS and the difference technique (100 wt.% - analytical total of major and volatile elements by EPMA; Anderson, 1974).

Twenty-three glass inclusions in olivine were analyzed for S, Cl, and F (Figure 11; Table 15). Nineteen of these were recalculated for post-entrapment olivine crystallization using the thermodynamic model of Kress & Ghiorso (2001). This correction calculation is performed iteratively by incrementally adding back into the liquid (corresponding to the glass composition) instantaneous equilibrium solid in 0.01 wt.% increments. Initial glass composition is assumed to have been reached when the inclusion composition most closely approaches equilibrium with the bulk host phenocryst. The method assumes that the inclusions were sealed throughout the crystallization process and that crystallization was rapid relative to diffusive processes in the crystal. S, Cl, and F concentrations are adjusted by assuming that they are totally incompatible. The magnitude of post-entrapment crystallization of olivine varies between 1 and 10 wt.%. Thus, recalculated volatile contents can be up to 10% lower than the measured values.

Eighteen glass inclusions in orthopyroxene and twenty-three glass inclusions in clinopyroxene were analyzed for S, Cl, and F (Figure 11; Tables 16 & 17). Post-entrapment crystallization correction calculations were performed on thirteen orthopyroxene-hosted glass inclusions using the thermodynamic model of Kress & Ghiorso (2001). The amount of post-entrapment crystallization in orthopyroxene-hosted glass inclusions has the range 0 to 5 wt.%. Post-entrapment crystallization correction calculations for clinopyroxene-hosted glass inclusions were not possible due to unresolved problems with the MELTS algorithm forming the basis for the entrapment adjustment program (Ghiorso and Sack, 1995). We assume a low degree of post-entrapment crystallization in the clinopyroxene-hosted glass inclusions analogous to what we found in the orthopyroxene-hosted glass inclusions.

Figure 11. Volatile content measured by EPMA and SIMS in glass inclusions and matrix glasses plotted as SiO_2 versus **a)** Sulfur, **b)** Chlorine, **c)** Fluorine, and **d)** H_2O. H_2O concentrations obtained from EPMA data are determined by difference. Glass inclusions are hosted by olivine microphenocrysts (OL, *open diamonds*), clinopyroxene (CPX, *open squares*), orthopyroxene (OPX, *open triangles*), and hornblende (HBL, *X's*). Glass inclusions hosted by olivine and orthopyroxene have been recalculated for post-entrapment crystallization. Matrix glasses are denoted by *crosses*. SIMS and EPMA errors based on counting statistics are similar in size or smaller than the symbols for S, Cl, F, SiO_2, and H_2O (SIMS only). Errors associated with calculating H_2O by difference from EPMA analyses are estimated at ±0.5 wt. %. EPMA minimum detection limits are estimated to be 24 ppm for sulfur, 16 ppm for chlorine, 52 ppm for fluorine, and ~1 wt. % for H_2O. MDL for SIMS data are lower.

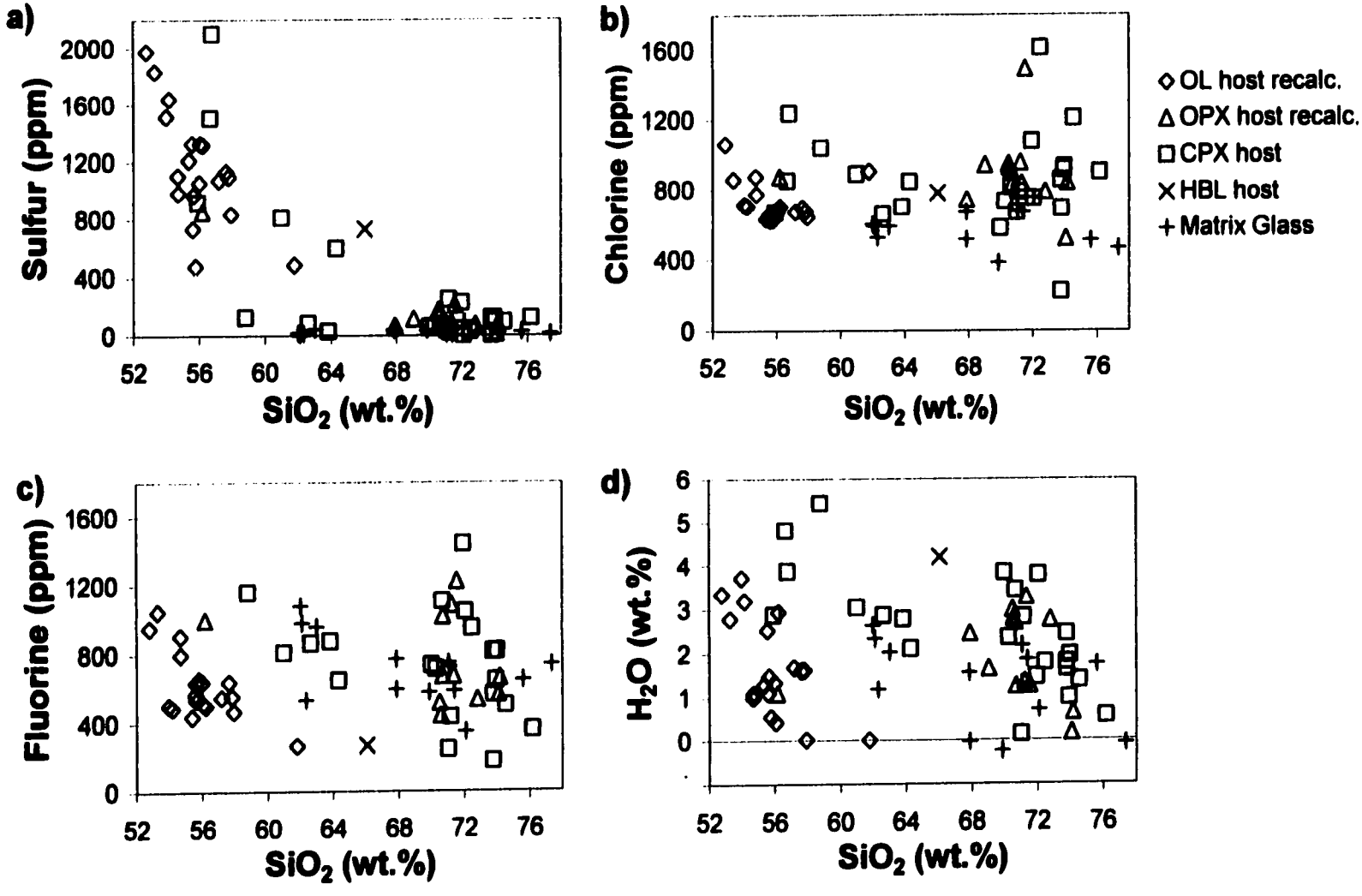
a)
Sulfur (ppm)
2000
1600
1200
800
400
0
52
56
60
64
68
72
76
SiO2 (wt.%)
b)
Chlorine (ppm)
1600
1200
800
400
0
52
56
60
64
68
72
76
SiO2 (wt.%)
OL host recalc.
OPX host recalc.
CPX host
HBL host
Matrix Glass
c)
Fluorine (ppm)
1600
1200
800
400
0
52
56
60
64
68
72
76
SiO2 (wt.%)
d)
H2O (wt.%)
6
5
4
3
2
1
0
52
56
60
64
68
72
76
SiO2 (wt.%)

Table 15. Compositions of olivine-hosted glass inclusions and host olivines (in wt.% except where noted)

Major and volatile element composition determined by EPMA

Eruption of June 30, 1997 -- Brown andesite pumice

Label	MI1ol22ts1	MI3ol22ts1	MI4ol22ts1	MI5ol22ts1	MI1ol7tsSCa
SiO_2	59.3	58.4	58.6	57.9	56.5
TiO_2	1.12	0.97	1.14	1.01	1.26
Al_2O_3	18.3	18.1	17.7	17.4	18.4
Cr_2O_3	0.00	0.00	0.00	0.01	0.00
FeO	5.23	5.47	5.47	5.66	4.71
MnO	0.11	0.08	0.10	0.06	0.10
MgO	2.35	2.46	2.70	3.74	3.34
CaO	6.90	7.17	6.64	6.33	7.25
Na_2O	4.77	3.86	4.17	4.36	4.02
K_2O	1.49	1.25	1.31	1.43	1.21
P_2O_5	0.26	0.26	0.24	0.25	0.32
S (ppm)	895	1143	1190	1104	1416
Cl (ppm)	689	717	731	682	711
F (ppm)	498	585	671	560	613
Total	100.0	98.2	98.3	98.4	97.3
H_2O by Diff. [c]	0.0	1.8	1.7	1.6	2.7
SIMS analyses of volatiles					
S (ppm)	n/a	n/a	n/a	n/a	n/a
Cl (ppm)	n/a	n/a	n/a	n/a	n/a
F (ppm)	n/a	n/a	n/a	n/a	n/a
H_2O (wt.%)	n/a	n/a	n/a	n/a	n/a
Host olivine composition [c]					
SiO_2	39.2	39.6	38.7	39.4	41.0
MgO	44.1	44.2	44.2	43.8	48.0
FeO^T	15.5	15.4	15.3	15.8	12.0
MnO	0.08	0.09	0.09	0.08	0.15
CaO	0.14	0.16	0.12	0.15	0.14
NiO	n/a	n/a	n/a	n/a	0.33
Total	99.0	99.4	98.4	99.2	101.6
Fo	83.5	83.6	83.7	83.2	87.7
Recalculated major and volatile element composition of glass inclusion [a]					
SiO_2	57.9	57.2	57.6	57.8	55.6
TiO_2	1.05	0.91	1.09	1.01	1.19
Al_2O_3	17.0	17.0	16.9	17.3	17.3
Cr_2O_3	0.00	0.00	0.00	0.01	0.00
FeO	6.29	6.42	6.20	5.74	5.33
MnO	0.13	0.09	0.11	0.06	0.11
MgO	4.84	4.66	4.50	3.97	5.61
CaO	6.46	6.76	6.33	6.30	6.86
Na_2O	4.45	3.63	3.97	4.33	3.79
K_2O	1.39	1.18	1.25	1.43	1.14
P_2O_5	0.24	0.25	0.23	0.25	0.30
S (ppm)	835	1075	1133	1097	1330
Cl(ppm)	643	675	696	677	658
F(ppm)	465	550	639	557	567
Total	100.0	98.3	98.4	98.4	97.5
H_2O	0.0	1.7	1.6	1.6	2.5
wt.% OL [d]	6.7	5.9	4.8	0.6	5.5

Table 15. continued

Major and volatile element composition determined by EPMA

Eruption of June 30, 1997 -- Brown andesite pumice

Label	MI2ol9tsSCa [b]	MI3ol9tsSCa [b]	MI1ol10tsSCa	MI1ol17tsSCa	MI2ol17tsSCa
SiO_2	54.1	54.8	57.1	55.2	57.2
TiO_2	1.23	1.15	0.99	1.14	1.17
Al_2O_3	17.6	17.8	18.8	18.5	18.1
Cr_2O_3	0.04	0.11	0.05	0.00	0.01
FeO	5.21	4.52	4.36	5.22	5.44
MnO	0.09	0.06	0.08	0.09	0.12
MgO	4.26	4.68	2.12	2.33	2.58
CaO	7.93	7.81	7.63	8.22	7.60
Na_2O	4.01	4.34	4.15	4.10	4.40
K_2O	1.18	1.12	1.16	1.10	1.48
P_2O_5	0.33	0.35	0.30	0.29	0.27
S (ppm)	1745	1708	1380	1759	1130
Cl (ppm)	807	696	738	756	712
F (ppm)	622	555	523	522	686
Total	96.3	97.1	96.9	96.6	98.6
H_2O by Diff. [c]	3.7	2.9	3.1	3.4	1.4
SIMS analyses of volatiles					
S (ppm)	n/a	n/a	n/a	n/a	n/a
Cl (ppm)	n/a	n/a	n/a	n/a	n/a
F (ppm)	n/a	n/a	n/a	n/a	n/a
H_2O (wt.%)	n/a	n/a	n/a	n/a	n/a
Host olivine composition [c]					
SiO_2	40.5	40.6	40.1	40.0	40.7
MgO	46.3	46.0	45.1	46.2	46.0
FeO^T	13.7	13.9	15.0	13.9	14.4
MnO	0.22	0.22	0.23	0.22	0.24
CaO	0.17	0.16	0.16	0.14	0.13
NiO	0.17	0.17	0.14	0.16	0.15
Total	101.1	101.0	100.7	100.7	101.5
Fo	85.7	85.5	84.3	85.6	85.1
Recalculated major and volatile element composition of glass inclusion [a]					
SiO_2	n.r.	n.r.	56.2	54.2	56.0
TiO_2	n.r.	n.r.	0.95	1.06	1.10
Al_2O_3	n.r.	n.r.	17.9	17.3	16.9
Cr_2O_3	n.r.	n.r.	0.05	0.00	0.01
FeO	n.r.	n.r.	5.09	6.18	6.37
MnO	n.r.	n.r.	0.09	0.10	0.13
MgO	n.r.	n.r.	3.85	4.91	5.06
CaO	n.r.	n.r.	7.29	7.69	7.12
Na_2O	n.r.	n.r.	3.96	3.82	4.11
K_2O	n.r.	n.r.	1.11	1.02	1.38
P_2O_5	n.r.	n.r.	0.29	0.27	0.25
S (ppm)	n.r.	n.r.	1316	1641	1057
Cl(ppm)	n.r.	n.r.	703	705	666
F(ppm)	n.r.	n.r.	499	487	642
Total	n.r.	n.r.	97.0	96.8	98.6
H_2O	n.r.	n.r.	2.9	3.2	1.3
wt.% OL [d]	n.r.	n.r.	4.6	6.7	6.5

Table 15. continued

Major and volatile element composition determined by EPMA

Eruption of June 30, 1997 -- Brown andesite pumice

Label	MI3ol17tsSCa	MI1ol25tsSCa	MI1aol9tsSCb	MI2ol9tsSCb	GI1OL2tsA
SiO_2	57.2	55.2	57.0	56.7	53.7
TiO_2	1.07	1.45	1.28	0.91	1.29
Al_2O_3	18.5	17.6	18.2	18.1	19.5
Cr_2O_3	0.02	0.02	0.01	0.03	0.00
FeO	5.63	5.05	5.55	5.84	4.23
MnO	0.12	0.13	0.12	0.08	0.07
MgO	2.71	1.68	2.75	2.82	3.29
CaO	7.22	8.62	7.48	7.72	9.19
Na_2O	4.80	4.52	4.36	4.63	3.89
K_2O	1.76	1.08	1.14	1.27	1.08
P_2O_5	0.28	0.30	0.25	0.26	0.32
S (ppm)	1414	1640	1052	1315	1514
Cl (ppm)	721	771	692	687	910
F (ppm)	548	543	581	473	750
Total	99.6	96.0	98.4	98.6	97.0
H_2O by Diff. [c]	0.4	4.0	1.6	1.4	3.0
SIMS analyses of volatiles					
S (ppm)	n/a	n/a	n/a	n/a	1900
Cl (ppm)	n/a	n/a	n/a	n/a	891
F (ppm)	n/a	n/a	n/a	n/a	1083
H_2O (wt.%)	n/a	n/a	n/a	n/a	2.9
Host olivine composition [c]					
SiO_2	39.8	39.7	40.1	39.7	40.3
MgO	45.9	45.6	46.3	46.3	46.9
FeO^T	14.6	15.1	13.4	13.4	12.0
MnO	0.20	0.21	0.07	0.07	0.17
CaO	0.13	0.16	0.14	0.15	0.16
NiO	0.16	0.11	n/a	n/a	0.29
Total	100.7	100.9	100.0	99.6	99.8
Fo	84.9	84.3	86.1	86.1	87.4
Recalculated major and volatile element composition of glass inclusion [a]					
SiO_2	56.0	54.0	55.6	55.4	53.3
TiO_2	1.01	1.34	1.18	0.83	1.25
Al_2O_3	17.3	16.3	16.8	16.7	18.9
Cr_2O_3	0.02	0.02	0.01	0.03	0.00
FeO	6.52	6.33	6.58	6.84	4.63
MnO	0.14	0.14	0.13	0.09	0.07
MgO	5.15	4.43	5.79	5.86	4.71
CaO	6.78	8.00	6.91	7.14	8.89
Na_2O	4.49	4.18	4.02	4.27	3.76
K_2O	1.64	1.00	1.05	1.17	1.05
P_2O_5	0.26	0.28	0.23	0.24	0.31
S (ppm)	1324	1518	970	1213	1837
Cl(ppm)	675	713	638	633	861
F(ppm)	513	503	536	436	1046
Total	99.6	96.3	98.5	98.7	97.2
H_2O	0.4	3.7	1.5	1.3	2.8
wt.% OL [d]	6.4	7.4	7.8	7.8	3.4

Table 15. continued

Major and volatile element composition determined by EPMA

Eruption of June 30, 1997 -- Brown andesite pumice

Label	GI2OL4tsA	GI1OL5tsB	GI2aOL5tsB	GI1OL6tsB	GI1OL4tsE
SiO_2	56.6	56.8	53.1	53.7	56.7
TiO_2	1.14	1.05	1.29	1.26	0.97
Al_2O_3	19.4	18.5	18.9	19.6	18.9
Cr_2O_3	0.02	0.02	0.02	0.01	0.00
FeO	5.41	5.36	4.16	4.94	6.09
MnO	0.09	0.12	0.10	0.10	0.10
MgO	2.21	3.08	3.70	2.31	2.58
CaO	7.87	7.40	9.12	8.58	7.39
Na_2O	4.27	4.41	4.33	4.35	4.86
K_2O	1.55	1.39	1.05	1.03	1.53
P_2O_5	0.29	0.29	0.33	0.30	0.30
S (ppm)	1028	n/a	n/a	n/a	741
Cl (ppm)	727	n/a	n/a	n/a	605
F (ppm)	803	n/a	n/a	n/a	622
Total	99.1	98.7	96.7	96.6	99.6
H_2O by Diff. [c]	0.9	1.3	3.3	3.4	0.4
SIMS analyses of volatiles					
S (ppm)	1095	627	2815	2100	769
Cl (ppm)	862	581	1326	1125	656
F (ppm)	884	575	1130	1007	667
H_2O (wt.%)	1.2	0.8	3.6	3.5	1.1
Host olivine composition [c]					
SiO_2	40.1	n/a	n/a	40.0	39.1
MgO	45.9	n/a	n/a	45.6	42.9
FeO^T	13.1	n/a	n/a	13.4	17.0
MnO	0.18	n/a	n/a	0.18	0.23
CaO	0.13	n/a	n/a	0.16	0.11
NiO	0.20	n/a	n/a	0.25	0.13
Total	99.5	n/a	n/a	99.6	99.5
Fo	86.2	n/a	n/a	85.8	81.8
Recalculated major and volatile element composition of glass inclusion [a]					
SiO_2	54.7	n.r.	n.r.	52.8	55.6
TiO_2	1.03	n.r.	n.r.	1.19	0.92
Al_2O_3	17.4	n.r.	n.r.	18.5	18.0
Cr_2O_3	0.02	n.r.	n.r.	0.01	0.00
FeO	6.82	n.r.	n.r.	5.75	6.67
MnO	0.11	n.r.	n.r.	0.11	0.11
MgO	5.94	n.r.	n.r.	4.52	3.99
CaO	7.11	n.r.	n.r.	8.10	7.06
Na_2O	3.84	n.r.	n.r.	4.10	4.63
K_2O	1.39	n.r.	n.r.	0.97	1.45
P_2O_5	0.26	n.r.	n.r.	0.28	0.29
S (ppm)	986	n.r.	n.r.	1978	733
Cl(ppm)	776	n.r.	n.r.	1060	625
F(ppm)	796	n.r.	n.r.	949	636
Total	98.9	n.r.	n.r.	96.7	98.9
H_2O	1.1	n.r.	n.r.	3.3	1.1
wt.% OL [d]	9.7	n.r.	n.r.	5.6	3.9

Table 15. continued

Major and volatile element composition determined by EPMA

	Eruption of June 30, 1997 Brown andesite pumice		January 1, 1998 Dacite dome rock
Label	GI3OL4tsE	GI1OL4tsA	MI2ol7tsPUMc
SiO_2	57.2	56.4	64.2
TiO_2	1.07	1.16	1.29
Al_2O_3	19.0	18.6	19.9
Cr_2O_3	0.01	0.01	0.01
FeO	6.10	5.79	2.26
MnO	0.07	0.10	0.07
MgO	2.79	3.22	1.06
CaO	7.54	7.81	3.21
Na_2O	5.09	4.68	5.39
K_2O	1.63	1.57	3.59
P_2O_5	0.27	0.24	0.30
S (ppm)	n/a	985	526
Cl (ppm)	n/a	721	981
F (ppm)	n/a	732	286
Total	101.0	99.8	101.5
H_2O by Diff. [c]	-1.0	0.2	0.0
SIMS analyses of volatiles			
S (ppm)	500	1203	n/a
Cl (ppm)	658	955	n/a
F (ppm)	686	981	n/a
H_2O (wt.%)	0.6	1.1	n/a
Host olivine composition [e]			
SiO_2	39.1	40.2	39.9
MgO	42.9	46.2	46.8
FeO^T	16.7	12.4	13.2
MnO	0.23	0.18	0.21
CaO	0.12	0.13	0.15
NiO	0.20	0.26	0.17
Total	99.2	99.3	100.4
Fo	82.1	87.0	86.3
Recalculated major and volatile element composition of glass inclusion [a]			
SiO_2	55.8	54.7	61.8
TiO_2	1.02	1.07	1.20
Al_2O_3	18.1	17.1	18.4
Cr_2O_3	0.01	0.01	0.01
FeO	6.51	6.57	3.34
MnO	0.07	0.11	0.09
MgO	3.95	6.03	3.49
CaO	7.20	7.21	2.97
Na_2O	4.85	4.31	4.98
K_2O	1.56	1.45	3.32
P_2O_5	0.26	0.22	0.28
S (ppm)	476	1107	486
Cl(ppm)	627	878	906
F(ppm)	654	903	264
Total	99.5	99.0	100.0
H_2O	0.5	1.0	0.0
wt.% OL [d]	3.2	7.1	6.2

Table 15. continued

[a] SIMS values for volatile content used in preference to EPMA values for recalculation where possible

[b] Post-entrapment crystallization correction not possible due to Fe-Ti oxide grain in glass inclusion

[c] H_2O calculated by difference from 100 wt.% for EPMA data

[d] amount of post-entrapment crystallization of host olivine in wt.%; n/a = not analyzed; n.r. = not reported

[e] Host phenocryst analyzed within 10 microns of glass inclusion

Table 16. Compositions of orthopyroxene-hosted glass inclusions and host orthopyroxenes (in wt.% except where noted)

Major and volatile element composition determined by EPMA

Eruption of June 30, 1997 -- Brown andesite pumice

Label	MI1opx8tsSCa	MI2opx8tsSCa	MI3opx8tsSCa	MI4opx8tsSCa	MI1opx2tsSCb
SiO_2	71.1	73.2	71.5	70.8	67.3
TiO_2	0.41	0.38	0.32	0.52	1.09
Al_2O_3	12.3	12.0	12.3	12.6	13.8
Cr_2O_3	0.00	0.01	0.00	0.00	0.00
FeO	3.56	2.75	3.49	3.36	5.45
MnO	0.07	0.08	0.08	0.07	0.05
MgO	0.85	0.72	0.98	0.88	1.16
CaO	2.24	0.99	2.06	1.70	2.81
Na_2O	3.71	3.42	3.43	3.65	5.40
K_2O	2.46	3.48	2.28	3.15	2.39
P_2O_5	0.32	0.02	0.09	0.08	0.31
S (ppm)	163	80	89	160	136
Cl (ppm)	929	809	849	965	706
F (ppm)	692	551	684	525	650
Total	97.2	97.1	96.6	96.9	100.0
H_2O by Diff. [c]	2.8	2.9	3.4	3.1	0.0
SIMS analyses of volatiles					
S (ppm)	n/a	n/a	n/a	n/a	n/a
Cl (ppm)	n/a	n/a	n/a	n/a	n/a
F (ppm)	n/a	n/a	n/a	n/a	n/a
H_2O (wt.%)	n/a	n/a	n/a	n/a	n/a
Host orthopyroxene composition [c]					
SiO_2	53.0	53.6	53.5	53.4	n/a
TiO_2	0.28	0.17	0.27	0.20	n/a
Al_2O_3	1.18	0.59	0.91	0.85	n/a
Cr_2O_3	0.11	0.06	0.07	0.02	n/a
FeO	20.6	20.5	20.1	20.3	n/a
MnO	0.44	0.67	0.48	0.47	n/a
MgO	23.8	24.3	23.9	24.0	n/a
CaO	1.31	1.04	1.40	1.22	n/a
Na_2O	0.04	0.03	0.04	0.03	n/a
NiO	0.01	0.01	0.02	0.04	n/a
Total	100.8	101.0	100.6	100.5	n/a
Mg#	67.3	67.9	67.9	67.8	n/a

Table 16. continued

Recalculated major and volatile element composition of glass inclusion [a]

Eruption of June 30, 1997 -- Brown andesite pumice

Label	MI1opx8tsSCa	MI2opx8tsSCa	MI3opx8tsSCa	MI4opx8tsSCa	MI1opx2tsSCb
SiO_2	70.7	72.8	71.3	70.5	n.r.
TiO_2	0.40	0.36	0.32	0.51	n.r.
Al_2O_3	12.0	11.8	12.1	12.4	n.r.
Cr_2O_3	0.00	0.01	0.00	0.00	n.r.
FeO	4.02	3.14	3.68	3.67	n.r.
MnO	0.07	0.08	0.08	0.07	n.r.
MgO	1.42	1.21	1.23	1.29	n.r.
CaO	2.20	0.98	2.04	1.68	n.r.
Na_2O	3.62	3.35	3.39	3.59	n.r.
K_2O	2.40	3.40	2.25	3.09	n.r.
P_2O_5	0.30	0.02	0.09	0.08	n.r.
S (ppm)	159	78	88	157	n.r.
Cl(ppm)	905	792	840	948	n.r.
F(ppm)	675	539	676	515	n.r.
Total	97.3	97.2	96.7	97.0	n.r.
H_2O	2.7	2.8	3.3	3.0	n.r.
wt.% OPX [d]	2.5	2.1	1.1	1.8	n.r.

Table 16. continued

Major and volatile element composition determined by EPMA

Eruption of June 30, 1997 -- Brown andesite pumice

Label	MI2opx2tsSCb	GI1opx1tsA	GI1opx4tsD	GI1opx1tsE	GI1opx3tsE
SiO_2	67.6	61.3	56.3	72.3	71.5
TiO_2	0.43	1.42	1.11	0.33	0.35
Al_2O_3	12.2	14.3	17.7	12.6	12.5
Cr_2O_3	0.00	0.02	0.01	0.00	0.01
FeO	6.38	6.79	6.20	3.29	3.75
MnO	0.02	0.08	0.11	0.07	0.08
MgO	2.62	1.59	2.98	0.58	0.69
CaO	2.70	4.84	7.05	1.18	1.30
Na_2O	3.98	4.12	5.13	3.94	3.59
K_2O	1.69	1.92	1.72	4.06	3.50
P_2O_5	0.18	0.40	0.26	0.07	0.27
S (ppm)	254	n/a	763	130	23
Cl (ppm)	959	n/a	791	793	631
F (ppm)	765	n/a	839	697	767
Total	98.0	97.5	98.9	98.7	97.7
H_2O by Diff. [c]	2.1	2.5	1.1	1.3	2.3
SIMS analyses of volatiles					
S (ppm)	n/a	812	898	219	25
Cl (ppm)	n/a	1338	922	1555	995
F (ppm)	n/a	5205	1050	1270	1126
H_2O (wt.%)	n/a	2.5	1.1	1.2	1.4
Host orthopyroxene composition [c]					
SiO_2	n/a	n/a	53.2	52.5	52.6
TiO_2	n/a	n/a	0.34	0.23	0.24
Al_2O_3	n/a	n/a	3.07	1.03	0.73
Cr_2O_3	n/a	n/a	0.02	0.01	0.02
FeO	n/a	n/a	12.5	20.8	20.0
MnO	n/a	n/a	0.26	0.51	0.57
MgO	n/a	n/a	28.3	23.4	24.0
CaO	n/a	n/a	2.30	1.54	1.41
Na_2O	n/a	n/a	0.05	0.04	0.03
NiO	n/a	n/a	n/a	n/a	n/a
Total	n/a	n/a	100.0	100.0	99.6
Mg#	n/a	n/a	80.2	66.6	68.2

Table 16. continued

Recalculated major and volatile element composition of glass inclusion [a]

Eruption of June 30, 1997 -- Brown andesite pumice

Label	MI2opx2tsSCb	GI1opx1tsA	GI1opx4tsD	GI1opx1tsE	GI1opx3tsE
SiO_2	n.r.	n.r.	56.2	71.5	71.2
TiO_2	n.r.	n.r.	1.07	0.32	0.34
Al_2O_3	n.r.	n.r.	17.0	12.2	12.1
Cr_2O_3	n.r.	n.r.	0.01	0.00	0.01
FeO	n.r.	n.r.	6.52	4.05	4.63
MnO	n.r.	n.r.	0.11	0.07	0.08
MgO	n.r.	n.r.	4.21	1.39	1.73
CaO	n.r.	n.r.	6.82	1.15	1.27
Na_2O	n.r.	n.r.	4.89	3.79	3.46
K_2O	n.r.	n.r.	1.63	3.91	3.37
P_2O_5	n.r.	n.r.	0.25	0.07	0.26
S (ppm)	n.r.	n.r.	854	211	24
Cl(ppm)	n.r.	n.r.	877	1496	958
F(ppm)	n.r.	n.r.	999	1223	1084
Total	n.r.	n.r.	98.9	98.7	98.6
H_2O	n.r.	n.r.	1.1	1.2	1.4
wt.% OPX [d]	n.r.	n.r.	4.9	3.8	4.6

Table 16. continued

Major and volatile element composition determined by EPMA

	6/30/97 Brown andesite pumice		6/30/97 White dacite pumice	
Label	GI3opx3tsE	GI1opx1tsF	MI1opx14ts2 [b]	MI2opx1tsPumc
SiO_2	71.1	70.8	64.4	71.2
TiO_2	0.53	0.33	0.83	0.37
Al_2O_3	12.6	12.7	14.0	12.3
Cr_2O_3	0.02	0.01	0.00	0.00
FeO	4.16	3.16	5.81	3.86
MnO	0.08	0.05	0.17	0.04
MgO	0.74	0.67	3.76	0.67
CaO	1.70	1.79	4.24	1.51
Na_2O	4.10	3.68	1.55	3.52
K_2O	2.88	3.55	1.27	3.39
P_2O_5	0.04	0.05	0.48	0.12
S (ppm)	58	n/a	622	184
Cl (ppm)	653	n/a	541	963
F (ppm)	718	n/a	648	458
Total	98.1	97.0	96.7	97.1
H_2O by Diff. [c]	1.9	3.0	3.3	2.9
SIMS analyses of volatiles				
S (ppm)	63	184	n/a	n/a
Cl (ppm)	868	1166	n/a	n/a
F (ppm)	1057	1264	n/a	n/a
H_2O (wt.%)	1.3	1.3	n/a	n/a
Host orthopyroxene composition [c]				
SiO_2	52.9	n/a	53.6	51.8
TiO_2	0.21	n/a	0.23	0.24
Al_2O_3	1.31	n/a	0.80	1.11
Cr_2O_3	0.25	n/a	0.01	0.03
FeO	19.1	n/a	18.2	21.5
MnO	0.55	n/a	0.64	0.49
MgO	24.6	n/a	25.8	22.9
CaO	1.35	n/a	1.27	1.37
Na_2O	0.03	n/a	0.01	0.05
NiO	n/a	n/a	0.02	0.03
Total	100.3	n/a	100.6	99.6
Mg#	69.6	n/a	71.7	65.5

Table 16. continued

Recalculated major and volatile element composition of glass inclusion [a]

	6/30/97 Brown andesite pumice		6/30/97 White dacite pumice	
Label	Gl3opx3tsE	Gl1opx1tsF	Ml1opx14ts2 [b]	Ml2opx1tsPumc
SiO_2	70.7	n.r.	n.r.	70.5
TiO_2	0.51	n.r.	n.r.	0.35
Al_2O_3	12.2	n.r.	n.r.	11.9
Cr_2O_3	0.02	n.r.	n.r.	0.00
FeO	4.98	n.r.	n.r.	4.52
MnO	0.08	n.r.	n.r.	0.04
MgO	1.71	n.r.	n.r.	1.39
CaO	1.66	n.r.	n.r.	1.47
Na_2O	3.95	n.r.	n.r.	3.40
K_2O	2.77	n.r.	n.r.	3.28
P_2O_5	0.04	n.r.	n.r.	0.12
S (ppm)	61	n.r.	n.r.	178
Cl(ppm)	836	n.r.	n.r.	930
F(ppm)	1017	n.r.	n.r.	443
Total	98.7	n.r.	n.r.	97.2
H_2O	1.3	n.r.	n.r.	2.8
wt.% OPX [d]	4.3	n.r.	n.r.	3.3

Table 16. continued

Major and volatile element composition determined by EPMA

	6/30/97 Banded Pumice		1/1/98 Dacite dome rock	
Label	MI1aopx1tsmixb	MI1bopx1tsmixb	MI1opx56ts5	MI1opx12tsPumd
SiO_2	69.2	67.9	75.1	75.0
TiO_2	0.59	0.67	0.40	0.64
Al_2O_3	13.4	13.8	12.5	12.7
Cr_2O_3	0.01	0.00	0.02	0.00
FeO	4.21	3.81	2.38	2.15
MnO	0.03	0.10	0.04	0.02
MgO	1.19	1.24	0.35	0.29
CaO	2.05	2.24	1.19	0.78
Na_2O	4.60	4.59	3.62	3.98
K_2O	2.91	2.87	3.52	4.14
P_2O_5	0.13	0.15	0.08	0.06
S (ppm)	118	67	79	16
Cl (ppm)	953	746	880	544
F (ppm)	n/a	n/a	692	590
Total	98.4	97.6	99.3	99.8
H_2O by Diff. [c]	1.6	2.5	0.7	0.2
SIMS analyses of volatiles				
S (ppm)	n/a	n/a	n/a	n/a
Cl (ppm)	n/a	n/a	n/a	n/a
F (ppm)	n/a	n/a	n/a	n/a
H_2O (wt.%)	n/a	n/a	n/a	n/a
Host orthopyroxene composition [e]				
SiO_2	52.0	52.3	53.2	53.1
TiO_2	0.26	0.24	0.27	0.14
Al_2O_3	1.01	0.91	0.91	0.96
Cr_2O_3	0.07	0.04	0.03	0.01
FeO	21.0	21.0	21.1	21.8
MnO	0.52	0.51	0.46	0.58
MgO	23.8	23.3	22.7	22.5
CaO	1.27	1.29	1.43	1.21
Na_2O	0.06	0.06	0.10	0.05
NiO	0.03	0.00	0.01	0.05
Total	99.9	99.7	100.2	100.3
Mg#	66.9	66.4	65.8	64.8

Table 16. continued

Recalculated major and volatile element composition of glass inclusion [a]

	6/30/97 Banded Pumice		1/1/98 Dacite dome rock	
Label	MI1aopx1tsmixb	MI1bopx1tsmixb	MI1opx56ts5	MI1opx12tsPumd
SiO_2	69.0	67.9	74.2	74.1
TiO_2	0.59	0.67	0.39	0.62
Al_2O_3	13.2	13.8	12.0	12.3
Cr_2O_3	0.01	0.00	0.02	0.00
FeO	4.36	3.81	3.32	3.08
MnO	0.03	0.10	0.04	0.02
MgO	1.42	1.24	1.19	1.07
CaO	2.03	2.24	1.16	0.76
Na_2O	4.55	4.59	3.47	3.82
K_2O	2.88	2.87	3.37	3.98
P_2O_5	0.12	0.15	0.08	0.06
S (ppm)	117	67	76	15
Cl(ppm)	944	746	844	523
F(ppm)	n/a	n/a	663	567
Total	98.3	97.6	99.4	99.8
H_2O	1.7	2.5	0.6	0.2
wt.% OPX [d]	1.0	0.0	4.1	3.9

[a] SIMS values for volatile content used in preference to EPMA values for recalculation where possible

[b] Orthopyroxene host zoned in region of glass inclusion. Recalculation not possible.

[c] H_2O calculated by difference from 100 wt.% for EPMA data

[d] amount of post-entrapment crystallization of host orthopyroxene in wt.%; n/a = not analyzed; n.r. = not reported

[e] Host phenocryst analyzed within 10 microns of glass inclusion

Table 17. Compositions of clinopyroxene-hosted glass inclusions and host clinopyroxenes (in wt.% except where noted)

Major and volatile element composition determined by EPMA

Eruption of June 30, 1997 -- Brown andesite pumice

Label	MI1cpx20ts1	MI2cpx20ts1	MI1cpx25ts1	MI2cpx25ts1	MI3cpx25ts1
SiO_2	63.8	62.6	70.7	72.1	58.8
TiO_2	1.03	0.83	0.10	0.87	0.85
Al_2O_3	13.6	13.6	12.1	11.1	13.1
Cr_2O_3	0.00	0.00	0.01	0.00	0.06
FeO	5.43	5.83	3.28	3.16	5.58
MnO	0.13	0.14	0.04	0.02	0.01
MgO	2.86	3.37	0.95	0.64	4.23
CaO	4.76	5.64	2.07	1.95	6.42
Na_2O	2.89	2.52	3.48	2.88	3.14
K_2O	2.25	2.20	3.63	3.21	1.76
P_2O_5	0.27	0.27	0.06	0.09	0.41
S (ppm)	30	84	75	0	129
Cl (ppm)	703	661	815	752	1038
F (ppm)	873	861	1105	1043	1157
Total	97.2	97.1	96.6	96.2	94.6
H_2O by Diff. [a]	2.8	2.9	3.4	3.8	5.4
SIMS analyses of volatiles					
S (ppm)	n/a	n/a	n/a	n/a	n/a
Cl (ppm)	n/a	n/a	n/a	n/a	n/a
F (ppm)	n/a	n/a	n/a	n/a	n/a
H_2O (wt.%)	n/a	n/a	n/a	n/a	n/a
Host clinopyroxene composition [b]					
SiO_2	51.7	50.7	51.7	51.1	50.9
TiO_2	0.64	1.09	0.37	0.35	0.78
Al_2O_3	2.05	3.30	1.74	1.25	2.68
Cr_2O_3	0.01	0.03	0.06	0.04	0.04
FeO	8.32	8.15	9.86	9.04	7.99
MnO	0.24	0.20	0.28	0.30	0.23
MgO	15.9	15.7	14.3	14.9	15.6
CaO	19.9	20.3	21.0	21.1	20.1
Na_2O	0.34	0.37	0.52	0.38	0.36
NiO	0.00	0.02	0.04	0.00	0.01
Total	99.0	99.8	99.9	98.5	98.7
Mg#	77.3	77.4	72.1	74.6	77.7

Table 17. continued

Major and volatile element composition determined by EPMA

Eruption of June 30, 1997 -- White dacite pumice

Label	MI1cpx5tsSCa	MI2cpx5tsSCa	GI1cpx3tsD	MI1cpx12ts2	MI3cpx12ts2
SiO_2	64.3	61.0	72.5	73.8	70.0
TiO_2	0.94	1.64	0.38	0.76	0.40
Al_2O_3	15.2	15.6	11.0	12.4	11.3
Cr_2O_3	0.04	0.00	0.00	0.01	0.00
FeO	5.40	5.44	3.50	3.47	3.19
MnO	0.10	0.08	0.06	0.09	0.05
MgO	1.51	1.93	0.71	0.53	1.25
CaO	3.30	3.70	1.92	1.56	2.66
Na_2O	4.24	4.91	3.01	1.51	4.04
K_2O	2.33	2.12	4.07	3.23	3.18
P_2O_5	0.36	0.27	0.03	0.06	0.02
S (ppm)	598	810	n/a	1	60
Cl (ppm)	848	891	n/a	859	582
F (ppm)	648	809	n/a	813	737
Total	97.9	97.0	97.4	97.6	96.2
H_2O by Diff. [a]	2.1	3.0	2.6	2.4	3.8
SIMS analyses of volatiles					
S (ppm)	n/a	n/a	30	n/a	n/a
Cl (ppm)	n/a	n/a	1611	n/a	n/a
F (ppm)	n/a	n/a	948	n/a	n/a
H_2O (wt.%)	n/a	n/a	1.8	n/a	n/a
Host clinopyroxene composition [b]					
SiO_2	52.9	52.6	52.5	53.3	53.3
TiO_2	0.34	0.34	0.21	0.29	0.29
Al_2O_3	1.40	1.31	0.96	0.92	0.92
Cr_2O_3	0.00	0.00	0.05	0.04	0.04
FeO	8.22	9.01	11.5	9.09	9.09
MnO	0.29	0.36	0.30	0.39	0.39
MgO	15.3	15.4	13.4	14.9	14.9
CaO	21.9	20.5	20.7	21.5	21.5
Na_2O	0.37	0.31	0.37	0.42	0.42
NiO	0.00	0.01	n/a	0.01	0.01
Total	100.7	99.9	100.0	100.8	100.8
Mg#	76.9	75.3	67.5	74.4	74.4

Table 17. continued

Major and volatile element composition determined by EPMA

	6/30/97 White dacite pumice		6/30/97 -- Banded pumice		
Label	MI1cpx1tsPumc	MI1cpx2tsPumc	MI3cpx1tsmixa	MI4cpx1tsmixa	MI5cpx1tsmixa
SiO_2	70.3	73.8	56.7	55.9	56.8
TiO_2	0.93	0.88	0.94	1.02	1.14
Al_2O_3	13.1	11.5	19.5	17.5	18.6
Cr_2O_3	0.02	0.01	0.00	0.03	0.01
FeO	2.77	2.40	4.73	5.17	5.05
MnO	0.05	0.08	0.11	0.08	0.10
MgO	0.56	0.64	1.51	3.89	2.16
CaO	1.89	1.45	3.67	7.04	4.39
Na_2O	4.26	3.59	6.08	4.73	5.77
K_2O	3.37	3.72	1.54	1.37	1.58
P_2O_5	0.34	0.09	0.25	0.26	0.24
S (ppm)	52	18	1507	918	2100
Cl (ppm)	733	223	852	671	1237
F (ppm)	714	174	n/a	n/a	n/a
Total	97.7	98.2	95.2	97.1	96.1
H_2O by Diff. [a]	2.3	1.8	4.8	2.9	3.9
SIMS analyses of volatiles					
S (ppm)	n/a	n/a	n/a	n/a	n/a
Cl (ppm)	n/a	n/a	n/a	n/a	n/a
F (ppm)	n/a	n/a	n/a	n/a	n/a
H_2O (wt.%)	n/a	n/a	n/a	n/a	n/a
Host clinopyroxene composition [b]					
SiO_2	51.5	52.7	52.4	53.0	52.3
TiO_2	0.70	0.33	0.47	0.50	0.61
Al_2O_3	3.61	1.01	2.92	2.73	2.60
Cr_2O_3	0.70	0.00	0.70	0.52	0.24
FeO	5.64	9.48	4.90	5.03	6.21
MnO	0.15	0.36	0.13	0.13	0.17
MgO	16.5	14.8	17.0	17.3	16.9
CaO	20.7	20.9	21.1	21.3	20.9
Na_2O	0.38	0.38	0.36	0.34	0.33
NiO	0.02	0.03	0.00	0.05	0.02
Total	99.9	100.1	99.9	100.8	100.2
Mg#	83.9	73.6	86.1	86.0	82.9

Table 17. continued

Major and volatile element composition determined by EPMA

Eruption of January 1, 1998 -- Dacite dome rock

Label	MI3cpx56ts5	MI1cpx14tsPumc	MI1cpx17tsPumc	MI2cpx17tsPumc
SiO_2	74.0	71.2	76.2	73.8
TiO_2	0.28	0.59	0.34	0.39
Al_2O_3	12.1	13.6	11.8	12.6
Cr_2O_3	0.00	0.00	0.03	0.00
FeO	1.78	1.88	1.92	1.69
MnO	0.07	0.03	0.09	0.05
MgO	0.51	0.57	0.36	0.44
CaO	1.38	1.91	1.19	1.30
Na_2O	3.68	3.90	4.14	3.74
K_2O	4.02	3.34	3.23	4.10
P_2O_5	0.06	0.07	0.02	0.10
S (ppm)	95	251	124	125
Cl (ppm)	932	790	903	693
F (ppm)	816	433	357	566
Total	98.1	97.2	99.4	98.4
H_2O by Diff. [a]	1.9	2.8	0.6	1.6
SIMS analyses of volatiles				
S (ppm)	n/a	n/a	n/a	n/a
Cl (ppm)	n/a	n/a	n/a	n/a
F (ppm)	n/a	n/a	n/a	n/a
H_2O (wt.%)	n/a	n/a	n/a	n/a
Host clinopyroxene composition [b]				
SiO_2	52.4	51.8	52.4	52.2
TiO_2	0.44	0.65	0.39	0.47
Al_2O_3	1.50	2.43	1.38	2.11
Cr_2O_3	0.07	0.10	0.07	0.06
FeO	10.2	10.1	9.95	10.7
MnO	0.37	0.25	0.38	0.32
MgO	13.9	13.8	14.4	14.1
CaO	20.3	20.4	20.7	19.4
Na_2O	0.56	0.54	0.51	0.60
NiO	0.00	0.00	0.00	0.04
Total	99.7	100.0	100.2	100.0
Mg#	70.9	70.9	72.1	70.3

Table 17. continued

Major and volatile element composition determined by EPMA

Eruption of January 1, 1998 -- Dacite dome rock

Label	MI3cpx17tsPumc	MI1cpx10tsPumd	GI5cpx1tsA	GI1cpx2tsB
SiO_2	73.9	74.5	71.9	71.0
TiO_2	0.40	0.46	0.40	0.86
Al_2O_3	12.8	12.4	13.2	13.9
Cr_2O_3	0.00	0.01	0.00	0.01
FeO	1.80	1.83	1.90	2.33
MnO	0.06	0.03	0.02	0.04
MgO	0.42	0.66	0.38	0.26
CaO	1.60	1.37	1.16	1.13
Na_2O	3.90	3.93	4.41	3.52
K_2O	3.90	3.18	4.08	4.31
P_2O_5	0.07	0.03	0.04	0.08
S (ppm)	125	94	171	46
Cl (ppm)	916	1211	813	684
F (ppm)	645	503	906	218
Total	99.0	98.6	97.8	97.6
H_2O by Diff. [a]	1.0	1.4	2.2	2.4
SIMS analyses of volatiles				
S (ppm)	n/a	n/a	231	35
Cl (ppm)	n/a	n/a	1077	670
F (ppm)	n/a	n/a	1440	244
H_2O (wt.%)	n/a	n/a	1.5	0.1
Host clinopyroxene composition [b]				
SiO_2	51.7	51.5	52.1	51.4
TiO_2	0.41	0.50	0.56	0.46
Al_2O_3	1.89	2.12	1.94	1.79
Cr_2O_3	0.05	0.15	0.06	0.08
FeO	10.1	10.3	8.21	10.5
MnO	0.32	0.26	0.24	0.25
MgO	14.3	13.8	14.2	14.1
CaO	20.4	20.3	22.1	20.1
Na_2O	0.52	0.61	0.67	0.60
NiO	0.04	0.03	n/a	n/a
Total	99.7	99.5	100.0	99.3
Mg#	71.6	70.5	75.5	70.5

[a] H_2O calculated by difference from 100 wt.% for EPMA data

[b] Host phenocryst analyzed within 10 microns of glass inclusion

Post-entrapment crystallization correction for clinopyroxene-hosted glass inclusions not possible

n/a = not analyzed; n.r. = not reported

One glass inclusion in hornblende was analyzed for S, Cl, and F (Table 18). A post-entrapment crystallization correction for hornblende-hosted glass inclusions was not possible due to lack of a suitable thermodynamic model for hornblende.

Glass inclusions were chosen for analysis by observation of two-dimensional thin sections. Unseen cracks or re-entrants intersecting a glass inclusion in the third dimension may escape detection. These potentially allow for volatile leakage from the glass inclusion during ascent and eruption. In an attempt to filter out a possible volatile leakage bias in our data we used the average volatile content of glass inclusions with the highest sulfur and water concentrations to represent pre-eruptive volatile contents (Figure 12). Glass inclusions with the highest sulfur and water contents generally have the highest Cl contents.

Volatile-rich glass inclusions hosted by olivine are basaltic andesite in composition. The two olivine-hosted glass inclusions with the highest volatile contents contain an average of 1910±100 ppm S, 960±140 ppm Cl, 1000±70 ppm F, and 3.1±0.4 wt.% H_2O (±1σ). The five glass inclusions in orthopyroxene with the highest volatile contents are rhyolitic and average 130±50 ppm S, 880±70 ppm Cl, 570±100 ppm F, and 2.9±0.2 wt.% H_2O (±1σ). The five glass inclusions in clinopyroxene with the highest volatile contents are also rhyolitic and average 80±100 ppm S, 760±110 ppm Cl, 830±270 ppm F, and 3.3±0.6 wt.% H_2O (±1σ). The volatile contents of intermediate composition (andesite to dacite) glass inclusions hosted by olivine, orthopyroxene, clinopyroxene, and hornblende are highly variable.

Matrix Glasses

Thirteen analyses of S, Cl, and F in matrix glass were performed by EPMA (Figure 11; Table 19). Care was taken to avoid the solid phases in microlite-rich glass by inspecting the region of interest with high magnification BSE imaging. The concentration of H_2O in the matrix was calculated using the difference technique (Anderson, 1974). Our major and volatile element analyses are comparable to those

Table 18. Composition of hornblende-hosted glass inclusion (in wt.% except where noted)

Major and volatile element composition determined by EPMA

Eruption of January 1, 1998 -- Dacite dome rock

Label	MI2hbl1tsPumc
SiO_2	66.1
TiO_2	0.25
Al_2O_3	16.9
Cr_2O_3	0.03
FeO	0.01
MnO	0.06
MgO	1.25
CaO	2.14
Na_2O	5.25
K_2O	3.70
P_2O_5	0.01
S (ppm)	734
Cl (ppm)	783
F (ppm)	267
Total	95.8
H_2O by Diff. [a]	4.2

[a] H_2O calculated by difference from 100 wt.%

Post-entrapment crystallization correction for hornblende-hosted glass inclusions not possible

Figure 12. Average of the two most volatile rich basaltic andesite glass inclusions (GI) in olivine and the five most volatile-rich rhyolite glass inclusions in clinopyroxene (CPX) and orthopyroxene (OPX). Average matrix glass volatile content also plotted. **a)** Sulfur, **b)** Chlorine, **c)** Fluorine, and **d)** H_2O. Error bars are 1σ standard deviation on the glass inclusions and matrix glasses (n=15). Minimum detection limits (MDL) shown are for EPMA data. MDL for SIMS data are lower.

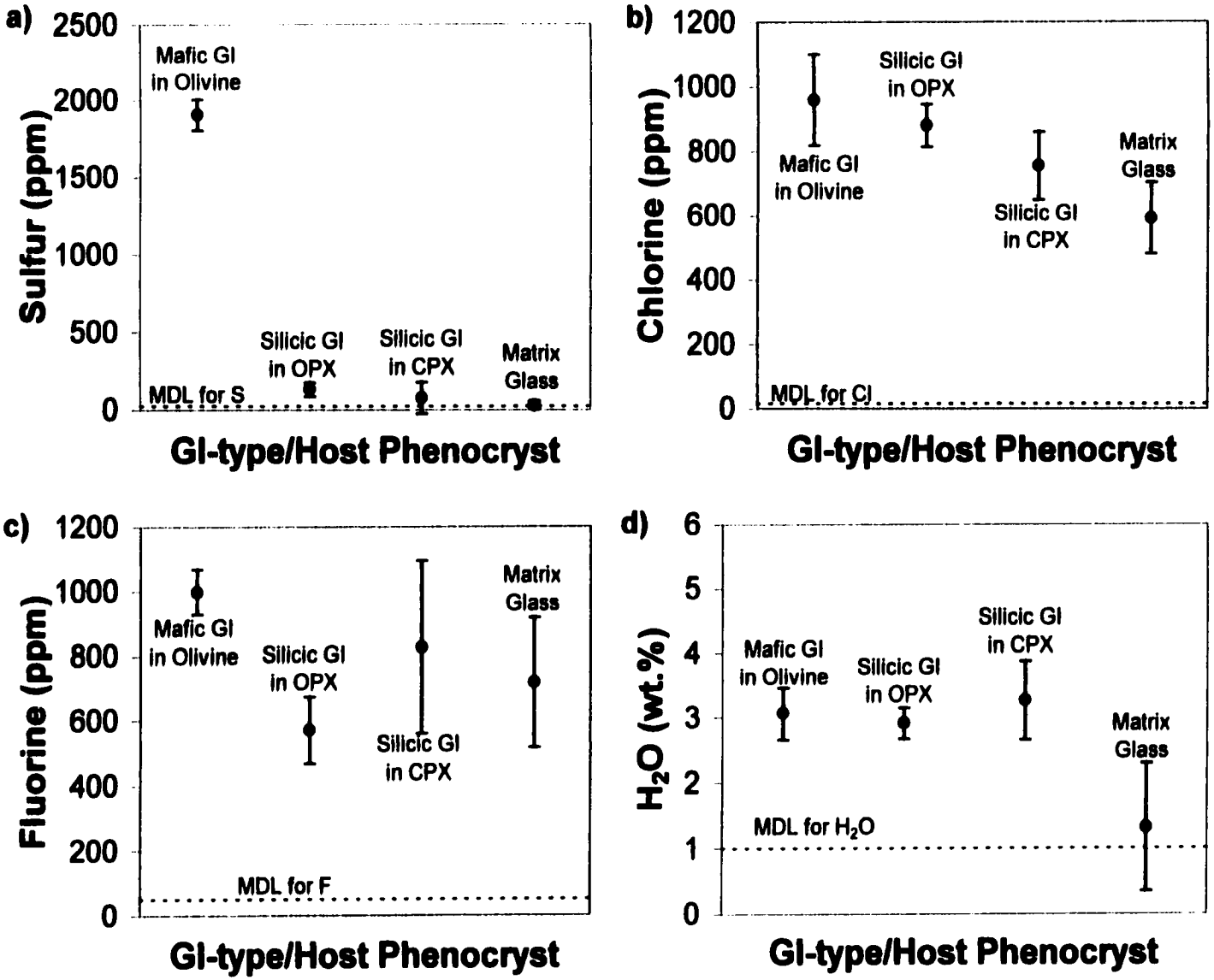
a)
Sulfur (ppm)
2500
2000
1500
1000
500
0
Mafic GI in Olivine
Silicic GI in OPX
Silicic GI in CPX
Matrix Glass
MDL for S
GI-type/Host Phenocryst
b)
Chlorine (ppm)
1200
1000
800
600
400
200
0
Mafic GI in Olivine
Silicic GI in OPX
Silicic GI in CPX
Matrix Glass
MDL for Cl
GI-type/Host Phenocryst
c)
Fluorine (ppm)
1200
1000
800
600
400
200
0
Mafic GI in Olivine
Silicic GI in OPX
Silicic GI in CPX
Matrix Glass
MDL for F
GI-type/Host Phenocryst
d)
H2O (wt.%)
6
5
4
3
2
1
0
Mafic GI in Olivine
Silicic GI in OPX
Silicic GI in CPX
Matrix Glass
MDL for H2O
GI-type/Host Phenocryst

Table 19. EPMA analyses of matrix glasses (in wt.% except where noted)

Eruption of June 30, 1997 -- Brown andesite pumice

Label	SiO_2	Al_2O_3	TiO_2	Cr_2O_3	FeO	MgO	MnO	CaO	Na_2O	K_2O	P_2O_5	S(ppm)	Cl(ppm)	F(ppm)	Total	H_2O*
matrix100newts1	62.0	15.3	1.49	0.00	5.47	2.82	0.10	4.62	2.81	2.27	0.31	16	604	1079	97.4	2.6
matrix104ts1	62.1	15.0	0.98	0.06	5.60	2.37	0.08	4.83	4.02	2.20	0.29	0	591	981	97.7	2.3
matrix3cpx20ts1	63.0	14.9	1.08	0.00	5.27	2.46	0.09	4.37	4.17	2.17	0.31	42	591	958	98.0	2.0
matrix1cpx25ts1	67.8	14.5	0.80	0.00	4.84	1.44	0.08	3.18	2.78	2.57	0.27	42	674	773	98.4	1.6
matrix1opx8tsPopoSC63097a	72.1	13.3	0.68	0.01	2.98	0.70	0.07	1.90	4.23	3.14	0.12	95	759	348	99.3	0.7
matrix1ol25tsPopoSC63097a	62.3	15.0	1.53	0.02	5.80	2.41	0.05	4.62	4.17	2.44	0.37	13	527	536	98.8	1.2
Eruption of June 30, 1997 -- White dacite pumice																
matrix1ts2	71.0	13.5	1.16	0.00	2.30	0.68	0.05	1.36	4.68	3.49	0.30	2	758	750	98.7	1.3
matrix4ts2	71.1	13.4	1.26	0.00	2.24	0.64	0.07	1.28	4.04	3.44	0.28	46	680	728	97.8	2.2
matrix3opx8ts2	67.9	17.0	0.67	0.00	2.43	0.37	0.05	3.68	5.40	2.34	0.11	33	516	598	100.0	0.0
matrix2cpx10ts2	69.9	15.7	0.71	0.00	2.88	0.52	0.06	3.06	4.42	2.81	0.16	34	384	581	100.2	-0.2
matrix1cpx1tsPopoPum63097c	71.4	12.9	0.75	0.00	2.97	0.55	0.02	1.44	4.22	3.64	0.15	0	675	588	98.1	1.9
Eruption of January 1, 1998 -- Dacite dome rock																
matrix2opx56ts5	77.4	12.1	0.41	0.01	1.92	0.22	0.09	0.71	3.18	3.87	0.07	14	466	739	100.1	-0.1
matrix1hbl1tsPopoPum1198c	75.6	11.5	0.53	0.01	1.77	0.25	0.00	0.81	3.59	4.01	0.07	27	510	652	98.2	1.8

* H_2O calculated by difference from 100 wt.%

of light and dark matrix glasses found in the March 1996 dome rocks of Popocatépetl reported in Athanasopoulos (1997).

The averages of all matrix glass volatile analyses are 30±30 ppm S, 600±110 ppm Cl, 720±200 ppm F, and 1.3±1.0 wt.% H_2O by difference (Figure 12). Our data suggests a relatively high retention of H_2O in the matrix glasses. Typically, degassed unaltered glasses at the surface will contain < 0.3 wt.% H_2O (Newman *et al.*, 1988). The low measured sulfur contents suggest the matrix glass is completely degassed. The estimated minimum detection limit using the H_2O by difference technique is ~1 wt.% H_2O. We believe the anomalously high H_2O contents reported here for matrix glass are the result of the cumulative errors in the H_2O by difference technique. There appears to be no systematic variation in volatile content of the matrix glass, regardless of the matrix glass color, microlite content, or silica content.

Discussion

Degassing from Erupted Silicate Melt

Volatile contents of glass inclusions and co-existing degassed matrix glasses can be compared to estimate the extent of SO_2 degassed from silicate melt during eruption. This calculation is performed using the equation (Gerlach *et al.*, 1996):

$$E_{SO_2} = (2\text{x}10^{-15}) V \rho_{melt} \Delta S \, X_{melt}, \qquad (4)$$

where E_{SO_2} = the emission of SO_2 in Mt (1 megaton = 10^9 kg), V is the volume of erupted magma in m^3, ρ_{melt} is the density of the silicate melt phase in kg/m^3, ΔS is the difference between sulfur concentration in glass inclusions and matrix glass in ppm, X_{melt} is the volume fraction of melt (i.e. 1-crystallinity). The factor of 10^{-15} includes a factor of 10^{-6}, which converts ppm S to kg S and an additional factor of 10^{-9}, which converts kg S to Mt S. The factor of 2 converts the mass of S to SO_2.

In order to estimate the amount of degassing from the silicate melt portion of erupted magma, the relative contribution of volatiles from the melts of the two end-member magmas must be determined. The major element bulk composition,

mineralogy, and the values of pre-eruptive intensive variables for the dacite and basaltic andesite end-member magmas erupted at Popocatépetl from 1994-present are estimated in Chapter 1 (Table 13). Using these end-member compositions as well as the whole-rock composition of an individual pyroclast or lava sample, the relative proportion of dacite and basaltic andesite that make up an individual rock sample can be calculated. The range of pumice, scoria, and lava samples collected from the current eruption of Popocatépetl suggests that the mixing proportion ranges from 45 wt.% dacite and 55 wt.% basaltic andesite to 85 wt.% dacite and 15 wt.% basaltic andesite (see Chapter 1).

Since the bulk proportion of mixing between the end-member magmas prior to eruption is unknown and/or may vary with time, we investigate the entire range of mixing proportions represented by individual clasts. We use a crystallinity of 20 vol.% for the 45:55 mixture and 30 vol.% for the 85:15 mixture (based on modal analyses; see Table 4), 3.1×10^7 m^3 magma erupted (from aerial photography as estimated by De la Cruz-Reyna *et al.*, unpubl. data), and a melt density of 2300 kg/m^3.

The amount of sulfur each magmatic end member contributes to degassing can be estimated by taking the difference in sulfur content between glass inclusions and the matrix glass for mafic and silicic end members. For the mafic end member, we use a sulfur content in olivine-hosted glass inclusions of 1910 ppm S. For the silicic end member we use rhyolitic glass inclusions in orthopyroxene, which have an S content of 130 ppm. Using an average matrix glass S content of 30 ppm implies that the mafic and silicic end members degassed 1880 and 100 ppm S, respectively. This results in a degassing value $\Delta S = 1080$ ppm for the 45:55 mixture and $\Delta S = 370$ ppm for the 85:15 mixture. Equation (4) yields 0.12 Mt SO_2 for the 45:55 mixture and 0.04 Mt SO_2 for the 85:15 mixture. Regardless of mixing proportion, sulfur dioxide emitted from the melt portion of 3.1×10^7 m^3 of erupted magma is over two orders of magnitude less than the 14.8 Mt SO_2 emission measured by COSPEC during the magmatic period under scrutiny. Note that this analysis does not consider the ~1.2 Mt

SO_2 emitted during the pre-magmatic period (1994 to early-1996). Even if 100% of the exsolved gas came from the melt phase of an aphyric mafic end-member, SO_2 emission increases to only 0.27 Mt.

By analogy with Equation (4), HCl and HF emissions can be estimated with the expressions:

$$E_{HCl} = (1.03 \times 10^{-15}) V \rho_{melt} \Delta Cl \; X_{melt} \quad (5)$$

and

$$E_{HF} = (1.05 \times 10^{-15}) V \rho_{melt} \Delta F \; X_{melt} \quad (6)$$

where ΔCl and ΔF are the differences in Cl and F content in glass inclusions and matrix glass in ppm. The factors 1.03 and 1.05 convert kg Cl to HCl and kg F to HF, respectively. E_{HCl} and E_{HF} are given in units of megatons. Passive FTIR measurements of the gas plume at Popocatépetl give HCl and HF emission rates of ~1000 and ~100 tons/day, respectively (Goff *et al.*, 2001). If we assume these values are representative, then the total emission of HCl and HF gases, during the 4-year 10-month magmatic period under scrutiny, is 1.8 Mt HCl and 0.2 Mt HF

We again use the 45:55 and 85:15 mixtures of mafic and silicic end members to calculate the magnitude of HCl emission from the melt portion of erupted magma. For the mafic end member, we use a chlorine content in olivine-hosted glass inclusions of 960 ppm Cl. For the silicic end member, we use rhyolitic glass inclusions in orthopyroxenes that have a Cl content of 880 ppm. Using a matrix glass Cl content of 600 ppm implies that the mafic and silicic end members degassed 360 and 280 ppm Cl, respectively. This results in a degassing value $\Delta Cl = 320$ ppm for the 45:55 mixture and $\Delta Cl = 290$ ppm for the 85:15 mixture. Equation (5) yields 0.019 Mt HCl for the 45:55 mixture and 0.015 Mt HCl for the 85:15 mixture. Similar to the case for SO_2 described above, the calculated HCl emission is approximately two orders of magnitude less than the ~1.8 Mt HCl emission measured by passive FTIR.

The amount of fluorine that has exsolved from the melt portion of erupted magma is difficult to assess because the matrix glass F content is highly variable (350-1080 ppm F with average 720±200 ppm F). The range in matrix glass F content significantly overlaps the F contents in glass inclusions in phenocrysts from the mafic and silicic end-members (Figure 11c). For the mafic end member, the average F content in volatile-rich, olivine-hosted glass inclusions is 1000 ppm. For the silicic end member, the average F content in volatile-rich, rhyolitic glass inclusions in orthopyroxene is 570 ppm. If the lowest matrix glass F content (350 ppm F) is representative of degassed matrix glass, this implies that the mafic and silicic end members degassed 650 and 220 ppm F, respectively. This results in a degassing value $\Delta F = 460$ ppm for the 45:55 mixture and $\Delta F = 280$ ppm for the 85:15 mixture. Equation (6) yields 0.027 Mt HF for the 45:55 mixture and 0.015 Mt HF for the 85:15 mixture. Even for this scenario, predicted HF emissions are still about an order of magnitude less than the ~0.2 Mt HF emission measured by passive FTIR. This assessment, however, leaves unexplained some matrix glasses that contain concentrations of F that are higher than those recorded in glass inclusions.

Degassing from shallow unerupted magma

Degassing of magma emplaced at shallow levels within the volcanic edifice has been proposed as a source of "excess" sulfur and other volatiles (Rose et al., 1982; Andres et al., 1991). To produce 14.8 Mt SO_2, melt degassing from a hypothetical silicic end-member composition ($\Delta S = 100$ ppm, $\rho_{melt} = 2300$ kg/m^3, $X_{melt} = 0.65$) would require complete degassing of ~50 km^3 magma. Melt degassing from a mafic end-member composition ($\Delta S = 1880$ ppm, $\rho_{melt} = 2350$ kg/m^3, $X_{melt} = 0.9$) would require a volume of ~2 km^3 magma to completely degas.

Efficient degassing of silicate melt requires either high degrees of crystallization or low pressure. Our analyses of glass inclusions suggest Popocatépetl mafic and silicic melts contain ~3 wt.% H_2O prior to eruption. According to the H_2O solubility model of Moore *et al.* (1998), the mafic and silicic magma compositions of

Popocatépetl are saturated with 3 wt.% H_2O at a pressure of ~700 bars (~ 3 km depth). Dissolved CO_2 in the melt will increase the depth of gas saturation of the magma. Infrared spectroscopic analyses of glass inclusions are needed to ascertain the pre-eruptive CO_2 content of Popocatépetl's end-member magmas. In the absence of this data, we take 3 km as the minimum saturation depth.

In the absence of crystallization, Popocatépetl magma must be emplaced at depths shallower than about ~3 km to exsolve a multi-component, water-rich vapor. Magmas emplaced at any level between the surface and 3 km depth, however, will not completely degas. They will lose only a portion of their dissolved volatiles that is inversely related to the depth of emplacement. According to the mafic case outlined above, a minimum of ~2 km^3 of magma must *completely* degas, to produce the observed SO_2 emissions. Partial degassing of magma will require a correspondingly greater volume of magma.

If we assume complete degassing of a 2 km^3 magma body intruded at 3 km depth due to crystallization, we can employ modified Mogi modeling (Okada, 1992) to estimate surface deformation associated with intrusion of such a magma body. Calculations using the Mogi.m code by P. Cervelli (http://kilauea.stanford.edu/cervelli/software/mogi.html) predict 57 m of vertical displacement. Incomplete degassing would require more magma leading to greater surface deformation. Likewise, emplacement at depths shallower than ~3 km would also lead to greater vertical deformation than the 57 meters predicted above. Continuous GPS deformation monitoring of Popocatépetl has so far shown negligible deformation (Cabral-Cano *et al.*, 1999). In conclusion, degassing from a recently emplaced, shallow static magma body is an unlikely source of "excess" sulfur at Popocatépetl.

Fumarolic Remobilization

Some sulfur emissions may be derived by fumarolic remobilization of pre-existing sulfur deposits within the volcanic edifice (M. O. Garcia, pers. comm., 1998). Such sulfur deposits may take the form of fumarolic precipitates filling cracks

in wall rocks as native sulfur and a variety of other sulfur-bearing minerals. Intrusion of fresh magma could provide the heat necessary to liberate sulfur from these deposits. Native sulfur and other low temperature precipitates may be liberated with relatively modest heating in the presence of oxygen. Many of the important vein-filling minerals will require relatively high temperatures to liberate their sulfur. Furthermore, a portion of this re-mobilized sulfur can be expected to re-precipitate in the cooler margins of the volcanic edifice.

It is unlikely that all the sulfur emissions from Popocatépetl are derived from fumarolic remobilization. To produce the 14.8 Mt SO_2 would require remobilization of 7.4 Mt of native sulfur. Such a mass of native sulfur would occupy 3.6×10^6 m^3 (ρ=2070 kg/m^3 for native sulfur). This volume is equivalent to a 15 m wide, 1000 m long annulus of pure sulfur around a hypothetical 30 m radius cylindrical conduit. The existence of a pure sulfur deposit of this size seems unlikely. Additionally, remobilization of much smaller volume sulfur deposits that are widely disseminated in narrow cracks would require heating of an unreasonably large volume of wall rock to produce the observed sulfur emissions. The flux of sulfur derived from fumarolic remobilization is probably small compared to the total sulfur output. Isotopic investigation of evolved sulfur would be useful in this regard.

Breakdown of sulfur-bearing magmatic phases: anhydrite and sulfide

The volume of silicate melt required to produce the observed SO_2 emission can be reduced if melt degassing is supplemented by significant breakdown of sulfur-bearing phases such as anhydrite or sulfide. The only report of anhydrite in Popocatépetl rocks known to the authors is by Martin-Del Pozzo *et al.* (1995) who note anhydrite as a secondary mineral of hydrothermal origin in some recent phreatic deposits. Although anhydrite can be lost to dissolution and weathering, the freshness of our samples and complete lack of anhydrite, as phenocrysts or mineral inclusions in other solid phases, suggests that anhydrite was not a stable phase in recent Popocatépetl magmas. The moderately oxidizing conditions of Popocatépetl magma

(~ΔNNO+0.5 log units) are consistent with this observation. Higher oxygen fugacities would be necessary to saturate anhydrite. Thus, breakdown of primary magmatic anhydrite is an unlikely source of sulfur at Popocatépetl.

Breakdown of sulfide globules might be a source of sulfur at Popocatépetl. Fe-rich sulfide globules are found as inclusions in pyroxene. In addition, Fe-Ni- and Fe-Cu-rich sulfide globules are found among the breakdown products in hornblende reaction rims and on edges of phenocrysts in contact with silicate melt (see Chapter 1). Larocque *et al.* (2000) proposed that immiscible sulfide liquids break down during depressurization and degassing to form spongy Fe-oxides and sulfur gas. Rare spongy Fe-oxide grains are found on vesicle walls of recent pumices and lava blocks of Popocatépetl.

If we assume a modal abundance of 0.01 vol.% sulfide liquid (an average value; see Larocque *et al.*, 2000) and use 4600 kg/m^3 as the density and 34 wt.% S as the average S content of the sulfide liquid and assume 100% conversion of sulfur in the sulfide liquid to sulfur gas then the 3.1 x 10^7 m^3 of magma erupted would produce only 0.01 Mt SO_2 by the process of sulfide breakdown. To produce the entire 14.7 Mt of SO_2 gas not accounted for by melt degassing would require breakdown of ~15 vol.% sulfide liquid. If this occurred, we would expect to find a sub-equal amount of spongy Fe-oxide breakdown products in the recent Popocatépetl eruptives. Since such a large concentration of sulfide liquid is unlikely and we find only trace amounts of spongy Fe-oxides, breakdown of sulfide liquid is unlikely to have produced the measured SO_2 emissions. Thus, solid sulfur-bearing phases probably contribute only a small proportion of the degassed SO_2.

Assimilation of Carbonate and Evaporite Country Rock

Cretaceous marine carbonate, shale, and evaporite form outcrops near Popocatépetl and are presumed to compose part of the basement rocks that underlie the volcano. Early Tertiary intrusive bodies cut these marine rocks and it seems plausible that dikes feeding Popocatépetl would also intersect these rocks (Goff *et al.*,

2001). Volatile-bearing carbonate and evaporite country rocks could be assimilated into Popocatépetl magma and provide a rich non-magmatic source for the emitted volatiles.

Goff *et al.* (2001) hypothesize that ingestion and assimilation of carbonate country rocks explain huge excursions in the CO_2 flux from Popocatépetl. Large, short-term increases in the CO_2/SO_2 mass ratio, the presence of metamorphosed carbonate xenoliths in eruptives from the last 14,000 years, and the lack of an adequate alternate source of CO_2 are provided as support for their hypothesis. Unfortunately, we do not have CO_2 data from glass inclusions in phenocrysts and matrix glasses from the recent eruptives of Popocatépetl to address this hypothesis.

Goff *et al.* (1998) presented sulfur isotope data for Popocatépetl gases of $\delta^{34}S$ = +1.5 to +6.5‰ with an average of +3.4‰. Gypsum from a regional evaporite deposit yielded a $\delta^{34}S$ value of 16.4‰. The sulfur isotopic composition of Popocatépetl gases falls within the range for gases from continental margins and island arcs ($\delta^{34}S$ = 0 to ~12‰; Taylor, 1986). Sulfur originating from the primitive mantle has $\delta^{34}S \sim 1$‰. Goff *et al.* (1998) argued that up to 16 wt.% of the total sulfur emission at Popocatépetl could be derived from assimilated evaporite country rocks. Their argument implies that the ~2.4‰ enrichment in ^{34}S above the primitive mantle value is wholly due to assimilation of gypsum. If one assumes that the evaporite is contaminating a typical arc $\delta^{34}S$ magmatic signature, then little to no contamination is required to produce observed $\delta^{34}S$ values. It must also be noted that gas samples for the sulfur isotope measurements at Popocatépetl were collected with volatile traps during the phreatic, initial period of unrest in 1994 and prior to the magmatic phase of the current eruptive period. We are concerned that the sulfur isotopic measurements may be biased toward heavy sulfur due to contamination by remobilized (heavy) hydrothermal anhydrite during vent-clearing eruptions either in the gas-phase or as fine gypsum dust that entered the volatile trap.

Goff *et al.*'s (1998) original arguments for evaporite contamination did not consider complexities associated with isotopic fractionation of sulfur between various

phases and oxidation states (Ohmoto and Rye, 1979). A full treatment of the fractionation of sulfur isotopes between silicate melt and gas at the oxygen fugacity inferred for Popocatépetl magma suggests that the sulfur isotopic composition of the pre-degassing Popocatépetl magma has the range $\delta^{34}S = +1.8$ to $+6.8‰$. This is only slightly higher than the measured sulfur isotopic composition of the gas. For comparison, Imai *et al.* (1993) report $\delta^{34}S$ of +8 to +9‰ for Pinatubo. McKibben *et al.* (1996) dismissed the hypothesis of assimilation of large amounts of heavy (hydrothermal) anhydrite at Pinatubo based on textural arguments. Instead, they proposed a model of long-term passive degassing of the pre-eruptive Pinatubo magma that involves heavy sulfur enrichment in the magma. Periodic intrusion of basalt without eruption into the Pinatubo sub-volcanic dacite magma body maintains volatile saturation in the magma while allowing for steady-state passive loss of ^{34}S-depleted gases from the dacite over long time periods. This is accompanied by a buildup of ^{34}S-enriched SO_4^{2-} in the melt. We propose that the same model may apply to Popocatépetl. Etna and Stromboli, like Popocatépetl, are volcanoes characterized by passive degassing and have $\delta^{34}S$ values of the gas phase similar to Popocatépetl (Allard et al., 1994; Allard, 1997). Progressive, long-term enrichment of the pre-eruptive magma with ^{34}S due to passive degassing may be characteristic of these volcanoes as well. Similarly, high $\delta^{34}S$ values (+3 to +16‰) found in explosively erupted tephra from the 1883 eruption of Krakatau (Mandeville *et al.*, 1998) and the climactic eruptions of Mt. Mazama (Mandeville *et al.*, 2001) have been explained by pre-eruptive, open-system degassing.

It is interesting to note that S, Cl, and F emissions are decoupled from CO_2 emissions. During large increases in the CO_2/SO_2 mass ratio, SO_2/HCl, and SO_2/HF ratios remain stable (Goff *et al.*, 2001). If the "excess" CO_2 is caused by carbonate assimilation then this suggests that the assimilated country rock does not contain appreciable quantities of S-, Cl-, and F-bearing minerals.

Sulfur isotope compositions of the gases emitted from Popocatépetl can be explained by ^{34}S accumulation in the magma by passive degassing over long time

periods. Small contributions to the SO_2, HCl, and HF flux from assimilated evaporites are possible but large contributions are unlikely. Measurements of the sulfur isotopic composition of melt inclusions in phenocrysts from the mafic and silicic magmatic end members at Popocatépetl would be useful in addressing this issue.

Separate Volatile Phase in Erupted Magma

Research by several workers over the past two decades has suggested that magma at depth is commonly volatile saturated and some magma bodies may also harbor a co-existing volatile-rich phase (Luhr et al., 1984; Anderson et al., 1989; Lowenstern et al., 1991; Westrich and Gerlach, 1992; Lowenstern, 1993; Gerlach and McGee, 1994; Gerlach et al., 1994; Wallace and Gerlach, 1994; Wallace et al., 1995; Gerlach et al., 1996; Wallace, 2001). A separate volatile phase that exists at depth and ascends with silicate liquid could be a rich source of magmatic gases to account for the large-magnitude gas emissions at Popocatépetl. The low dissolved Cl content measured in glass inclusions (<1000 ppm) is insufficient for the formation of a hydrosaline brine in equilibrium with Popocatépetl silicate melt (Webster *et al.*, 1999). A separate volatile phase at Popocatépetl is more likely dominated by H_2O and CO_2. The composition of such a volatile-rich fluid can be calculated (Table 20) if we assume Popocatépetl's separate volatile phase contains 98 mol% H_2O+CO_2 at ~2 kbar (similar to Pinatubo; Gerlach *et al.*, 1996) and an average CO_2/SO_2 mass ratio of 4 (Goff *et al.*, 2001). The calculated proportions of the major gas species contained in the hypothetical separate volatile phase are 88.7 mol% H_2O, 9.3 mol% CO_2, 1.6 mol% SO_2, 0.3 mol% HCl, and <0.1 mol% HF (Table 20). Unfortunately, there exist no high-temperature, pre-eruption fumarolic gas analyses from Popocatépetl for comparison. Pre-1994 summit fumaroles were low-temperature, boiling-point fumaroles and no samples were obtained (Y. Taran, T. P. Fischer, pers. comm. 2001).

Table 20. Volatile Degassing at Popocatépetl

	Total mass of volatiles degassed (Mt)* Column A	Degassed from erupted silicate melt (Mt) Column B	Degassed from sulfide breakdown (Mt) Column C	Potentially degassed from separate volatile phase? (Mt) Column D	Separate Volatile Phase (mol%) Column E
SO_2	14.8[a]	0.08[c]	0.01[h]	14.7	1.6[e]
HCl	1.8[b]	0.017[c]	0	1.8	0.3[e]
HF	0.2[b]	0.02[c]	0	0.2	<0.1[e]
H_2O	232.4[g]	1.6[c]	0	230.8[e]	88.7[e]
CO_2[f]	59.2[g]	n/a[d]	0	59.2[e]	9.3[e]
Total	308.4	1.7	0.01	306.7	100

The mass of volatiles contained in the separate volatile phase equals the total mass of emitted volatiles minus that degassed from erupted silicate melt minus that degassed from sulfide breakdown.

(Column D = Column A - Column B - Column C)

* From the time period March 1996 to December 2000 Mt = 10^9 kg = 10^{12} g

[a] Measured by COSPEC; (Delgado and Cárdenas-G, 1997; Delgado-Granados et al., 2001; National Center for Disaster Prevention, Mexico City (CENAPRED), unpubl. data; Goff et al., 1998)

[b] Measured by passive FTIR (Love et al., 1998; Goff et al., 2001)

[c] Estimated by EPMA measurements of S, Cl, and F in glass inclusions and matrix glasses (this study) considering erupted melt only and assuming a 65:35 mass ratio of silicic:mafic end members.

[d] CO_2 contents of glass inclusions and matrix glasses were not analyzed in this study. We estimate that the CO_2 contents of glass inclusions are low and would result in a negligible amount of degassing of CO_2 from silicate melt.

[e] Calculated by assuming the separate volatile phase contains 98 mol% H_2O + CO_2 (similar to Pinatubo; see Gerlach et al. 1996) and CO_2/SO_2 mass ratio = 4 (Goff et al., 1998).

[f] CO_2 estimates do not include CO_2 degassing potentially derived from assimilated carbonate rocks (Goff et al., 2001).

[g] Calculated by summing Columns B thru D.

[h] Estimated (see text for explanation)

If we accept that 0.08 Mt SO_2, 0.017 Mt HCl, and 0.02 Mt HF were degassed from the silicate melt of erupted magma as inferred from volatile analyses of glass inclusions and matrix glasses, then the hypothetical separate volatile phase must contain the remainder of the acid gas emissions. This separate volatile phase would then contain 14.7 Mt SO_2, 1.8 Mt HCl, and 0.2 Mt HF. Using the mole ratios presented above, we calculate that the separate volatile phase also contained ~231 Mt H_2O and ~59 Mt CO_2 (Table 20). The total mass of gases contained in the separate volatile phase is therefore ~307 Mt.

For the sake of argument, let us assume that the separate volatile phase at Popocatépetl is carried entirely as bubbles within the 3.1 x 10^7 m^3 magma erupted from March 1996 to December 2000. The erupted magma has a mass of only 74 Mt (3.1 x 10^7 m^3 silicate liquid plus crystals with ρ = 2400 kg/m^3). If we assume unidirectional, homogeneous flow of only the erupted silicate liquid and crystals and the separate volatile phase, the ascending mixture would have consisted of ~20 wt.% silicate and ~80 wt.% of a separate volatile phase. For comparison, the Pinatubo magma is inferred to have contained only ~1-6 wt.% separate volatile phase (Gerlach *et al.*, 1996).

If we assume the Popocatépetl magma body resides at a depth of less than 8 km (i.e. < 2 kbar pressure), then the ideal gas density of the separate volatile phase is <500 kg/m^3. The ~307 Mt of separate volatile phase, therefore, would have occupied >6 x 10^8 m^3 prior to eruption. Thus, prior to ascent, the mixture would have consisted of >95 vol.% low-density volatile phase and <5 vol.% silicate liquid plus crystals. A gas-silicate mixture such as this, if it exists, would live up to Giggenbach's (1996) declaration:

> "andesitic melts may simply be considered an almost incidental fluid medium facilitating the release of excess volatiles."

The bulk density of such a mixture at 8 km depth would be ~600 kg/m^3 and subject to strong buoyancy forces. Such low-density gas-silicate mixtures would probably ascend rapidly. Long-term storage of such a volatile-dominated mixture is

unlikely. Apart from the unreasonably high gas-silicate ratio, the hypothesis that the entire gas output of the volcano is carried by and emitted only with the erupted magma is inconsistent with the observations of discontinuous magma effusion and continuous gas emission (CENAPRED, unpubl. data).

Compared to the mass of gases carried by the hypothesized separate volatile phase, the H_2O and CO_2 exsolved and degassed from erupted silicate melt is probably very small. Based on ~3 wt.% H_2O degassed from the melt, ~1.6 Mt H_2O are produced. We have no data to estimate degassing of CO_2 from the melt. The total volatile emission from Popocatépetl for the 4-year 10-month period under scrutiny can be estimated as ~232 Mt H_2O, ~59 Mt CO_2, 14.8 Mt SO_2, 1.8 Mt HCl, and 0.2 Mt HF for a total of ~308 Mt total volatiles emitted. These values do not include CO_2 degassing potentially derived from assimilated carbonate rocks (Goff *et al.*, 2001).

The observed volatile output of the most recent eruptive activity at Popocatépetl cannot be from degassing of erupted magma or magma that could have been accommodated in the volcanic edifice. A separate volatile phase that ascends with and is expelled from only *erupted* magma would have to comprise an unreasonably high proportion of the gas-silicate mixture to account for the observed gas emissions. Though remobilization of fumarolic deposits may supplement the sulfur output of this volcano, it cannot provide sufficient quantities on its own. In addition, evidence from sulfur isotope data and gas mass ratios suggests that upper crustal assimilation cannot be called upon to provide the observed sulfur and halogen flux.

Viable Sources for Popocatépetl Volatiles

We have effectively narrowed the range of feasible sources of volatiles at Popocatépetl to two: unerupted silicate melt or a separate volatile phase. If the volatiles are wholly derived from silicate melt then 2 km^3 of basaltic andesite, 50 km^3 of dacite, or some mixture of the two with an intermediate volume must *completely* degas to account for the observed volatile emissions. Alternatively, volatiles emitted

from Popocatépetl may have originally resided in a separate vapor phase contained in the magma at depth.

If the volatiles liberated from Popocatépetl are derived from melt degassing alone, then one must provide a mechanism for extracting these volatiles from the melt without erupting more than a small portion of the degassed residue or accumulating significant quantities of this degassed residue in the volcanic edifice. Circulation of magma in the volcanic conduit could explain shallow, non-explosive degassing of large volumes of magma without excessive surface deformation or implausibly large gas-silicate mass ratios. Kazahaya *et al.* (1994) proposed convection of magma in the volcanic conduit as a mechanism for passive degassing at Izu-Oshima (basaltic) and Sakurajima (andesitic) volcanoes. Allard (1997) suggested a similar process at Mount Etna. Shinohara *et al.* (1995) modeled convection of granitic magma in a 300 m diameter conduit to explain volatile transport and the development of porphyry Mo deposits. Stevenson and Blake (1998) refined the fluid dynamic equations presented in Kazahaya *et al.* (1994) with experimental data. They used this revised formulation to explain degassing at Stromboli (basaltic) and the June 1980 gas emissions at Mount St. Helens (dacitic) by convective overturn of dense degassed magma with buoyant volatile-rich magma in a conduit connected to a deep magma chamber.

The conceptual model for conduit convection at Popocatépetl is as follows. Magma ascends to very shallow levels through a cylindrical or dike-shaped conduit from a magma body located at deeper levels. At a level where the bubble content reaches ~30-60 vol.% (Eichelberger et al., 1986; Klug and Cashman, 1996), collapse of magmatic foam would force exsolved magmatic gases to travel out of the magma and into wall rocks (Jaupart and Allègre, 1991). The relatively dense, degassed magma descends back down into the volcano's plumbing system making room for influx of fresh, low-density, volatile-rich magma. Following magma-gas separation, gases ascend vertically through permeable wall rocks to be emitted from the crater walls or margins of the dome. This model is similar to that presented by Kazahaya *et al.* (2002) for the rhyolitic volcano Satsuma-Iwojima.

The required volume of convecting magma is greatly reduced if the majority of the observed volatile output at Popocatépetl resides in a separate volatile phase. Slow accumulation of exsolved gas could take place at the saturated cap of a large magma chamber (Wallace, 2001). This type of bubble accumulation by compositional convection in a stratified magma body has been modeled numerically by Simakin & Botcharnikov (2001) to explain passive degassing at volcanoes like Popocatépetl. In the model of Simakin & Botcharnikov (2001) exsolved volatiles are transported from the cap of the magma chamber to the surface through fumarole pipes. Emplacement of a large magma body to shallow depths is, however, rejected at Popocatépetl due to the lack of observed surface deformation.

To understand the specific case of Popocatépetl, an estimate of the depth of gas-saturation of Popocatépetl magma is needed. If we use a CO_2/SO_2 mass ratio of 4 (Goff *et al.*, 2001) and an H_2O/SO_2 mass ratio of 15.7 based on calculations of the total gas flux (Table 20) and assume that all of the volatiles were originally dissolved in silicate melt, we can calculate initial melt CO_2 and H_2O contents and use these estimates to place constraints on the depth of gas saturation. A magma mixture that consists of 35 wt.% mafic end-member and 65 wt.% silicic end-member (an average proportion based on erupted clasts; see Chapter 1) would have a bulk initial S content of ~720 ppm S. The gas mass ratios presented above imply 3000 ppm initial CO_2 content and 1.2 wt.% initial H_2O content. The calculated initial H_2O content is significantly lower than the ~3 wt.% initial H_2O estimates obtained from glass inclusions in phenocrysts which suggests the H_2O /SO_2 mass ratio may be low. Using 3 wt.% and 3000 ppm as the initial H_2O and CO_2 contents of the melt, the VolatileCalc 1.1 program (Newman and Lowenstern, 2002) calculates saturation pressures > 5 kbar utilizing either the basalt or rhyolite solubility models. This suggests that Popocatépetl magma begins to exsolve gas bubbles to depths > 20 km. The first bubbles to exsolve will be CO_2-dominated; however, once the magma reaches low pressures (< 1.5 kbar) the co-existing vapor will be H_2O-rich (Newman and Lowenstern, 2002). From initial saturation to about 6 km depth, the CO_2-

dominated vapor phase will make up an insignificant portion of the magma (<2 vol.%). It is not until the magma reaches less than 2 km depth before volatiles can make up a sufficient proportion of the magma (30 vol.% or more) to facilitate efficient magma/gas segregation.

For the case of Popocatépetl, we propose: 1) silicate melt and exsolved gas are both sources of volatiles and 2) the mechanism for passive degassing of the large quantities of volatiles involves convection of volatile saturated magma in the volcanic conduit (Figure 13). If one assumes small volumes of silicate material then large proportions of exsolved gas are required and vice versa. We explored a range of volumes of silicate material (0.1 to 3 km^3) that consists of 65:35 wt.% silicic:mafic end-members with 25 vol.% crystals (Table 21). The masses of SO_2 and HCl derived from the silicate material are supplemented by a separate volatile phase (with the calculated composition shown in Table 20) until the observed masses of SO_2 and HCl emissions are most closely matched. The calculated weight proportion of exsolved gas has the range ~2 – 56 wt.% (Table 21). HF emissions were not included in the calculation because of large uncertainties in the mass of HF emission from silicate melt. Volumes of silicate material less than 0.1 km^3 require high proportions of exsolved gas (> 56 wt.%). Volumes of silicate material greater than ~3.3 km^3 would release quantities of HCl that are greater than the observed HCl emission. The best match between calculated and observed SO_2 and HCl emissions (the lowest Σr^2) is obtained from degassing ~1 km^3 (2.4×10^{12} kg) silicate with an additional 2.5×10^{11} kg separate volatile phase (~9 wt.% exsolved gas; Table 21).

To illustrate the best match example, our data suggest that complete degassing of ~1 km^3 of magma (consisting of 65 wt.% dacite, 35 wt.% basaltic andesite, having ~25 vol.% crystals, and no exsolved gas) would release ~2.5 Mt SO_2 and ~0.6 Mt HCl from the melt. Chemical breakdown of sulfide in the ~1 km^3 of Popocatépetl magma would supply an additional ~0.3 Mt SO_2. An accompanying separate volatile phase that comprises ~9 wt.% of the magma, with volatile proportions as outlined in Table 20, would contain ~12.0 Mt SO_2 and ~1.3 Mt HCl. In sum, this scenario would

Figure 13. Schematic illustration of magma convection and passive degassing processes at Popocatépetl. Magma is saturated with a CO_2-dominated vapor phase to pressures greater than 5 kbar (?). Ascending magma crystallizes olivine (at P=1-4 kbar) and pyroxene (at P<1.5 kbar) trapping gas-saturated melt inclusions. At shallow levels (< 1 kbar) exsolved vapor is H_2O-rich. Sulfur dioxide, HCl, and HF partition into the hydrous vapor phase. Accumulation and expansion of bubbles produces a magmatic foam. Collapse of the magmatic foam drives exolved magmatic gases into cracks in wall rock. Gases travel up through the volcanic edifice and are released to the atmosphere through fumaroles. Meanwhile, dense degassed magma descends in the volcanic conduit. The illustration shown corresponds to ~1 wt. % H_2O retained in the silicate melt (equivalent to ~150 bars or 600 m depth). Diagram not to scale.

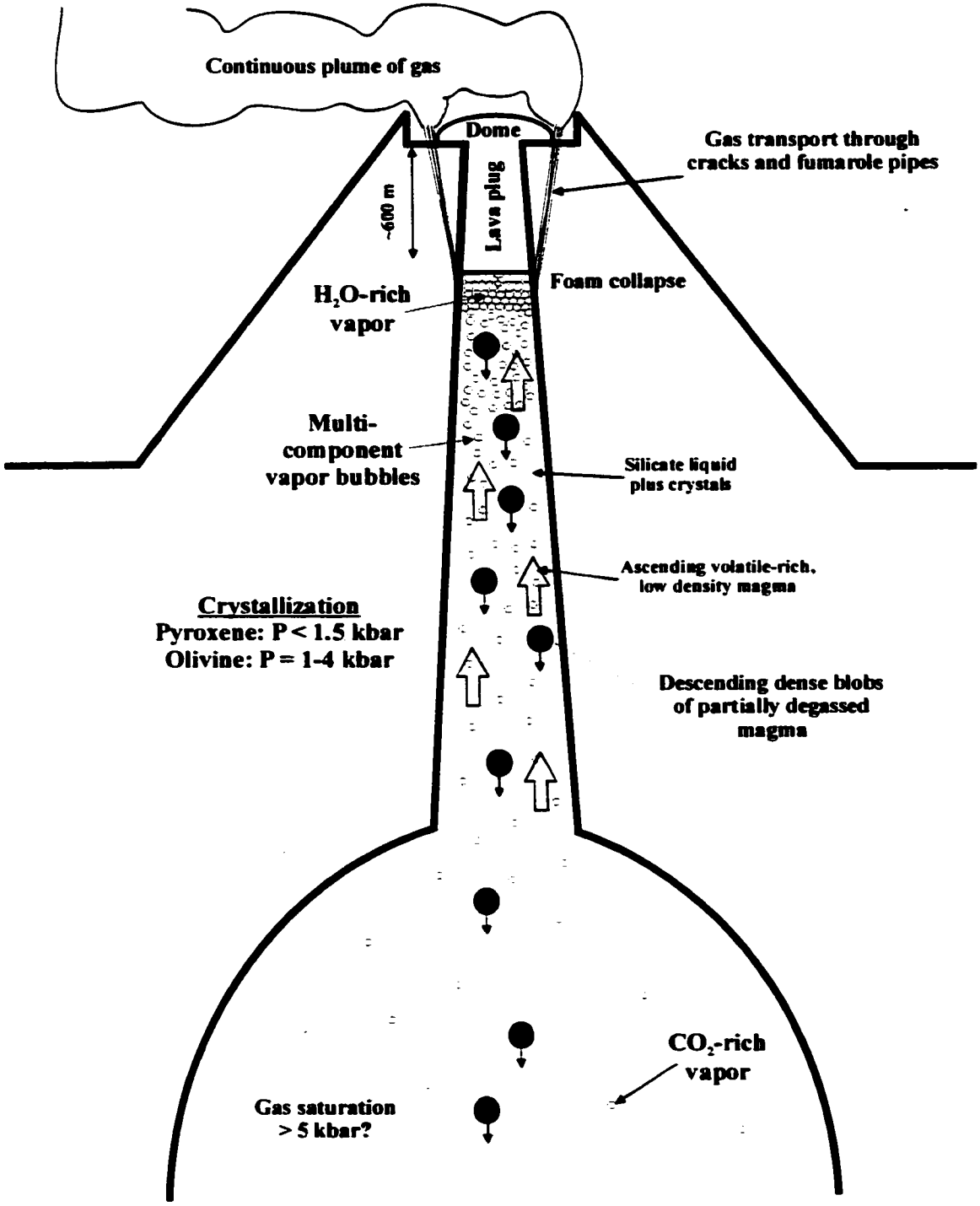
Continuous plume of gas
Dome
Gas transport through cracks and fumarole pipes
~600 m
Lava plug
Foam collapse
H_2O-rich vapor
Multi-component vapor bubbles
Silicate liquid plus crystals
Ascending volatile-rich, low density magma
Crystallization
Pyroxene: P < 1.5 kbar
Olivine: P = 1-4 kbar
Descending dense blobs of partially degassed magma
CO_2-rich vapor
Gas saturation > 5 kbar?

Table 21. Volatile contributions to the total gas flux from unerupted magma with silicate melt, breakdown of sulfide liquid, and a separate volatile phase as the sources of volatiles. Optimized values in bold type.

Separate volatile phase has the composition:

	mol%	wt.%
SO_2	1.6	4.8
HCl	0.3	0.5
HF	<0.1	<0.1
H_2O	88.7	75.3
CO_2	9.3	19.3

Silicate material =
65 wt. % silicic end-member plus
35 wt. % mafic end-member
with 25 vol. % crystals, ρ = 2400 kg/m^3

0.031 km^3 (7.4 x 10^{10} kg) silicate + 3.1 x 10^{11} SVP = 19.5 wt. % silicate and 80.5 wt. % SVP

	melt[a]	sulfide liquid[b]	SVP[c]	Sum	Observed[d]
SO_2	0.08	0.01	14.73	14.82	14.8
HCl	0.02	0	1.58	1.59	1.8
				Σr^2	0.044

0.1 km^3 (2.4 x 10^{11} kg) silicate + 3.0 x 10^{11} SVP = 44.3 wt. % silicate and 55.7 wt. % SVP

	melt[a]	sulfide liquid[b]	SVP[c]	Sum	Observed[d]
SO_2	0.25	0.03	14.57	14.85	14.8
HCl	0.05	0	1.56	1.61	1.8
				Σr^2	0.038

0.5 km^3 (1.2 x 10^{12} kg) silicate + 2.8 x 10^{11} SVP = 81.2 wt. % silicate and 18.8 wt. % SVP

	melt[a]	sulfide liquid[b]	SVP[c]	Sum	Observed[d]
SO_2	1.25	0.16	13.41	14.82	14.8
HCl	0.27	0	1.43	1.71	1.8
				Σr^2	0.009

1 km^3 (2.4 x 10^{12} kg) silicate + 2.5 x 10^{11} SVP = 90.6 wt. % silicate and 9.4 wt. % SVP

	melt[a]	sulfide liquid[b]	SVP[c]	Sum	Observed[d]
SO_2	2.49	0.31	12.02	14.83	14.8
HCl	0.55	0	1.29	1.83	1.8
				Σr^2	0.002

Table 21. continued

		melt[a]	sulfide liquid[b]	SVP[c]	Sum	Observed[d]
2 km^3 (4.8 x 10^{12} kg) silicate + 1.9 x 10^{11} SVP = 96.2 wt. % silicate and 3.8 wt. % SVP	SO_2	4.99	0.63	9.15	14.77	14.8
	HCl	1.09	0	0.98	2.07	1.8
					Σr^2	0.075
		melt[a]	sulfide liquid[b]	SVP[c]	Sum	Observed[d]
3 km^3 (7.2 x 10^{12} kg) silicate + 1.3 x 10^{11} SVP = 98.2 wt. % silicate and 1.8 wt. % SVP	SO_2	7.48	0.94	6.37	14.79	14.8
	HCl	1.64	0	0.68	2.32	1.8
					Σr^2	0.273

Greater than 5.9 km^3 silicate material would release quantities of SO_2 that are greater than the observed SO_2 emission

Greater than 3.3 km^3 silicate material would release quantities of HCl that are greater than the observed HCl emission

SVP = separate volatile phase

All data listed as megatons of gas (1 megaton = 10^9 kg)

[a] mass of SO_2 and HCl derived from degassing of silicate melt

[b] mass of SO_2 and HCl derived from breakdown of sulfide liquid

[c] mass of SO_2 and HCl derived from a separate volatile phase

[d] observed mass of SO_2 and HCl emissions

Σr^2 = sum of squared residuals between calculated and observed SO_2 and HCl emissions. The lowest Σr^2 value implies the best match.

liberate ~14.8 Mt SO_2 and ~1.8 Mt HCl. These values closely match measured gas emissions for the 4-year 10-month time period under study.

Our results imply that the hypothesized 1 km^3 of silicate material degassed at an average rate of nearly 7 m^3 magma per second from March 1996 to December 2000. If we assume an average magma ascent velocity of 1 cm/sec, the ascending magma would occupy a cylinder with a 15 m radius to supply the calculated 7 m^3 magma per second. These magma ascent rates and conduit diameters are comparable to other andesitic and dacitic, dome-producing volcanoes (Swanson and Holcomb, 1990; Rutherford and Hill, 1993; Nakada and Motomura, 1999; Murphy et al., 2000).

Although circulation of magma in the volcanic conduit is easily imagined for low-viscosity basaltic systems such as Izu-Oshima (Kazahaya *et al.*, 1994), Etna (Allard, 1997), and Stromboli (Stevenson and Blake, 1998), the higher viscosities found in the andesitic to dacitic system of Popocatépetl might inhibit magma convection that is confined to the volcanic conduit. As a test of the feasibility of convection of the Popocatépetl magma we use a simple fluid dynamic model. The following equation is based on the theory of laminar flow in a vertical cylindrical conduit and experiments by Stevenson and Blake (1998):

$$Q = \pi\left(R^*\right)^2 Ps\left(g\,\Delta\rho\,R_c^4/\mu_d\right) \qquad (7)$$

where Q = rate of magma degassing (m^3/s), $R^* = R_a/R_c$ is the dimensionless ratio of the radius of the ascending flow of magma (R_a) to the radius of the conduit (R_c), Ps is the dimensionless Poiseuille number (Koyaguchi and Blake, 1989), g = 9.8 m/s^2, $\Delta\rho$ = the density difference between degassed and undegassed magma (kg/m^3), and μ_d = viscosity of the descending, degassed magma (Pa·s). We can rearrange Equation (7) to solve for conduit radius, R_c:

$$R_c = \sqrt[4]{\frac{Q\ \mu_d}{\pi\left(R^*\right)^2 Ps\,g\,\Delta\rho}} \qquad (8)$$

For the case of conduit circulation at Popocatépetl, we use Q = 7 m^3/s. Ps has a constant value of 0.064 and R^* has a value of 0.6 based on experiments (Stevenson

and Blake, 1998). For density and viscosity we use the same 65 wt.% dacite/35 wt.% basaltic andesite mixture with 25 vol.% crystals as above. This mixture has a melt with 67 wt.% SiO_2, T = 1000 °C, and 3 wt.% H_2O dissolved in the melt prior to degassing. We consider two cases: degassing of 2.0 wt.% H_2O with 1.0 wt.% H_2O remaining in the melt (equivalent to ~150 bar or ~600 m depth; Figure 13) and degassing of 2.9 wt.% H_2O with 0.1 wt.% H_2O remaining in the melt (equivalent to 1 bar or surface conditions). These two cases result in calculated density differences of 59 kg/m^3 and 92 kg/m^3, respectively, using the model of Lange (1994). This density difference does not include the dramatic density decrease due to bubble growth at low pressures. The viscosities of the undegassed and degassed magmas are estimated by taking the average viscosity calculated from the non-Arrhenian viscosity models for andesite melts (Richet *et al.*, 1996) and rhyolite melts (Hess and Dingwell, 1996) coupled with the Einstein-Roscoe equation (Lejeune and Richet, 1995) which accounts for the effect of crystals on the bulk viscosity. The effect of bubbles on viscosity is expected to be small (less than a 5-fold decrease; Stein and Spera, 2002) and is not included in the following calculations. The viscosity of undegassed magma is $10^{4.0}$ Pa·s. The viscosities of the descending magmas (μ_d) that have 1.0 wt.% H_2O and 0.1 wt.% H_2O remaining in the melt are $10^{5.3}$ and $10^{7.3}$ Pa·s, respectively. Utilizing Equation (8), calculated conduit radius (R_c) is 14 m for the 1.0 wt.% H_2O remaining case and 38 m for the 0.1 wt.% H_2O remaining case. These values for conduit radii are entirely plausible for Popocatépetl. For comparison, Kazahaya *et al.* (2002) calculated a conduit radius R_c of 25 m for the rhyolitic magma of Satsuma-Iwojima with a degassing rate Q = 10 m^3/s, $\Delta\rho$ = 50 kg/m^3, and $\mu_d = 10^{6.1}$ Pa·s. Based on the dimensionless ratio $R^* = R_a/R_c = 0.6$ (Stevenson and Blake, 1998) and magma flux of 7 m^3/s, the calculated values of R_c for Popocatépetl correspond to ascending cylinders of magma with radii (R_a) of 8 m and ascent rates of 3.2 cm/s for the 1.0 wt.% H_2O remaining case and 23 m and 0.4 cm/s for the 0.1 wt.% H_2O remaining case. These calculated values of R_a bracket the radius of the ascending cylinder of magma (15 m) that is predicted by assuming a magma ascent velocity of 1 cm/s.

The high temperature of the mixed magma (~950-1050 °C; see Chapter 1) enhances the potential for conduit circulation at Popocatépetl. An elevated magmatic temperature reduces magma viscosity and eases silicate-gas separation. The presence of a low-density, separate volatile phase could serve to initiate magma ascent and would enhance circulation by adding a potent buoyancy force. Circulation of magma in the volcanic conduit and degassing from both the silicate melt and a modest separate volatile phase is a plausible explanation to explain the observed gas emissions at Popocatépetl.

Conclusions

1) Degassing from erupted silicate melt in addition to sulfide breakdown in that same magma accounts for only 0.7 wt.% of the observed SO_2 emission, 0.6 wt.% of the observed HCl emission and none of the observed HF emission at Popocatépetl.
2) Although, assimilation of carbonate country rocks appears to be a plausible source for large excursions in CO_2 emission, evaporite assimilation as a source of S, Cl and F gases seems unlikely.
3) If the source of volatiles at Popocatépetl is a separate volatile phase formerly contained only in the erupted magma then the silicate/volatile mixture would consist of ~80 wt.% (or >95 vol.%) low-density volatile phase and ~20 wt.% silicate liquid plus crystals. This is implausible.
4) If there is no excess volatile phase at depth, then between 2 and 50 km^3 of magma must completely degas to account for the observed gas emissions.
5) Complete degassing of ~1 km^3 of magma with ~9 wt.% separate pre-existing volatile phase can account for the observed gas emissions.
6) Circulation of magma in the volcanic conduit may be an effective mechanism for non-explosive degassing of large quantities of volatiles (Kazahaya *et al.*, 1994). High magmatic temperatures deduced for Popocatépetl magma reduces viscosity

to enhance circulation. A separate volatile phase would provide more than enough buoyancy forces necessary to initiate and sustain conduit circulation.

7) We envision circulation of bubble-bearing magma from depths as deep as ~20 km up to a turnaround depth of <600 m (high in the volcanic conduit). About 7 m^3/s of magma would be 2/3 to completely degassed if a 8 – 23 m radius cylinder of magma rises ~0.4 – 3.2 cm/s. Dense, degassed magma sinks back down the conduit.

Chapter 3:

Volatile Degassing, Petrology, and Magma Dynamics of the Villarrica Lava Lake, Southern Chile

Introduction

Villarrica is a 2847 m high symmetrical volcanic cone located in the southern Andes of Chile (Figure 14). It is one of the three most active volcanoes in South America. Activity at Villarrica has been characterized in the past by frequent small eruptions (59 mild-to-moderately explosive, fire-fountaining, and/or lava effusion events since 1558) as well as highly explosive, caldera-forming pyroclastic eruptions involving up to 10 km^3 of basaltic andesite magma (Clavero and Moreno, 1994). Villarrica is notable that it has maintained an active lava lake in its summit crater for the past 17 years. During this period, Villarrica has continuously degassed from the lava lake but the eruption of magmatic material has been negligible.

The persistence of the lava lake perched in Villarrica's summit crater as well as the continuous emission of gases raises several important questions: 1) What is the immediate source of volatiles that supplies the continuous emission of volcanic gases? 2) What is the heat source that prevents the magma in the lava lake and volcanic conduit from solidifying? 3) What is the mechanism of gas and heat transport? 4) Is the persistent presence of the lava lake and continuous gas emission related to the lack of explosive and effusive eruptions at Villarrica over the last 17 years?

Since magmatic gases are continually emitted from Villarrica's lava lake but the liquid and solid portions of the magma are not erupted, then one of two scenarios must be occurring: either 1) gas bubbles rise through a static magma column in the volcanic conduit by buoyant ascent (non-homogeneous two-phase flow) or 2) magma ascends to the surface and degasses, but is not erupted. The unerupted, degassed

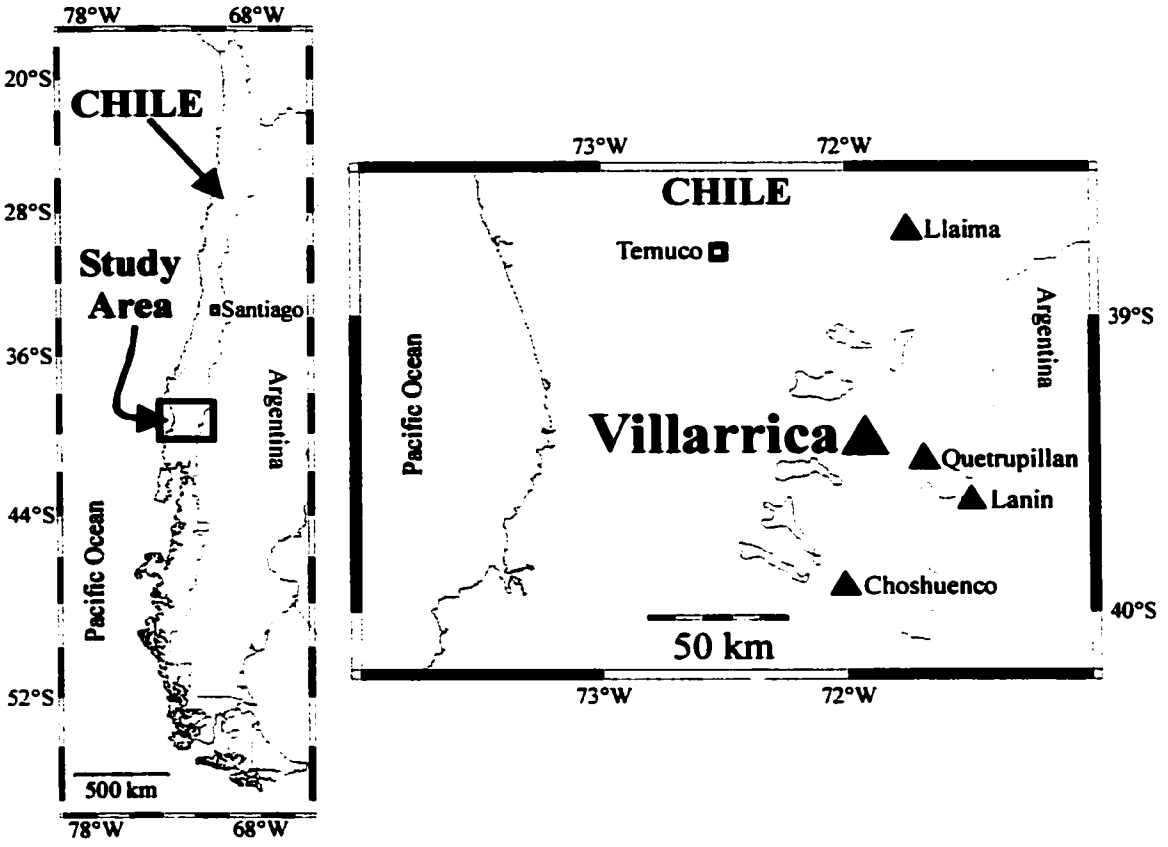

Figure 14. Location map for Chile and the study area. Holocene stratovolcanoes are denoted by *solid triangles* and labeled. The city of Temuco is shown with an *open square*. Map made with GMT (Wessel and Smith, 1991).

magma could either be intruded into the volcanic edifice or descend to deeper levels to allow additional gas-rich magma to ascend and degas.

This study has four goals: 1) quantify the present-day flux of acid gases (SO_2, HCl, and HF) at Villarrica, 2) define the pressure, temperature, composition and oxygen fugacity of Villarrica magma through thermodynamic modeling of major and volatile element compositions of the bulk rock, minerals, matrix glasses, and glass inclusions in phenocrysts in magmatic material obtained from Villarrica's summit lava lake, 3) use the collected chemical data to calculate physical parameters of Villarrica magma (e.g. density and viscosity) and, from them, estimate the potential magnitude and rates of magmatic degassing, 4) discuss mechanisms for passive degassing and heat transport. In this study we also present analyses of samples of magma ejected in 1999 and lava from the 1984-85 eruption for purposes of comparison with the 2000 magma. The data presented here serve as the foundation for a larger study aimed at understanding the fluid dynamics of passive degassing at restless volcanoes.

Geologic Setting

Villarrica is part of the N-S trending volcanic cordillera of the Andes, associated with east-dipping subduction of the Nazca plate beneath the South American plate. Villarrica lies at the NW end of the NW-SE trending, trans-Andean, Villarrica-Quetrupillán-Lanín volcanic chain which, itself, may represent a line of crustal weakness (Moreno et al., 1994b). The Villarrica volcanic edifice is constructed of pyroclastic flow and scoria fall deposits as well as aa and pahoehoe lavas. The symmetrical, modern cone is located on the NW rim of a glaciated 6.5 x 4.2 km caldera (Moreno, 1994). Post-glacial eruptive activity at Villarrica is characterized by both explosive and effusive activity. At least 14 explosive eruptions have generated pyroclastic flows at Villarrica in post-glacial time including the ~10 km^3 basaltic andesite Licán Ignimbrite (~14,000 BP) and the ~5 km^3 basaltic andesite Pucón Ignimbrite (~3500 BP) both of which formed calderas (Clavero and Moreno,

1994; Moreno et al., 1994a). The most recent pyroclastic flow eruption at Villarrica occurred ~1620 BP (Moreno et al., 1994a).

Fifty-nine eruptions since 1558 make Villarrica one of the most active volcanoes in South America (Petit-Breuilh, 1994; Simkin and Siebert, 1994). Historic eruptions have ranged from effusive, lava-producing eruptions to mildly explosive eruptions (up to VEI 3). Three eruptions, in 1948-49, 1963-64, and 1971-72 resulted in fatalities due to lahar inundation. In the most recent eruption (VEI 2), from October 1984 to January 1985, a small scoria cone formed in the summit crater and ~10^6 m^3 of lava poured from the summit crater, burrowed through glaciers on the volcano's flanks, and generated lahars in downstream valleys (Fuentealba, 1984; Simkin and Siebert, 1994).

Activity since the 1984-85 eruption has consisted of continuous, passive degassing from a persistent summit lava lake without effusion of lava (e.g. GVN, 1992; GVN, 1995; GVN, 1999). The surface of the lava lake has been observed to rise and fall by several tens of meters over a period of weeks to months. A descending lava lake surface is often accompanied by break-up and foundering of the lava lake crust on the crater floor. Lava spattering and emission of fine-grained tephra that accompanies gas emission is generally confined to the summit crater. Although Villarrica's summit crater has a diameter of ~150 m, the aperture in the crater floor that leads to the surface of the lava lake, has a diameter of only ~2 to 30 m, based on measurements made in 2000-2001 using a laser rangefinder and inclinometer.

Previous Work

Prior studies of Villarrica have focused on reconstructing the eruptive history of the volcano through analysis of historical records (Petit-Breuilh, 1994), mapping of volcanic deposits (Clavero and Moreno, 1994; Moreno et al., 1994a; Clavero-Ribes, 1996) and the geochemistry of Villarrica lavas and nearby scoria cones (Lopez-Escobar et al., 1977; Hickey-Vargas et al., 1989; Tormey et al., 1991; Hickey-Vargas et al., 2002; Sigmarsson et al., 2002).

Analytical Methods

Correlation Spectrometry (COSPEC)

Sulfur dioxide emission rates were measured using a correlation spectrometer (COSPEC; Stoiber and Jepsen, 1973; Stoiber et al., 1983). The COSPEC contains an ultraviolet spectrometer which measures the concentration-path length of SO_2 (in units of ppm·m) in a vertical column of atmosphere above the instrument's upwardly-pointing telescope. The COSPEC is driven or flown beneath, and roughly perpendicular to, the downwind direction of the gas plume. The concentration-path length of SO_2 is integrated across the width of the gas plume, and multiplied by the wind velocity and a conversion factor to put the gas flux in units of tons/day SO_2. A trigonometric correction is made for portions of the transect that are not perpendicular to the gas plume.

The largest source of error in COSPEC measurements is in estimating wind velocity. We used three methods to estimate wind velocity. 1) The same day that ground-based COSPEC measurements were made, we measured wind velocity at the summit of Villarrica using a hand-held anemometer. These measurements may slightly overestimate wind velocity due to the orographic effect of the volcano. 2) During airborne COSPEC traverses, wind data were obtained from in-flight GPS as well as by differencing the upwind and downwind groundspeed and dividing by two. This method had the advantage of being a direct measurement of wind velocity at the same altitude as the gas plume. The air-based estimates of wind velocity are more accurate than the hand-held anemometer measurements but could only be made during airborne COSPEC measurements. 3) We supplemented our wind velocity measurements with winds aloft forecasts for 9000 feet elevation obtained from the meteorological division of the Temuco airport. Air- and ground-based wind velocity measurements and winds aloft data were generally in agreement. Errors in the SO_2 emission rate associated with COSPEC data collection and reduction are estimated to be ~20% relative.

In the year 2000, COSPEC measurements were made between January 29 and April 1. We performed a total of forty-six COSPEC traverses of the gas plume over the course of 11 days during the study period using both airborne (17 traverses) and ground-based (29 traverses) methods. There is no systematic difference in the results obtained from airborne and ground-based methods. In the year 2001, COSPEC measurements were made between January 15 and February 2. We made twenty-five COSPEC traverses of the gas plume over the course of 4 days during the study period using only ground-based methods. Unfortunately, more COSPEC traverses were not possible in 2001 due to mechanical breakdown of the instrument.

Diffuse Degassing of CO_2

We measured CO_2 gas flux through soil to test for diffuse degassing on the flanks of Villarrica using an instrument manufactured by West Systems of Pisa, Italy on loan from J. Rogie (USGS, Menlo Park). The instrument consists of an accumulation chamber connected through a pump and tubing to a Dräger infrared gas analyzer. The instrument measures CO_2 flux in units of ppm/s which is then multiplied by the molecular weight of CO_2 and corrected for ambient pressure and temperature conditions (assuming ideal gas behavior). Accounting for the volume and footprint (area) of the accumulation chamber, the CO_2 flux is converted to units of $g/m^2/day$. Prior to CO_2 flux measurements, we calibrated our instrument using a 1% CO_2 gas mixture supplied by Scott Specialty gases. Details of this technique are outlined in Evans et al. (2001b).

Volatile Traps

One method we used to measure the relative concentrations of acid gas species (S, Cl, and F) emitted from Villarrica is the method of volatile traps (Noguchi and Kamiya, 1963; Goff et al., 1998). This method involves the absorption of soluble volcanic gases into a highly alkaline solution placed near an actively degassing vent. Relative concentrations of SO_4, Cl, and F were obtained by ion chromatography in

the Dept. of Atmospheric Sciences, University of Washington (S. Gao, analyst) and Dept. des sciences du sol, Universite Catholique de Louvain (P. Delmelle, analyst). Prior to ion chromatographic analysis, all volatile trap solutions were filtered with a Spartan-RC 0.2 μm cellulose filter from Schleicher & Schuell.

In the year 2000, four to six volatile traps were deployed within a few tens of meters of the actively degassing summit crater of Villarrica. Our volatile traps consisted of 200 mL of 6N KOH solution in a plastic beaker covered by a perforated protective plastic bucket. The traps were deployed on four separate occasions for periods ranging from 9 to 22 days. In 2001, four volatile traps were deployed at the active crater on three occasions for periods ranging from 8 to 13 days. Rain and snowstorms, high winds, and extended periods of sunshine likely contributed to addition of meteoric water to the traps, addition of small amounts of fine-grained ash to the traps, and evaporation of solution from the traps, respectively. Occasionally we found dead insects in the alkaline solutions as well. We have no evidence to suggest that these influences significantly altered the ratios of the acid gas species absorbed into the volatile traps.

Filter Packs

To supplement our data obtained from the volatile traps, we also used filter packs in 2001 to measure the relative concentrations of acid gases (S, Cl, and F) in Villarrica's gas plume. The filter pack method we employed (developed by P. Delmelle, Dept. des sciences du sol, Universite Catholique de Louvain) collects trace gases in the atmosphere using impregnated filters. It is analogous to gas filtration methods used at Masaya (Stoiber et al., 1986), Erebus (Zreda-Gostynska et al., 1993), and Etna (Pennisi and LeCloarec, 1998). We collected samples of gases using filter packs while standing in Villarrica's gas plume on the rim of the actively degassing summit crater. The filter pack instrument consists of a small vacuum pump which sucks the ambient gases (a mixture of atmospheric air and volcanic gases) through a series of three paper filters (Whatman 2.2 cm diameter ashless Grade 42 filters) each

impregnated with a saturated sodium bicarbonate solution. The gases are pre-filtered with a 10 μm Teflon mesh to minimize intake of airborne ash particles. Total filtration time varied from 3 to 46½ minutes. Filtration time was chosen so that nearly all of the acid gases were absorbed by the first two filters in the filter stack. Relative concentrations of the acid gas species (SO_4, Cl, and F) absorbed onto the filter paper were obtained by ion chromatography at Dept. des sciences du sol, Universite Catholique de Louvain (P. Delmelle, analyst). Twenty-three gas measurements were made using filter packs over the course of eight summit days.

Whole Rock Analyses

Major and trace element compositions of the following were analyzed by X-Ray Fluorescence at the WSU Geoanalytical Laboratory: two samples of reticulite pumice ejected onto the crater rim in the year 2000, two samples of metallic scoria ejected onto the crater rim in 1999, and one sample of pahoehoe lava erupted in 1984.

Electron Probe Micro-Analysis (EPMA)

Year 2000 reticulite pumice was lightly crushed; the light and heavy ash fractions were separated using LST heavy liquids from Geoliquids. Plagioclase and olivine mineral separates with glass adhering to the minerals were hand-picked, mounted in epoxy and then polished for EPMA analysis. Thin sections of 1999 metallic scoria and 1984 lava were also prepared for EPMA analysis.

All EPMA analyses were conducted on a 4-spectrometer JEOL 733 Superprobe at the University of Washington. Mineral analyses were conducted at 15 kV accelerating voltage, ~1-3 μm beam diameter, and 10-25 nA beam current with a maximum count time of 40 seconds for each element. Elements were calibrated using mineral standards, which were also analyzed at the end of each analytical session to check for instrumental drift. Matrix effects were corrected using the ZAF model of Armstrong (1984).

Major element glass analyses were performed at 15 kV accelerating voltage and 10 nA with a 5 μm beam diameter and maximum count time of 40 seconds for Si, Al, Na, Ca, Fe, and Mg; 60 seconds for K, P, and Ti; and 80 seconds for Cr and Mn. Before and after each analytical session, accuracy was checked on glass standards VG-2 and A-99 (basalts). The combination of analyzing sodium first and a defocused beam minimized Na-loss during analysis. Plots of intensity vs. time suggest Na-loss of <0.2 wt. % Na_2O over a 40-second count time using an anhydrous glass standard. Na-loss during analysis of glass inclusions, however, may be significant due to enhanced Na-mobility in hydrous glasses (Devine et al., 1995). No correction was applied for this potential alkali-loss in hydrous inclusions. Matrix effects were corrected using the ZAF model of Armstrong (1984). Mean standard errors as well as errors based on counting statistics for the major element mineral and glass analyses are shown in Tables 22 & 23.

Volatile elements S, Cl, and F were analyzed in glasses using an improved analytical method originally developed by T. Thordarson at the University of Hawaii (Thordarson et al., 1996). With this method, we achieved very low minimum detection limits while maintaining high analytical precision and accuracy. Analytical conditions were 10 kV accelerating voltage, 180 nA beam current, 5 μm beam diameter, and 400 second total peak count time. To minimize volatile loss, an iterative scheme was employed in which the beam was blanked every ten seconds for a period of ten seconds to allow the sample to cool. We conducted a test of volatile mobility under the electron beam and found X-ray count rates for S, Cl, and F remain stable during the entire period of analysis. Sulfur and chlorine were analyzed using PET diffraction crystals with the spectrometer aperture window set at its widest setting to maximize the number of X-ray counts. Fluorine was analyzed using an LDE1 diffraction crystal. Fluorine analysis proved challenging due to peak overlap problems with the Fe $K\alpha$ line. We created an empirical correction factor for F by analyzing several F-free standards of varying Fe content. We calculated the amount of interference with the F-analysis as a function of Fe and incorporated this correction

Table 22. Mean error associated with analysis of mineral and glass standards (in wt.%)

	Olivine 197			Ilm 128			52NL11 Cr-spinel*		
	This study[a]	1σ [b]	Accepted[c]	This study[a]	1σ [b]	Accepted[c]	This study[a]	1σ [b]	Accepted[c]
SiO_2	38.90	0.08	38.50	0.01	0.01	0.00	0.03	0.00	n/a
TiO_2	n/a	n/a	n/a	50.60	1.00	49.59	0.42	0.02	0.45
Al_2O_3	n/a	n/a	n/a	0.05	0.01	0.06	19.45	0.37	19.40
Cr_2O_3	n/a	n/a	n/a	0.01	0.01	0.00	47.21	0.59	44.55
FeO^T	18.72	0.06	18.90	46.61	0.73	47.43	21.27	0.22	22.12
MnO	0.26	0.01	0.26	1.01	0.08	0.85	0.32	0.03	0.33
NiO	0.15	0.02	0.15	0.03	0.04	0.00	0.11	0.02	0.07
ZnO	n/a	n/a	n/a	0.03	0.03	0.00	0.06	0.02	n/a
MgO	41.63	0.37	41.65	1.26	0.12	1.09	12.10	0.05	12.20
CaO	0.18	0.01	0.18	0.00	0.00	0.00	0.01	0.01	n/a
Total	99.84	0.21	99.64	99.60	0.48	99.02	100.97	0.56	99.12
n	3			2			3		

Table 22. continued

	Anorthoclase 2110F			VG-2 Glass			A-99 Glass		
	This study[a]	1σ [b]	Accepted[c]	This study[a]	1σ [b]	Accepted[c]	This study[a]	1σ [b]	Accepted[c]
SiO_2	64.58	0.14	64.38	50.78**	0.36	50.81	50.77	0.19	50.94
TiO_2	n/a	n/a	n/a	1.89	0.11	1.85	3.91	0.19	4.06
Al_2O_3	20.47	0.18	20.96	14.08**	0.09	14.06	12.51	0.14	12.49
Cr_2O_3	n/a	n/a	n/a	0.02	0.01	0.00	0.01	0.01	0.00
FeO^T	0.20	0.03	0.16	11.67**	0.22	11.84	13.08	0.08	13.30
MnO	n/a	n/a	n/a	0.20	0.02	0.22	0.20	0.01	0.15
MgO	0.00	0.00	0.00	6.90	0.04	6.71	4.97	0.08	5.08
CaO	1.16	0.04	1.20	11.13	0.10	11.12	9.31	0.10	9.30
Na_2O	8.64	0.08	8.58	2.67	0.03	2.62	2.52	0.24	2.66
K_2O	3.10	0.10	3.30	0.19	0.01	0.19	0.83	0.02	0.82
P_2O_5	n/a	n/a	n/a	0.27	0.02	0.20	0.47	0.02	0.38
Total	98.16	0.29	98.58	99.81	0.35	99.62	98.57	0.37	99.18
n	6			5			7		

[a] EPMA analysis from this study

[b] One-sigma standard deviation of the analyses

[c] Value accepted in the literature

* 52NL11 inhomogeneous in Cr

** Si, Al, and Fe were calibrated on VG-2 glass therefore the values test precision and not accuracy

n = number of analyses, n/a = not analyzed

FeO^T = all Fe as FeO

Table 23. Average relative errors based on counting statistics for analyses of minerals and glasses

	Cr-sp	Ol	Plag	Glass
Si	13.0%	0.3%	0.5%	0.5%
Ti	1.1%	n/a	n/a	5.0%
Al	0.6%	n/a	0.6%	0.7%
Cr	0.5%	n/a	n/a	57.9%
Fe	0.6%	0.8%	4.8%	1.3%
Mn	9.6%	3.5%	n/a	11.2%
Ni	42.7%	14.6%	n/a	n/a
Zn	86.1%	n/a	n/a	n/a
Mg	0.8%	0.3%	5.5%	1.0%
Ca	22.5%	3.7%	0.9%	1.1%
Na	n/a	n/a	1.5%	1.8%
K	n/a	n/a	11.9%	3.2%
P	n/a	n/a	n/a	4.9%

Cr-sp = chromian spinel, Ol = olivine,
Plag = plagioclase, n/a = not analyzed

into the iterative analytical routine (see Appendix A). Since the volatile elements were analyzed in a separate analytical session, we reprocessed the volatile data with major element glass data to correct for matrix effects using the ZAF model of Armstrong (1984). Prior to each analytical session, volatile elements were calibrated on the following standards: Troilite (sulfur), Scapolite 17120 (chlorine), and Synthetic F-phlogopite (fluorine). Analytical accuracy was checked using NIST soda-lime glasses SRM 610, 620 & 621 as well as basaltic glass A-99. Minimum detection limits are calculated to be ~25 ppm for sulfur, ~16 ppm for chlorine, and ~35 ppm for fluorine. Average relative errors (2σ) based on counting statistics are 3.5% at ~1000 ppm and 22% at ~120 ppm for sulfur, 5% at ~400 ppm for chlorine, and 13% at ~300 ppm for fluorine (Table 24). Reproducibility of S and Cl analyses was also tested on the SRM 621. The 1σ variations for 10 analyses are 2% at 500 ppm for sulfur and 7% at 160 ppm for chlorine (Table 24).

Secondary Ion Mass Spectrometry analysis (SIMS)

A separate set of one-inch round thin sections of the 1984 lava and an olivine mineral separate from the 2000 reticulite were made with Araldite epoxy for SIMS analysis. H_2O, CO_2, S, Cl, and F in glass inclusions were analyzed using secondary ion mass spectrometry (SIMS) at the Department of Terrestrial Magnetism, Carnegie Institution, Washington, D.C. The analytical methods for this technique are described in Hauri et al. (2002).

Results

Volatile Flux

COSPEC

In the year 2000, COSPEC measurements yielded an average ($\pm1\sigma$) SO_2 flux of 260±170 tons/day SO_2. In 2001, COSPEC measurements yielded an average ($\pm1\sigma$) SO_2 flux of 460±260 tons/day SO_2 (Table 25). This is greater than, but within the 1σ variation of SO_2 flux measured in 2000. Considering the ~20% relative error inherent

Table 24. EPMA analyses of S, Cl, and F in various standard glasses from this study compared with data from the literature

	A-99					
Reference:	this study	de Hoog EPMA	D & G EPMA	Th (CSIRO) EPMA	Th (Cam) EPMA	Dixon EPMA
S conc.	**120(7)**	**132(32)**	**153(3)**	**220(29)**	**135(62)**	**170(80)**
S err (2σ)	26	n.r.	26	n.r.	n.r.	n.r.
n	2	15	10	139	134	19
S MDL	23	45	30	n.r.	n.r.	n.r.
Cl conc.	**250(13)**	**238(91)**	**218(7)**	**227(19)**	**229(52)**	n.r.
Cl err (2σ)	19	n.r.	24	n.r.	n.r.	n.r.
n	2	15	10	139	134	n.r.
Cl MDL	17	70	30	n.r.	n.r.	n.r.
F conc.	**976(4)**	n.r.	**745(11)**	**765(72)**	n.r.	n.r.
F err (2σ)	45	n.r.	40	n.r.	n.r.	n.r.
n	2	n.r.	10	139	n.r.	n.r.
F MDL	36	n.r.	80	n.r.	n.r.	n.r.

	SRM 620						
Reference:	this study	Saito EPMA	Saito W.C.	P & S EPMA	Devine EPMA	Devine LECO	NIST
S conc.	**1178(28)**	**1080(80)**	**1160**	**1154(67)**	**1124(38)**	**1155**	**1121(80)**
S err (2σ)	36	n.r.	n.r.	n.r.	n.r.	n.r.	n.r.
n	4	n.r.	n.r.	15	17	2	n.r.
S MDL	22	n.r.	n.r.	50	~50	n.r.	n.r.
Cl conc.	**199(5)**	**180(20)**	**170**	n.r.	n.r.	n.r.	n.r.
Cl err (2σ)	19	n.r.	n.r.	n.r.	n.r.	n.r.	n.r.
n	4	n.r.	n.r.	n.r.	n.r.	n.r.	n.r.
Cl MDL	16	n.r.	n.r.	n.r.	n.r.	n.r.	n.r.
F conc.	**0(0)**	n.r.	n.r.	n.r.	n.r.	n.r.	n.r.
F err (2σ)	n.r.	n.r.	n.r.	n.r.	n.r.	n.r.	n.r.
n	4	n.r.	n.r.	n.r.	n.r.	n.r.	n.r.
F MDL	30	n.r.	n.r.	n.r.	n.r.	n.r.	n.r.

Table 24. continued

	SRM 621			
Reference:	this study	Saito EPMA	Saito W.C.	NIST
S conc.	**520(11)**	**460(20)**	**450**	**521(80)**
S err (2σ)	30	n.r.	n.r.	n.r.
n	10	n.r.	n.r.	n.r.
S MDL	22	n.r.	n.r.	n.r.
Cl conc.	**159(11)**	**160(20)**	**140**	n.r.
Cl err (2σ)	16	n.r.	n.r.	n.r.
n	10	n.r.	n.r.	n.r.
Cl MDL	16	n.r.	n.r.	n.r.
F conc.	**13(12)**	n.r.	n.r.	n.r.
F err (2σ)	26	n.r.	n.r.	n.r.
n	10	n.r.	n.r.	n.r.
F MDL	30	n.r.	n.r.	n.r.

	SRM 610							
Reference:	this study	de Hoog EPMA	Saito EPMA	Saito W.C.	Rocholl LIMS	Pearce EPMA	Hoskin SIMS	Devine EPMA
S conc.	**563(32)**	**403(44)**	**530(30)**	**510**	**456(27)**	n.r.	n.r.	**514(35)**
S err (2σ)	31	n.r.	n.r.	n.r.	n.r.	n.r.	n.r.	n.r.
n	2	6	n.r.	n.r.	n.r.	n.r.	n.r.	36
S MDL	23	45	n.r.	n.r.	n.r.	n.r.	n.r.	~50
Cl conc.	**401(2)**	**416(45)**	**390(20)**	**300**	n.r.	**470(160)**	n.r.	n.r.
Cl err (2σ)	20	n.r.	n.r.	n.r.	n.r.	n.r.	n.r.	n.r.
n	2	6	n.r.	n.r.	n.r.	20	n.r.	n.r.
Cl MDL	16	70	n.r.	n.r.	n.r.	n.r.	n.r.	n.r.
F conc.	**336(12)**	n.r.	n.r.	n.r.	n.r.	n.r.	**295(16)**	n.r.
F err (2σ)	42	n.r.	n.r.	n.r.	n.r.	n.r.	n.r.	n.r.
n	2	n.r.	n.r.	n.r.	n.r.	n.r.	49	n.r.
F MDL	31	n.r.	n.r.	n.r.	n.r.	n.r.	~1	n.r.

Table 24. continued

SRM 610 continued
P & S EPMA
565(55)
n.r.
231
50
n.r.
n.r.
n.r.
n.r.
n.r.
n.r.
n.r.
n.r.
n.r.

Analytical conditions for EPMA analyses in this study are: 10 kV accelerating voltage, 180 nA beam current, 5 micron beam diameter, 400 second total peak count time done in forty 10 second intervals with the beam blanked for ~10 seconds between each interval to allow the sample to cool. Total background count time is 400 seconds.
Calibration standards: Troilite (S), Scapolite 17120 (Cl), Synthetic F-phlogopite (F)
All data reported in ppm; Standard deviation (1-sigma) shown in parentheses; n.r. = not reported; n = number of analyses
conc. = concentration; MDL = minimum detection limit; err = error based on counting statistics (2-sigma)
D & G EPMA = EPMA analysis by M. Davis and M. Garcia, unpubl. data, University of Hawaii, 2000.
Th (CSIRO) EPMA = Thordarson et al. (1996) CSIRO trace routine EPMA analysis
Th (Cam) EPMA = Thordarson et al. (1996) Cameca trace routine EPMA analysis
Dixon EPMA = Dixon (1991) EPMA analysis
Saito EPMA = Saito et al. (2001) EPMA analysis
Saito W.C. = Saito et al. (2001) wet chemistry analysis
Devine EPMA = Devine et al. (1984) EPMA analysis
Devine LECO = Devine et al. (1984) average of two LECO analyses
P & S EPMA = Palais and Sigurdsson (1989) EPMA analysis
de Hoog EPMA = de Hoog et al. (2001) EPMA analysis
Rocholl LIMS = Rocholl et al. (1997) Laser plasma ionization mass spectrometry
Pearce EPMA = Pearce et al. (1997) EPMA analysis
Hoskin SIMS = Hoskin (1999) SIMS analysis
NIST = National Institute of Standards certified value

Table 25. Summary of results of COSPEC measurements at Villarrica Volcano in 2000 and 2001

Air COSPEC	SO_2 flux (tons/day)
February 5, 2000	
Villa 1 - Pass#3	297
Villa 1 - Pass#4	352
Villa 1 - Pass#5	255
Villa 1 - Pass#6	203
Villa 1 - Pass#7	129
Villa 2 - Pass#1	136
Villa 2 - Pass#2	211
Villa 2 - Pass#3	95
Villa 2 - Pass#4	216
Villa 2 - Pass#5	200
Villa 2 - Pass#6	206
Average	**209**
February 14, 2000	
Pass#1	162
Pass#3	126
Pass#4	138
Pass#5	142
Pass#6	142
Pass#7	195
Average	**151**

Auto COSPEC	SO_2 flux (tons/day)
January 29, 2000	
Traverse#1	**178**
January 30, 2000	
Traverse#1	379
Traverse#2	327
Average	**353**
February 2, 2000	
Traverse#1	203
Traverse#2	338
Traverse#3	276
Traverse#4	206
Traverse#5	310
Traverse#6	308
Average	**274**
February 7, 2000	
Traverse#1	**121**
February 13, 2000	
Traverse#1	177
Traverse#2	231
Average	**204**

Auto COSPEC	SO_2 flux (tons/day)
March 3, 2000	
Traverse#1	150
Traverse#2	142
Traverse#3	127
Traverse#4	161
Traverse#5	163
Average	**149**
March 7, 2000	
Traverse#1	**174**
March 18, 2000	
Traverse#1	267
Traverse#2	241
Traverse#3	614
Average	**374**
March 21, 2000	
Traverse#1	490
Traverse#2	1064
Traverse#3	714
Traverse#4	766
Traverse#5	1115
Traverse#6	475
Traverse#7	429
Traverse#8	502
Average	**694**

Ave. Air COSPEC in 2000	**180**
Std. Dev. (1σ)	41
Ave. Auto COSPEC in 2000	**280**
Std. Dev. (1σ)	179
Ave. all COSPEC in 2000	**262**
Std. Dev. (1σ)	166

Table 25. continued

Auto COSPEC	SO_2 flux (tons/day)
January 15, 2001	
Traverse#1	96
Traverse#2	142
Traverse#3	176
Traverse#4	87
Traverse#5	107
Traverse#8	101
Average	**118**
January 25, 2001	
Traverse#1	264
Traverse#2	257
Traverse#3	358
Traverse#4	472
Traverse#5	336
Traverse#6	961
Average	**441**

Auto COSPEC	SO_2 flux (tons/day)
January 28, 2001	
Traverse#1	653
Traverse#2	705
Traverse#3	664
Traverse#4	441
Traverse#6	324
Traverse#7	595
Average	**564**
February 2, 2001	
Traverse#1	939
Traverse#2	924
Traverse#3	724
Traverse#4	592
Traverse#5	565
Traverse#6	710
Traverse#7	669
Average	**732**

Ave. all COSPEC in 2001	**464**
Std. Dev. (1σ)	259

to the COSPEC method, the daily to weekly variations in SO_2 flux measured at Villarrica during 2000 and 2001 are real. Variations of this magnitude, however, are not unusual for a volcano of this type.

Volatile Traps and Filter Packs

In 2000, measurements of acid gas species emitted from the summit crater using volatile traps yielded an average SO_2/HCl ratio of 9.3±2.6 and HCl/HF ratio of 3.0±0.4. In 2001, volatile traps yielded an average SO_2/HCl ratio of 5.9±1.2 and HCl/HF ratio of 4.1±0.7 (Table 26). Measurements of the acid gas species with filter packs in 2001 yielded an average SO_2/HCl ratio of 4.5±0.7 and HCl/HF ratio of 7.8±1.6 (Table 27).

The volatile trap method is based on the assumption that the proportions of acid species absorbed into the alkaline solution are the same as those in the volcanic gas. Simultaneous collection of gas data using volatile traps and filter packs allows for a comparison of the two methods and an evaluation of this assumption. Filter packs yielded lower average SO_2/HCl ratios but higher average HCl/HF and SO_2/HF ratios. These results imply that the KOH solution in the volatile traps does not absorb S-gases and Cl as readily as it does F.

As a result of the uncertainty in the relative rates of absorption of acid gases in the volatile traps, we prefer data obtained from filter packs. Using gas ratios from filter pack measurements and the absolute flux of SO_2 from COSPEC measurements, we calculate average HCl and HF fluxes from Villarrica's summit crater of 102±42 tons/day and 13±3 tons/day, respectively for 2001.

HCl and HF emission rates for Villarrica can be compared with halogen emission rates measured at other volcanoes. Based on COSPEC and fumarole measurements, Stromboli emits 60-130 tons/day HCl and 2-4 tons/day HF (Allard et al., 1994). Francis et al. (1998) report emissions of 700 tons/day HCl and 190 tons/day HF from Etna based on solar occultation Fourier Transform infrared spectroscopy data. Recent FTIR measurements by Burton et al. (2000) for Masaya volcano give emission rates of 600-675 tons/day HCl and 75-80 tons/day HF.

Table 26. Volatile trap data for S, Cl, and F collected in 2000 and 2001 at Villarrica volcano
All traps start with 200 mL KOH solution, n.r. = not reported

Year 2000 Volatile Trap Solutions
Analyzed at the University of Washington Atmospheric Sciences Ion Chromatography Lab, analyst S. Gao

	RAW DATA MINUS BLANK									Vol. of solution	Vol. of solution	Sediment
	F	Cl	SO_3	SO_4	ΣSO_4	GAS RATIOS		H_2O	Days	in trap	recovered	in trap
Sample	(ppm)	(ppm)	(ppm)	(ppm)	(ppm)	SO_2/HCl	HCl/HF	batch	deployed	(mL)	(mL)	(mm)
Villa#1	707	815	5473	3089	9657	7.7	1.1	#1	17	600	250	5-7
Villa#3	80	162	1832	1033	3231	12.9	2.0	#1	17	450	250	1
Villa#4	250	368	3542	1661	5911	10.4	1.4	#1	17	400	250	2
Villa#5	758	711	1546	5534	7389	6.7	0.9	#1	17	1100	250	2-3
Villa#6	841	2091	19507	3178	26586	8.2	2.4	#1	17	250	150	7
Villa#7	234	829	6645	980	8954	7.0	3.5	#1	10	200	150	0.5
Villa#8	275	661	5146	1103	7278	7.1	2.3	#1	10	200	100	1
Villa#9	219	822	6517	1008	8828	7.0	3.7	#1	10	200	125	2
Villa#10	159	401	2391	1118	3987	6.4	2.5	#1	10	300	200	trace
Villa#12	21	92	511	561	1174	8.3	4.3	#1	10	350	200	1
Villa#14	174	520	3883	1406	6066	7.6	2.9	#2	9	350	200	trace
Villa#16	204	960	7432	993	9911	6.7	4.6	#2	9	180	150	trace
Villa#17	134	817	6504	780	8585	6.8	6.0	#2	9	175	125	0.25
Villa#18	98	388	2988	794	4380	7.3	3.9	#2	9	225	175	1
Villa#19	1147	2053	20691	5234	30063	9.5	1.7	#3	22	n.r.	125	n.r.
Villa#20	768	1537	12482	4429	19407	8.2	2.0	#3	22	n.r.	200	n.r.
Villa#21	563	657	4219	3372	8435	8.3	1.1	#3	22	n.r.	200	n.r.
Villa#22	450	718	318	1877	2259	2.0	1.6	#3	22	n.r.	200	n.r.
Villa#23	263	638	1424	2239	3948	4.0	2.4	#3	22	n.r.	200	n.r.
					Average	**7.5**	**2.6**					
					Std. Dev. (1σ)	2.2	1.4					

Table 26. continued

Splits of selected year 2000 trap solutions were re-analyzed by ion chromatography at the Dept. of Environmental Sciences and Land Use Planning, Soil Sciences Unit, Universite Catholique de Louvain, analyst P. Delmelle

	RAW DATA MINUS BLANK								
	F	Cl	SO_3	SO_4	ΣSO_4	GAS RATIOS		GAS RATIOS*	
Sample	(ppm)	(ppm)	(ppm)	(ppm)	(ppm)	SO_2/HCl	HCl/HF	SO_2/HCl	HCl/HF
Villa#3	147	231	2491	1384	4373	12.3	1.5	12.9 +/- 0.5	3.0 +/- 0.2
Villa#8	351	1062	7987	1796	11380	6.9	3.0	6.9 +/- 0.2	2.7 +/- 0.2
Villa#19	3030	6969	69204	24456	107501	10.0	2.2	9.1 +/- 0.1	2.7 +/- 0.1
Villa#20	865	1364	10445	4563	17097	8.1	1.5	8.2 +/- 0.2	3.6 +/- 0.3
					Average	9.3	2.1	9.3	3.0
					Std. Dev. (1σ)	2.3	0.7	2.6	0.4

* Results from multiple analyses (up to six) of the same sample using various dilutions and dealing with the matrix effects. These values are preferred.

Sample	Comments
Villa#1	Dead Bug found in solution
Villa#3	Dead Bug found in solution
Villa#6	White acicular crystals on inner wall of beaker. Yellow crystals (sulfur?) on upper part of inner wall of beaker.
Villa#7	Outside of bucket half buried in snow. Yellow precipitate on inner wall of beaker
Villa#8	Small amount of snow inside bucket. Rime ice on N side outside bucket
Villa#9	Outside of bucket half buried in snow. Dead bug found in solution. Yellow and white platy precipitates in bottom of beaker.
Villa#10	10 cm of snow accumulated inside and outside of bucket
Villa#12	Inside and outside of bucket half buried in snow
Villa#14	Green protective bucket had blown away. Endured crater floor collapse (i.e. ash emission), lightning storm, hail, and rain.
Villa#16	Endured crater floor collapse (i.e. ash emission), lightning storm, hail, and rain.
Villa#17	Endured crater floor collapse, lightning storm, hail, and rain. Patchy yellow and white crystals on outside of beaker
Villa#18	Endured crater floor collapse, lightning storm, hail, and rain.

Table 26. continued

Year 2001 Volatile Trap Solutions

Analyzed by ion chromatography at the Dept. of Environmental Sciences and Land Use Planning, Soil Sciences Unit, Universite Catholique de Louvain, analyst P. Delmelle

	RAW DATA MINUS BLANK							Vol. of solution	Vol. of solution	Sediment
	F	Cl	ΣSO_4	GAS RATIOS		H_2O	Days	in trap	recovered	in trap
Sample	(ppm)	(ppm)	(ppm)	SO_2/HCl	HCl/HF	batch	deployed	(mL)	(mL)	(mm)
Villa#53	39.9	195.4	1715.2	5.7	4.8	#5	14	160	155	trace
Villa#55	88.6	370.6	3499.9	6.1	4.1	#5	8	150	137	trace
Villa#56	92.4	402.5	4070.4	6.6	4.3	#5	8	125	120	trace
Villa#57	22.6	119.2	1221.5	6.6	5.1	#5	8	170	167	trace
Villa#58	158.2	533.7	6474.6	7.9	3.3	#6	11	250	180	1
Villa#59	125.5	384.9	4335.6	7.3	3.0	#6	11	150	120	1
Villa#60	27.3	91.1	889.3	6.3	3.3	#6	11	325	240	<1
Villa#62	173.5	805.8	5552.1	4.5	4.5	#7	13	125	93	2
Villa#63	280.7	1152.2	6990.6	3.9	4.0	#7	13	100	85	2
Villa#64	40.2	186.2	1373.7	4.8	4.5	#7	13	175	156	1
Villa#65	26.8	116.7	945.6	5.3	4.3	#7	13	240	187	trace
			Average	**5.9**	**4.1**					
			Std. Dev. (1σ)	**1.2**	**0.7**					

Table 26. continued

Sample	Comments
Villa#53	Spotty white precipitate on inside of beaker. Traps #50, 51, 52, and 54 destroyed in storm.
Villa#55	Spotty yellow precipitate on inside of beaker
Villa#56	Spotty yellow precipitate on inside of beaker
Villa#57	Starting volume of solution was 170 mL because 30 mL were set aside as blank. Spotty white and yellow precipitate on inside of beaker.
Villa#58	Starting volume of solution was 170 mL because 30 mL were set aside as blank. Lots of yellow and white precipitate on inside and outside of beaker.
Villa#59	Lots of yellow and white precipitate on inside and outside of beaker.
Villa#60	Small amount of yellow precipitate on beaker. Trap #61 fell over and solution lost
Villa#62	Spotty yellow precipitate on inside and outside of beaker
Villa#63	Spotty yellow precipitate on inside and outside of beaker
Villa#64	Spotty white precipitate on inside and outside of beaker
Villa#65	Spotty white and yellow precipitate on inside and outside of beaker. Dead bug found in solution.

Table 27. Filter pack data on S, Cl, and F from 2001 for Villarrica volcano
Filters soaked in 10 mL of deionized water to extract S, Cl, and F
Acid-bearing solution then analyzed by ion chromatography

	mg/L	mg/L	mg/L	mg/L
Blank #	**F**	**Cl**	**SO3**	**SO4**
blank # 1	0.0	0.8	0.0	2.2
blank # 2	0.0	0.7	0.0	2.0
blank # 3	0.0	0.7	0.0	1.8
Blank Average	0.0	0.7	0.0	2.0

	RAW DATA				RAW DATA MINUS BLANK					GAS RATIOS			Total Filtration Time
	mg/L	mg/L	mg/L	mg/L	mg/L	mg/L	mg/L	mg/L	mg/L				
Sample #	**F**	**Cl**	**SO_3**	**SO_4**	**F**	**Cl**	**SO_3**	**SO_4**	**ΣSO_4**	**SO_4/Cl**	**SO_2/HCl**	**HCl/HF**	**(mins)**
1/20/01 - A	**0.4**	**3.5**	**3.8**	**20.0**	**0.4**	**2.8**	**3.8**	**18.0**	**22.6**	**8.1**	**5.2**	**7.0**	**3**
1/20/01 - B	**1.3**	**8.3**	**20.0**	**47.5**	**1.3**	**7.6**	**20.0**	**45.5**	**69.6**	**9.2**	**6.0**	**5.9**	**12.25**
1/25/01 - A	**3.2**	**22.6**	**90.3**	**62.0**	**3.2**	**21.8**	**90.3**	**60.0**	**168.3**	**7.7**	**5.0**	**6.8**	**30**
1/25/01 - B	**1.9**	**15.7**	**46.0**	**39.4**	**1.9**	**15.0**	**46.0**	**37.4**	**92.6**	**6.2**	**4.0**	**7.8**	**46.5**
1/25/01 - C	**0.4**	**4.7**	**4.9**	**14.6**	**0.4**	**3.9**	**4.9**	**12.6**	**18.4**	**4.7**	**3.0**	**9.0**	**15.5**
1/28/01 - A1	4.8	36.5	85.7	53.5									
1/28/01 - A2	0.3	2.4	70.9	40.9									
1/28/01 - A3	n.d.	0.5	4.4	7.2									
1/28/01 - A	**5.1**	**39.5**	**160.9**	**101.6**	**5.1**	**38.8**	**160.9**	**99.6**	**292.7**	**7.6**	**4.9**	**7.4**	**32**
1/28/01 - B1	2.8	18.1	50.5	24.1									
1/28/01 - B2	0.1	1.4	28.9	17.8									
1/28/01 - B3	n.d.	0.5	2.0	4.6									
1/28/01 - B	**2.9**	**20.1**	**81.3**	**46.5**	**2.9**	**19.3**	**81.3**	**44.5**	**142.1**	**7.3**	**4.8**	**6.5**	**15**
1/28/01 - C1	1.3	10.6	33.3	20.5									
1/28/01 - C2	n.d.	0.6	8.2	9.3									
1/28/01 - C3	n.d.	0.6	0.0	1.3									
1/28/01 - C	**1.3**	**11.8**	**41.5**	**31.0**	**1.3**	**11.1**	**41.5**	**29.0**	**78.9**	**7.1**	**4.6**	**8.2**	**10**

Table 27. continued

	RAW DATA				RAW DATA MINUS BLANK					GAS RATIOS			Total Filtration Time
	mg/L	mg/L	mg/L	mg/L	mg/L	mg/L	mg/L	mg/L	mg/L				
Sample #	**F**	**Cl**	**SO_3**	**SO_4**	**F**	**Cl**	**SO_3**	**SO_4**	**ΣSO_4**	**SO_4/Cl**	**SO_2/HCl**	**HCl/HF**	**(mins)**
2/2/01 - A	**4.5**	**30.2**	**145.4**	**82.6**	**4.5**	**29.5**	**145.4**	**80.6**	**255.1**	**8.6**	**5.6**	**6.4**	**37.5**
2/2/01 - B	**3.3**	**20.3**	**88.3**	**54.0**	**3.3**	**19.6**	**88.3**	**52.0**	**158.0**	**8.1**	**5.2**	**5.9**	**15.5**
2/2/01 - C	**3.3**	**19.6**	**78.4**	**51.7**	**3.3**	**18.9**	**78.4**	**49.7**	**143.7**	**7.6**	**4.9**	**5.6**	**11**
2/8/01 - A1	2.4	18.8	63.0	42.8									
2/8/01 - A2	0.0	0.5	4.8	9.3									
2/8/01 - A3	0.0	0.6	0.0	2.0									
2/8/01 - A	**2.4**	**19.8**	**67.8**	**54.1**	**2.4**	**19.1**	**67.8**	**52.1**	**133.4**	**7.0**	**4.5**	**7.8**	**25**
2/8/01 - B1	1.9	14.0	44.4	31.5									
2/8/01 - B2	0.0	0.5	8.3	10.5									
2/8/01 - B3	0.0	0.5	0.0	2.2									
2/8/01 - B	**1.9**	**15.1**	**52.6**	**44.3**	**1.9**	**14.3**	**52.6**	**42.3**	**105.4**	**7.4**	**4.8**	**7.2**	**15**
2/8/01 - C1	0.7	5.1	14.0	15.1									
2/8/01 - C2	0.0	0.5	0.0	2.6									
2/8/01 - C3	0.0	0.6	0.0	1.0									
2/8/01 - C	**0.7**	**6.1**	**14.0**	**18.7**	**0.7**	**5.4**	**14.0**	**16.7**	**33.5**	**6.2**	**4.0**	**8.0**	**7**
2/13/01 - A	**2.4**	**21.6**	**64.9**	**53.7**	**2.4**	**20.9**	**64.9**	**51.7**	**129.5**	**6.2**	**4.0**	**8.7**	**20**
2/13/01 - B	**1.4**	**10.9**	**25.7**	**37.3**	**1.4**	**10.2**	**25.7**	**35.4**	**66.2**	**6.5**	**4.2**	**7.2**	**11**
2/13/01 - C	**0.6**	**5.6**	**9.3**	**17.8**	**0.6**	**4.9**	**9.3**	**15.8**	**27.0**	**5.5**	**3.6**	**7.5**	**5**
2/17/01 - A	**0.8**	**11.3**	**32.9**	**35.0**	**0.8**	**10.6**	**32.9**	**33.0**	**72.6**	**6.8**	**4.4**	**12.3**	**20.5**
2/17/01 - B	**0.7**	**6.1**	**15.0**	**18.9**	**0.7**	**5.4**	**15.0**	**16.9**	**34.9**	**6.4**	**4.2**	**8.1**	**10**
2/17/01 - C	**0.2**	**3.1**	**3.7**	**11.5**	**0.2**	**2.3**	**3.7**	**9.5**	**13.9**	**5.9**	**3.8**	**9.6**	**4.8**
2/21/01 - A	**0.8**	**9.2**	**26.7**	**28.5**	**0.8**	**8.5**	**26.7**	**26.6**	**58.6**	**6.9**	**4.5**	**10.2**	**20**
2/21/01 - B	**0.5**	**5.2**	**13.6**	**14.7**	**0.5**	**4.5**	**13.6**	**12.7**	**29.0**	**6.5**	**4.2**	**9.1**	**10**
2/21/01 - C	**0.0**	**1.6**	**0.0**	**4.9**	**0.0**	**0.9**	**0.0**	**2.9**	**2.9**	**3.1**	**2.0**	**n/a**	**5**
											SO_2/HCl	**HCl/HF**	
										Average	**4.5**	**7.8**	
										Std. Dev. (1σ)	**0.7**	**1.6**	

Table 27. continued

For samples 1/28/01 A,B,C and 2/8/01 A,B,C each filter in the stack was analyzed separately for S, Cl, and F and the results summed.

Sample #	Comments
1/20/01 - A	Had teflon filter on backwards for 30 sec. May have ash contamination. Four filter holders in stack instead of normal three plus teflon mesh.
1/20/01 - B	May have ash contamination. Four filter holders in stack instead of normal three plus teflon mesh. Accidentally put two filters in one holder.
1/25/01 - A	Open vent, surging lava swashing back and forth, continuous degassing. Gas unpleasant to breathe.
1/25/01 - B	Gas unpleasant to breathe.
1/25/01 - C	None
1/28/01 - A	Open vent, continuous degassing.
1/28/01 - B	Open vent, continuous degassing
1/28/01 - C	Open vent, continuous degassing
2/2/01 - A	None
2/2/01 - B	None
2/2/01 - C	Only used two filter holders instead of three plus teflon mesh
2/8/01 - A	Good, noxious gas today
2/8/01 - B	Good, noxious gas today
2/8/01 - C	Good, noxious gas today
2/13/01 - A	Good, noxious gas today
2/13/01 - B	Good, noxious gas today
2/13/01 - C	Good, noxious gas today. May have ash contamination
2/17/01 - A	Lots of good noxious gas today
2/17/01 - B	Lots of good noxious gas today
2/17/01 - C	Lots of good noxious gas today
2/21/01 - A	Moderate amount of gas today
2/21/01 - B	Moderate amount of gas today
2/21/01 - C	Moderate amount of gas today. Sampling time too short. Gas ratios meaningless.

Flank Degassing

We have not found any point sources of volatile degassing (i.e. fumaroles) on the flanks of Villarrica. To test for diffuse soil degassing through the flanks of the volcano, we conducted a soil CO_2 flux survey. Using an accumulation chamber configured with a continuous infrared CO_2 gas analyzer, we found diffuse degassing of CO_2 to be undetectable. We assume diffuse degassing of other gases through the flanks of the volcano is similarly low. As a result, we infer that the measured volatiles (SO_2, HCl, and HF) emitted from the summit crater represent the total flux of these volatiles out of the volcano. However, we have no data to quantify the volatiles that may potentially degas out of a subsurface magma body that are absorbed by hot or cold groundwater.

Rock Descriptions

Samples of reticulite pumice were collected on February 29, 2000 and March 1, 2000 from the rim of the summit crater. The reticulite is inferred to have been ejected onto Villarrica's crater rim sometime in the three days prior to February 29 because it was found deposited on the surface of new snow that blanketed the summit during a storm on February 26-27. After the first week of March, no samples of the fragile reticulite could be found, presumably carried away or destroyed by winds, or crushed by tourist foot traffic. Reticulite samples are commonly contaminated with a yellow surface coating, most likely vapor-phase precipitates. The reticulite samples are especially important in this study because rapid quenching made these samples more suitable for analysis by electron microprobe.

Samples of scoria with a conspicuous metallic luster were collected in March 2000 from the rim of Villarrica's summit crater. Preservation of the shiny, metallic surface luster suggests recent eruption and quenching of the scoria. Conversations with local mountain guides suggest that these conspicuous metallic rocks (quite different from the dull black-to-red scoria and bombs found in the crater area) were ejected onto the crater rim sometime between October and November 1999.

Lava erupted in 1984 was also collected from two separate locations: pahoehoe lava ~150 m from the summit crater on the uppermost flank of the cone and aa lava ~4 km from the summit crater on the flank of the volcano. Chemical analysis of the minerals and bulk composition of the 1984 lava samples were made primarily for comparison purposes with the more recent samples of magma.

Petrography and Igneous Textures

All Villarrica magmatic products in this study contain abundant phenocrysts and microphenocrysts of olivine and plagioclase as well as rare microphenocrysts of chromian spinel. Olivine commonly contains inclusions of chromian spinel ~30 μm in diameter.

For the 2000 reticulite sample, olivine grains are euhedral (0.1 to 0.5 mm) and commonly contain one or two spherical to lozenge-shaped inclusions of clear, light-brown glass (5-30 μm). Plagioclase is lath-shaped, euhedral to subhedral and commonly 0.1 to 0.6 mm in length with some grains up to 1.1 mm long. Many plagioclase grains do not contain glass inclusions while others, generally the larger sized plagioclase grains, contain abundant lozenge-shaped, irregular, and/or elongate inclusions of clear, light-brown glass commonly 5-50 μm in diameter with some elongate glass inclusions up to 100 μm in length. The matrix of the 2000 reticulite is clear, light-brown glass with rare plagioclase microlites (<30 μm).

For the 1999 metallic scoria sample, olivine and plagioclase are similar in size to those found in the reticulite. Glass inclusions in olivine and plagioclase in the 1999 metallic scoria are crystallized and opaque under the petrographic microscope. Most of the olivine grains in the 1999 metallic scoria have undergone breakdown evidenced by the presence of wormy trains of vermicular magnetite. The matrix of the 1999 metallic scoria consists of a dense network of lath-shaped plagioclase microlites (1 x 10 μm to 5 x 100 μm) and dendritic magnetite microlites arranged in long chains and cross- or ladder-shapes. Individual magnetite microlites are 3-10 μm in diameter and magnetite crosses and ladders are up to 100 μm in length. Very little interstitial brown

glass remains. We suggest that the ubiquity of magnetite microlites in the groundmass gives the 1999 scoria its metallic luster.

In the 1984 lava samples, olivine phenocrysts range in size from 0.1 to 0.7 mm in diameter. Some olivine grains appear to have suffered breakdown and contain vermicular magnetite. Plagioclase phenocrysts are generally 0.5 to 1.5 mm with some grains up to 4 mm in size. The majority of glass inclusions found in olivine and plagioclase are crystallized and opaque under the petrographic microscope. The matrix of the 1984 lava samples contains a dense network of euhedral lath-shaped and hopper-shaped plagioclase microlites as well as euhedral olivine and magnetite microlites with a small amount of residual brown glass. Samples of 1984 lava lack the distinctive cross- and ladder-shaped groundmass magnetite found in 1999 metallic scoria. We suggest that textural differences in the groundmass of the different rock samples from Villarrica reflect differing cooling histories. A detailed treatment of the relationships between cooling and igneous textures is beyond the scope of this study.

Whole Rock Analyses

Whole rock analyses by XRF of 2000 reticulite, 1999 scoria, and 1984 lava from Villarrica are shown in Table 28. A whole rock analysis of 1984 lava by Hickey-Vargas et al. (1989) is also shown for comparison. The major and trace element compositions of these rocks are remarkably similar despite the textural differences and the 17 year time span that separates ejection and quenching of the magmatic products. In general, the variation in the major and trace element composition of the six whole rock analyses is similar in magnitude to the error associated with the XRF technique.

Modes and Mineral Chemistry

The relative abundance of mineral phases in Villarrica's magmatic products is as follows: plagioclase > olivine > spinel. The modal abundance of plagioclase and olivine was calculated for 2000 reticulite samples by mass balance using average

Table 28. Whole rock analyses of Villarrica 2000 Reticulite, 1999 Metallic Scoria and 1984 Lava

Sample	2000 Reticulite		1999 Metallic Scoria		Average	1984 Lava		Average	Average	WSU-XRF Precision
Sample#	6R	7R	10R	11R	Recent Samples	13R	H-V	1984 Lava	all samples	1σ Std Dev
	Major and minor elements (oxide wt. %)									
SiO_2	52.53	52.64	52.79	52.52	52.62 (0.13)	52.89	52.76	52.83 (0.09)	52.69 (0.15)	0.09
TiO_2	1.23	1.24	1.23	1.23	1.23 (0.00)	1.19	1.17	1.18 (0.01)	1.21 (0.03)	0.00
Al_2O_3	17.19	17.07	17.15	17.11	17.13 (0.05)	16.90	17.03	16.97 (0.09)	17.08 (0.10)	0.07
FeO^T	8.97	9.06	9.08	9.07	9.04 (0.05)	9.07	9.07	9.07 (0.00)	9.05 (0.04)	0.01
MnO	0.16	0.16	0.16	0.16	0.16 (0.00)	0.16	0.16	0.16 (0.00)	0.16 (0.00)	0.00
MgO	5.77	5.90	5.74	5.64	5.76 (0.11)	6.05	5.91	5.98 (0.10)	5.84 (0.15)	0.10
CaO	9.52	9.46	9.49	9.47	9.49 (0.03)	9.58	9.54	9.56 (0.03)	9.51 (0.05)	0.01
Na_2O	3.22	3.20	3.18	3.16	3.19 (0.03)	3.16	3.20	3.18 (0.03)	3.19 (0.02)	0.05
K_2O	0.68	0.68	0.68	0.67	0.68 (0.01)	0.66	0.67	0.67 (0.01)	0.67 (0.01)	0.07
P_2O_5	0.25	0.25	0.25	0.25	0.25 (0.00)	0.24	0.24	0.24 (0.00)	0.25 (0.01)	0.00
Total	99.51	99.66	99.75	99.27	99.55	99.90	99.75	99.82	99.64	

Table 28. continued

Sample	2000 Reticulite		1999 Metallic Scoria		Average	1984 Lava		Average	Average	WSU-XRF Precision
Sample#	6R	7R	10R	11R	Recent Samples	13R	H-V	1984 Lava	all samples	1σ Std Dev
Trace Elements (ppm)										
Ni	67	66	65	64	66 (1)	78	67	73 (8)	68 (5)	1
Cr	144	138	131	135	137 (5)	163	161	162 (1)	145 (14)	2
Sc	35	38	35	28	34 (4)	29	33	31 (3)	33 (4)	2
V	267	293	292	287	285 (12)	286	279	283 (5)	284 (10)	5
Ba	199	209	200	215	206 (8)	201	202	202 (1)	204 (6)	9
Rb	16	15	15	16	16 (1)	15	15	15 (0)	15 (1)	1
Sr	460	453	458	456	457 (3)	448	473	461 (18)	458 (8)	1
Zr	93	95	94	96	95 (1)	91	103	97 (8)	95 (4)	1
Y	26	26	25	26	26 (1)	25	23	24 (1)	25 (1)	1
Nb	3.3	3.5	3.0	3.2	3.3 (0.2)	3.1	3.1	3.1 (0.0)	3.2 (0.2)	0.5
Ga	17	17	20	16	18 (2)	16	19	17 (2)	17 (2)	1
Cu	137	141	132	116	132 (11)	133	n.d.	133	132 (10)	2
Zn	82	85	89	83	85 (3)	85	95	90 (7)	87 (5)	2
Pb	8	6	7	7	7 (1)	5	n.d.	5	7 (1)	2
La	12	5	5	5	7 (4)	7	8	7 (1)	7 (3)	10
Ce	25	31	25	25	27 (3)	40	22	31 (12)	28 (7)	10
Th	2	1	2	0	1 (1)	2	1	2 (1)	1 (1)	2

FeO^T = all Fe as FeO

H-V = Hickey-Vargas et al. (1989)

1σ variation in the sample sets are shown in parentheses for each oxide and trace element

whole rock, matrix glass, olivine, and plagioclase compositions (Table 29). We calculate 6.7 wt. % olivine and 33.1 wt. % plagioclase crystallized from the whole rock composition to give the matrix glass composition. The very low sum of squared residuals from this analysis (Σr^2=0.05) implies that spinel crystallized in such insignificant quantities in 2000 reticulite that the effect of omitting it from the mass balance modal analysis calculation is negligible. This method was not applied to 1999 scoria and 1984 lava samples due to extensive crystallization of the groundmass and the lack of clear patches of matrix glass for analysis.

We focused our efforts on studying the mineral chemistry of the 2000 reticulite because of the freshness and well-quenched nature of the samples. We also analyzed a few minerals in the 1984 lava for comparison with the 2000 reticulite data.

Olivine

Cores and rims of fifteen olivine grains in 2000 reticulite and 1984 lava were analyzed by EPMA along with an additional 17 analyses of the olivine-host near glass inclusions (Table 30). Olivine phenocrysts in 2000 reticulite are remarkably uniform with an average composition of $Fo_{76.7\pm0.6}$. The variation in olivine analyses is less than the EPMA error based on counting statistics (~1% relative or ±0.8 mol% Fo). Olivine grains also lack core-to-rim zonation. Olivine in 1984 lava has a slightly wider range with an average composition of $Fo_{77.8\pm1.5}$. Despite all attempts to avoid vermicular magnetite when analyzing olivine in the 1984 lava, the higher variability in MgO and FeO contents may be an effect of olivine breakdown. Villarrica olivines also contain relatively uniform amounts of the minor elements Ca and Ni: 0.26±0.03 wt. % CaO and 0.11±0.02 wt. % NiO. This variation in Ca and Ni content is greater than the error based on counting statistics for the EPMA analysis technique; however, there is no systematic correlation between CaO or NiO and Fo-content.

Chromian Spinel

Core and rim analyses of sixteen grains of chromian spinel were obtained by EPMA (Table 31). The majority of chromian spinel grains are unzoned with cores and rims that are remarkably uniform in composition with average Mg#

Table 29. Modal analysis of 2000 Reticulite by mass balance.

	A	B	C	D	E	F	G	H
		Olivine		Plagioclase			Calculated	Measured
	Matrix Glass	Fo_{77}	Add OL	An_{62}	Add PLAG	Sum	Whole Rock	Whole Rock
SiO_2	53.9	38.6	2.59	52.4	17.3	73.8	52.85	52.84
TiO_2	1.70					1.70	1.21	1.24
Al_2O_3	14.5			29.0	9.60	24.1	17.23	17.20
Cr_2O_3	0.00					0.00	0.00	0.02
FeO^T	11.0	21.6	1.45	0.9	0.30	12.7	9.11	9.08
MnO	0.20					0.20	0.14	0.16
NiO	0.00					0.00	0.00	0.008
MgO	5.29	39.9	2.67	0.2	0.07	8.03	5.75	5.78
CaO	8.88	0.3	0.02	12.7	4.20	13.1	9.38	9.53
Na_2O	3.29			4.2	1.39	4.68	3.35	3.20
K_2O	0.90			0.2	0.05	0.95	0.68	0.68
P_2O_5	0.40		6.7		33.1	0.40	0.29	0.25
Total	100.0		wt.% OL added		wt.% Plag added	139.7	100.0	100.0

Sum of squared residuals* 0.05

Column A: Average major element matrix glass composition normalized to 100 wt. %
Column B: Average major element composition of olivine normalized to 100 wt. %
Column C: Proportions of oxide components for adding olivine to the matrix glass (Col. B * 6.7 wt. %)
Column D: Average major element composition of plagioclase normalized to 100 wt. %
Column C: Proportions of oxide components for adding plagioclase to the matrix glass (Col. D * 33.1 wt. %)
Column F: Sum of the oxide weight percents of the matrix glass (Col. A), added olivine (Col. C), and added plagioclase (Col. E)
Column G: Sum of matrix glass plus the added olivine and plagioclase is normalized to 100 wt. %
Column H: Average major element whole rock composition normalized to 100 wt. %
* Represents the sum of the squared difference between the calculated and measured whole rock compositions.
The amounts of olivine and plagioclase were varied until the sum of squared residuals was minimized.
FeO^T = all Fe as FeO

Table 30. EPMA analyses of olivine (wt.% oxides)

Year 2000 Reticulite	SiO_2	MgO	FeO^T	MnO	NiO	CaO	Total	Fo
ol2corets8Rrnd	38.5	40.1	21.2	0.34	0.10	0.27	100.5	77.1
ol2rimts8Rrnd	38.2	39.8	21.0	0.35	0.10	0.31	99.7	77.2
ol3corets8Rrnd	38.5	40.3	21.3	0.35	0.12	0.25	100.8	77.1
ol3rimts8Rrnd	39.0	40.9	20.9	0.36	0.11	0.29	101.6	77.7
ol3core1ts8Rrnd	38.8	40.1	21.5	0.35	0.10	0.25	101.0	76.9
ol3rim1ts8Rrnd	38.5	39.8	21.1	0.34	0.11	0.28	100.1	77.1
ol4corets8Rrnd	38.5	39.8	21.3	0.36	0.10	0.24	100.3	76.9
ol4rimts8Rrnd	38.7	40.4	21.3	0.34	0.10	0.26	101.2	77.2
ol4rim1ts8Rrnd	38.6	40.4	21.3	0.35	0.11	0.27	101.0	77.2
ol5corets8Rrnd	38.5	40.0	21.3	0.35	0.09	0.27	100.5	77.0
ol5rimts8Rrnd	37.5	39.6	21.1	0.35	0.12	0.28	99.0	77.0
ol6corets8Rrnd	38.4	39.0	22.2	0.35	0.10	0.25	100.2	75.8
ol6rimts8Rrnd	37.6	39.6	21.1	0.34	0.08	0.32	99.0	77.0
ol7corets8Rrnd	38.4	39.7	22.0	0.36	0.11	0.24	100.9	76.3
ol7rimts8Rrnd	37.8	39.5	21.5	0.34	0.13	0.27	99.5	76.7
ol8corets8Rrnd	38.7	39.9	21.3	0.34	0.11	0.23	100.6	76.9
ol8rimts8Rrnd	38.2	40.0	21.0	0.34	0.11	0.32	100.0	77.2
ol9corets8Rrnd	38.8	41.1	20.2	0.30	0.12	0.19	100.7	78.4
ol9rimts8Rrnd	38.5	40.3	20.9	0.35	0.11	0.28	100.3	77.5
ol10corets8Rrnd	38.5	39.8	21.6	0.37	0.10	0.26	100.6	76.7
ol10rimts8Rrnd	38.6	40.0	21.2	0.35	0.10	0.29	100.5	77.1
ol10core1ts8Rrnd	38.5	39.4	21.4	0.36	0.11	0.27	100.1	76.7
ol10rim1ts8Rrnd	37.4	39.4	21.2	0.33	0.10	0.28	98.7	76.8
ol10rim1ats8Rrnd	38.6	40.0	21.1	0.33	0.08	0.29	100.4	77.2
ol11corets8Rrnd	38.3	39.8	21.4	0.35	0.08	0.25	100.1	76.8
ol11rimts8Rrnd	38.8	39.8	21.4	0.35	0.11	0.29	100.7	76.8
OL7nrGI1tsAral8R	38.1	39.4	21.9	0.32	0.08	0.26	100.1	76.2
OL7nrGI2tsAral8R	37.9	39.4	21.7	0.43	0.11	0.25	99.8	76.3
OL8nrGI1tsAral8R	38.1	39.1	22.2	0.33	0.09	0.26	100.1	75.8
OL9nrGI1tsAral8R	38.6	39.0	21.9	0.34	0.09	0.24	100.2	76.0
OL10nrGI1&2tsAral8R	38.5	38.7	22.6	0.32	0.10	0.25	100.4	75.3
OL11nrGI1tsAral8R	37.8	39.4	22.0	0.32	0.13	0.25	99.9	76.2
OL12nrGI1tsAral8R	38.9	38.7	21.9	0.34	0.08	0.25	100.1	75.9
OL12nrGI2tsAral8R	38.7	38.9	21.8	0.32	0.07	0.27	100.1	76.0
OL13nrGI1tsAral8R	38.6	39.3	21.7	0.33	0.05	0.26	100.3	76.4
OL15nrGI1tsAral8R	38.0	40.1	21.7	0.34	0.08	0.27	100.4	76.8
OL18nrGI2tsAral8R	38.4	38.9	22.0	0.29	0.08	0.26	100.0	75.9
OL18nrGI1tsAral8R	38.4	39.5	21.4	0.34	0.12	0.21	100.0	76.7
OL18nrGI3tsAral8R	39.0	39.2	21.5	0.33	0.11	0.28	100.4	76.5
OL19nrGI1tsAral8R	38.4	39.9	21.6	0.32	0.10	0.23	100.5	76.8
Average	38.4	39.7	21.5	0.34	0.10	0.26	100.3	76.7
Std. Dev. (1σ)	0.4	0.5	0.4	0.02	0.02	0.03	0.6	0.6

Table 30. continued

1984 Lava	SiO_2	MgO	FeO^T	MnO	NiO	CaO	Total	Fo
ol1corets12Ra	38.3	39.7	20.4	0.34	0.11	0.27	99.1	77.6
ol1rimts12Ra	38.4	40.4	19.4	0.32	0.11	0.29	98.9	78.8
ol2corets12Ra	38.5	39.5	20.8	0.32	0.07	0.26	99.4	77.2
ol2rimts12Ra	38.7	41.0	19.4	0.30	0.13	0.28	99.8	79.0
ol3corets12Ra	38.6	39.4	21.4	0.33	0.10	0.24	100.0	76.6
ol3rimts12Ra	38.4	40.0	19.9	0.31	0.11	0.30	98.9	78.2
ol4corets12Ra	38.3	39.6	20.6	0.32	0.13	0.22	99.2	77.4
ol4rimts12Ra	38.3	41.2	19.5	0.29	0.12	0.23	99.6	79.0
ol12corets12Ra	38.9	41.6	18.1	0.27	0.16	0.21	99.2	80.4
ol12rimts12Ra	38.2	40.8	19.1	0.30	0.14	0.27	98.8	79.2
OL2nrGI1tsAral3Ra	38.3	39.5	21.6	0.31	0.11	0.27	100.0	76.5
OL4nrGI1tsAral3Ra	38.1	38.0	22.9	0.34	0.11	0.29	99.8	74.8
OL4nrGI2tsAral3Ra	37.9	39.9	21.9	0.32	0.12	0.23	100.4	76.5
Average	38.4	40.0	20.4	0.31	0.12	0.26	99.5	77.8
Std. Dev. (1σ)	0.2	1.0	1.3	0.02	0.02	0.03	0.5	1.5

FeO^T = all Fe as FeO
Fo = Mg/(Mg+Fe)

Table 31. EPMA analyses of chromian spinel (wt.% oxides)

Year 2000 Reticulite	SiO_2	TiO_2	Al_2O_3	Cr_2O_3	FeO	Fe_2O_3	MnO	NiO	ZnO	MgO	CaO	Total
Crsp1corets8ROS	0.11	3.73	9.45	22.9	25.1	30.1	0.35	0.10	0.09	7.10	0.02	99.1
Crsp2acorets8ROS	0.07	4.51	9.05	24.3	25.6	28.9	0.36	0.05	0.14	7.28	0.00	100.2
Crsp2arimts8ROS	0.08	4.61	9.23	22.2	25.5	30.3	0.28	0.09	0.05	7.37	0.07	99.8
Crsp2bcorets8ROS	0.07	4.53	9.10	24.3	25.7	28.8	0.35	0.09	0.12	7.21	0.00	100.2
Crsp2brimts8ROS	0.08	4.58	9.31	22.4	25.5	29.9	0.34	0.07	0.16	7.32	0.05	99.7
Crsp2ccorets8ROS	0.08	4.55	9.06	23.6	25.8	29.1	0.33	0.08	0.05	7.19	0.00	99.8
Crsp2crimts8ROS	0.08	4.56	9.28	22.6	25.5	29.9	0.33	0.07	0.03	7.31	0.11	99.7
Crsp3rimts8ROS	0.11	4.33	9.45	21.7	25.0	30.3	0.37	0.08	0.11	7.45	0.02	98.9
Crsp4corets8ROS	0.25	4.52	9.25	22.1	25.6	29.9	0.31	0.08	0.11	7.33	0.05	99.6
Crsp6corets8ROS	0.08	4.67	9.29	21.7	25.6	30.5	0.31	0.16	0.00	7.32	0.04	99.7
Crsp7corets8ROS	0.11	4.31	9.27	22.5	25.1	30.0	0.37	0.05	0.03	7.43	0.07	99.2
Crsp10corets8ROS	0.08	4.40	9.41	23.3	25.4	29.1	0.32	0.09	0.05	7.33	0.04	99.6
Crsp11acorets8ROS	0.07	2.94	14.21	25.7	23.5	24.8	0.31	0.09	0.10	8.27	0.03	100.0
Crsp11arimts8ROS	0.08	4.13	9.64	24.2	25.3	28.6	0.34	0.04	0.03	7.27	0.11	99.7
Crsp11bcorets8ROS	0.06	3.33	12.19	25.2	23.9	26.7	0.40	0.10	0.09	7.95	0.03	99.9
Crsp11brimts8ROS	0.10	4.28	9.64	24.0	25.4	28.5	0.34	0.10	0.00	7.31	0.09	99.8
Crsp12acorets8ROS	0.08	4.14	9.28	23.5	25.4	29.1	0.33	0.08	0.10	7.11	0.05	99.1
Crsp12bcorets8ROS	0.07	4.46	9.23	23.3	25.4	29.1	0.38	0.09	0.13	7.28	0.00	99.5
Crsp12brimts8ROS	0.10	4.34	9.45	22.6	25.8	29.5	0.32	0.07	0.06	7.07	0.05	99.3
Crsp12ccorets8ROS	0.08	4.33	9.44	22.8	25.4	29.4	0.36	0.13	0.07	7.17	0.03	99.2
Crsp12crimts8ROS	0.11	4.29	9.34	22.2	25.4	29.9	0.33	0.12	0.05	7.18	0.04	98.9
Crsp13a1ts8ROS	0.09	4.44	9.28	22.8	25.3	29.8	0.39	0.09	0.07	7.34	0.08	99.7
Crsp13a2ts8ROS	0.08	4.54	9.20	23.0	25.5	29.5	0.30	0.08	0.00	7.34	0.07	99.6
Crsp1corets8RAral	0.07	2.04	28.15	18.2	19.9	19.7	0.24	0.19	0.13	11.57	0.03	100.2
Crsp1midts8RAral	0.06	1.68	22.07	24.6	21.2	20.1	0.29	0.13	0.12	9.91	0.00	100.1
Crsp1rimts8RAral	0.08	4.23	9.34	24.3	25.7	28.2	0.38	0.11	0.15	6.92	0.03	99.4

Table 31. continued

Year 2000 Reticulite	Cr#	Mg#	Fe#	Size (μm)	Comments
Crsp1corets8ROS	75.8	18.0	50.5	10x10	Incl. in olivine
Crsp2acorets8ROS	77.6	18.1	48.5	80x70	microphenocryst rim in contact with melt
Crsp2arimts8ROS	75.7	18.3	51.3		
Crsp2bcorets8ROS	77.5	17.9	48.5	80x80	microphenocryst rim in contact with melt
Crsp2brimts8ROS	75.7	18.2	50.9		
Crsp2ccorets8ROS	77.1	17.8	49.3	60x60	microphenocryst rim in contact with melt
Crsp2crimts8ROS	75.9	18.2	50.6		
Crsp3rimts8ROS	74.8	18.8	51.7	30x30	Incl. in olivine
Crsp4corets8ROS	75.6	18.2	51.1	30x20	microphenocryst
Crsp6corets8ROS	75.1	18.1	51.9	20x20	Incl. in olivine
Crsp7corets8ROS	75.8	18.7	50.8	20x20	Incl. in olivine
Crsp10corets8ROS	76.2	18.3	49.3	40x30	microphenocryst
Crsp11acorets8ROS	70.0	21.5	40.9	30x30	Incl. on edge of olivine rim in contact with melt
Crsp11arimts8ROS	76.5	18.2	48.0		
Crsp11bcorets8ROS	72.8	20.5	44.1	40x30	Incl. on edge of olivine rim in contact with melt
Crsp11brimts8ROS	76.3	18.3	48.1		
Crsp12acorets8ROS	76.6	17.9	49.3	10x10	Incl. in olivine
Crsp12bcorets8ROS	76.6	18.2	49.4	20x20	Incl. in olivine rim in contact with olivine
Crsp12brimts8ROS	75.6	17.6	50.2		
Crsp12ccorets8ROS	75.7	17.9	50.0	10x10	Incl. in olivine rim in contact with olivine
Crsp12crimts8ROS	75.4	18.0	50.9		
Crsp13a1ts8ROS	76.1	18.4	50.4	70x70	Resorbed "wormy" microphenocryst
Crsp13a2ts8ROS	76.3	18.2	50.1		
Crsp1corets8RAral	45.5	31.1	33.6	200x200	Large zoned microphenocryst
Crsp1midts8RAral	59.0	26.7	33.0		
Crsp1rimts8RAral	77.1	17.3	47.7		

Cr# = Cr/(Cr+Al); Mg# = Mg/(Mg+Fe^{2+}); Fe# = Fe^{3+}/(Fe^{3+}+Cr+Al); μm = microns = 10^{-6} m

FeO/Fe_2O_3 recalculated after Stormer (1983), assumes perfect stoichiometry; Incl. = inclusion

(=Mg/Mg+Fe^{2+}) = 18.2±0.3, Cr# (=Cr/Cr+Al) = 76.1±0.7, and Fe# (=Fe^{3+}/Fe^{3+}+Cr+Al) = 50.0±1.2. Rims show little chemical variation regardless of whether they are in contact with silicate melt or host-olivine. Two chromian spinel cores are slightly more Cr-, Al-, and Mg-rich and Fe-poor with Mg#, Cr# and Fe# equal to 20-22, 70-73 and 41-44, respectively. One large, 200 x 200 μm microphenocryst of chromian spinel is zoned from a core, with Mg# = 31, Cr# = 46, and Fe# = 34, to a rim that is identical in composition to the majority of the analyzed chromian spinel grains. These more primitive core compositions may represent crystallization under more reducing conditions compared to the majority of Cr-spinel cores and rims.

Plagioclase

Plagioclase cores and rims were analyzed by EPMA on forty grains in 2000 reticulite and ten grains in 1984 lava (Table 32). For the 2000 reticulite, plagioclase microlites and microphenocrysts less than 100 μm in size are unzoned from core-to-rim and have the composition An_{58-60} (Figure 15). Many plagioclase grains greater than 100 μm in size are unzoned to weakly zoned and have core and rim compositions with the range An_{58-63}. Several plagioclase phenocrysts however, are strongly zoned with cores and rims of An_{58-63} and mid-sections with concentric bands or patchy zones of An_{71-73} (Figure 16). In general, glass inclusion-free plagioclase grains are unzoned while plagioclase phenocrysts that contain many glass inclusions and embayments have the oscillatory core-to-rim zonation.

Plagioclase phenocrysts in 1984 lava commonly have complex, oscillatory zonation with many concentric bands of varying An-content, evidence of dissolution and re-growth, and rim compositions that span the range An_{59-68}. Some cores and mid-sections of 1984 plagioclase phenocrysts have higher An-contents up to An_{80-85} (Figure 15; Table 32).

Table 32. EPMA analyses of plagioclase (wt. % oxides)

Year 2000 Reticulite	SiO_2	Al_2O_3	FeO^T	MgO	CaO	Na_2O	K_2O	Total	An	Ab	Or	Size (μm)	Crystal type	Gl's?	Shape	Comments
plag1acorets8ROS	53.3	28.7	0.97	0.19	12.1	4.35	0.18	99.8	59.9	39.0	1.1	300x100	μpheno	No	euhedral	
plag1arimts8ROS	52.9	28.3	1.03	0.19	12.2	4.29	0.18	99.1	60.4	38.5	1.1					
plag1bcorets8ROS	52.5	28.7	0.81	0.18	12.4	4.21	0.15	99.0	61.4	37.7	0.9	150x150	μpheno	No	euhedral	
plag1brimts8ROS	52.9	28.3	0.96	0.23	12.1	4.42	0.19	99.0	59.5	39.3	1.1					
plag2corets8ROS	52.2	28.9	0.84	0.20	12.4	4.27	0.19	99.1	61.0	37.9	1.1	400x200	PHENO	Yes	subhedral	
plag2rimts8ROS	52.6	29.1	0.80	0.18	12.2	4.31	0.15	99.3	60.4	38.7	0.9					
plag3corets8ROS	52.2	29.0	0.92	0.26	12.8	4.08	0.18	99.4	62.7	36.3	1.1	300x150	μpheno	Yes	euhedral	oscillatory zoning
plag3midts8ROS	49.6	30.7	0.68	0.16	14.5	3.11	0.12	98.9	71.6	27.8	0.7					
plag3mid2ts8ROS	49.9	30.9	0.77	0.14	14.6	3.20	0.10	99.6	71.2	28.3	0.6					
plag3rimts8ROS	53.2	28.2	0.97	0.19	12.3	4.56	0.18	99.6	59.2	39.8	1.1					
plag4corets8ROS	48.7	31.8	0.69	0.12	15.2	2.65	0.09	99.3	75.6	23.9	0.5	200x150	μpheno	No	subhedral	relict core
plag4rimts8ROS	52.2	28.9	0.95	0.20	12.6	4.22	0.18	99.3	61.6	37.3	1.1					
plag5corets8ROS	53.3	28.3	1.12	0.20	12.1	4.44	0.18	99.6	59.4	39.5	1.1	40x20	μpheno	No	euhedral	
plag5rimts8ROS	53.7	28.4	1.04	0.18	12.0	4.55	0.20	100.1	58.7	40.2	1.2					
plag6corets8ROS	52.9	28.6	1.19	0.21	11.9	4.49	0.18	99.3	58.7	40.2	1.1	30x20	microlite	No	euhedral	
plag6rimts8ROS	52.6	28.8	1.28	0.23	12.0	4.37	0.16	99.5	59.8	39.3	0.9					
plag7corets8ROS	52.6	28.5	1.02	0.19	12.1	4.41	0.15	99.0	59.7	39.4	0.9	120x20	μpheno	No	euhedral	
plag7rimts8ROS	52.9	28.3	1.02	0.19	11.7	4.48	0.16	98.8	58.5	40.5	0.9					
plag8corets8ROS	52.9	28.3	1.08	0.20	11.9	4.53	0.19	99.1	58.5	40.4	1.1	20x20	microlite	No	euhedral	
plag9corets8ROS	53.1	28.4	1.08	0.21	12.2	4.46	0.15	99.5	59.6	39.5	0.9	70x20	μpheno	No	subhedral	
plag10corets8ROS	53.1	28.4	1.02	0.21	12.1	4.51	0.18	99.5	59.1	39.8	1.0	60x60	μpheno	Yes	euhedral	
plag10rimts8ROS	53.0	28.5	1.02	0.20	11.9	4.57	0.20	99.4	58.3	40.6	1.2					
plag11corets8ROS	52.7	28.7	1.08	0.21	11.8	4.41	0.17	99.0	59.0	40.0	1.0	30x30	microlite	No	euhedral	
plag12corets8ROS	53.1	28.7	0.93	0.21	12.1	4.49	0.18	99.6	59.1	39.9	1.0	250x50	μpheno	Yes	euhedral	
plag12rimts8ROS	52.8	28.5	0.98	0.25	12.0	4.50	0.16	99.3	59.0	40.0	0.9					
plag13corets8ROS	53.1	28.0	1.00	0.19	12.0	4.65	0.17	99.1	58.2	40.8	1.0	100x100	μpheno	No	euhedral	
plag13rimts8ROS	53.1	28.4	1.09	0.21	12.0	4.59	0.16	99.5	58.5	40.6	0.9					
plag14corets8ROS	53.1	28.2	1.24	0.22	11.6	4.60	0.19	99.2	57.6	41.2	1.1	50x10	μpheno	No	euhedral	
plag15corets8ROS	52.9	28.8	0.90	0.19	12.2	4.47	0.17	99.6	59.5	39.5	1.0	150x100	μpheno	Yes	euhedral	
plag15rimts8ROS	52.6	28.9	0.91	0.18	12.7	4.33	0.15	99.8	61.3	37.8	0.9					
plag16corets8ROS	53.3	28.8	0.88	0.20	12.2	4.47	0.16	100.0	59.5	39.6	0.9	70x50	μpheno	No	euhedral	
plag17corets8ROS	53.7	28.3	0.90	0.18	12.3	4.56	0.18	100.1	59.3	39.7	1.0	200x100	μpheno	No	euhedral	

Table 32. continued

Year 2000 Reticulite	SiO_2	Al_2O_3	FeO^T	MgO	CaO	Na_2O	K_2O	Total	An	Ab	Or	Size (μm)	Crystal type	GI's?	Shape	Comments
plag17rimts8ROS	52.9	29.1	1.03	0.18	12.4	4.48	0.16	100.3	60.0	39.1	0.9					
plag18corets8ROS	52.4	28.7	1.22	0.20	12.0	4.36	0.16	99.0	59.7	39.4	0.9	100x30	μpheno	No	subhedral	
plag19corets8ROS	52.5	28.4	1.08	0.19	12.0	4.38	0.17	98.7	59.5	39.5	1.0	70x30	μpheno	No	euhedral	
plag19rimts8ROS	52.6	28.5	1.16	0.20	11.8	4.38	0.19	98.8	59.1	39.8	1.1					
plag2corets8RGS	52.6	28.5	0.83	0.22	12.5	4.23	0.17	99.0	61.4	37.6	1.0	600x400	PHENO	No	euhedral	
plag2midts8RGS	52.9	28.2	0.81	0.19	12.5	4.49	0.20	99.3	59.9	39.0	1.1					
plag2rimts8RGS	54.1	28.5	0.83	0.19	12.2	4.61	0.13	100.5	58.8	40.4	0.8					
plag3corets8RGS	53.0	28.6	0.85	0.18	12.4	4.31	0.15	99.5	60.9	38.2	0.9	400x150	PHENO	Yes	euhedral	highly embayed
plag3midts8RGS	51.7	29.6	0.87	0.17	13.1	3.96	0.15	99.5	64.0	35.1	0.9					
plag3rimts8RGS	52.0	29.1	0.96	0.18	13.1	4.02	0.14	99.6	63.8	35.4	0.8					
plag4corets8RGS	52.7	28.9	0.91	0.19	12.5	4.27	0.16	99.6	61.1	37.9	0.9	600x250	PHENO	Yes	subhedral	some embayments
plag4rimts8RGS	52.7	28.2	0.86	0.23	12.2	4.42	0.17	98.8	59.9	39.1	1.0					
plag5acorets8RGS	52.6	28.8	0.87	0.20	12.3	4.33	0.18	99.3	60.3	38.6	1.1	500x300	PHENO	Yes	subhedral	oscillatory zoning
plag5amidts8RGS	49.0	31.2	0.73	0.15	14.8	3.02	0.10	99.0	72.6	26.8	0.6					
plag5arimts8RGS	52.0	28.9	0.97	0.19	12.3	4.33	0.19	98.9	60.4	38.5	1.1					
plag5arim1ts8RGS	52.0	29.0	0.95	0.21	12.4	4.23	0.14	98.9	61.4	37.8	0.8					
plag5bcorets8RGS	52.6	29.1	0.81	0.20	12.4	4.29	0.13	99.5	60.9	38.3	0.8	450x300	PHENO	Yes	subhedral	oscillatory zoning
plag5bmidts8RGS	49.2	30.9	0.78	0.16	14.8	3.07	0.14	99.1	72.1	27.1	0.8					
plag5brimts8RGS	52.0	29.4	0.84	0.19	12.6	4.22	0.16	99.4	61.6	37.5	0.9					
plag6corets8RGS	52.3	29.1	0.89	0.19	12.8	4.36	0.03	99.7	61.8	38.1	0.2	450x100	PHENO	Yes	euhedral	
plag6rimts8RGS	52.7	29.0	0.87	0.20	12.5	4.41	0.22	99.9	60.2	38.5	1.3					
plag7corets8RGS	52.6	29.1	0.81	0.18	12.6	4.23	0.16	99.7	61.7	37.4	0.9	550x150	PHENO	No	euhedral	
plag7rimts8RGS	52.8	28.6	0.91	0.21	12.5	4.47	0.19	99.7	60.0	38.9	1.1					
plag8corets8RGS	53.0	29.2	0.78	0.22	12.8	4.30	0.15	100.5	61.6	37.5	0.8	500x350	PHENO	Yes	subhedral	oscillatory zoning
plag8midts8RGS	49.3	31.1	0.73	0.12	15.0	3.09	0.10	99.3	72.4	27.0	0.6					
plag8rimts8RGS	53.0	28.8	0.86	0.19	12.4	4.35	0.13	99.7	60.7	38.6	0.8					
plag9corets8RGS	53.0	29.2	0.85	0.19	12.4	4.47	0.16	100.3	60.0	39.1	0.9	850x450	PHENO	No	subhedral	
plag9rimts8RGS	52.8	29.4	0.89	0.19	12.3	4.40	0.19	100.1	60.0	38.9	1.1					
plag10acorets8RGS	52.3	29.2	0.91	0.21	12.5	4.37	0.19	99.6	60.5	38.4	1.1	500x200	PHENO	Yes	subhedral	
plag10arimts8RGS	53.0	28.9	1.02	0.17	12.3	4.48	0.20	100.0	59.6	39.2	1.1					
plag11acorets8RGS	52.1	29.6	0.82	0.20	13.0	4.32	0.11	100.1	62.0	37.4	0.6	600x300	PHENO	Yes	euhedral	oscillatory zoning
plag11amidts8RGS	49.7	31.4	0.66	0.15	15.2	3.10	0.08	100.3	72.7	26.9	0.4					
plag11arimts8RGS	50.0	31.2	0.76	0.15	14.9	3.05	0.09	100.2	72.6	26.8	0.5					

Table 32. continued

Year 2000 Reticulite	SiO_2	Al_2O_3	FeO^T	MgO	CaO	Na_2O	K_2O	Total	An	Ab	Or	Size (μm)	Crystal type	Gl's?	Shape	Comments
plag11bcorets8RGS	51.7	29.9	0.85	0.20	13.4	3.85	0.10	99.9	65.3	34.1	0.6	280x100	μpheno	Yes	euhedral	strongly zoned
plag11brimts8RGS	49.3	31.6	0.82	0.17	15.0	2.90	0.05	99.9	73.9	25.8	0.3					
plag12corets8RGS	52.9	28.9	0.72	0.19	12.1	4.54	0.14	99.5	59.1	40.1	0.8	350x200	PHENO	Yes	euhedral	oscillatory zoning
plag12midts8RGS	49.7	31.2	0.73	0.13	14.8	3.10	0.08	99.8	72.2	27.4	0.5					
plag12rimts8RGS	53.2	28.6	1.05	0.20	12.4	4.41	0.18	100.1	60.2	38.7	1.1					
plag13corets8RGS	53.4	28.7	0.95	0.20	12.4	4.51	0.15	100.2	59.7	39.5	0.9	1100x150	PHENO	Yes	subhedral	oscillatory zoning
plag13midts8RGS	50.1	31.1	0.72	0.15	14.7	3.17	0.13	100.0	71.4	27.9	0.7					
plag13mid2ts8RGS	49.3	31.7	0.74	0.14	14.6	3.15	0.09	99.7	71.6	27.9	0.5					
plag13rimts8RGS	52.5	29.2	0.95	0.19	13.2	4.21	0.14	100.4	62.9	36.3	0.8					
plag1corets8RAral	53.4	28.2	1.05	0.20	12.0	4.61	0.17	99.7	58.3	40.7	1.0	60x40	μpheno	No	euhedral	
plag1rimts8RAral	53.5	28.8	1.08	0.19	12.2	4.58	0.18	100.6	58.9	40.1	1.1					
plag2corets8RAral	53.8	28.0	1.15	0.19	12.3	4.69	0.19	100.3	58.6	40.3	1.0	20x20	microlite	No	euhedral	
plag3corets8RAral	53.2	28.5	0.82	0.21	12.2	4.46	0.18	99.5	59.5	39.5	1.0	500x150	PHENO	No	euhedral	
plag3rimts8RAral	52.3	29.2	1.06	0.20	12.2	4.35	0.17	99.6	60.2	38.8	1.0					
plag4corets8RAral	54.3	28.0	1.01	0.19	12.2	4.70	0.15	100.5	58.4	40.8	0.8	100x30	μpheno	No	euhedral	
plag4rimts8RAral	53.7	28.2	1.06	0.22	12.5	4.54	0.16	100.4	59.8	39.3	0.9					
plag5corets8RAral	54.0	27.4	1.00	0.20	12.4	4.71	0.17	99.9	58.6	40.4	0.9	40x10	μpheno	No	subhedral	
plag6corets8RAral	54.4	27.8	0.91	0.20	12.1	4.64	0.17	100.1	58.4	40.6	1.0	40x20	μpheno	No	subhedral	
plag6rimts8RAral	53.9	27.8	1.06	0.20	12.2	4.64	0.14	100.0	58.8	40.4	0.8					

1984 Lava	SiO_2	Al_2O_3	FeO^T	MgO	CaO	Na_2O	K_2O	Total	An	Ab	Or	Size (μm)	Crystal type	Gl's?	Shape	Comments
plag1corets12Ra	47.5	32.2	0.68	0.14	16.3	2.20	0.08	99.0	79.9	19.6	0.5	900x450	PHENO	Yes	euhedral	complex zoning
plag1core2ts12Ra	47.9	32.2	0.86	0.19	16.3	2.29	0.07	99.8	79.5	20.1	0.4					
plag1midts12Ra	46.5	33.1	0.68	0.12	16.9	1.79	0.01	99.1	83.9	16.0	0.1					
plag1mid2ts12Ra	46.5	33.0	0.61	0.11	17.1	1.79	0.02	99.1	83.9	15.9	0.1					
plag1mid3ts12Ra	52.6	29.1	0.75	0.22	12.6	4.40	0.16	99.8	60.7	38.4	0.9					
plag1rimts12Ra	50.7	30.0	0.85	0.20	14.0	3.54	0.10	99.4	68.2	31.2	0.6					
plag2corets12Ra	53.2	28.3	0.79	0.18	12.2	4.57	0.18	99.5	58.9	40.0	1.1	1200x450	PHENO	No	euhedral	
plag2midts12Ra	52.8	28.7	0.76	0.19	12.3	4.43	0.14	99.3	60.1	39.1	0.8					
plag2rimts12Ra	51.4	29.8	0.84	0.19	13.7	3.69	0.11	99.7	66.8	32.6	0.6					
plag3corets12Ra	53.2	28.6	0.76	0.20	12.4	4.39	0.17	99.7	60.3	38.7	1.0	600x200	PHENO	No	subhedral	
plag3rimts12Ra	51.4	29.9	0.82	0.22	13.8	3.80	0.11	100.1	66.3	33.1	0.6					
plag4corets12Ra	48.9	31.8	0.68	0.14	15.4	2.65	0.08	99.6	75.9	23.6	0.5	750x500	PHENO	Yes	euhedral	complex zoning

Table 32. continued

1984 Lava	SiO_2	Al_2O_3	FeO^T	MgO	CaO	Na_2O	K_2O	Total	An	Ab	Or	Size (μm)	Crystal type	Gl's?	Shape	Comments
plag4midts12Ra	47.6	32.5	0.64	0.12	16.6	2.03	0.08	99.6	81.5	18.0	0.4					
plag4rimts12Ra	51.6	29.5	0.94	0.21	13.4	3.83	0.14	99.7	65.4	33.8	0.8					
plag5corets12Ra	51.9	29.2	0.78	0.20	12.8	4.12	0.16	99.1	62.7	36.4	0.9	900x300	PHENO	Yes	euhedral	complex zoning
plag5midts12Ra	48.7	31.8	0.74	0.14	15.6	2.61	0.06	99.7	76.5	23.1	0.3					
plag5rimts12Ra	52.4	29.2	0.84	0.21	13.2	3.96	0.14	99.9	64.3	34.9	0.8					
plag6corets12Ra	52.4	29.4	0.72	0.19	13.2	4.10	0.17	100.1	63.4	35.6	1.0	650x300	PHENO	No	euhedral	
plag6rimts12Ra	51.9	29.7	0.81	0.20	13.6	3.85	0.11	100.2	65.7	33.6	0.7					
plag7corets12Ra	53.4	28.4	0.74	0.18	12.2	4.58	0.20	99.7	58.8	40.0	1.2	1000x500	PHENO	No	euhedral	
plag7midts12Ra	53.1	29.0	0.79	0.18	12.5	4.31	0.14	100.0	61.0	38.2	0.8					
plag7rimts12Ra	51.4	29.9	0.68	0.17	14.0	3.63	0.07	99.9	67.9	31.7	0.4					
plag8corets12Ra	53.5	28.5	0.76	0.21	12.2	4.67	0.18	99.9	58.4	40.6	1.0	250x400	PHENO	No	euhedral	
plag8rimts12Ra	51.6	29.8	0.85	0.18	13.4	3.86	0.13	99.8	65.2	34.0	0.8					
plag1corets3RaAral	48.2	32.7	0.65	0.12	16.3	2.24	0.07	100.2	79.7	19.9	0.4	4000x1500	PHENO	Yes	euhedral	complex zoning
plag1midts3RaAral	47.8	32.8	0.65	0.10	16.4	2.17	0.06	100.0	80.4	19.3	0.4					
plag1rimts3RaAral	51.0	30.6	0.80	0.19	13.9	3.66	0.09	100.1	67.4	32.1	0.5					
plag2corets3RaAral	47.2	33.0	0.67	0.13	16.9	2.02	0.03	99.9	82.0	17.8	0.2	800x500	PHENO	Yes	euhedral	complex zoning
plag2midts3RaAral	46.5	33.7	0.59	0.09	17.3	1.69	0.08	99.9	84.6	14.9	0.5					
plag2mid2ts3RaAral	52.2	29.6	0.77	0.19	13.0	4.12	0.15	100.1	63.1	36.1	0.9					
plag2rimts3RaAral	52.6	28.9	1.05	0.22	12.1	4.56	0.17	99.5	58.9	40.1	1.0					

PHENO = phenocryst; μpheno = microphenocryst; μm = microns = 10^{-6} m
An = Ca/(Ca+Na+K) = Anorthite; Ab = Na/(Ca+Na+K) = Albite; Or = K/(Ca+Na+K) = Orthoclase
Phenocrysts > 300 microns; microphencrysts = 30-300 microns; microlites < 30 microns (after Wilcox, 1954)
FeO^T = all Fe as FeO; GI = glass inclusion

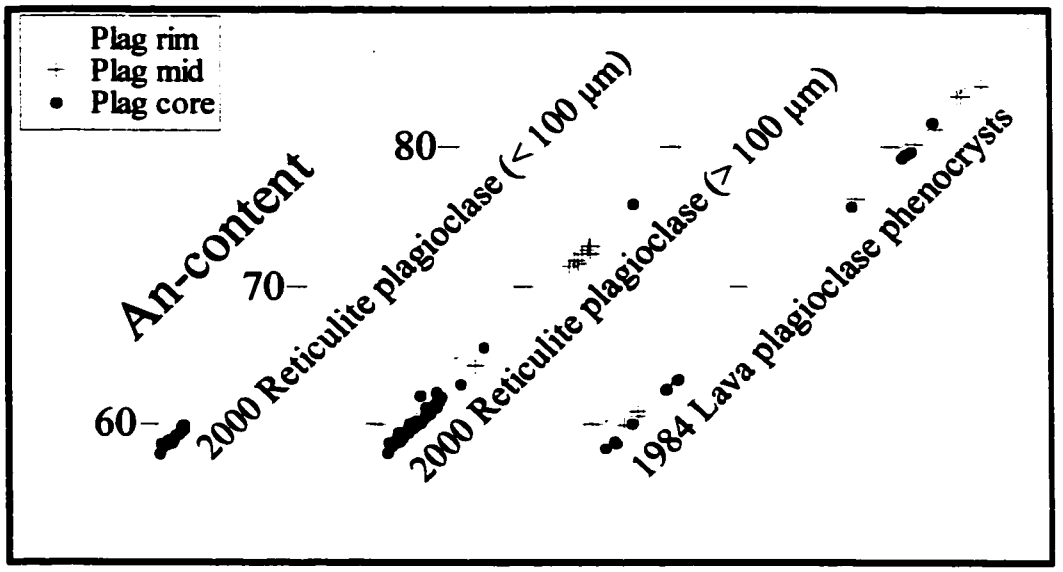

Figure 15. Portion of the Anorthite-Albite-Orthoclase ternary diagram showing the range in An-content for plagioclase grains < 100 μm and > 100 μm from the 2000 reticulite. Compositions of plagioclase phenocrysts from the 1984 lava are shown for comparison.

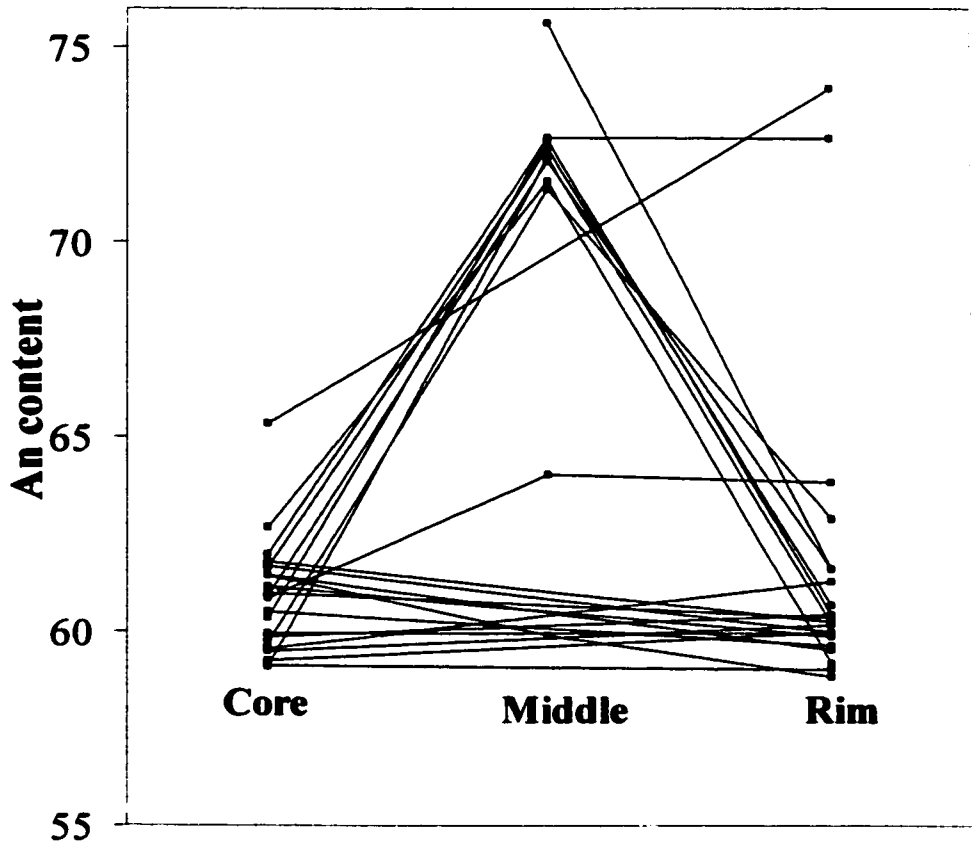

Figure 16. Chemical zonation in 23 plagioclase phenocrysts from the 2000 reticulite. Thirteen plagioclase grains are unzoned (An_{59-63}). Six plagioclase phenocrysts show oscillatory zoning with low An-content cores and rims (An_{59-63}) and high An-content areas (An_{71-72}) between the core and rim.

Glass Inclusions

We focused our efforts on analyzing glass inclusions (GI's) in the 2000 reticulite samples. Glass inclusions ≥10 μm in diameter, without intersecting cracks or visual evidence for post-entrapment crystallization were chosen for analysis. No successful glass inclusion analyses were made in the 1999 scoria samples due to crystallization in the glass inclusions. Only a few non-crystallized glass inclusions in olivine in the 1984 lava samples were found. These were analyzed for comparison with the 2000 reticulite samples. The concentration of H_2O in all analyzed glass inclusions was estimated using the difference technique (100 wt. % - analytical total of major and volatile elements; Anderson, 1974). Glass inclusions were chosen for analysis by observation of two-dimensional thin sections. Unseen cracks or re-entrants intersecting a glass inclusion in the third dimension may escape detection. These potentially allow for volatile leakage from the glass inclusion during ascent and eruption.

We used EPMA to characterize the major element chemistry of 46 glass inclusions in olivine from 2000 reticulite (Table 33). Of these, 18 olivine-hosted glass inclusions were also analyzed for S, Cl, and F by EPMA and 4 were analyzed for H_2O, CO_2, S, Cl, and F by SIMS. Twenty glass inclusions were recalculated for post-entrapment olivine crystallization using the thermodynamic model of Kress and Ghiorso (2001). A post-entrapment crystallization adjustment is necessary because host mineral growth on the walls of the glass inclusion increases the concentrations of volatiles as the micro-volume of melt evolves. The adjustment scheme adds back into the liquid (corresponding to the glass composition) instantaneous equilibrium solid in 0.01 wt. % increments. The program tracks changes in pressure, temperature, inclusion volume and redox, maintaining thermodynamic equilibrium as it tracks backward up the post-entrapment crystallization path. Entrapment conditions are assumed when the instantaneous solid most closely matches the host composition. Sulfur, Cl, and F concentrations are corrected by assuming that they are totally incompatible. The magnitude of post-entrapment crystallization of olivine varies

Table 33. Analyses of Glass Inclusions in Olivine in Villarrica samples

Year 2000 Reticulite: Major and volatile element composition determined by EPMA

Label	Gl1OL1tsAral8R	Gl1OL6tsAral8R	Gl1OL7tsAral8R	Gl2OL7tsAral8R
SiO_2	54.1	54.4	53.9	54.3
TiO_2	1.64	1.56	1.69	1.66
Al_2O_3	14.3	14.2	14.0	14.4
Cr_2O_3	0.03	0.03	0.03	0.02
FeO^T	11.6	11.7	11.4	11.3
MnO	0.20	0.20	0.22	0.22
MgO	5.08	5.15	5.00	4.77
CaO	8.76	8.61	8.74	8.81
Na_2O	3.50	3.47	3.31	3.36
K_2O	0.90	0.90	0.99	0.91
P_2O_5	0.40	0.37	0.38	0.36
S (ppm)	n/a	n/a	75	n/a
Cl (ppm)	n/a	n/a	216	n/a
F (ppm)	n/a	n/a	556	n/a
Total	100.5	100.6	99.7	100.1
H_2O by Diff. [a]	-0.5	-0.6	0.3	-0.1
SIMS analyses of volatiles				
H_2O (wt.%)	n/a	n/a	n/a	n/a
CO_2(ppm)	n/a	n/a	n/a	n/a
S (ppm)	n/a	n/a	n/a	n/a
Cl (ppm)	n/a	n/a	n/a	n/a
F (ppm)	n/a	n/a	n/a	n/a
Host olivine composition [b]				
SiO_2	n/a	n/a	38.1	37.9
MgO	n/a	n/a	39.4	39.4
FeO^T	n/a	n/a	21.9	21.7
MnO	n/a	n/a	0.32	0.43
CaO	n/a	n/a	0.26	0.25
NiO	n/a	n/a	0.08	0.11
Total	n/a	n/a	100.1	99.8
Fo	n/a	n/a	0.76	0.76
Recalculated major and volatile element composition of glass inclusion [c]				
SiO_2	n.r.	n.r.	53.8	54.0
TiO_2	n.r.	n.r.	1.68	1.63
Al_2O_3	n.r.	n.r.	13.9	14.2
Cr_2O_3	n.r.	n.r.	0.03	0.02
FeO^T	n.r.	n.r.	11.5	11.5
MnO	n.r.	n.r.	0.22	0.23
MgO	n.r.	n.r.	5.23	5.36
CaO	n.r.	n.r.	8.69	8.66
Na_2O	n.r.	n.r.	3.29	3.30
K_2O	n.r.	n.r.	0.98	0.89
P_2O_5	n.r.	n.r.	0.38	0.35
S (ppm)	n.r.	n.r.	75	n/a
Cl(ppm)	n.r.	n.r.	215	n/a
F(ppm)	n.r.	n.r.	552	n/a
Total	n.r.	n.r.	99.7	100.1
H_2O [d]	n.r.	n.r.	0.3	-0.1
wt.% OL [e]	n.r.	n.r.	0.7	1.9
T (° C) [f]	n.r.	n.r.	1151	1163
P (bars) [f]	n.r.	n.r.	138	197

Table 33. continued

Year 2000 Reticulite: Major and volatile element composition determined by EPMA

Label	GI1OL8tsAral8R	GI1OL9tsAral8R	GI1OL10tsAral8R	GI2OL10tsAral8R
SiO_2	53.8	53.9	54.4	54.0
TiO_2	1.75	1.61	1.79	1.70
Al_2O_3	14.0	14.8	14.4	14.5
Cr_2O_3	0.03	0.02	0.01	0.02
FeO^T	11.9	11.8	11.7	11.9
MnO	0.19	0.19	0.20	0.15
MgO	5.20	4.99	5.08	5.06
CaO	8.74	9.00	8.74	8.98
Na_2O	3.49	3.62	3.44	3.32
K_2O	0.90	0.84	0.95	0.90
P_2O_5	0.39	0.45	0.38	0.37
S (ppm)	59	63	n/a	78
Cl (ppm)	169	211	n/a	166
F (ppm)	496	599	n/a	491
Total	100.5	101.2	101.0	101.0
H_2O by Diff. [a]	-0.5	-1.2	-1.0	-1.0
SIMS analyses of volatiles				
H_2O (wt.%)	n/a	n/a	n/a	n/a
CO_2(ppm)	n/a	n/a	n/a	n/a
S (ppm)	n/a	n/a	n/a	n/a
Cl (ppm)	n/a	n/a	n/a	n/a
F (ppm)	n/a	n/a	n/a	n/a
Host olivine composition [b]				
SiO_2	38.1	38.6	38.5	38.5
MgO	39.1	39.0	38.7	38.7
FeO^T	22.2	21.9	22.6	22.6
MnO	0.33	0.34	0.32	0.32
CaO	0.26	0.24	0.25	0.25
NiO	0.09	0.09	0.10	0.10
Total	100.1	100.2	100.4	100.4
Fo	0.76	0.76	0.75	0.75
Recalculated major and volatile element composition of glass inclusion [c]				
SiO_2	53.8	53.8	54.3	54.0
TiO_2	1.75	1.60	1.79	1.69
Al_2O_3	14.0	14.6	14.4	14.4
Cr_2O_3	0.03	0.02	0.01	0.02
FeO^T	12.0	11.9	11.7	12.0
MnO	0.19	0.19	0.20	0.15
MgO	5.30	5.32	5.14	5.23
CaO	8.72	8.92	8.72	8.94
Na_2O	3.48	3.58	3.43	3.31
K_2O	0.90	0.83	0.95	0.90
P_2O_5	0.39	0.44	0.38	0.37
S (ppm)	59	62	n/a	78
Cl(ppm)	169	209	n/a	165
F(ppm)	495	593	n/a	488
Total	100.6	101.3	101.0	101.0
H_2O [d]	-0.6	-1.3	-1.0	-1.0
wt.% OL [e]	0.3	1.0	0.2	0.5
T (° C) [f]	1157	1154	1154	1151
P (bars) [f]	123	172	108	133

Table 33. continued

Year 2000 Reticulite: Major and volatile element composition determined by EPMA

Label	GI1OL11tsAral8R	GI1OL12tsAral8R	GI2OL12tsAral8R	GI1OL13tsAral8R
SiO_2	53.7	53.4	54.0	53.8
TiO_2	1.58	1.73	1.73	1.57
Al_2O_3	14.2	14.7	14.7	14.6
Cr_2O_3	0.01	0.04	0.03	0.01
FeO^T	11.3	11.7	11.2	12.0
MnO	0.17	0.20	0.21	0.20
MgO	5.40	5.24	4.64	5.12
CaO	8.60	8.99	9.20	9.11
Na_2O	3.43	3.50	3.41	3.33
K_2O	0.90	0.89	0.93	0.88
P_2O_5	0.33	0.36	0.40	0.34
S (ppm)	80	n/a	29	101
Cl (ppm)	135	n/a	169	200
F (ppm)	473	n/a	519	521
Total	99.7	100.7	100.4	101.0
H_2O by Diff. [a]	0.3	-0.7	-0.4	-1.0
SIMS analyses of volatiles				
H_2O (wt.%)	0.29	0.29	n/a	n/a
CO_2(ppm)	63	19	n/a	n/a
S (ppm)	101	69	n/a	n/a
Cl (ppm)	218	174	n/a	n/a
F (ppm)	370	339	n/a	n/a
Host olivine composition [b]				
SiO_2	37.8	38.9	38.7	38.6
MgO	39.4	38.7	38.9	39.3
FeO^T	22.0	21.9	21.8	21.7
MnO	0.32	0.34	0.32	0.33
CaO	0.25	0.25	0.27	0.26
NiO	0.13	0.08	0.07	0.05
Total	99.9	100.1	100.1	100.3
Fo	0.76	0.76	0.76	0.76
Recalculated major and volatile element composition of glass inclusion [c]				
SiO_2	n.r.	53.4	53.6	53.6
TiO_2	n.r.	1.73	1.69	1.55
Al_2O_3	n.r.	14.7	14.4	14.4
Cr_2O_3	n.r.	0.04	0.03	0.01
FeO^T	n.r.	11.7	11.5	12.1
MnO	n.r.	0.20	0.22	0.21
MgO	n.r.	5.24	5.27	5.58
CaO	n.r.	8.99	9.02	8.99
Na_2O	n.r.	3.50	3.35	3.29
K_2O	n.r.	0.89	0.91	0.87
P_2O_5	n.r.	0.36	0.39	0.34
S (ppm)	n.r.	69	283	100
Cl(ppm)	n.r.	174	166	197
F(ppm)	n.r.	339	509	513
Total	n.r.	100.7	100.4	101.0
H_2O [d]	n.r.	-0.7	-0.4	-1.0
wt.% OL [e]	n.r.	0.0	2.0	1.4
T (° C) [f]	n.r.	1147	1153	1162
P (bars) [f]	n.r.	100	209	159

Table 33. continued

Year 2000 Reticulite: Major and volatile element composition determined by EPMA

Label	GI1OL14tsAral8R	GI2OL15tsAral8R	GI1OL17tsAral8R	GI2OL17tsAral8R
SiO_2	54.1	55.1	53.7	53.9
TiO_2	1.65	1.52	1.65	1.77
Al_2O_3	14.0	13.4	14.6	14.4
Cr_2O_3	0.01	0.01	0.03	0.02
FeO^T	11.6	11.4	11.7	11.7
MnO	0.20	0.17	0.21	0.20
MgO	5.17	6.52	5.13	4.94
CaO	8.68	8.27	8.65	9.00
Na_2O	3.43	3.16	3.11	3.23
K_2O	0.90	0.90	0.89	0.89
P_2O_5	0.35	0.37	0.35	0.36
S (ppm)	n/a	n/a	n/a	n/a
Cl (ppm)	n/a	n/a	n/a	n/a
F (ppm)	n/a	n/a	n/a	n/a
Total	100.0	100.8	99.9	100.5
H_2O by Diff. [a]	0.0	-0.8	0.1	-0.5
SIMS analyses of volatiles				
H_2O (wt.%)	n/a	n/a	n/a	n/a
CO_2(ppm)	n/a	n/a	n/a	n/a
S (ppm)	n/a	n/a	n/a	n/a
Cl (ppm)	n/a	n/a	n/a	n/a
F (ppm)	n/a	n/a	n/a	n/a
Host olivine composition [b]				
SiO_2	n/a	38.0	n/a	n/a
MgO	n/a	40.1	n/a	n/a
FeO^T	n/a	21.7	n/a	n/a
MnO	n/a	0.34	n/a	n/a
CaO	n/a	0.27	n/a	n/a
NiO	n/a	0.08	n/a	n/a
Total	n/a	100.4	n/a	n/a
Fo	n/a	0.77	n/a	n/a
Recalculated major and volatile element composition of glass inclusion [c]				
SiO_2	n.r.	n.r.	n.r.	n.r.
TiO_2	n.r.	n.r.	n.r.	n.r.
Al_2O_3	n.r.	n.r.	n.r.	n.r.
Cr_2O_3	n.r.	n.r.	n.r.	n.r.
FeO^T	n.r.	n.r.	n.r.	n.r.
MnO	n.r.	n.r.	n.r.	n.r.
MgO	n.r.	n.r.	n.r.	n.r.
CaO	n.r.	n.r.	n.r.	n.r.
Na_2O	n.r.	n.r.	n.r.	n.r.
K_2O	n.r.	n.r.	n.r.	n.r.
P_2O_5	n.r.	n.r.	n.r.	n.r.
S (ppm)	n.r.	n.r.	n.r.	n.r.
Cl(ppm)	n.r.	n.r.	n.r.	n.r.
F(ppm)	n.r.	n.r.	n.r.	n.r.
Total	n.r.	n.r.	n.r.	n.r.
H_2O [d]	n.r.	n.r.	n.r.	n.r.
wt.% OL [e]	n.r.	n.r.	n.r.	n.r.
T (° C) [f]	n.r.	n.r.	n.r.	n.r.
P (bars) [f]	n.r.	n.r.	n.r.	n.r.

Table 33. continued

Year 2000 Reticulite: Major and volatile element composition determined by EPMA

Label	GI2OL18tsAral8R	GI3OL18tsAral8R	GI1OL19tsAral8R	GI1OL20tsAral8R
SiO_2	54.1	54.2	54.7	53.3
TiO_2	1.60	1.61	1.62	1.48
Al_2O_3	14.7	14.7	14.6	16.3
Cr_2O_3	0.02	0.03	0.01	0.00
FeO^T	11.5	11.3	11.4	10.1
MnO	0.19	0.19	0.20	0.17
MgO	5.25	5.62	5.52	5.61
CaO	8.79	8.49	8.56	9.37
Na_2O	3.34	3.46	3.31	3.28
K_2O	0.87	0.95	0.95	0.89
P_2O_5	0.36	0.34	0.36	0.38
S (ppm)	121	n/a	n/a	n/a
Cl (ppm)	196	n/a	n/a	n/a
F (ppm)	543	n/a	n/a	n/a
Total	100.8	100.9	101.2	100.9
H_2O by Diff. [a]	-0.8	-0.9	-1.2	-0.9
SIMS analyses of volatiles				
H_2O (wt.%)	n/a	0.32	0.31	n/a
CO_2(ppm)	n/a	69	52	n/a
S (ppm)	n/a	122	95	n/a
Cl (ppm)	n/a	250	221	n/a
F (ppm)	n/a	421	376	n/a
Host olivine composition [b]				
SiO_2	38.4	39.0	38.4	n/a
MgO	38.9	39.2	39.9	n/a
FeO^T	22.0	21.5	21.6	n/a
MnO	0.29	0.33	0.32	n/a
CaO	0.26	0.28	0.23	n/a
NiO	0.08	0.11	0.10	n/a
Total	100.0	100.4	100.5	n/a
Fo	0.76	0.77	0.77	n/a
Recalculated major and volatile element composition of glass inclusion [c]				
SiO_2	54.1	n.r.	n.r.	n.r.
TiO_2	1.60	n.r.	n.r.	n.r.
Al_2O_3	14.7	n.r.	n.r.	n.r.
Cr_2O_3	0.02	n.r.	n.r.	n.r.
FeO^T	11.5	n.r.	n.r.	n.r.
MnO	0.19	n.r.	n.r.	n.r.
MgO	5.25	n.r.	n.r.	n.r.
CaO	8.79	n.r.	n.r.	n.r.
Na_2O	3.34	n.r.	n.r.	n.r.
K_2O	0.87	n.r.	n.r.	n.r.
P_2O_5	0.36	n.r.	n.r.	n.r.
S (ppm)	121	n.r.	n.r.	n.r.
Cl(ppm)	196	n.r.	n.r.	n.r.
F(ppm)	543	n.r.	n.r.	n.r.
Total	100.8	n.r.	n.r.	n.r.
H_2O [d]	-0.8	n.r.	n.r.	n.r.
wt.% OL [e]	0.0	n.r.	n.r.	n.r.
T (° C) [f]	1153	n.r.	n.r.	n.r.
P (bars) [f]	100	n.r.	n.r.	n.r.

Table 33. continued

Year 2000 Reticulite: Major and volatile element composition determined by EPMA

Label	GI2OL20tsAral8R	GI3OL20tsAral8R	GI1ol3ts8Rrnd	GI1ol4ts8Rrnd
SiO_2	54.3	54.3	51.7	53.8
TiO_2	1.58	1.71	1.15	1.72
Al_2O_3	14.5	14.4	14.9	14.0
Cr_2O_3	0.02	0.02	0.04	0.03
FeO^T	11.3	11.4	11.8	11.4
MnO	0.17	0.20	0.22	0.20
MgO	5.36	5.08	5.07	4.72
CaO	8.43	8.83	9.12	8.69
Na_2O	3.34	3.11	3.53	3.18
K_2O	0.90	0.92	0.58	0.87
P_2O_5	0.36	0.34	0.36	0.38
S (ppm)	n/a	n/a	921	81
Cl (ppm)	n/a	n/a	529	234
F (ppm)	n/a	n/a	643	n/a
Total	100.2	100.2	98.6	99.0
H_2O by Diff. [a]	-0.2	-0.2	1.4	1.0
SIMS analyses of volatiles				
H_2O (wt.%)	n/a	n/a	n/a	n/a
CO_2(ppm)	n/a	n/a	n/a	n/a
S (ppm)	n/a	n/a	n/a	n/a
Cl (ppm)	n/a	n/a	n/a	n/a
F (ppm)	n/a	n/a	n/a	n/a
Host olivine composition [b]				
SiO_2	n/a	n/a	38.8	38.5
MgO	n/a	n/a	40.1	39.8
FeO^T	n/a	n/a	21.5	21.3
MnO	n/a	n/a	0.35	0.36
CaO	n/a	n/a	0.25	0.24
NiO	n/a	n/a	0.10	0.10
Total	n/a	n/a	101.0	100.3
Fo	n/a	n/a	0.77	0.77
Recalculated major and volatile element composition of glass inclusion [c]				
SiO_2	n.r.	n.r.	51.6	53.5
TiO_2	n.r.	n.r.	1.14	1.69
Al_2O_3	n.r.	n.r.	14.84	13.69
Cr_2O_3	n.r.	n.r.	0.04	0.03
FeO^T	n.r.	n.r.	11.8	11.6
MnO	n.r.	n.r.	0.22	0.21
MgO	n.r.	n.r.	5.18	5.33
CaO	n.r.	n.r.	9.09	8.53
Na_2O	n.r.	n.r.	3.52	3.12
K_2O	n.r.	n.r.	0.58	0.85
P_2O_5	n.r.	n.r.	0.36	0.37
S (ppm)	n.r.	n.r.	918	79
Cl(ppm)	n.r.	n.r.	527	230
F(ppm)	n.r.	n.r.	n/a	n/a
Total	n.r.	n.r.	98.6	99.0
H_2O [d]	n.r.	n.r.	1.4	1.0
wt.% OL [e]	n.r.	n.r.	0.3	1.9
T (° C) [f]	n.r.	n.r.	1134	1146
P (bars) [f]	n.r.	n.r.	1028*	262

Table 33. continued

Year 2000 Reticulite: Major and volatile element composition determined by EPMA

Label	Gl1ol5ts8Rmd	Gl2ol5ts8Rmd	Gl1ol6ts8Rmd	Gl1ol7ts8Rmd
SiO_2	54.6	54.3	53.3	53.8
TiO_2	1.60	1.53	1.56	1.53
Al_2O_3	14.4	14.2	14.2	14.6
Cr_2O_3	0.03	0.02	0.00	0.01
FeO^T	11.5	11.1	11.9	11.7
MnO	0.17	0.22	0.21	0.21
MgO	4.88	4.81	4.76	5.06
CaO	8.55	8.61	8.97	8.77
Na_2O	3.37	3.28	3.13	3.38
K_2O	0.92	0.97	0.89	0.78
P_2O_5	0.35	0.38	0.36	0.31
S (ppm)	75	41	156	380
Cl (ppm)	196	196	268	362
F (ppm)	n/a	n/a	n/a	n/a
Total	100.4	99.5	99.3	100.2
H_2O by Diff. [a]	-0.4	0.5	0.7	-0.2
SIMS analyses of volatiles				
H_2O (wt.%)	n/a	n/a	n/a	n/a
CO_2(ppm)	n/a	n/a	n/a	n/a
S (ppm)	n/a	n/a	n/a	n/a
Cl (ppm)	n/a	n/a	n/a	n/a
F (ppm)	n/a	n/a	n/a	n/a
Host olivine composition [b]				
SiO_2	38.5	38.5	38.4	38.4
MgO	40.0	40.0	39.0	39.7
FeO^T	21.3	21.3	22.2	22.0
MnO	0.35	0.35	0.35	0.36
CaO	0.27	0.27	0.25	0.24
NiO	0.09	0.09	0.10	0.11
Total	100.5	100.5	100.2	100.9
Fo	0.77	0.77	0.76	0.76
Recalculated major and volatile element composition of glass inclusion [c]				
SiO_2	54.3	54.0	n.r.	53.6
TiO_2	1.57	1.50	n.r.	1.51
Al_2O_3	14.0	14.0	n.r.	14.4
Cr_2O_3	0.03	0.02	n.r.	0.01
FeO^T	11.8	11.4	n.r.	11.9
MnO	0.18	0.23	n.r.	0.21
MgO	5.58	5.37	n.r.	5.44
CaO	8.37	8.46	n.r.	8.68
Na_2O	3.30	3.22	n.r.	3.35
K_2O	0.90	0.94	n.r.	0.77
P_2O_5	0.34	0.37	n.r.	0.31
S (ppm)	73	40	n.r.	376
Cl(ppm)	192	193	n.r.	358
F(ppm)	n/a	n/a	n.r.	n/a
Total	100.5	99.5	n.r.	100.2
H_2O [d]	-0.5	0.5	n.r.	-0.2
wt.% OL [e]	2.2	1.7	n.r.	1.2
T (° C) [f]	1171	1157	n.r.	1160
P (bars) [f]	226	205	n.r.	169

Table 33. continued

Year 2000 Reticulite: Major and volatile element composition determined by EPMA

Label	Gl1ol8ts8Rrnd	Gl1ol9ts8Rrnd	Gl1ol10ts8Rrnd	Gl2ol10ts8Rrnd
SiO_2	54.4	54.8	54.8	54.2
TiO_2	1.54	1.48	1.76	1.56
Al_2O_3	14.4	15.3	14.4	14.2
Cr_2O_3	0.02	0.03	0.01	0.02
FeO^T	11.1	10.5	10.7	11.3
MnO	0.23	0.17	0.21	0.22
MgO	5.11	4.88	4.70	4.66
CaO	8.76	8.63	8.79	9.02
Na_2O	3.26	3.32	3.28	3.21
K_2O	0.89	0.86	0.89	0.86
P_2O_5	0.37	0.38	0.38	0.36
S (ppm)	66	69	26	n/a
Cl (ppm)	198	201	202	n/a
F (ppm)	n/a	n/a	596	n/a
Total	100.1	100.4	99.9	99.6
H_2O by Diff. [a]	-0.1	-0.4	0.1	0.4
SIMS analyses of volatiles				
H_2O (wt.%)	n/a	n/a	n/a	n/a
CO_2(ppm)	n/a	n/a	n/a	n/a
S (ppm)	n/a	n/a	n/a	n/a
Cl (ppm)	n/a	n/a	n/a	n/a
F (ppm)	n/a	n/a	n/a	n/a
Host olivine composition [b]				
SiO_2	38.7	38.8	38.5	38.5
MgO	39.9	41.1	39.4	39.8
FeO^T	21.3	20.2	21.4	21.6
MnO	0.34	0.30	0.36	0.37
CaO	0.23	0.19	0.27	0.26
NiO	0.11	0.12	0.11	0.10
Total	100.6	100.7	100.1	100.6
Fo	0.77	0.78	0.77	0.77
Recalculated major and volatile element composition of glass inclusion [c]				
SiO_2	54.2	54.4	54.5	53.8
TiO_2	1.52	1.45	1.73	1.52
Al_2O_3	14.2	15.0	14.1	13.9
Cr_2O_3	0.02	0.03	0.01	0.02
FeO^T	11.3	10.9	10.9	11.6
MnO	0.23	0.17	0.22	0.23
MgO	5.49	5.69	5.35	5.45
CaO	8.66	8.43	8.61	8.80
Na_2O	3.21	3.23	3.22	3.13
K_2O	0.88	0.83	0.87	0.84
P_2O_5	0.37	0.37	0.36	0.35
S (ppm)	66	67	26	n/a
Cl(ppm)	196	196	198	n/a
F(ppm)	n/a	n/a	584	n/a
Total	100.2	100.5	99.9	99.7
H_2O [d]	-0.2	-0.5	0.1	0.3
wt.% OL [e]	1.2	2.5	2.0	2.6
T (° C) [f]	1165	1173	1158	1160
P (bars) [f]	182	188	205	243

Table 33. continued

Year 2000 Reticulite: Major and volatile element composition determined by EPMA

Label	Gl1ol11ts8Rrnd	Gl1ol13ts8Rrnd	Gl1ol14ts8Rrnd	Gl1ol15ts8Rrnd
SiO_2	54.7	54.2	54.1	54.4
TiO_2	1.47	1.46	1.62	1.67
Al_2O_3	14.4	14.6	15.3	14.4
Cr_2O_3	0.01	0.03	0.02	0.04
FeO^T	10.9	11.3	10.6	11.2
MnO	0.18	0.21	0.17	0.22
MgO	4.97	5.18	5.17	5.11
CaO	8.51	8.65	9.23	8.73
Na_2O	3.33	3.33	3.26	3.33
K_2O	0.93	0.95	0.90	1.03
P_2O_5	0.39	0.38	0.39	0.39
S (ppm)	52	n/a	n/a	n/a
Cl (ppm)	231	n/a	n/a	n/a
F (ppm)	594	n/a	n/a	n/a
Total	99.8	100.3	100.6	100.5
H_2O by Diff. [a]	0.2	-0.3	-0.6	-0.5
SIMS analyses of volatiles				
H_2O (wt.%)	n/a	n/a	n/a	n/a
CO_2(ppm)	n/a	n/a	n/a	n/a
S (ppm)	n/a	n/a	n/a	n/a
Cl (ppm)	n/a	n/a	n/a	n/a
F (ppm)	n/a	n/a	n/a	n/a
Host olivine composition [b]				
SiO_2	38.3	n/a	n/a	n/a
MgO	39.8	n/a	n/a	n/a
FeO^T	21.4	n/a	n/a	n/a
MnO	0.35	n/a	n/a	n/a
CaO	0.25	n/a	n/a	n/a
NiO	0.08	n/a	n/a	n/a
Total	100.1	n/a	n/a	n/a
Fo	0.77	n/a	n/a	n/a
Recalculated major and volatile element composition of glass inclusion [c]				
SiO_2	54.5	n.r.	n.r.	n.r.
TiO_2	1.46	n.r.	n.r.	n.r.
Al_2O_3	14.3	n.r.	n.r.	n.r.
Cr_2O_3	0.01	n.r.	n.r.	n.r.
FeO^T	11.0	n.r.	n.r.	n.r.
MnO	0.18	n.r.	n.r.	n.r.
MgO	5.25	n.r.	n.r.	n.r.
CaO	8.44	n.r.	n.r.	n.r.
Na_2O	3.30	n.r.	n.r.	n.r.
K_2O	0.92	n.r.	n.r.	n.r.
P_2O_5	0.39	n.r.	n.r.	n.r.
S (ppm)	52	n.r.	n.r.	n.r.
Cl(ppm)	229	n.r.	n.r.	n.r.
F(ppm)	589	n.r.	n.r.	n.r.
Total	99.8	n.r.	n.r.	n.r.
H_2O [d]	0.2	n.r.	n.r.	n.r.
wt.% OL [e]	0.8	n.r.	n.r.	n.r.
T (° C) [f]	1156	n.r.	n.r.	n.r.
P (bars) [f]	145	n.r.	n.r.	n.r.

Table 33. continued

Year 2000 Reticulite: Major and volatile element composition determined by EPMA

Label	GI2ol15ts8Rmd	GI1aol16ts8Rmd	GI1bol16ts8Rmd	GI1aol17ts8Rmd
SiO_2	54.5	53.7	54.0	53.5
TiO_2	1.57	1.76	1.65	1.22
Al_2O_3	14.6	14.5	14.5	15.0
Cr_2O_3	0.00	0.03	0.02	0.02
FeO^T	11.7	11.1	11.1	11.7
MnO	0.21	0.19	0.23	0.22
MgO	5.29	5.23	5.14	5.20
CaO	8.86	8.71	8.77	9.04
Na_2O	3.32	3.30	3.35	3.58
K_2O	0.90	0.91	0.90	0.74
P_2O_5	0.38	0.37	0.37	0.30
S (ppm)	n/a	n/a	n/a	n/a
Cl (ppm)	n/a	n/a	n/a	n/a
F (ppm)	n/a	n/a	n/a	n/a
Total	101.3	99.7	100.1	100.6
H_2O by Diff. [a]	-1.3	0.3	-0.1	-0.6
SIMS analyses of volatiles				
H_2O (wt.%)	n/a	n/a	n/a	n/a
CO_2(ppm)	n/a	n/a	n/a	n/a
S (ppm)	n/a	n/a	n/a	n/a
Cl (ppm)	n/a	n/a	n/a	n/a
F (ppm)	n/a	n/a	n/a	n/a
Host olivine composition [b]				
SiO_2	n/a	n/a	n/a	n/a
MgO	n/a	n/a	n/a	n/a
FeO^T	n/a	n/a	n/a	n/a
MnO	n/a	n/a	n/a	n/a
CaO	n/a	n/a	n/a	n/a
NiO	n/a	n/a	n/a	n/a
Total	n/a	n/a	n/a	n/a
Fo	n/a	n/a	n/a	n/a
Recalculated major and volatile element composition of glass inclusion [c]				
SiO_2	n.r.	n.r.	n.r.	n.r.
TiO_2	n.r.	n.r.	n.r.	n.r.
Al_2O_3	n.r.	n.r.	n.r.	n.r.
Cr_2O_3	n.r.	n.r.	n.r.	n.r.
FeO^T	n.r.	n.r.	n.r.	n.r.
MnO	n.r.	n.r.	n.r.	n.r.
MgO	n.r.	n.r.	n.r.	n.r.
CaO	n.r.	n.r.	n.r.	n.r.
Na_2O	n.r.	n.r.	n.r.	n.r.
K_2O	n.r.	n.r.	n.r.	n.r.
P_2O_5	n.r.	n.r.	n.r.	n.r.
S (ppm)	n.r.	n.r.	n.r.	n.r.
Cl(ppm)	n.r.	n.r.	n.r.	n.r.
F(ppm)	n.r.	n.r.	n.r.	n.r.
Total	n.r.	n.r.	n.r.	n.r.
H_2O [d]	n.r.	n.r.	n.r.	n.r.
wt.% OL [e]	n.r.	n.r.	n.r.	n.r.
T (° C) [f]	n.r.	n.r.	n.r.	n.r.
P (bars) [f]	n.r.	n.r.	n.r.	n.r.

Table 33. continued

Year 2000 Reticulite: Major and volatile element composition determined by EPMA

Label	Gl1bol17ts8Rmd	Gl1ol18ts8Rmd	Gl2ol18ts8Rmd
SiO_2	53.4	54.6	54.3
TiO_2	1.15	1.71	1.51
Al_2O_3	15.0	14.4	14.7
Cr_2O_3	0.03	0.01	0.02
FeO^T	11.4	11.5	11.3
MnO	0.21	0.23	0.21
MgO	5.13	5.02	5.20
CaO	9.00	8.64	8.83
Na_2O	3.59	3.26	3.30
K_2O	0.74	0.98	0.91
P_2O_5	0.27	0.38	0.38
S (ppm)	n/a	n/a	n/a
Cl (ppm)	n/a	n/a	n/a
F (ppm)	n/a	n/a	n/a
Total	99.9	100.8	100.7
H_2O by Diff. [a]	0.1	-0.8	-0.7
SIMS analyses of volatiles			
H_2O (wt.%)	n/a	n/a	n/a
CO_2(ppm)	n/a	n/a	n/a
S (ppm)	n/a	n/a	n/a
Cl (ppm)	n/a	n/a	n/a
F (ppm)	n/a	n/a	n/a
Host olivine composition [b]			
SiO_2	n/a	n/a	n/a
MgO	n/a	n/a	n/a
FeO^T	n/a	n/a	n/a
MnO	n/a	n/a	n/a
CaO	n/a	n/a	n/a
NiO	n/a	n/a	n/a
Total	n/a	n/a	n/a
Fo	n/a	n/a	n/a
Recalculated major and volatile element composition of glass inclusion [c]			
SiO_2	n.r.	n.r.	n.r.
TiO_2	n.r.	n.r.	n.r.
Al_2O_3	n.r.	n.r.	n.r.
Cr_2O_3	n.r.	n.r.	n.r.
FeO^T	n.r.	n.r.	n.r.
MnO	n.r.	n.r.	n.r.
MgO	n.r.	n.r.	n.r.
CaO	n.r.	n.r.	n.r.
Na_2O	n.r.	n.r.	n.r.
K_2O	n.r.	n.r.	n.r.
P_2O_5	n.r.	n.r.	n.r.
S (ppm)	n.r.	n.r.	n.r.
Cl(ppm)	n.r.	n.r.	n.r.
F(ppm)	n.r.	n.r.	n.r.
Total	n.r.	n.r.	n.r.
H_2O [d]	n.r.	n.r.	n.r.
wt.% OL [e]	n.r.	n.r.	n.r.
T (° C) [f]	n.r.	n.r.	n.r.
P (bars) [f]	n.r.	n.r.	n.r.

Table 33. continued

Year 2000 Reticulite: Major and volatile element composition determined by EPMA

Label	Gl1aol20ts8Rrnd	Gl2ol20ts8Rrnd	Gl3ol20ts8Rrnd
SiO_2	54.2	54.1	54.6
TiO_2	1.59	1.18	1.66
Al_2O_3	14.8	14.9	14.7
Cr_2O_3	0.02	0.03	0.12
FeO^T	11.3	11.5	11.4
MnO	0.18	0.20	0.14
MgO	5.35	5.11	5.14
CaO	8.70	9.14	9.07
Na_2O	3.28	3.61	3.37
K_2O	0.92	0.63	0.89
P_2O_5	0.34	0.34	0.35
S (ppm)	n/a	n/a	n/a
Cl (ppm)	n/a	n/a	n/a
F (ppm)	n/a	n/a	n/a
Total	100.6	100.7	101.5
H_2O by Diff. [a]	-0.6	-0.7	-1.5
SIMS analyses of volatiles			
H_2O (wt.%)	n/a	n/a	n/a
CO_2(ppm)	n/a	n/a	n/a
S (ppm)	n/a	n/a	n/a
Cl (ppm)	n/a	n/a	n/a
F (ppm)	n/a	n/a	n/a
Host olivine composition [b]			
SiO_2	n/a	n/a	n/a
MgO	n/a	n/a	n/a
FeO^T	n/a	n/a	n/a
MnO	n/a	n/a	n/a
CaO	n/a	n/a	n/a
NiO	n/a	n/a	n/a
Total	n/a	n/a	n/a
Fo	n/a	n/a	n/a
Recalculated major and volatile element composition of glass inclusion [c]			
SiO_2	n.r.	n.r.	n.r.
TiO_2	n.r.	n.r.	n.r.
Al_2O_3	n.r.	n.r.	n.r.
Cr_2O_3	n.r.	n.r.	n.r.
FeO^T	n.r.	n.r.	n.r.
MnO	n.r.	n.r.	n.r.
MgO	n.r.	n.r.	n.r.
CaO	n.r.	n.r.	n.r.
Na_2O	n.r.	n.r.	n.r.
K_2O	n.r.	n.r.	n.r.
P_2O_5	n.r.	n.r.	n.r.
S (ppm)	n.r.	n.r.	n.r.
Cl(ppm)	n.r.	n.r.	n.r.
F(ppm)	n.r.	n.r.	n.r.
Total	n.r.	n.r.	n.r.
H_2O [d]	n.r.	n.r.	n.r.
wt.% OL [e]	n.r.	n.r.	n.r.
T (° C) [f]	n.r.	n.r.	n.r.
P (bars) [f]	n.r.	n.r.	n.r.

Table 33. continued

1984 Lava: Major and volatile element composition determined by EPMA

Label	GI1OL2tsAral3Ra	GI1OL3tsAral3Ra	GI1OL4tsAral3Ra
SiO_2	54.1	53.7	56.0
TiO_2	1.18	1.72	1.59
Al_2O_3	18.2	19.9	17.1
Cr_2O_3	0.01	0.01	0.01
FeO^T	9.55	6.10	7.96
MnO	0.16	0.12	0.17
MgO	2.28	2.37	1.86
CaO	11.2	12.7	11.3
Na_2O	3.64	3.51	3.36
K_2O	0.55	0.58	0.83
P_2O_5	0.24	0.29	0.35
S (ppm)	929	n/a	n/a
Cl (ppm)	527	n/a	n/a
F (ppm)	641	n/a	n/a
Total	101.3	101.0	100.5
H_2O by Diff. [a]	-1.3	-1.0	-0.5
SIMS analyses of volatiles			
H_2O (wt.%)	n/a	n/a	0.10
CO_2(ppm)	n/a	n/a	n/a
S (ppm)	n/a	n/a	222
Cl (ppm)	n/a	n/a	289
F (ppm)	n/a	n/a	476
Host olivine composition [b]			
SiO_2	38.3	n/a	38.1
MgO	39.5	n/a	38.0
FeO^T	21.6	n/a	22.9
MnO	0.31	n/a	0.34
CaO	0.27	n/a	0.29
NiO	0.11	n/a	0.11
Total	100.0	n/a	99.8
Fo	0.77	n/a	0.75
Recalculated major and volatile element composition of glass inclusion [c]			
SiO_2	52.2	n.r.	54.2
TiO_2	1.05	n.r.	1.44
Al_2O_3	16.1	n.r.	15.4
Cr_2O_3	0.01	n.r.	0.01
FeO^T	12.1	n.r.	10.2
MnO	0.21	n.r.	0.23
MgO	5.69	n.r.	4.50
CaO	9.96	n.r.	10.3
Na_2O	3.22	n.r.	3.04
K_2O	0.49	n.r.	0.75
P_2O_5	0.21	n.r.	0.32
S (ppm)	821	n.r.	201
Cl(ppm)	466	n.r.	262
F(ppm)	567	n.r.	432
Total	101.3	n.r.	100.5
H_2O [d]	-1.3	n.r.	-0.5
wt.% OL [e]	11.6	n.r.	9.3
T (° C) [f]	1157	n.r.	1103
P (bars) [f]	1230*	n.r.	927*

Table 33. continued

All data reported in oxide wt. % except where noted; FeO^T = total Fe as FeO

n/a = not analyzed; n.r. = not reported

EPMA = Electron Probe Micro-Analysis; SIMS = Secondary Ion Mass Spectrometry

[a] H_2O by Diff. = H_2O content estimated as 100 wt.% minus the sum of major element oxides and volatile elements

[b] Host phenocryst analyzed within 10 microns of glass inclusion

[c] recalculation uses post-entrapment correction scheme of Kress and Ghiorso (2001)

[d] SIMS values for volatile content used in preference to EPMA values for recalculation where possible

[e] amount of post-entrapment crystallization of host olivine in wt.%

[f] temperature and pressure of entrapment calculated using the scheme of Kress and Ghiorso (2001)

[*] P_{Final} = 1000 bar assumed; P_{Final} = 50-100 bar assumed for all other glass inclusions

between 0 and 2.6 wt.%. The recalculated volatile contents are <3% (relative) lower than the measured values.

The major element compositions of 28 glass inclusions in plagioclase from 2000 reticulite were analyzed by EPMA (Table 34). Eleven of these plagioclase-hosted glass inclusions were analyzed for S, Cl, and F by EPMA. Three glass inclusions were recalculated for post-entrapment plagioclase crystallization using the thermodynamic model of Kress and Ghiorso (2001). The magnitude of post-entrapment crystallization of plagioclase varies between 4.3 and 8.8 wt. % (Table 35). Chemical heterogeneity in the host plagioclase crystals made it difficult to ascertain the composition of the equilibrium plagioclase at the time of glass inclusion entrapment. Several glass inclusions were found to be out of equilibrium with the arbitrary spot in the host mineral that was analyzed near the glass inclusion.

Variation diagrams of SiO_2 vs. the major elements for glass inclusions are shown in Figure 17. According to the classification scheme of LeBas et al. (1986) corrected GI's in olivine and uncorrected GI's in plagioclase are basaltic andesite. A plot of SiO_2 vs. volatile content in glass inclusions is shown in Figure 18. For olivine-hosted glass inclusions, only the ones that have been adjusted for post-entrapment crystallization are shown. For plagioclase-hosted glass inclusions, all values are shown.

Adjusted olivine-hosted glass inclusions in 2000 reticulite contain 30-380 ppm S, 170-360 ppm Cl, 490-590 ppm F, and 20-70 ppm CO_2 (SIMS). Water contents average -0.4±0.6 wt.% H_2O (by difference) and 0.3 wt. % H_2O (SIMS). One additional olivine-hosted glass inclusion is gas-rich and contains 920 ppm S, 530 ppm Cl, and 1.4 wt. % H_2O (by difference). H_2O and F were not measured for this gas-rich glass inclusion. Plagioclase-hosted glass inclusions in 2000 reticulite contain 60-440 ppm S, 220-320 ppm Cl, 500-600 ppm F, and -0.1±0.4 wt.% H_2O (by difference).

Table 34. EPMA analyses of Glass Inclusions in Plagioclase in Villarrica 2000 Reticulite samples

Major and volatile element composition determined by EPMA

Label	GI1plag2ts8ROS	GI1plag3ts8ROS	GI2plag3ts8ROS	GI1plag15ts8ROS
SiO_2	53.1	54.5	54.1	55.0
TiO_2	1.55	1.29	1.65	1.55
Al_2O_3	14.8	14.7	14.4	14.6
Cr_2O_3	0.01	0.01	0.03	0.00
FeO^T	11.1	9.93	10.7	10.6
MnO	0.21	0.20	0.22	0.21
MgO	5.35	5.60	5.29	5.25
CaO	8.76	8.80	8.36	8.23
Na_2O	3.45	3.42	3.22	3.33
K_2O	1.00	0.91	0.98	1.02
P_2O_5	0.35	0.28	0.35	0.31
S (ppm)	125	366	n/a	101
Cl (ppm)	247	254	n/a	219
F (ppm)	597	575	n/a	589
Total	99.8	99.7	99.4	100.1
H_2O by Diff. [a]	0.2	0.3	0.6	-0.1

Label	GI3plag3ts8RGS	GI2plag5ats8RGS	GI3plag5ats8RGS	GI4plag5ats8RGS
SiO_2	54.0	53.4	52.8	53.3
TiO_2	1.56	1.54	1.54	1.55
Al_2O_3	14.6	14.9	14.6	14.5
Cr_2O_3	0.02	0.00	0.02	0.01
FeO^T	11.0	11.4	11.6	11.3
MnO	0.21	0.21	0.21	0.20
MgO	5.34	5.71	5.68	5.67
CaO	8.63	8.90	8.93	8.92
Na_2O	3.54	3.22	3.26	3.24
K_2O	0.90	0.92	0.94	0.93
P_2O_5	0.37	0.32	0.32	0.30
S (ppm)	n/a	n/a	n/a	n/a
Cl (ppm)	n/a	n/a	n/a	n/a
F (ppm)	n/a	n/a	n/a	n/a
Total	100.2	100.6	99.9	99.9
H_2O by Diff. [a]	-0.2	-0.6	0.1	0.1

Table 34. continued

Major and volatile element composition determined by EPMA

Label	GI1plag2ts8RGS	GI1plag3ts8RGS	GI7plag5ats8RGS	GI8plag5bts8RGS
SiO_2	54.1	54.0	54.1	54.1
TiO_2	1.71	1.70	1.62	1.60
Al_2O_3	14.7	14.4	14.7	14.8
Cr_2O_3	0.00	0.01	0.01	0.01
FeO^T	11.1	10.8	10.6	10.6
MnO	0.22	0.19	0.20	0.22
MgO	5.33	5.31	5.11	5.36
CaO	8.64	8.76	8.70	8.81
Na_2O	3.39	3.36	3.41	3.60
K_2O	0.95	1.00	0.94	0.99
P_2O_5	0.34	0.35	0.37	0.36
S (ppm)	n/a	n/a	n/a	n/a
Cl (ppm)	n/a	n/a	n/a	n/a
F (ppm)	n/a	n/a	n/a	n/a
Total	100.4	99.9	99.8	100.4
H_2O by Diff. [a]	-0.4	0.1	0.3	-0.4

Label	GI5plag5ats8RGS	GI6plag5ats8RGS	GI3plag8ts8RGS	GI1plag11ts8RGS
SiO_2	53.5	53.7	53.8	53.9
TiO_2	1.72	1.87	1.68	1.30
Al_2O_3	15.0	14.4	14.6	15.7
Cr_2O_3	0.01	0.02	0.02	0.01
FeO^T	10.6	11.1	10.6	9.87
MnO	0.18	0.19	0.20	0.16
MgO	5.24	5.37	5.18	5.95
CaO	8.76	8.62	8.64	8.59
Na_2O	3.44	3.25	3.42	3.70
K_2O	0.97	0.94	0.93	0.90
P_2O_5	0.36	0.36	0.35	0.29
S (ppm)	n/a	136	n/a	438
Cl (ppm)	n/a	240	n/a	319
F (ppm)	n/a	604	n/a	563
Total	99.7	99.9	99.3	100.5
H_2O by Diff. [a]	0.3	0.1	0.7	-0.5

Table 34. continued

Major and volatile element composition determined by EPMA

Label	GI9plag5bts8RGS	GI10plag5bts8RGS	GI2plag8ts8RGS
SiO_2	54.0	54.3	54.3
TiO_2	1.96	1.72	1.58
Al_2O_3	14.7	14.5	15.1
Cr_2O_3	0.01	0.03	0.02
FeO^T	11.2	10.8	10.6
MnO	0.16	0.20	0.21
MgO	5.29	5.40	5.08
CaO	8.63	8.51	8.94
Na_2O	3.46	3.39	3.29
K_2O	0.94	0.93	0.92
P_2O_5	0.37	0.37	0.34
S (ppm)	59	n/a	91
Cl (ppm)	232	n/a	254
F (ppm)	531	n/a	n/a
Total	100.8	100.2	100.4
H_2O by Diff. [a]	-0.8	-0.2	-0.4

Label	GI2plag11ts8RGS	GI3plag11ts8RGS	GI4plag11ts8RGS
SiO_2	53.5	54.7	54.8
TiO_2	1.48	1.36	1.13
Al_2O_3	15.5	14.8	16.4
Cr_2O_3	0.00	0.03	0.00
FeO^T	9.84	10.3	9.28
MnO	0.19	0.16	0.14
MgO	5.86	5.78	5.44
CaO	8.59	8.41	8.48
Na_2O	3.71	3.55	3.79
K_2O	0.88	0.92	0.96
P_2O_5	0.30	0.27	0.19
S (ppm)	n/a	182	306
Cl (ppm)	n/a	297	308
F (ppm)	n/a	548	567
Total	99.9	100.4	100.7
H_2O by Diff. [a]	0.1	-0.4	-0.7

Table 34. continued

Major and volatile element composition determined by EPMA

Label	Gl1plag12ts8RGS	Gl2plag12ts8RGS	Gl3plag12ts8RGS
SiO_2	53.8	54.3	54.2
TiO_2	1.52	1.42	1.49
Al_2O_3	14.8	14.6	14.5
Cr_2O_3	0.02	0.00	0.00
FeO^T	10.5	10.9	10.9
MnO	0.20	0.23	0.24
MgO	6.25	5.64	5.63
CaO	8.49	8.83	8.76
Na_2O	3.26	3.30	3.39
K_2O	0.92	0.95	0.92
P_2O_5	0.33	0.29	0.29
S (ppm)	n/a	n/a	n/a
Cl (ppm)	n/a	n/a	n/a
F (ppm)	n/a	n/a	n/a
Total	100.1	100.4	100.3
H_2O by Diff. [a]	-0.1	-0.4	-0.3

All data reported in oxide wt. % except where noted; FeO^T = total Fe as FeO

n/a = not analyzed

[a] H_2O by Diff. = H_2O content estimated as 100 wt.% minus the sum of major element oxides and volatile elements

Table 35. Analyses of Glass Inclusions in Plagioclase in Villarrica 2000 Reticulite adjusted for post-entrapment crystallization

Major and volatile element composition determined by EPMA

Label	Gl3plag3ts8ROS	Gl2plag3ts8RGS	Gl1plag5ats8RGS
SiO_2	52.3	54.5	53.9
TiO_2	1.57	1.73	1.64
Al_2O_3	15.2	14.8	14.7
Cr_2O_3	0.03	0.01	0.02
FeO^T	11.0	10.8	10.8
MnO	0.20	0.21	0.20
MgO	5.72	5.34	5.34
CaO	9.09	8.61	8.70
Na_2O	3.30	3.40	3.43
K_2O	0.89	0.98	0.92
P_2O_5	0.32	0.38	0.37
S (ppm)	n/a	121	120
Cl (ppm)	n/a	243	225
F (ppm)	n/a	549	604
Total	99.6	100.7	100.1
H_2O by Diff. [a]	0.4	-0.8	-0.2
Host plagioclase composition [b]			
Ab	27.8	35.1	38.6
An	71.6	64	60.3
Or	0.7	0.9	1.1
Recalculated major and volatile element composition of glass inclusion [c]			
SiO_2	52.2	53.9	53.8
TiO_2	1.50	1.58	1.58
Al_2O_3	15.9	15.9	15.3
Cr_2O_3	0.03	0.01	0.02
FeO^T	10.6	9.8	10.4
MnO	0.19	0.19	0.19
MgO	5.47	4.86	5.12
CaO	9.33	8.90	8.83
Na_2O	3.30	3.44	3.46
K_2O	0.86	0.90	0.89
P_2O_5	0.31	0.35	0.36
S (ppm)	n/a	110	115
Cl(ppm)	n/a	221	216
F(ppm)	n/a	500	580
Total	99.6	100.0	100.0
H_2O	0.4	0.0	0.0
wt.% PLAG [d]	4.4	8.8	4.3
T (° C) [e]	1158	1174	1156
P (bars) [e]	473	1022	1140

All data reported in oxide wt. % except where noted; FeO^T = total Fe as FeO

n/a = not analyzed; n.r. = not reported

[a] H_2O by Diff. = H_2O content estimated as 100 wt.% minus the sum of major element oxides

[b] Host phenocryst analyzed within 10 microns of glass inclusion

[c] recalculation uses post-entrapment correction scheme of Kress and Ghiorso (2001)

[d] amount of post-entrapment crystallization of host plagioclase in wt.%

[e] temperature and pressure of entrapment calculated using the scheme of Kress and Ghiorso (2001)

Figure 17. Variation diagrams showing compositional variations of SiO_2 versus **a)** Al_2O_3, **b)** MgO, **c)** FeO^T, **d)** CaO, **e)** Na_2O, **f)** K_2O, **g)** TiO_2, and **h)** P_2O_5 for glass inclusions in phenocrysts and matrix glasses from the 2000 reticulite of Villarrica. All Fe is reported as FeO^T. Glass inclusions are hosted by olivine (OL, *open circles*), and plagioclase (PLAG, *gray X's*). Matrix glasses are denoted by *crosses*. Plotted for comparison are two analyses of olivine-hosted glass inclusions (OL, *solid triangles*) from lava erupted from Villarrica in 1984. All glass inclusions hosted by olivine have been recalculated for post-entrapment crystallization. Also plotted are silicate liquid compositions of the Villarrica magma (*large filled circles*) derived from thermodynamic modeling using MELTS (Ghiorso and Sack, 1995) and the Villarrica bulk rock composition. The MELTS-derived silicate liquid is in equilibrium with olivine Fo_{76-77} and plagioclase An_{62-63} and Cr-spinel at T = 1130-1140 °C, P = 1 bar, f_{O_2} = NNO, and water-saturated conditions. See text for further explanation.

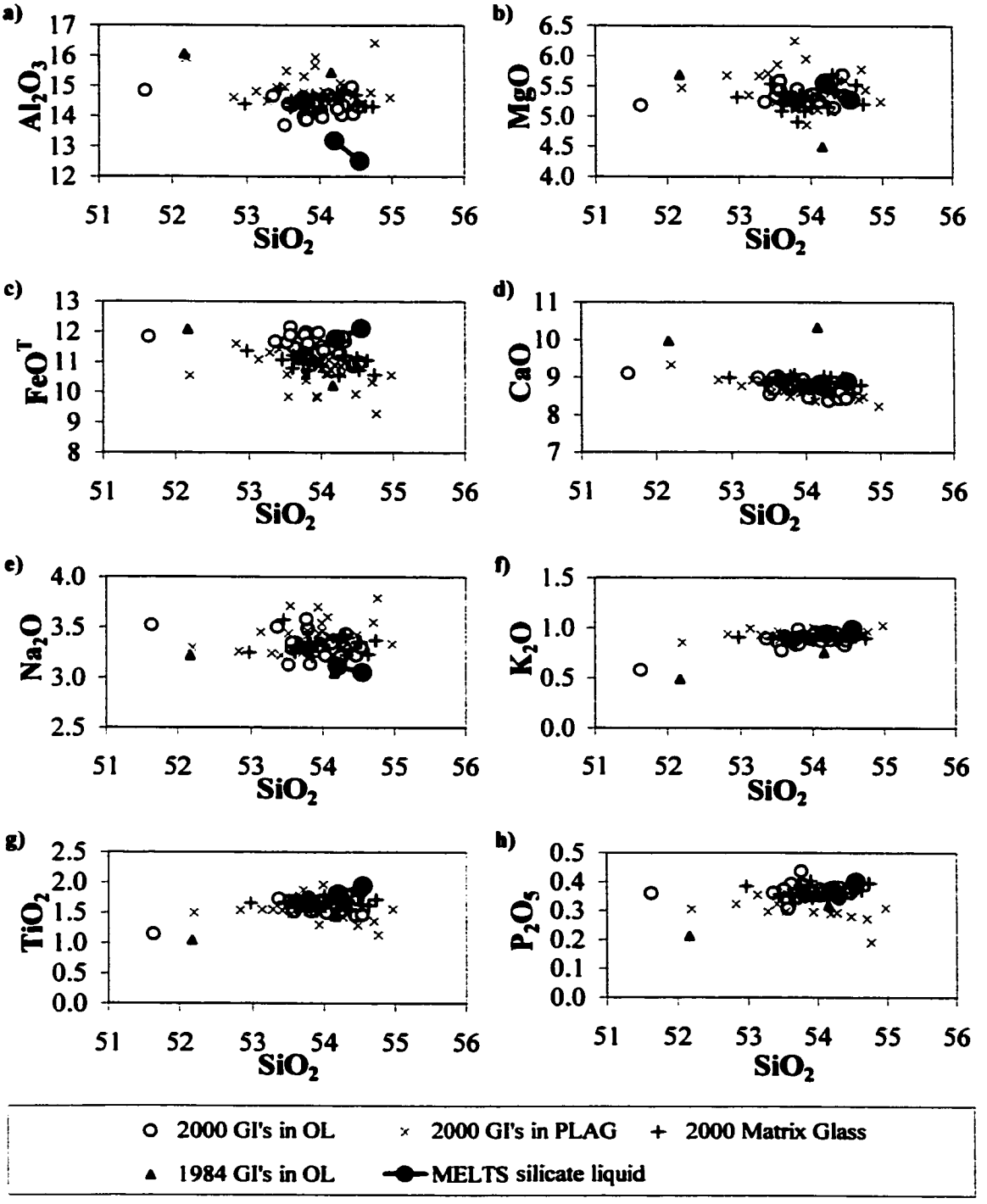
a)
Al_2O_3
17
16
15
14
13
12
51 52 53 54 55 56
SiO_2
b)
MgO
6.5
6.0
5.5
5.0
4.5
4.0
51 52 53 54 55 56
SiO_2
c)
FeO^T
13
12
11
10
9
8
51 52 53 54 55 56
SiO_2
d)
CaO
11
10
9
8
7
51 52 53 54 55 56
SiO_2
e)
Na_2O
4.0
3.5
3.0
2.5
51 52 53 54 55 56
SiO_2
f)
K_2O
1.5
1.0
0.5
0.0
51 52 53 54 55 56
SiO_2
g)
TiO_2
2.5
2.0
1.5
1.0
0.5
0.0
51 52 53 54 55 56
SiO_2
h)
P_2O_5
0.5
0.4
0.3
0.2
0.1
0.0
51 52 53 54 55 56
SiO_2
2000 GI's in OL
2000 GI's in PLAG
2000 Matrix Glass
1984 GI's in OL
MELTS silicate liquid

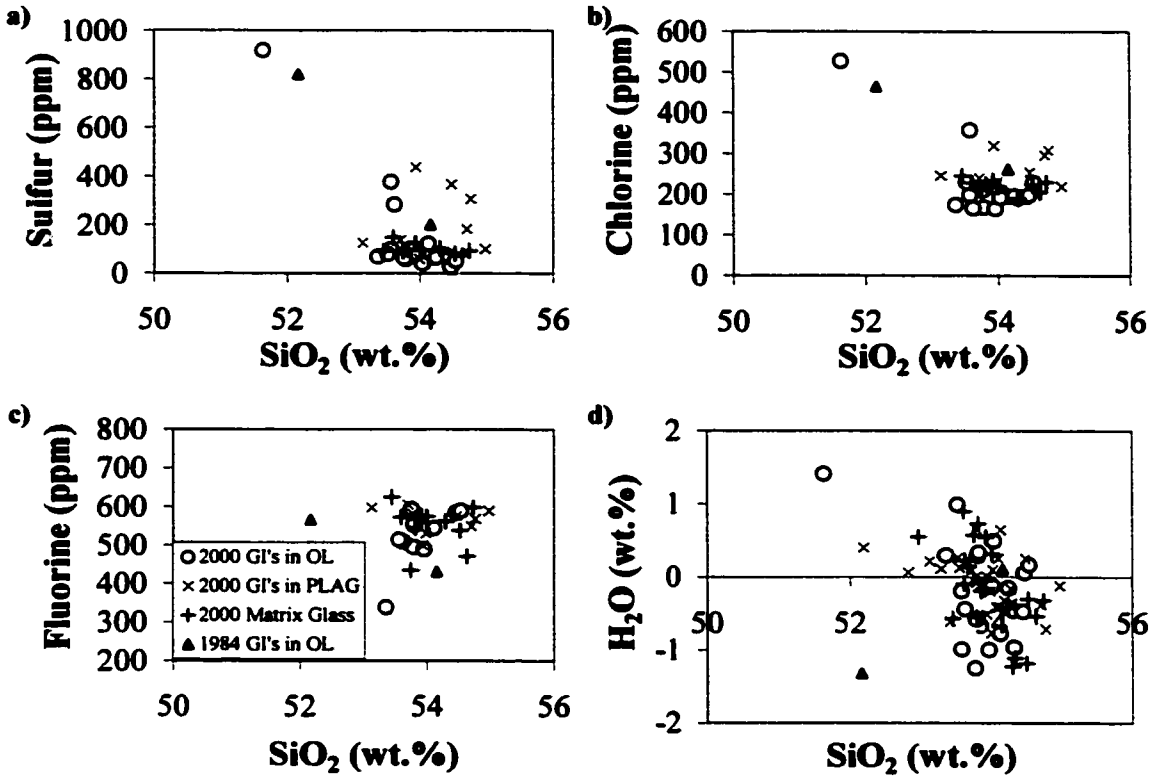

Figure 18. Volatile content in glass inclusions and matrix glasses from the 2000 reticulite of Villarrica plotted as SiO_2 versus **a)** Sulfur, **b)** Chlorine, **c)** Fluorine, and **d)** H_2O. Glass inclusions are hosted by olivine (OL, *open circles*), and plagioclase (PLAG, *gray X's*). Matrix glasses are denoted by *crosses*. Plotted for comparison are two analyses of olivine hosted glass inclusions (OL, *solid triangles*) from lava erupted from Villarrica in 1984. All glass inclusions hosted by olivine have been recalculated for post-entrapment crystallization. Errors based on counting statistics are similar in size or smaller than the symbols for S, Cl, F, and SiO_2. Errors for H_2O are estimated at ±0.5 wt.%. Minimum detection limits are estimated to be 25 ppm for sulfur, 16 ppm for chlorine, and 35 ppm for fluorine.

Matrix Glasses

Twenty major element analyses of matrix glass in the 2000 reticulite samples were made by EPMA (Table 36). Of these ten were analyzed for S, Cl, and F by EPMA. The concentration of H_2O in the matrix was calculated by difference (Anderson, 1974). No analyses of matrix glass in 1999 scoria or 1984 lava were obtained due to extensive crystallization of the groundmass in these samples.

The matrix glass of the 2000 reticulite is uniform in major and volatile element composition (Figures 17 & 18). According to the classification scheme of LeBas et al. (1986) matrix glasses are basaltic andesite. The volatile content of the analyzed matrix glasses has the range 80-150 ppm S, 190-250 ppm Cl, 470-630 ppm F, and -0.2±0.6 wt. % H_2O by difference. The variation in major and volatile elements is generally of the same order as the EPMA errors based on counting statistics.

Discussion

Estimation of Intensive Parameters: P, T, f_{O_2}

Thermodynamic modeling of post-entrapment crystallization in glass inclusions

Host mineral-glass inclusion equilibrium calculated by the post-entrapment crystallization scheme of Kress and Ghiorso (2001) provides loose constraints on the pressure, oxygen fugacity, and temperature at the time of glass inclusion entrapment. Calculations on degassed olivine-hosted glass inclusions indicate low entrapment pressures (<300 bars) and f_{O_2} <NNO. For the single gas-rich olivine-hosted glass inclusion, pressure is estimated at >1000 bars and f_{O_2} <NNO. Magmatic temperatures at the time of entrapment of silicate melt in olivine phenocrysts are calculated to have the range 1134-1173 °C. Post-entrapment crystallization calculations for three plagioclase-hosted glass inclusions indicate entrapment conditions of 470-1140 bars and 1156-1174 °C at an oxygen fugacity of NNO to NNO+1.

Table 36. EPMA analyses of matrix glasses. Results reported in oxide wt.% unless otherwise noted.

Year 2000 Reticulite	SiO_2	TiO_2	Al_2O_3	Cr_2O_3	FeO^T	MnO	MgO	CaO	Na_2O	K_2O	P_2O_5	S(ppm)	Cl(ppm)	F(ppm)	Total	H_2O^*
MGnrol18tsAral8R	54.3	1.55	14.8	0.02	11.2	0.21	5.70	8.71	3.42	0.92	0.34	102	190	561	101.2	-1.2
MG2nrol18tsAral8R	54.6	1.61	14.3	0.02	11.1	0.17	5.53	8.57	3.23	0.95	0.37	75	206	471	100.5	-0.5
MG2ts8Rmd	53.9	1.67	14.2	0.02	11.0	0.20	5.09	8.76	3.34	0.90	0.34	125	234	576	99.5	0.5
MG3ts8Rmd	53.7	1.68	14.3	0.00	10.9	0.17	5.19	8.81	3.28	0.87	0.39	90	213	435	99.4	0.6
MG4ts8Rmd	53.8	1.61	14.4	0.01	10.7	0.21	4.91	8.94	3.34	0.91	0.36	98	225	545	99.3	0.7
MG5ts8Rmd	54.5	1.63	14.4	0.02	10.7	0.19	5.29	8.88	3.35	0.87	0.38	82	224	537	100.3	-0.3
MG6ts8Rmd	54.7	1.72	14.3	0.03	10.6	0.19	5.21	8.79	3.37	0.90	0.39	94	229	597	100.3	-0.3
MG8ts8Rmd	53.6	1.58	14.3	0.00	10.8	0.20	5.09	8.94	3.26	0.90	0.35	149	228	572	99.1	0.9
MG9ts8Rmd	54.0	1.78	14.3	0.00	10.9	0.18	5.16	8.76	3.32	0.88	0.36	96	219	573	99.7	0.3
matrix1ts8ROS	53.5	1.67	14.9	0.03	11.1	0.21	5.54	8.79	3.57	0.89	0.35	92	245	625	100.6	-0.6
MG10ts8Rmd	53.0	1.65	14.4	0.04	11.4	0.19	5.32	8.99	3.25	0.90	0.39	n/a	n/a	n/a	99.5	0.5
MG11ts8Rmd	53.9	1.71	14.4	0.02	11.1	0.19	5.36	9.07	3.21	0.92	0.36	n/a	n/a	n/a	100.2	-0.2
MG12ts8Rmd	53.6	1.73	14.5	0.01	11.2	0.17	5.40	8.93	3.25	0.90	0.36	n/a	n/a	n/a	100.1	-0.1
MG13ts8Rmd	53.8	1.74	14.6	0.01	11.3	0.18	5.31	9.03	3.35	0.88	0.36	n/a	n/a	n/a	100.6	-0.6
MG14ts8Rmd	53.9	1.53	14.7	0.01	11.0	0.15	5.27	8.92	3.35	0.91	0.40	n/a	n/a	n/a	100.2	-0.2
MG15ts8Rmd	53.6	1.65	14.4	0.01	11.1	0.21	5.22	8.99	3.31	0.91	0.35	n/a	n/a	n/a	99.8	0.2
MG16ts8Rmd	54.3	1.69	14.8	0.02	11.2	0.17	5.41	9.00	3.22	0.88	0.35	n/a	n/a	n/a	101.1	-1.1
MG17ts8Rmd	53.7	1.62	14.5	0.04	11.2	0.15	5.33	8.87	3.32	0.88	0.33	n/a	n/a	n/a	99.8	0.2
MG18ts8Rmd	54.5	1.79	14.7	0.01	11.1	0.19	5.27	8.98	3.35	0.92	0.36	n/a	n/a	n/a	101.2	-1.2
MG19ts8Rmd	54.2	1.80	14.7	0.01	10.6	0.18	5.16	9.02	3.42	0.92	0.38	n/a	n/a	n/a	100.4	-0.4
Average	**54.0**	**1.7**	**14.5**	**0.0**	**11.0**	**0.2**	**5.3**	**8.9**	**3.3**	**0.9**	**0.4**	**100**	**221**	**549**	**100.2**	**-0.2**
Std. Dev. (1σ)	0.4	0.1	0.2	0.0	0.2	0.0	0.2	0.1	0.1	0.0	0.0	22	15	57	0.6	0.6

* H_2O reported as 100 wt.% minus the sum of major element oxides and volatile elements

n/a = not analyzed; FeO^T = total Fe as FeO

Saturation of dissolved H_2O and CO_2

Using the VolatileCalc 1.0 program of Newman and Lowenstern (2002) and the concentrations of H_2O and CO_2 in degassed olivine-hosted glass inclusions measured by SIMS, we calculated a pressure of 50-160 bars at an assumed temperature of 1150 °C. The results do not change for temperatures from 1050-1250 °C. This pressure estimate is consistent with the <300 bars obtained by thermodynamic modeling of post-entrapment crystallization in degassed olivine-hosted glass inclusions.

Liquidus phase MELTS simulations

Thermodynamic modeling using the MELTS algorithm (Ghiorso and Sack, 1995) is a useful tool for placing bounds on permissible ranges of intensive magmatic parameters in light of measured silicate liquid and mineral phase compositions. The uniformity in composition of the matrix glass in 2000 reticulite samples facilitates effective use of MELTS in constraining magmatic T, P, and f_{O_2} using liquidus mineral phases. The measured compositions of mineral phases that we attempt to match using MELTS are: 1) olivine phenocrysts and microphenocrysts (Fo_{76-77}), 2) plagioclase microlites and microphenocrysts < 100 μm as well as rims of plagioclase phenocrysts (An_{58-63}), and 3) high An-content concentric bands and patches in the interior of plagioclase phenocrysts (An_{71-73}). We ran MELTS simulations at varying water contents, oxygen fugacities, and pressures from 100 to 2000 bar.

The results of the MELTS modeling (Table 37) suggests that the measured olivine composition is stable under water-saturated conditions at an oxygen fugacity of QFM at P = 500-2000 bar as well as NNO at P = 100 bar. MELTS also suggests that plagioclase rims, microlites and microphenocrysts < 100 μm are stable at an oxygen fugacity of QFM and P = 100-500 bar in a relatively dry silicate liquid (H_2O = 0.1 wt. %).

To investigate the origin of the high-An concentric bands and patchy areas in the interiors of plagioclase phenocrysts, we conducted MELTS simulations with all phases suppressed except plagioclase to constrain the H_2O content and intensive

Table 37. Results of MELTS simulations showing permissible ranges of magmatic conditions that saturate the liquidus phase with the appropriate composition.

Olivine Fo_{76-77} stable liquidus phase at:

H_2O (wt. %)	fO_2	P (bar)	T_{liq} (°C)
1	QFM	500	1115-1125
1	NNO	100	1115-1125
2	QFM	500-1000	1110-1120
4	QFM	500-2000	1110-1115

Feldspar An_{58-63} stable liquidus phase at:

H_2O (wt. %)	fO_2	P (bar)	T_{liq} (°C)
0.1	QFM	100-500	1155

Feldspar An_{71-73} stable liquidus phase at:

H_2O (wt. %)	fO_2	P (bar)	T_{liq} (°C)
2	QFM	1000-2000	1040-1045
H_2O-saturated	NNO	100	1110

T_{liq} = liquidus temperature

parameters in which An_{71-73} saturates (Table 37). At H_2O = 2 wt. %, an oxygen fugacity of QFM, P = 1000-2000 bar, and T = 1040-1045 °C, plagioclase with the composition An_{72-73} is stable. In addition, An_{70} is stable under water-saturated conditions, NNO, P = 100 bar, T = 1110 °C. At higher H_2O-contents and higher oxygen fugacities, An-content is too high.

There are two physical scenarios to explain the oscillatory chemical zonation in plagioclase that are consistent with the MELTS simulations. For both scenarios, we infer that the An_{58-63} plagioclase rims, microlites, and microphenocrysts < 100 μm formed in degassed magma (~0.1 wt. % H_2O), at QFM, and low pressure (~100 bar). In the first scenario, the high-An content concentric bands and patchy areas (An_{71-73}) formed under water-saturated conditions, P = 100 bar, and at higher oxygen fugacity (NNO). In the second scenario, the An_{71-73} plagioclase formed at the same oxygen fugacity (QFM) with a higher water-content (~2 wt. % H_2O) and at higher pressure (1000-2000 bar). For both scenarios, higher water-content appears to have stabilized the higher An-content feldspar.

Bulk rock MELTS simulations

Another technique for investigating the intensive parameters of the Villarrica magma is to run MELTS simulations on the bulk rock composition using the P, T, f_{O_2} estimates from the liquidus phase simulations as a starting point. We isothermally decompressed the Villarrica bulk rock composition (chemically uniform for rocks erupted from 1984 to 2000, see Table 28) using T = 1130-1140 °C, f_{O_2} = NNO, H_2O = 2 wt. % (water-saturated conditions for P < 450 bar) and assumed equilibrium crystallization. For these conditions, MELTS predicts that all crystallization occurs at < 170 bar. At P = 1 bar, 27-31 wt. % feldspar (An_{62-63}), 5.0-6.3 wt. % olivine (Fo_{76-77}), and 0.09-0.16 wt.% spinel have crystallized and ~0.1 wt. % H_2O remains dissolved in the silicate liquid. These compositions compare well with the mineral chemistry of 2000 reticulite samples from Villarrica measured by EPMA. In addition, the mass fractions of crystallized feldspar and olivine predicted by MELTS are in

close agreement with the modal abundance of these minerals calculated by mass balance (Table 29). Higher oxygen fugacity increases the An-content of plagioclase and the Fo-content of olivine to values that are higher than observed. Lower oxygen fugacity fails to stabilize spinel. Higher initial water contents are permissible since crystallization occurs under water-saturated conditions; however, we cannot place an upper bound on pre-eruptive water content of the Villarrica magma. The silicate liquid composition calculated by MELTS is in agreement with EPMA analyses of 2000 reticulite matrix glass (Figure 17).

Magma Degassing Rate

If we assume that the volcanic gases emitted from Villarrica are derived from the silicate melt phase of magma that ascends from depth and reaches the surface at the crater-bound lava lake, we can use volatile data from gas-rich glass inclusions and co-existing degassed matrix glasses to estimate the mass rate of magma degassing. We use data collected on the three acid gases (S, Cl, and F) and the following equations (adapted from Gerlach et al., 1996):

$$M.D.R._{SO_2} = \frac{1000\ kg/ton}{86400\ sec/day} \frac{E_{SO_2}}{\left(2 \times 10^{-6}\right) \Delta S\ X_{melt}} \quad (9)$$

$$M.D.R._{HCl} = \frac{1000\ kg/ton}{86400\ sec/day} \frac{E_{HCl}}{\left(1.03 \times 10^{-6}\right) \Delta Cl\ X_{melt}} \quad (10)$$

$$M.D.R._{HF} = \frac{1000\ kg/ton}{86400\ sec/day} \frac{E_{HF}}{\left(1.05 \times 10^{-6}\right) \Delta F\ X_{melt}} \quad (11)$$

The magma degassing rate (M.D.R.) is calculated for each of the acid gases SO_2, HCl, and HF in units of kg of magma degassed per second. ΔS, ΔCl, ΔF are the average differences in S, Cl, and F content in gas-rich glass inclusions and degassed matrix glasses in ppm. The factor of 10^{-6} converts ppm to kg. The factors of 2, 1.03, and 1.05 convert kg S to SO_2, kg Cl to HCl, and kg F to HF, respectively. X_{melt} = mass fraction of silicate melt (i.e. 1 – mass fraction crystals). E_{SO_2}, E_{HCl}, and E_{HF} are the emission rates of SO_2, HCl, and HF, respectively in tons/day.

To estimate the acid gas emission rates, we assume data collected by COSPEC and filter packs in 2001 are representative of degassing rates at Villarrica. For 2001, COSPEC measurements show E_{SO_2} = 460±260 tons/day. Gas mass ratios determined from filter packs for 2001 are SO_2/HCl = 4.5±0.7 and HCl/HF = 7.8±1.6. Dividing E_{SO_2} by the SO_2/HCl gas mass ratio results in E_{HCl} = 102±42 tons/day. Dividing E_{HCl} by the HCl/HF gas mass ratio results in E_{HF} = 13±3 tons/day. To estimate the mass of melt from which this gas flux is derived, we use ΔS = 820 ppm and ΔCl = 310 ppm from the most gas-rich glass inclusion and the average of matrix glasses from 2000 reticulite (Figure 18). Due to complete overlap of the glass inclusion and matrix glass data for fluorine, we have no value for ΔF. We use X_{melt} = 0.6 based on ~40 wt. % crystals calculated from mass balance (Table 29).

Using the sulfur and chlorine flux and concentration data we calculate 5400±3050 and 6150±2550 kg/s of magma are degassed, respectively. If we use a basaltic andesite density of 2640 kg/m^3 (employing the model of Lange, 1994) we calculate 2.0±1.2 and 2.3±1.0 m^3 of magma is degassed per second for the sulfur and chlorine data, respectively. If we use an average magma degassing rate of 2.2 m^3/sec (or 5800 kg/sec) and E_{HF}=13±3 tons/day, we can back calculate a value for ΔF = 40±10 ppm. This difference is within the variation in average matrix glass and glass inclusion F contents (Figure 18). It is also about the same magnitude as the resolution of the EPMA technique used to analyze fluorine (Table 24).

If we assume a cylindrical conduit of 2-30 m radius (an estimate based on visual observations of the floor of the summit crater) and homogeneous flow of gas bubbles and silicate liquid, an average magma degassing rate of 2.2 m^3/sec implies an average magma ascent rate of 0.1-18 cm/s. If 2.2 m^3 of magma/sec is a representative volumetric rate of magma degassing over the last 17 years, this implies that a total ~1.2 km^3 of magma has degassed since the end of Villarrica's last eruption in 1985.

Initial H_2O and CO_2 contents of Villarrica magma

Burton et al. (2000) made measurements of H_2O and CO_2 emission rates at Masaya volcano (Nicaragua) using open-path Fourier transform infrared spectroscopy and derived gas mass ratios of $H_2O/SO_2 = 19.0$ and $CO_2/SO_2 = 1.62$. If we assume these mass ratios are applicable to Villarrica, this implies the emission rates E_{H_2O} and E_{CO_2} at Villarrica are 8740±4940 H_2O and 745±421 CO_2 tons/day, respectively. We can also calculate the initial concentrations of H_2O and CO_2 in the melt using the following equations:

$$H_2O\,(\text{wt.}\%) = \frac{1000\ \text{kg/ton}}{86400\ \text{sec/day}} \frac{E_{H_2O}}{(10^{-2})\text{M.D.R.}} + 0.1 \qquad (12)$$

$$CO_2\,(\text{ppm}) = \frac{1000\ \text{kg/ton}}{86400\ \text{sec/day}} \frac{E_{CO_2}}{(10^{-6})\text{M.D.R.}} \qquad (13)$$

The factor of 10^{-2} gives H_2O concentration in wt. % and the factor of 10^{-6} gives CO_2 concentration in ppm. The addition of 0.1 in Equation (12) assumes 0.1 wt. % H_2O remains in the degassed matrix glass. We assume no retention of CO_2 in degassed matrix glass. For initial H_2O and CO_2 contents, we assume no crystallization has occurred (i.e. $X_{melt} = 1$). Using M.D.R. = 5800 kg/s, we calculate initial volatile contents of 3.0±1.6 wt. % H_2O and 2480±1400 ppm CO_2. These initial H_2O and CO_2 contents, if correct, imply saturation with a gas phase at pressures > 5 kbar (VolatileCalc1.0; Newman and Lowenstern, 2002).

Mechanisms for passive degassing and heat transport

Non-homogeneous two-phase flow

Vergniolle and Jaupart (1986) modeled non-homogeneous two-phase flow of bubbles and melt in magmas of varying compositions. They found that homogeneous flow of gas and magma prevails for silicic compositions because viscosity impedes bubble motion relative to the bulk magma. For mafic volcanoes that have lower viscosity magma like Villarrica, non-homogeneous two-phase flow is likely to occur. However, such a mechanism is not efficient for transporting large volumes of gas

through a column of magma. For example, if we assume a static mafic melt with a viscosity of 100 Pa·s, the rise velocity of 1 cm radius bubbles is on the order of 1 cm/sec. Assuming a uniform distribution of 1 cm radius bubbles, spaced 10 cm apart in a 15 m radius conduit, such a geometry can be expected to produce a total volatile emission rate of only ~0.4 tons/day or an SO_2 emission rate of ~0.02 tons/day SO_2. These calculations suggest that non-homogeneous two-phase flow by itself is too inefficient to produce the high gas fluxes of passively degassing mafic volcanoes similar to Villarrica such as Etna (~5700 tons/day SO_2; Bruno et al., 1999), Stromboli (400-800 tons/day SO_2; Allard et al., 1994), and Masaya (~1800 tons/day SO_2; Burton et al., 2000).

Another argument against non-homogeneous two-phase flow as the dominant degassing mechanism at Villarrica involves heat flow. The amount of heat supplied by gas bubbles rising through a static magma column must outpace conductive cooling through the walls to prevent solidification of the volcanic conduit. The persistence of Villarrica's lava lake for 17 years requires a substantial and continuous heat flux. Using a simple model of conductive cooling (Turcotte and Schubert, 1982), static mafic magma in a 15 m radius conduit loses ~3300 Joules/sec per vertical meter by conduction. With no heat added, a 15 m radius magma-filled conduit will solidify in less than 3 years. If heat is added from an ascending gas phase, we require a flux of ~9 m^3/sec (or ~150 tons/day) of gas as bubbles to prevent the magma in the conduit from solidifying for an arbitrary conduit length of 1 km. A gas flux of this magnitude is unlikely to rise through the conduit without generating its own convective flow in the surrounding magma. Thus, non-homogeneous flow of gas bubbles in a static magma column is not a sufficient heat transport mechanism to explain the persistence of the summit lava lake observed at Villarrica for the last 17 years.

We hypothesize that ascending magma is continuously introduced to the summit crater. This magma could potentially supply both the volatiles that continually degas from Villarrica as well as the heat to prevent solidification of the

conduit. The volcanic conduit presumably connects the summit lava lake to a larger reservoir of magma at depth.

Using petrologic, gas, and thermal remote sensing data, several workers have hypothesized that 1) endogenous growth of the volcanic edifice due to intrusion of degassed magma or 2) magma convection in the volcanic conduit are mechanisms by which volatiles and heat can be supplied to the surface at passively degassing volcanoes and lava lakes (Allard et al., 1994; Kazahaya et al., 1994; Allard, 1997; Harris and Stevenson, 1997; Stevenson and Blake, 1998; Harris et al., 1999; Kazahaya et al., 2002). For the case of Villarrica, if a small volume of magma is needed in order to supply the volatiles and heat emitted over the last 17 years, then storage of the degassed magma in the volcanic edifice might seem feasible. However, storage of ever increasing volumes of degassed magma in the flanks of the volcano could eventually cause deformation and perhaps gravitational destabilization of the edifice. At Villarrica, another possible transport mechanism for both volatiles and heat is convective circulation of magma in the volcanic conduit which does not require intrusion of large volumes of magma into the volcanic edifice.

Endogenous growth of the volcanic edifice

To test the hypothesis of endogenous growth of the Villarrica volcanic edifice by intrusion of degassed magma, we employ modified Mogi modeling (Okada, 1992) to estimate surface deformation associated with intrusion of 1.2 km^3 of magma. The Villarrica volcanic edifice has a maximum vertical relief of ~2.5 km on its western side therefore intrusion of magma to depths shallower than 2.5 km would be contained within the volcanic edifice. Calculations using the Mogi.m code by P. Cervelli (http://kilauea.stanford.edu/ cervelli/software/mogi.html) predict 50 m of vertical displacement for 1.2 km^3 emplaced at 2.5 km depth. Intrusion of degassed magma to depths shallower than 2.5 km would result in vertical deformation greater than the 50 m predicted above. At the time of writing, degassing at Villarrica shows no signs of abatement; further production of degassed magma would result in greater amounts of deformation. Although there are no published measurements of

deformation of the flanks of Villarrica, deformation of the magnitude predicted above would be apparent visually and/or could potentially cause landslides and debris avalanches by causing oversteepening and gravitational instability of parts of the cone. Since the end of Villarrica's last eruption, there have been no reports of mass movements on the flanks of Villarrica. Careful GPS deformation measurements at Villarrica would be useful to more accurately test this hypothesis.

Intrusion of degassed magma to depths greater than 2.5 km, thereby reducing surface deformation to a minimum, may be possible, however, it seems unlikely since there is no pressure source to propagate a dike of degassed magma downward into the crust. One plausible mechanism to avoid excess accumulation of degassed magma in the volcanic edifice is to transport the degassed magma back down the volcanic conduit allowing more gas-rich magma to ascend and degas.

Magma convection in the conduit

To test the hypothesis of magma convection in the conduit as a mechanism for volatile and heat transport at Villarrica we use a simple fluid dynamic model (Figure 19). The following equation is based on the theory of laminar flow in a vertical cylindrical conduit as well as experiments by Stevenson and Blake (1998):

$$Q = \pi\left(R^{*}\right)^{2} Ps\left(g\,\Delta\rho\,R_{c}^{4}/\mu_{d}\right) \qquad (14)$$

where Q = volumetric rate of magma degassing (m^3/s), $R^{*} = R_a/R_c$ is the dimensionless ratio of the radius of the ascending flow of magma (R_a) to the radius of the conduit (R_c), Ps is the dimensionless Poiseuille number (Koyaguchi and Blake, 1989), g = 9.8 m/s^2, $\Delta\rho$ = the density difference between degassed and undegassed magma (kg/m^3), and μ_d = viscosity of the descending, degassed magma (Pa·s). We can rearrange Equation (14) to solve for conduit radius, R_c:

$$R_{c} = \sqrt[4]{\frac{Q\ \ \mu_{d}}{\pi\left(R^{*}\right)^{2} Ps\,g\,\Delta\rho}} \qquad (15)$$

For the case of conduit convection at Villarrica, we use Q = 2.2 m^3/s from the calculations above. Ps has a constant value of 0.064 and R^{*} has a value of 0.6 based

Figure 19. Schematic illustration of magma convection in the volcanic conduit at Villarrica. Magma may be saturated with a CO_2-dominated gas phase to pressures greater than 5 kbar (?). Ascending, volatile-rich magma crystallizes olivine and plagioclase, trapping melt inclusions, at shallow levels ($P < 170$ bar). Magma degasses to the atmosphere from the lava lake. Dense, degassed, crystal-rich magma descends in the volcanic conduit. Diagram not to scale.

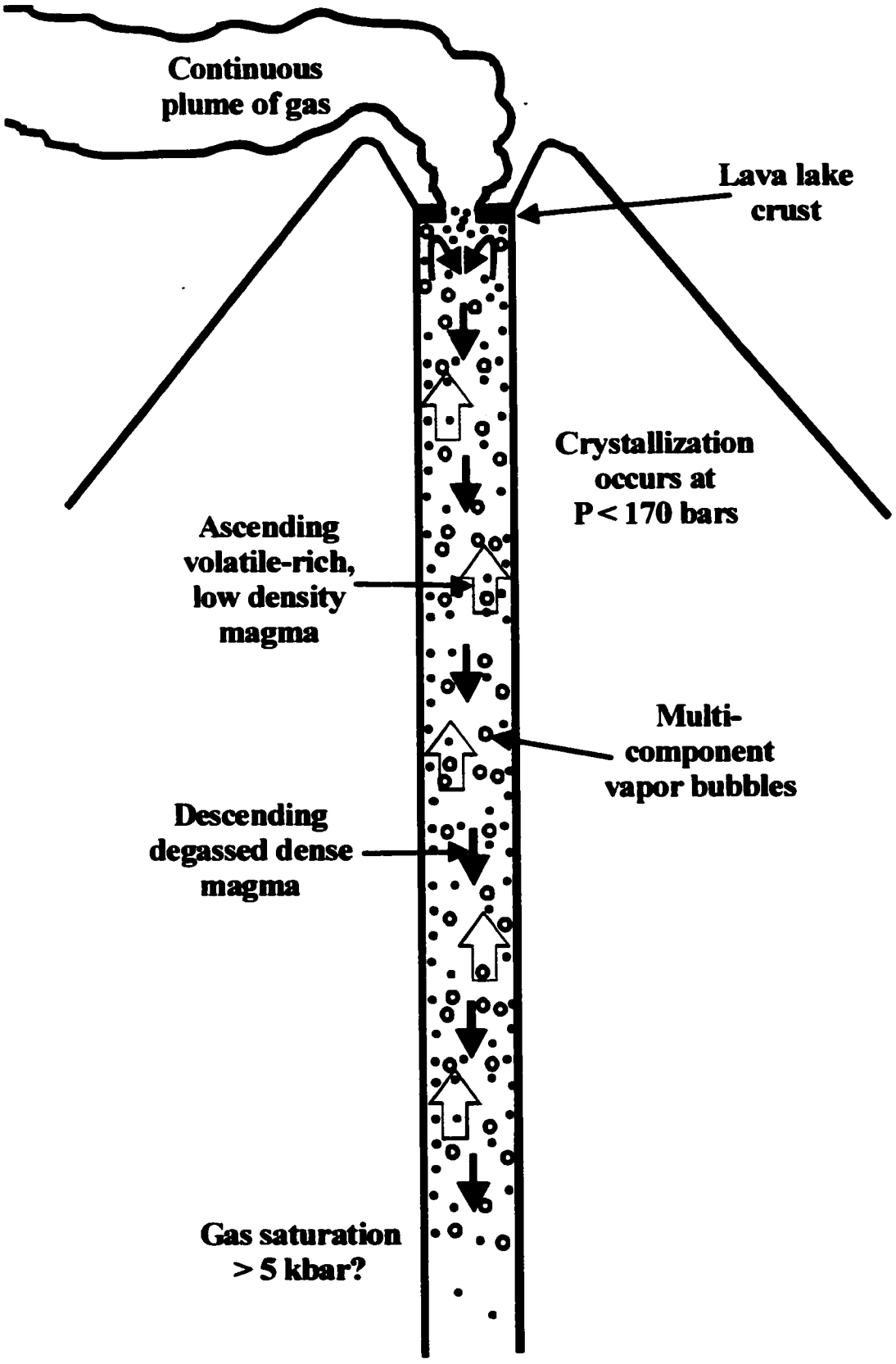
Continuous plume of gas
Lava lake crust
Crystallization occurs at P < 170 bars
Ascending volatile-rich, low density magma
Multi-component vapor bubbles
Descending degassed dense magma
Gas saturation > 5 kbar?

on experiments (Stevenson and Blake, 1998). For density and viscosity calculations of the degassed and undegassed magma we use 38 vol. % and 0 vol. % crystals, respectively at T = 1140 °C. We consider two cases: pre-eruptive H_2O contents of 1 wt. % and 4 wt. % that completely degas to 0.1 wt. % H_2O. The calculated density differences between the degassed and undegassed magma for these two cases are 100 kg/m^3 and 280 kg/m^3, respectively, using the density model of Lange (1994). This density difference does not include the dramatic density decrease due to bubble growth.

The viscosities of the undegassed and degassed magmas are calculated using the non-Arrhenian viscosity model for Mt. Etna basaltic melt (Giordano and Dingwell, 2003). Melt viscosity is weakly dependent on the major element bulk composition of the magma (Giordano and Dingwell, 2003). The differences in bulk composition of Etna basaltic melt and Villarrica basaltic andesite melt are minor. Therefore, the viscosity calculations using Giordano and Dingwell (2003) are likely very close to the viscosity of Villarrica silicate melt and are sufficiently accurate for our purposes. Villarrica melt viscosity values calculated by Giordano and Dingwell (2003) and Shaw (1972) are very similar for anhydrous compositions. However, for hydrous compositions, the Shaw model predicts viscosities that are higher than those predicted by Giordano and Dingwell (2003). At higher H_2O contents, the discrepancy between the two models increases reaching an order of magnitude at 3 wt. % H_2O.

The calculated melt viscosity for degassed magma is coupled with the Einstein-Roscoe equation (Lejeune and Richet, 1995) which accounts for the effect of crystals on the bulk viscosity. The effect of bubbles on viscosity is minor and is ignored. The crystal-free viscosities of undegassed magma are 18 Pa·s and 0.5 Pa·s for 1 wt. % H_2O and 4 wt. % H_2O, respectively. The viscosity of the descending magma (μ_d) that has degassed to 0.1 wt. % H_2O is 145 Pa·s for crystal-free magma and 1780 Pa·s for 38 vol. % crystals. Utilizing Equation (15), the calculated conduit radius R_c is 2.7 m for the 1 wt. % H_2O case and 2.1 m for the 4 wt. % H_2O case. These values are within the range of conduit radius estimates based on visual

observations. For comparison, Kazahaya et al. (1994) calculated a conduit radius of ~2.5 m for the basaltic Izu-Oshima volcano with a degassing rate $Q = 4\ m^3/s$, $\Delta\rho = 70\ kg/m^3$, and $\mu_d = 100$ Pa·s.

Heat transport

Considering the calculated estimates for magma flux and conduit radius presented above for Villarrica, we can use the equations for heat transport to test the hypothesis that circulation of magma in the conduit can carry sufficient heat to keep the magma in the conduit molten and explain the long-lived nature of the summit lava lake. To do this we solve the one-dimensional, time-dependent, heat conduction equation (Turcotte and Schubert, 1982):

$$\frac{\partial T}{\partial t} = \kappa \frac{\partial^2 T}{\partial x^2} \tag{16}$$

Thermal diffusivity κ is defined as (Turcotte and Schubert, 1982):

$$\kappa = \frac{k}{\rho C_P} \tag{17}$$

Using an average magma density of $\rho = 2500\ kg/m^3$, specific heat $C_P = 1500$ J/kg·K (Spera, 2000) and thermal conductivity $k = 3.0$ J/s·m·K (Spera, 2000) implies $\kappa = 8 \times 10^{-7}\ m^2/s$. Geologically reasonable variations in these variables will not affect the outcome. The heat equation can be solved using the similarity variable approach (Turcotte and Schubert, 1982). The solution to the heat equation is incorporated into Fourier's law,

$$q_{heat} = -k \frac{dT}{dx} \tag{18}$$

where q_{heat} is the heat flux (in $J/s \cdot m^2$), and dT/dx is the temperature gradient. Evaluated at x = 0 (wall of conduit):

$$q_{heat} = \frac{k(T_m - T_0)}{\sqrt{\kappa t \pi}} \tag{19}$$

where $T_m = 1413$ K (1140 °C, magma temperature), $T_0 = 298$ K (25 °C, country rock temperature), and t is time in seconds. By setting t = 18 years (5.7×10^8 s), the age of

the present lava lake, we calculate the current heat flux across the conduit wall $q_{heat} = 88$ J/s·m^2. This is based on the assumption that Villarrica's conduit has been filled with magma from the beginning of the last eruption in 1984 up to the present.

To apply this heat flux to the geometry of the Villarrica conduit, we need to multiply q_{heat} by the surface area of the walls of the conduit through which heat is transported. For an arbitrary vertical interval in the conduit with length $\ell = 1$ m, and using an average value for the conduit radius, r = 2.4 m, we can calculate the amount of heat transport out through the conduit walls and into the country rock per vertical meter of the conduit (q_{out}) in units of J/s:

$$q_{out} = q_{heat} A_{wall} \qquad (20)$$

where $A_{wall} = 2\pi r\ell$. This equation gives $q_{out} = 1327$ J/s per vertical meter of conduit. If magma ascending through this vertical meter of the conduit can supply more heat than that which is lost by conduction through the conduit walls, then the magma in the conduit will remain molten and the conduit will not solidify.

The magma flux Q = 2.2 m^3/s and conduit radius r = 2.4 m imply a magma ascent rate of v = 0.12 m/s. This ascent velocity implies a time $t_{transit} = 8.2$ sec for magma to transit a 1 m section of conduit. Multiplying q_{out} by $t_{transit}$ gives 1.1×10^4 J which is the amount of heat lost by the 1 m packet of magma filling the conduit during an ascent of 1 m. Ascending through and arbitrary conduit length of 1 km, the 1 m packet of magma will lose $H_{lost} = 1.1 \times 10^7$ J. We can calculate the amount of heat, H_0 (in Joules), originally contained in the 1 m packet of magma before ascent using the following equation:

$$H_0 = C_P T_m \rho \pi r^2 \ell \qquad (21)$$

Using values for the variables from above, $H_0 = 9.5884 \times 10^{10}$ J. We can calculate the temperature decrease attributable to the heat lost by modifying and rearranging Equation (21):

$$\Delta T = T_m - \frac{H_0 - H_{lost}}{C_P \rho \pi r^2 \ell} \qquad (22)$$

The calculated temperature decrease ΔT due to conductive heat loss is negligible (~0.2 °C).

Based on the negligible temperature decrease, we conclude that convection of magma in the volcanic conduit at Villarrica is a feasible mechanism for transporting both the volatiles to produce the observed gas emissions and the heat necessary to prevent the conduit and lava lake from solidifying.

Conclusions

1) In 2001, Villarrica emitted 460±260 tons/day SO_2, 102±42 tons/day HCl, and 13±3 tons/day HF.
2) The major and trace element bulk composition of Villarrica magma (basaltic andesite) has been identical from 1984 to the present.
3) Samples of Villarrica magma obtained in 2000 from the lava lake contain 33 wt. % zoned and unzoned plagioclase (An_{58-71}), 7 wt. % unzoned olivine (Fo_{76-77}), and trace amounts of chromian spinel.
4) Glass inclusions in olivine and plagioclase are basaltic andesite in composition, are mostly degassed, and contain 30-440 ppm S, 170-360 ppm Cl, 490-600 ppm F, 0.1±0.6 wt.% H_2O, and 20-70 ppm CO_2. One gas-rich glass inclusion in olivine contains 920 ppm S, 530 ppm Cl, and ~ 2 wt. % H_2O.
5) Matrix glasses are basaltic andesite and contain 80-150 ppm S, 190-250 ppm Cl, 470-630 ppm F, and 0.1±0.6 wt. % H_2O.
6) MELTS modeling suggests that all crystallization occurred at shallow depth, P < 170 bar, T = 1130-1140 °C, f_{O_2} = NNO under water-saturated conditions. The upper bound for the initial amount of dissolved H_2O in Villarrica melt is unconstrained but it is at least 2 wt. % H_2O.
7) The current average magma degassing rate at Villarrica is 2.2 m^3/sec (or 5800 kg/sec) which implies ~1.2 km^3 of magma has degassed since the end of the last eruption in 1985.

8) Intrusion of 1.2 km^3 of degassed magma into the volcanic edifice would cause >50 m of vertical deformation. GPS measurements on the flanks of Villarrica would be useful to test if deformation is occurring. Large-scale endogenous growth of the edifice, however, is unlikely due to the lack of visible bulging of the edifice and absence of mass wasting of the cone as a result of deformation-induced gravitational instability.
9) Convection of magma in a volcanic conduit with ~5 m diameter is a viable mechanism for transporting both the volatiles and heat to produce the observed gas emissions and prevent the lava lake from solidifying.

Chapter 4:

An analysis of magma convection in volcanic conduits

Introduction

Convection of magma in the volcanic conduit is a hypothesis that has been proposed to explain long-term, continuous, high rates of gas emission and heat loss at non-explosive, passively degassing volcanoes. (Allard et al., 1994; Kazahaya et al., 1994; Allard, 1997; Harris and Stevenson, 1997; Harris et al., 1999; Simakin and Botcharnikov, 2001; Kazahaya et al., 2002). A potential candidate for convection of magma in the volcanic conduit is any volcano that: 1) emits large quantities of volatiles, 2) has no viable alternate sources of volatiles other than magma, 3) does not erupt sufficient quantities of magma to produce the observed gas emission, and for which 4) endogenous growth of the volcanic edifice from intruded magma is minimal. Conduit convection processes have been inferred at volcanoes that cover a wide spectrum of magma compositions from basaltic (e.g. Etna, Izu-Oshima), through andesitic and dacitic (e.g. Sakurajima, Mt. St. Helens), to rhyolitic (e.g. Satsuma-Iwojima). Although conduit convection may be a viable magma transport mechanism at these and other volcanoes, direct evidence of this process is lacking. A test for the feasibility of conduit convection under a variety of magmatic conditions might provide additional support for the conduit convection hypothesis.

The purpose of this chapter is to explore the range of magmatic conditions for which conduit convection may or may not occur. The Reynolds number (Re), velocity scale (W), and average ascent velocity (V) of magma in a conduit are calculated for a range of viscosity, density difference, magma flux, and conduit size values. We also explore the effect of cylindrical vs. dike-shaped conduits. Magma velocity results are compared with calculations of the Stokes ascent velocity for bubbles of varying diameter in order to assess the effects of differential motion between bubbles and the surrounding silicate liquid (i.e. separate two-phase flow). This analysis is applied to

two passively degassing volcanoes Popocatépetl (Mexico) and Villarrica (Chile) where conduit convection is thought to be the dominant degassing mechanism.

Background

Convection of magma in volcanic conduits is driven by degassing (Kazahaya et al., 1994). During degassing, gas bubbles escape from magma either directly into the atmosphere from the exposed surface of the magma column or through the wall of the volcanic conduit into country rock. Magma-gas separation leaves behind a crystal-rich residue that is much denser than the bubble-rich magma beneath it that has not yet degassed. The density difference between the degassed magma and the underlying bubble-rich magma creates an inherently unstable density gradient. This gravitational instability causes the dense, degassed magma to sink. It is the negative buoyancy of degassed magma at the top of the volcanic conduit that initiates and sustains convection. Volatile-rich surrounding magma will ascend because it is less dense than and displaced by the descending degassed magma. Assuming there is no mixing between the degassed magma and the surrounding magma, the degassed magma will descend through magma with progressively lower bubble contents and higher bulk density. The negative buoyancy of descending degassed magma decreases with depth. At deeper levels in the volcanic conduit, below the level at which bubbles nucleate, small buoyancy contrasts persist between lower-density magma that is rich in dissolved volatiles and higher-density degassed magma. This density contrast continues to drive degassed magma downwards.

Convection of magma in volcanic conduits is hindered by the magma viscosity which is itself controlled by a variety of competing factors. The loss of dissolved volatiles from silicate melt during decompression sharply increases the viscosity of the melt phase of magma (Spera, 2000). Crystallization also increases the bulk viscosity of magma. Increasing the gas volume fraction of magma by bubble nucleation and expansion can either increase or decrease the bulk viscosity of magma (Manga et al., 1998; Stein and Spera, 2002). The complex interplay of these factors

and the changing value of magma viscosity during ascent provide one of the challenges for understanding magma convection in volcanic conduits.

An important, but subordinate, process that also drives magma ascent in volcanic conduits is separate two-phase flow (Vergniolle and Jaupart, 1986). At shallow levels in the conduit where confining pressure is low enough that volatile exsolution occurs, gas bubbles will ascend through the surrounding silicate liquid due to the large silicate-gas density difference. As the bubbles ascend, they drag with them some of the surrounding silicate liquid, continue to grow due to decompression and volatile diffusion, and subsequently rise faster. The ascent of magma as a result of separate two-phase flow is difficult to quantify because of uncertainties in the bubble size and bubble-size distribution with depth in the conduit and the amount of silicate melt carried upwards by viscous drag effects.

Figure 20 is a schematic diagram of a magma-filled volcanic conduit connecting a reservoir of magma at depth with the surface. At a certain depth all volatiles are dissolved in the magma and there is no separate bubble phase (Figure 20; this depth coincides with the top of the main magma reservoir, though saturation levels can be even deeper). At progressively lower pressures, magma contains a larger volumetric proportion of gas and has a lower bulk density. It is important to note that prior to degassing and with no relative motion between bubbles and silicate liquid, a stable vertical gradient in the magma's bulk density exists in the conduit. It is the combination of negative buoyancy of degassed magma and separate two-phase flow that this stable density gradient is destroyed and convection occurs.

Previous work

Kazahaya et al. (1994) presented a simple fluid dynamic treatment of convection of magma in the volcanic conduit using two models: 1) Poiseuille flow in a concentric double-walled pipe and 2) descent of degassed magma spheres through a gas-rich magma column. Stevenson and Blake (1998) refined the model of Kazahaya et al. (1994) with experiments. These simple fluid dynamic models have been used to

Figure 20. Schematic illustration of magma convection in the volcanic conduit. Diagram not to scale.

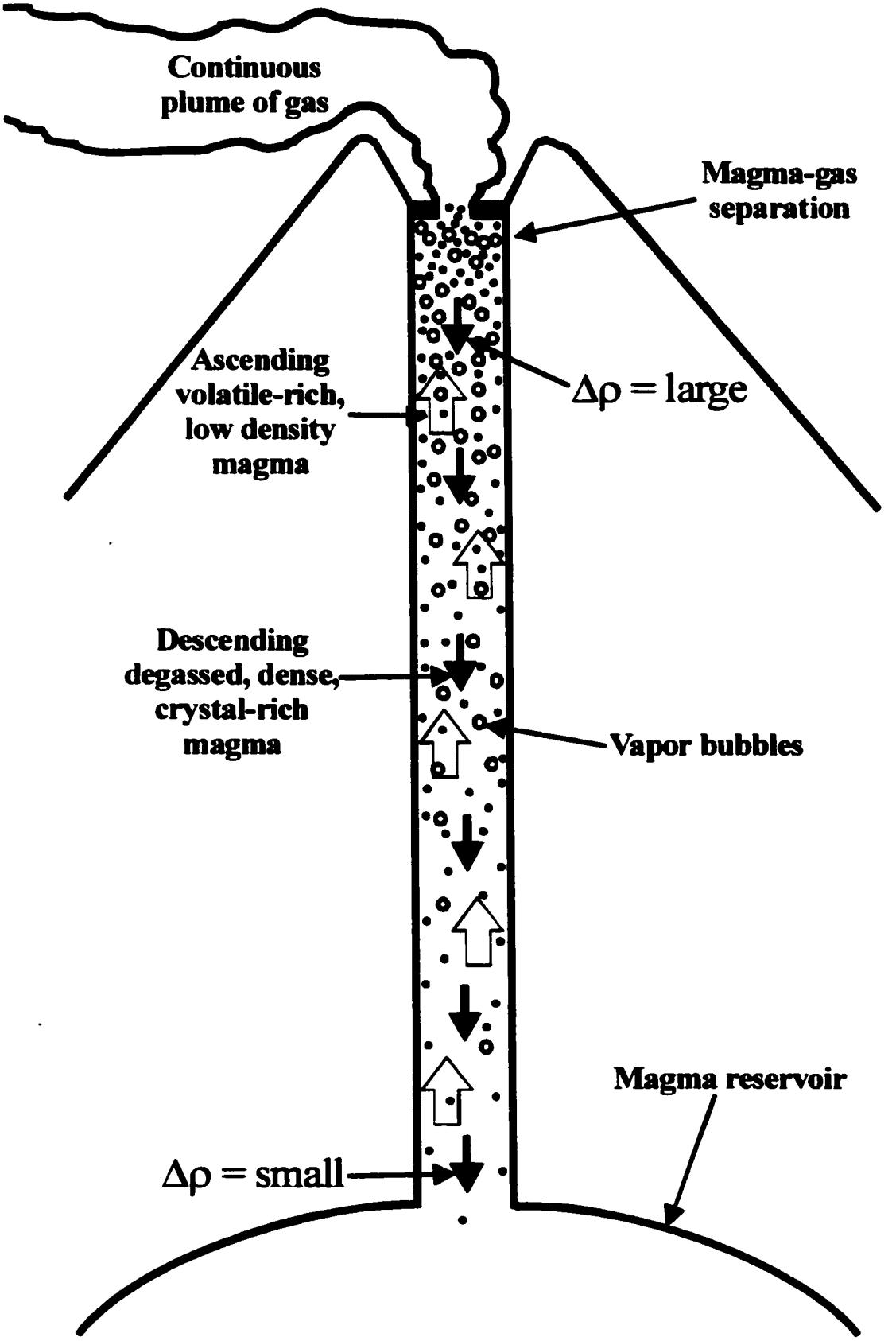
Continuous plume of gas
Magma-gas separation
Ascending volatile-rich, low density magma
Δρ = large
Descending degassed, dense, crystal-rich magma
Vapor bubbles
Magma reservoir
Δρ = small

explain high rates of passive degassing at several mafic and silicic volcanoes such as Izu-Oshima and Sakurajima (Kazahaya et al., 1994), Satsuma Iwojima (Kazahaya et al., 2002), Stromboli and Mt. St. Helens (Stevenson and Blake, 1998), Popocatépetl (Chapter 2), and Villarrica (Chapter 3).

These simple fluid dynamic models have four drawbacks. First, values for density difference and viscosity may be held constant in calculations of magma convection. In fact, the density difference between ascending and descending magma ranges over two orders of magnitude and the viscosity of magma varies by several orders of magnitude due to the combined effects of volatile loss and crystallization. Second, the density difference that drives convection is assumed to be the difference in density between magma rich in dissolved volatiles and degassed magma. The role of bubbles in creating density variations is ignored. Third, ascending gas-rich magmas and descending degassed magmas are not allowed to mix. In fact, the extent of mixing between ascending and descending magmas may play an important role in controlling magma convection in the volcanic conduit. Fourth, the volcanic conduit is assumed to be vertical. Inclined conduits may reduce viscous drag effects and facilitate magma convection by allowing degassed magma to descend along the footwall while gas-rich magma ascends along the hanging wall.

A more robust method for predicting convective magma flow in the volcanic conduit would involve finding simultaneous solutions to the equations for continuity, momentum, and heat transfer in an iterative, multi-phase, numerical model. A model such as this could account for the drawbacks in the simple fluid dynamic treatments discussed above, provide a detailed description of the changes in magmatic parameters (e.g. density, viscosity, gas volume fraction, etc.) during magma convection, and give an accurate assessment of magma ascent/descent velocity and rate of degassing. Our Reynolds number and velocity scale analysis provides important preliminary results for a more advanced and rigorous numerical investigation.

Numerical calculations and results

Reynolds number and velocity scale analysis

The flow regime of magma in a conduit can be described by a dimensionless parameter called the Reynolds number (Re). The Reynolds number is the ratio of inertial forces to viscous forces and has the following general definition (Bird et al., 1960):

$$\mathrm{Re} = \frac{W L}{\eta} \tag{23}$$

where W = velocity scale (m/s), L = length scale (m), and η = kinematic viscosity (m^2/s). Kinematic viscosity is the ratio of the dynamic viscosity (μ in Pa·s) to the ambient density (ρ in kg/m^3). Systems with Re > 1 are inertia-dominated; vortex instabilities, roll-ups, and eddies exist in the flow. Systems with Re < 1 are viscous-dominated and the flow is laminar. For our analysis of convection in volcanic conduits, we define the length scale (L) as the maximum eddy (vortex) size. Eddies generally have an aspect ratio of ~1 (Moore and Safman, 1974) so the maximum eddy size corresponds to the radius of a cylindrical conduit or the half-width of a dike, depending on the chosen geometry.

The equations for convective velocity scale take different forms for different values of Re based on numerical modeling (Deardorff, 1970) and dimensional analysis (Munson et al., 1998):

for Re > 1 $$W = \sqrt[3]{BL} \tag{24}$$

for Re < 1 $$W = \frac{BL^3}{\eta^2} \tag{25}$$

where the buoyancy flux (B in m^2/s^3) is defined by Jellinek et al. (1999) as:

$$B = g\frac{Q}{A}\frac{\Delta\rho}{\rho} \tag{26}$$

with g = gravitational acceleration (9.8 m/s^2), Q = volumetric flux of magma (m^3/s), A = cross-sectional area of the volcanic conduit, $\Delta\rho$ = difference in density between

ascending and descending magma (kg/m^3), and ρ = density of the ambient magma (kg/m^3).

Reynolds number

Combining the two definitions for the convective velocity scale (Equations 24 & 25), with the definition for Re (Equation 23), we obtain two equations to calculate the Reynolds number:

$$\text{for Re} > 1 \qquad \mathrm{Re} = \frac{B^{\frac{1}{3}} L^{\frac{4}{3}}}{\eta} \tag{27}$$

$$\text{for Re} < 1 \qquad \mathrm{Re} = \frac{B L^4}{\eta^3} \tag{28}$$

The density difference between ascending and descending magma as well as magma viscosity vary widely for different magmas. Values for these parameters also change with depth in the conduit. In addition, magma flux and conduit dimensions are different at different volcanoes. By investigating the values of Re for a range of magma viscosities, densities, flux, and conduit dimensions, we can gain insight into the flow regime for the specific conditions chosen.

Figures 21 & 22 show plots of dynamic viscosity (μ in Pa·s) of ascending magma vs. Reynolds number for convection in cylindrical and dike-shaped conduits. In these calculations, we explore length scales (L) with the range 1 to 50 m, volumetric fluxes of magma (Q) of 0.1 to 100 m^3/s, density differences ($\Delta\rho$) of 10 to 1000 kg/m^3, and dynamic viscosities (μ) of 10^0 to 10^8 Pa·s. We chose these ranges of values for the following reasons. The typical size of volcanic conduits for non-explosively degassing volcanoes is from a few meters to a few tens of meters (Swanson and Holcomb, 1990; Kazahaya et al., 1994) and magma fluxes range from a few m^3/s to several tens of m^3/s (Kazahaya et al., 1994; Sparks et al., 1998; Nakada et al., 1999). Small differences in the major element composition of magma result in $\Delta\rho \sim 10$ kg/m^3 (Lange, 1994). Due to the large partial molar volume of H_2O (Ochs and Lange, 1997), the loss of a few wt.% H_2O from silicate melt can produce $\Delta\rho \sim 10^2$ kg/m^3. In contrast, growth of bubbles in magma results in $\Delta\rho \sim 10^3$ kg/m^3. The

Figure 21. Dynamic viscosity (μ in Pa·s) of ascending magma vs. Reynolds number for cylindrical conduits with radii of **a)** r = 1 m, **b)** r = 20 m, and **c)** r = 50 m. Bulk density of the descending, degassed magma is $\rho = 2500$ kg/m^3. Plotted results cover a range in density difference $\Delta\rho = 10$ to 1000 kg/m^3 and magma flux Q of 0.1 to 100 m^3/s.

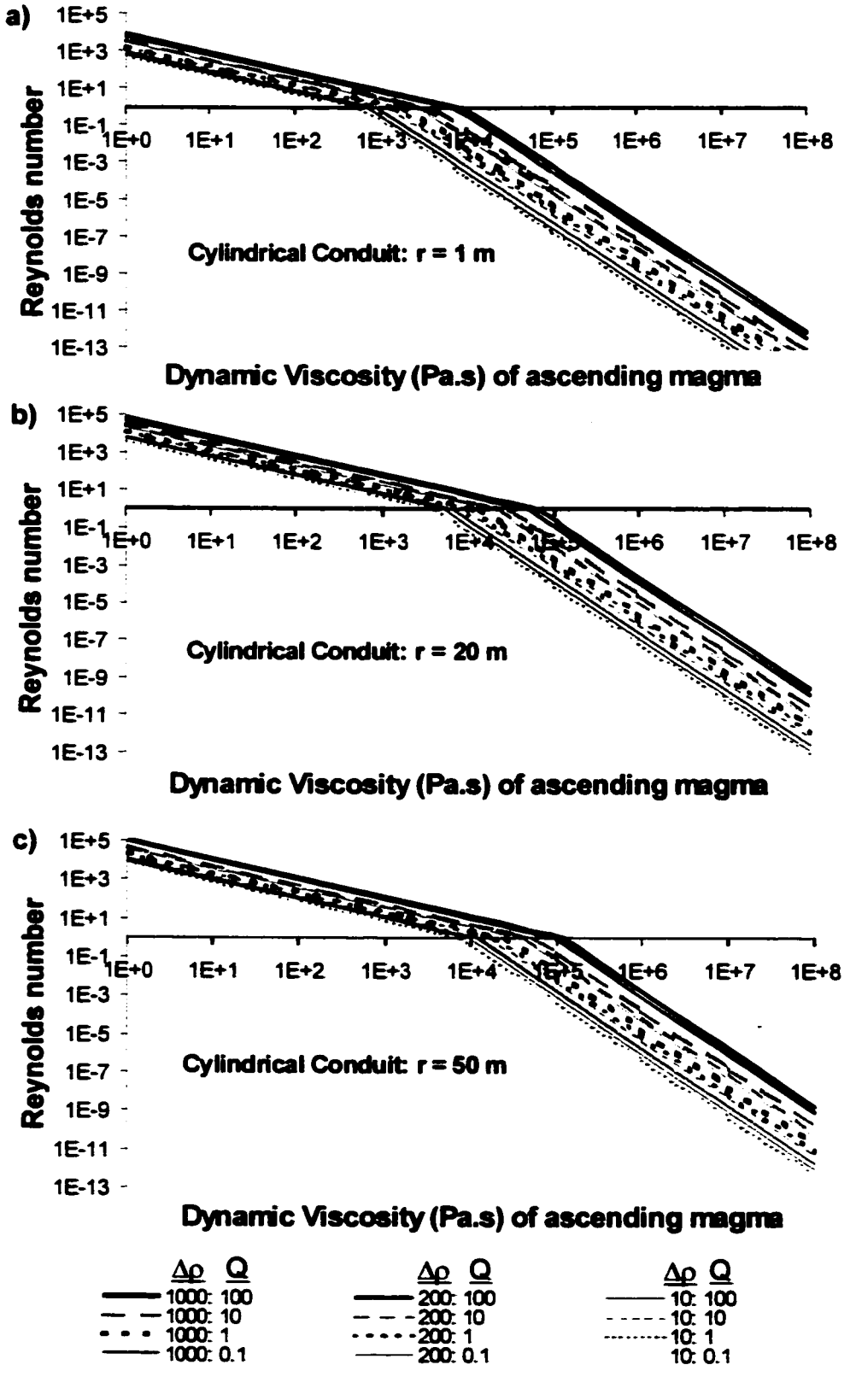
a)
Reynolds number
1E+5
1E+3
1E+1
1E-1
1E-3
1E-5
1E-7
1E-9
1E-11
1E-13
1E+0
1E+1
1E+2
1E+3
1E+4
1E+5
1E+6
1E+7
1E+8
Cylindrical Conduit: r = 1 m
Dynamic Viscosity (Pa.s) of ascending magma
b)
Reynolds number
Cylindrical Conduit: r = 20 m
Dynamic Viscosity (Pa.s) of ascending magma
c)
Reynolds number
Cylindrical Conduit: r = 50 m
Dynamic Viscosity (Pa.s) of ascending magma
Δρ Q
1000: 100
1000: 10
1000: 1
1000: 0.1
Δρ Q
200: 100
200: 10
200: 1
200: 0.1
Δρ Q
10: 100
10: 10
10: 1
10: 0.1

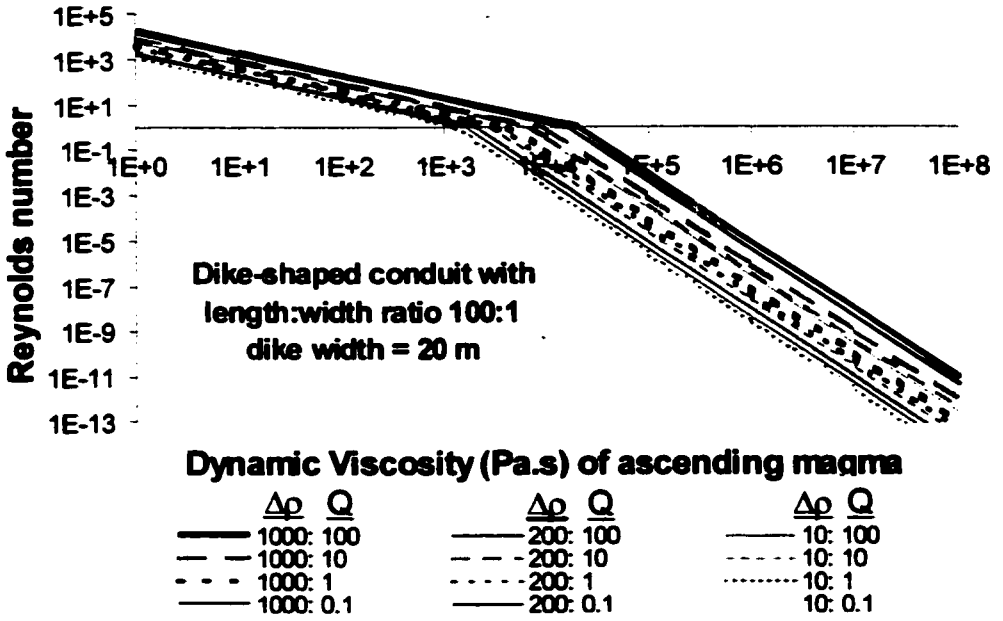

Figure 22. Dynamic viscosity (μ in Pa·s) of ascending magma vs. Reynolds number for a dike-shaped conduit with length:width ratio of 100:1 and width x = 20 m. Bulk density of the descending, degassed magma is $\rho = 2500$ kg/m^3. Plotted results cover a range in density difference $\Delta\rho = 10$ to 1000 kg/m^3 and magma flux Q of 0.1 to 100 m^3/s.

dynamic viscosity (μ) of magma generally varies from $10^0 - 10^2$ Pa·s for basalt and up to 10^8 Pa·s for dry, high-silica rhyolite (Spera, 2000).

Increasing the length scale (L), the density difference ($\Delta\rho$), and/or the volumetric magma flux (Q) results in a higher Reynolds number (Figure 21). However, the dominant parameter in determining the Reynolds number of the flowing magma is the dynamic viscosity (μ) of the ambient (ascending) magma. A dike-shaped conduit geometry (Figure 22) with a length:width aspect ratio of 100:1 and dike width x = 20 m, does not dramatically alter the μ vs. Re relationship.

Irrespective of conduit geometry or the values of the other parameters, dynamic viscosity has the range $\mu = 10^{2.5} - 10^5$ at Re ~ 1. Magmas flowing in conduits with $\mu < 10^{2.5}$ are inertia-dominated (Re > 1) and for $\mu > 10^5$, they are viscous-dominated (Re < 1). This Re analysis divides magma into the two flow regimes, based on dynamic viscosity while taking into consideration relevant variations in L, $\Delta\rho$, Q, and conduit geometry.

Convective velocity scale for Re > 1

For Re > 1, flow is inertia-dominated and the velocity scale (W) is independent of viscosity and proportional to the third root of the length scale (Equation 24). Velocity scale calculations for cylindrical conduits are shown as plots of conduit radius (m) vs. velocity (m/s) for the entire range of $\Delta\rho$ and Q (Figures 23a-d). For all conditions, W < 3 m/s except for the extreme case of Q = 100 m^3/s, $\Delta\rho$ = 1000 kg/m^3, and $r \leq 5$ m. For the case of a dike-shaped conduit, with a fixed length:width aspect ratio of 100:1 (Figures 24a-d), velocity scale values are lower than those in the cylindrical conduit case that have similar values of L, $\Delta\rho$, and Q.

Convective velocity scale for Re < 1

In viscous dominated systems (Re < 1) flow is laminar and the velocity scale is proportional to the cube of the length scale and inversely proportional to the square of the dynamic viscosity (Equation 25). As viscosity increases, convective velocity scale (W) decreases dramatically. Figures 25-28 show plots of dynamic viscosity (in

Figure 23. Conduit radius (in m) vs. velocity (in m/s) for inertia dominated flow regimes (Re > 1) in cylindrical conduits. Plotted results cover a range of conduit radii from r = 1 to 50 m, density differences of $\Delta\rho$ = 10 to 1000 kg/m^3 and magma fluxes of **a)** Q = 0.1 m^3/s, **b)** Q = 1 m^3/s, **c)** Q = 10 m^3/s and **d)** Q = 100 m^3/s. Calculated values for convective velocity scale (W) and average ascent velocity (V) are shown.

Cylindrical Conduit; Inertia dominated; Re > 1

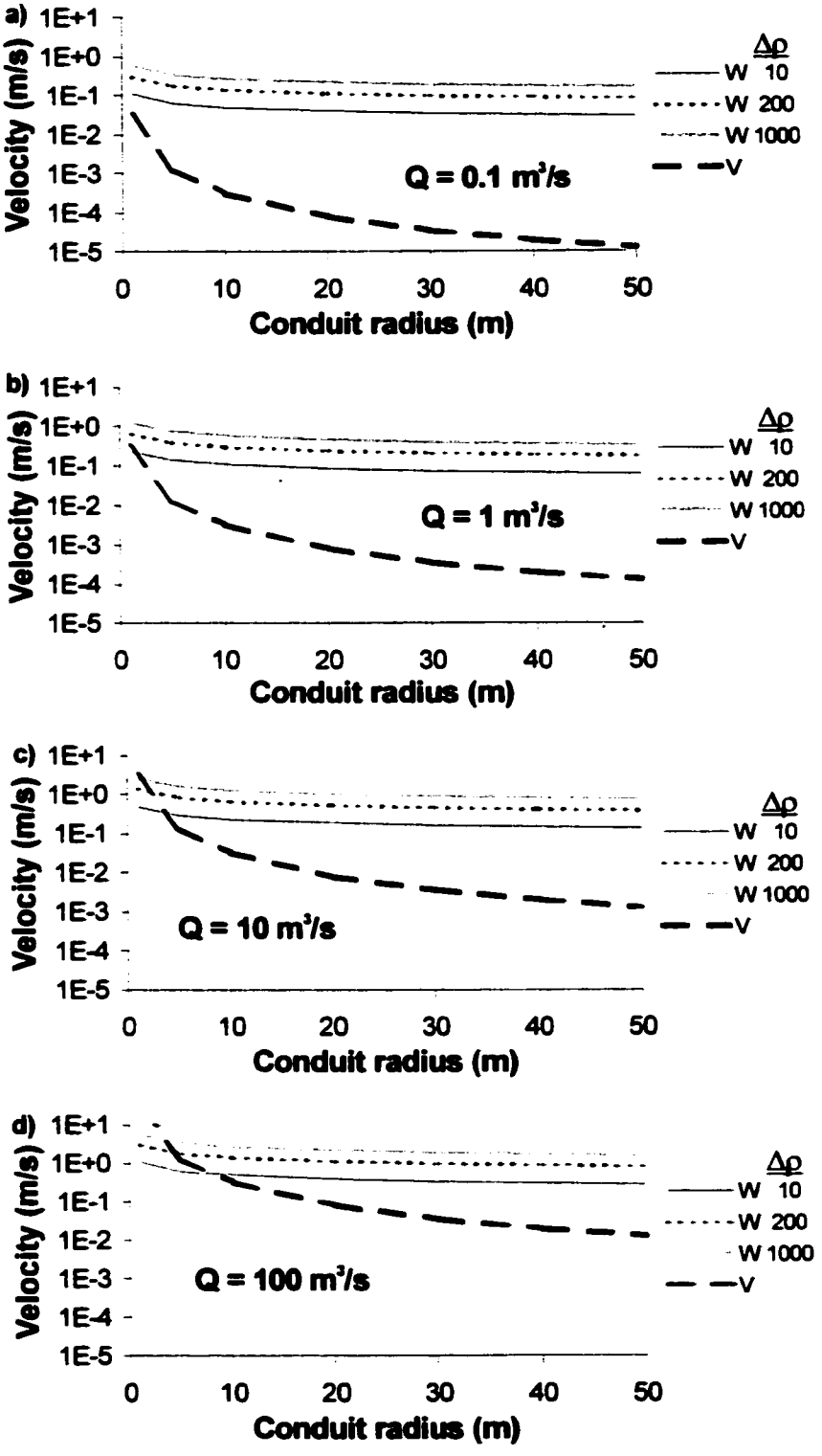

Figure 24. Dike width (in m) vs. velocity (in m/s) for inertia dominated flow regimes (Re > 1) in dike-shaped conduits. Plotted results cover a range of dike widths from x = 1 to 50 m, density differences of $\Delta\rho$ = 10 to 1000 kg/m^3 and magma fluxes of **a)** Q = 0.1 m^3/s, **b)** Q = 1 m^3/s, **c)** Q = 10 m^3/s and **d)** Q = 100 m^3/s. Calculated values for convective velocity scale (W) and average ascent velocity (V) are shown.

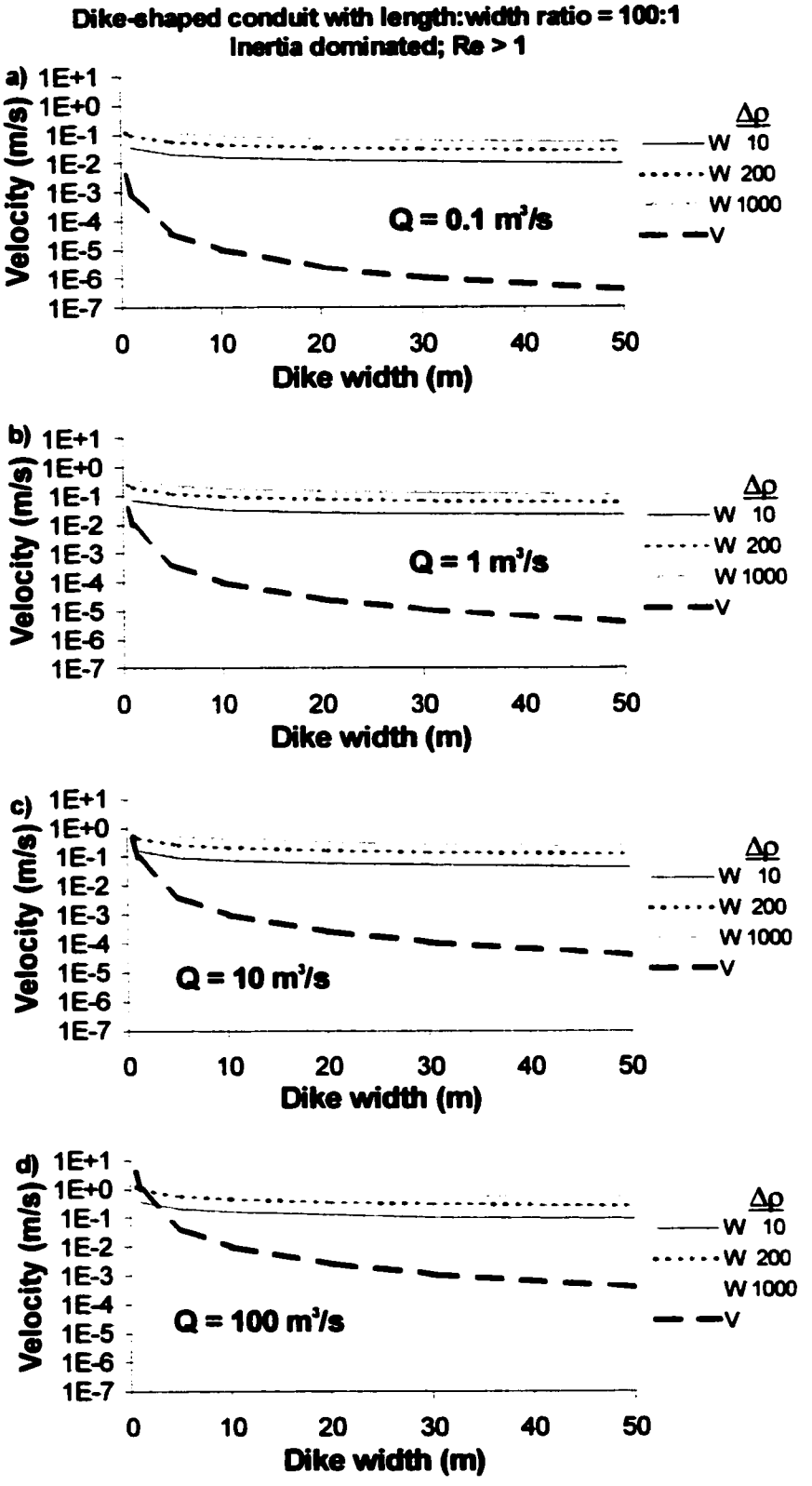
Dike-shaped conduit with length:width ratio = 100:1
Inertia dominated; Re > 1
a)
b)
c)
d)
Velocity (m/s)
1E+1
1E+0
1E-1
1E-2
1E-3
1E-4
1E-5
1E-6
1E-7
0
10
20
30
40
50
Dike width (m)
Δρ
W 10
W 200
W 1000
V
Q = 0.1 m³/s
Q = 1 m³/s
Q = 10 m³/s
Q = 100 m³/s

Figure 25. Dynamic viscosity (μ in Pa·s) of ascending magma vs. velocity (in m/s) for viscous dominated flow regimes (Re < 1) in cylindrical conduits of radius r = 1 m. Plotted results cover a range of density differences from $\Delta\rho$ = 10 to 1000 kg/m^3 and magma fluxes of **a)** Q = 0.1 m^3/s, **b)** Q = 1 m^3/s, **c)** Q = 10 m^3/s, and **d)** Q = 100 m^3/s. Calculated values for convective velocity scale (W) and average ascent velocity (V) are shown.

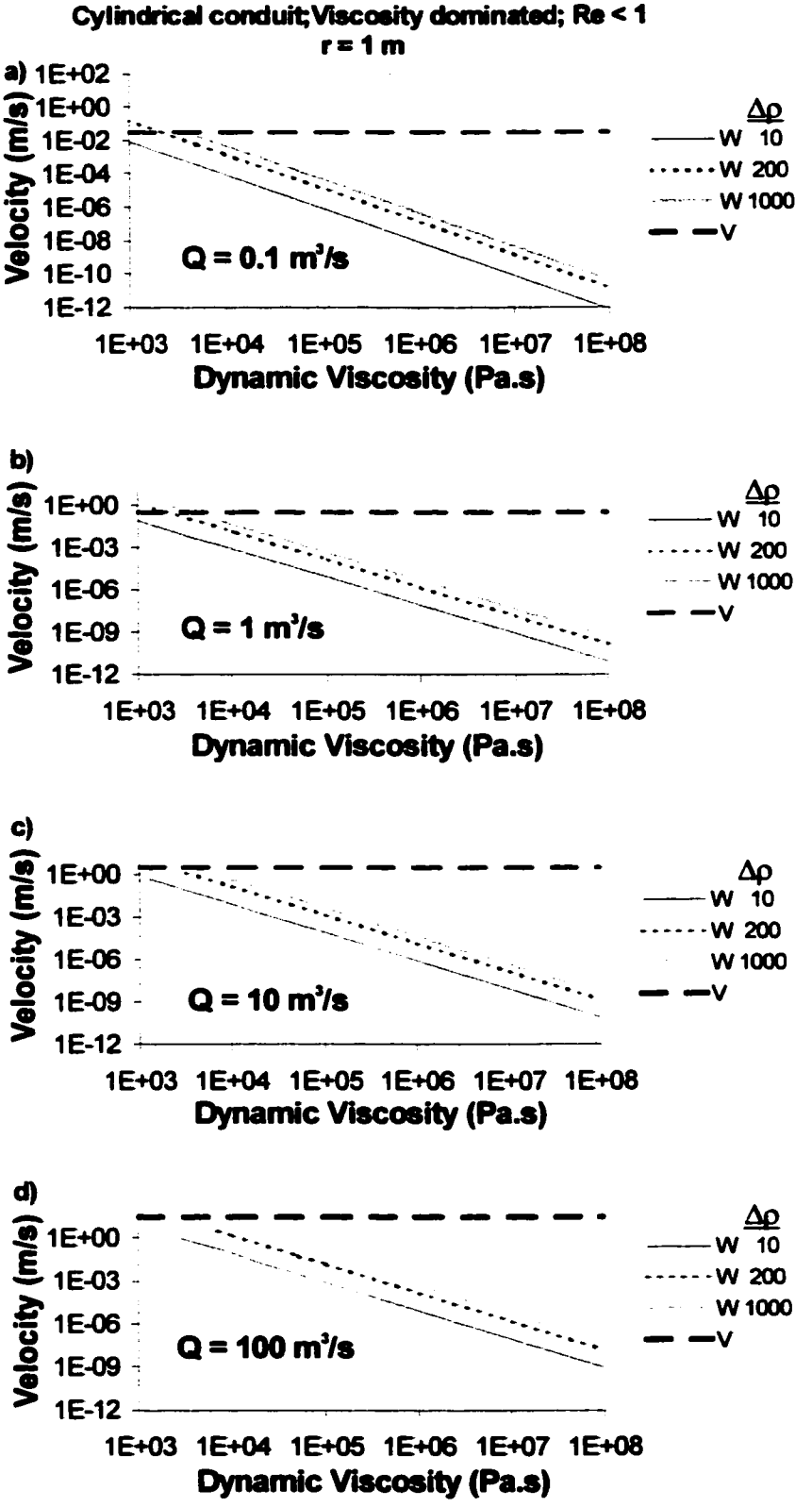
Cylindrical conduit;Viscosity dominated; Re < 1
r = 1 m
a)
Velocity (m/s)
1E+02
1E+00
1E-02
1E-04
1E-06
1E-08
1E-10
1E-12
Q = 0.1 m³/s
1E+03 1E+04 1E+05 1E+06 1E+07 1E+08
Dynamic Viscosity (Pa.s)
Δρ
W 10
W 200
W 1000
V
b)
Velocity (m/s)
1E+00
1E-03
1E-06
1E-09
1E-12
Q = 1 m³/s
1E+03 1E+04 1E+05 1E+06 1E+07 1E+08
Dynamic Viscosity (Pa.s)
Δρ
W 10
W 200
W 1000
V
c)
Velocity (m/s)
1E+00
1E-03
1E-06
1E-09
1E-12
Q = 10 m³/s
1E+03 1E+04 1E+05 1E+06 1E+07 1E+08
Dynamic Viscosity (Pa.s)
Δρ
W 10
W 200
W 1000
V
d)
Velocity (m/s)
1E+00
1E-03
1E-06
1E-09
1E-12
Q = 100 m³/s
1E+03 1E+04 1E+05 1E+06 1E+07 1E+08
Dynamic Viscosity (Pa.s)
Δρ
W 10
W 200
W 1000
V

Figure 26. Dynamic viscosity (μ in Pa·s) of ascending magma vs. velocity (in m/s) for viscous dominated flow regimes (Re < 1) in cylindrical conduits of radius r = 20 m. Plotted results cover a range of density differences from $\Delta\rho$ = 10 to 1000 kg/m^3 and magma fluxes of **a)** Q = 0.1 m^3/s, **b)** Q = 1 m^3/s, **c)** Q = 10 m^3/s, and **c)** Q = 100 m^3/s. Calculated values for convective velocity scale (W) and average ascent velocity (V) are shown.

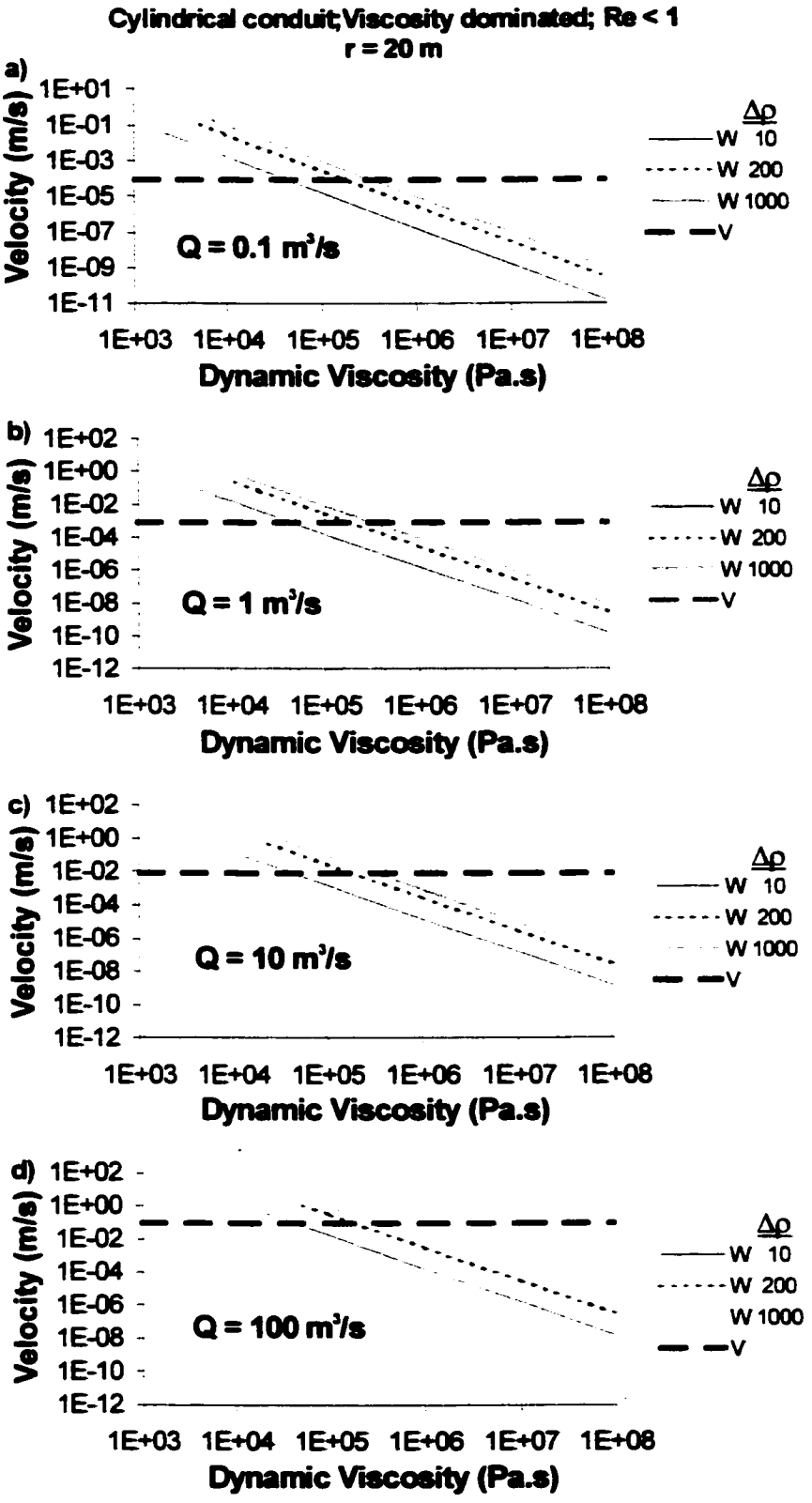
Cylindrical conduit;Viscosity dominated; Re < 1
r = 20 m
a)
Velocity (m/s)
1E+01
1E-01
1E-03
1E-05
1E-07
1E-09
1E-11
Q = 0.1 m³/s
Δρ
W 10
W 200
W 1000
V
1E+03 1E+04 1E+05 1E+06 1E+07 1E+08
Dynamic Viscosity (Pa.s)
b)
Velocity (m/s)
1E+02
1E+00
1E-02
1E-04
1E-06
1E-08
1E-10
1E-12
Q = 1 m³/s
Δρ
W 10
W 200
W 1000
V
1E+03 1E+04 1E+05 1E+06 1E+07 1E+08
Dynamic Viscosity (Pa.s)
c)
Velocity (m/s)
1E+02
1E+00
1E-02
1E-04
1E-06
1E-08
1E-10
1E-12
Q = 10 m³/s
Δρ
W 10
W 200
W 1000
V
1E+03 1E+04 1E+05 1E+06 1E+07 1E+08
Dynamic Viscosity (Pa.s)
d)
Velocity (m/s)
1E+02
1E+00
1E-02
1E-04
1E-06
1E-08
1E-10
1E-12
Q = 100 m³/s
Δρ
W 10
W 200
W 1000
V
1E+03 1E+04 1E+05 1E+06 1E+07 1E+08
Dynamic Viscosity (Pa.s)

Figure 27. Dynamic viscosity (μ in Pa·s) of ascending magma vs. velocity (in m/s) for viscous dominated flow regimes (Re < 1) in cylindrical conduits of radius r = 50 m. Plotted results cover a range of density differences from $\Delta\rho$ = 10 to 1000 kg/m^3 and magma fluxes of **a)** Q = 0.1 m^3/s, **b)** Q = 1 m^3/s, **c)** Q = 10 m^3/s and **d)** Q = 100 m^3/s. Calculated values for convective velocity scale (W) and average ascent velocity (V) are shown.

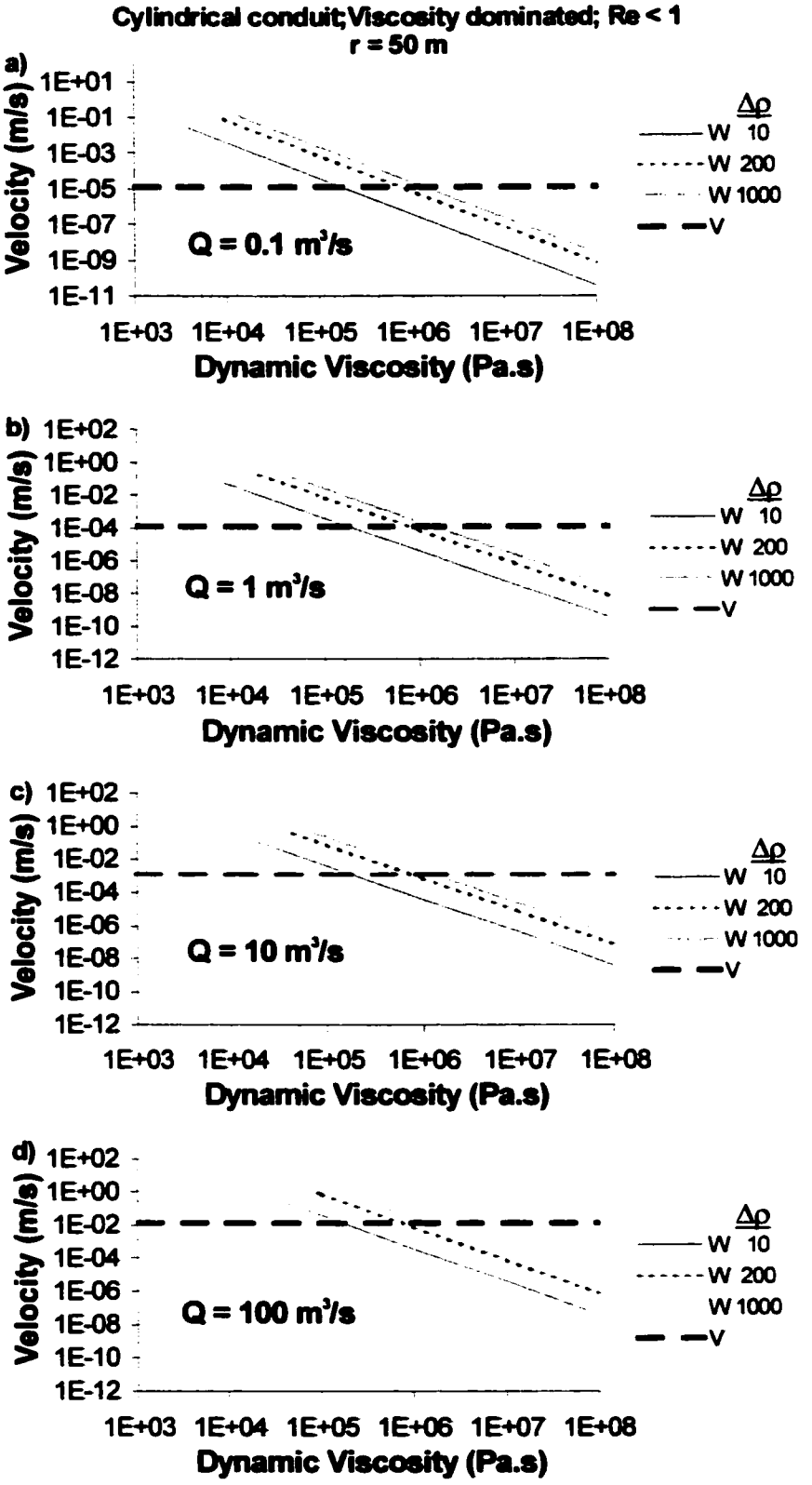
Cylindrical conduit;Viscosity dominated; Re < 1
r = 50 m
a)
Velocity (m/s)
1E+01
1E-01
1E-03
1E-05
1E-07
1E-09
1E-11
Q = 0.1 m³/s
Δρ
W 10
W 200
W 1000
V
1E+03 1E+04 1E+05 1E+06 1E+07 1E+08
Dynamic Viscosity (Pa.s)
b)
Velocity (m/s)
1E+02
1E+00
1E-02
1E-04
1E-06
1E-08
1E-10
1E-12
Q = 1 m³/s
Δρ
W 10
W 200
W 1000
V
1E+03 1E+04 1E+05 1E+06 1E+07 1E+08
Dynamic Viscosity (Pa.s)
c)
Velocity (m/s)
1E+02
1E+00
1E-02
1E-04
1E-06
1E-08
1E-10
1E-12
Q = 10 m³/s
Δρ
W 10
W 200
W 1000
V
1E+03 1E+04 1E+05 1E+06 1E+07 1E+08
Dynamic Viscosity (Pa.s)
d)
Velocity (m/s)
1E+02
1E+00
1E-02
1E-04
1E-06
1E-08
1E-10
1E-12
Q = 100 m³/s
Δρ
W 10
W 200
W 1000
V
1E+03 1E+04 1E+05 1E+06 1E+07 1E+08
Dynamic Viscosity (Pa.s)

Figure 28. Dynamic viscosity (μ in Pa·s) of ascending magma vs. velocity (in m/s) for viscous dominated flow regimes (Re < 1) in dike-shaped conduits. Length:width ratio of dike is 100:1. Plotted results cover a range of density differences from $\Delta\rho$ = 10 to 1000 kg/m^3 and magma fluxes of **a)** Q = 0.1 m^3/s, **b)** Q = 1 m^3/s, **c)** Q = 10 m^3/s, and **d)** Q = 100 m^3/s for a dike of width x = 20 m. Calculated values for convective velocity scale (W) and average ascent velocity (V) are shown.

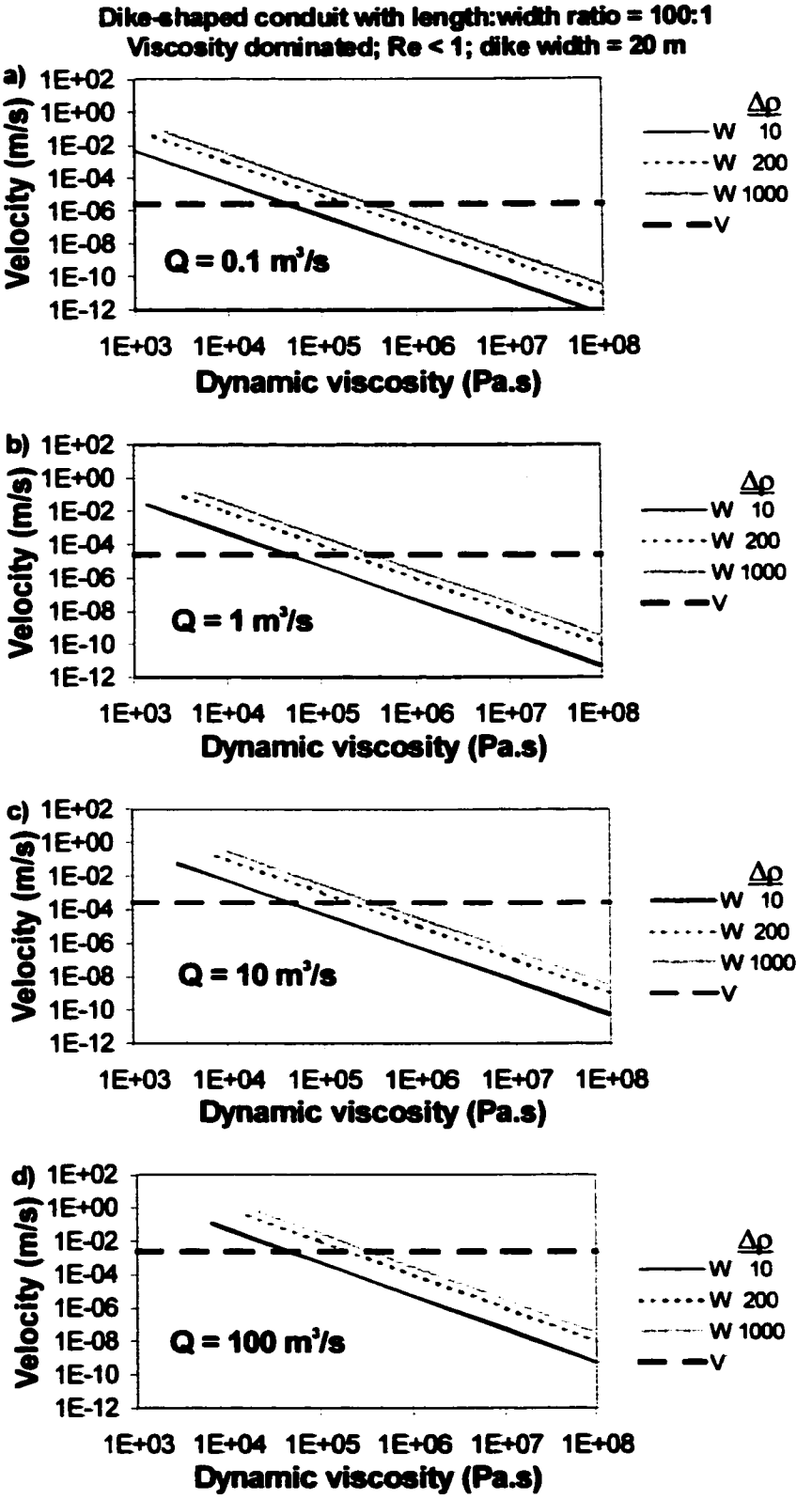
Dike-shaped conduit with length:width ratio = 100:1
Viscosity dominated; Re < 1; dike width = 20 m
a)
b)
c)
d)
Velocity (m/s)
1E+02
1E+00
1E-02
1E-04
1E-06
1E-08
1E-10
1E-12
Q = 0.1 m³/s
Q = 1 m³/s
Q = 10 m³/s
Q = 100 m³/s
1E+03 1E+04 1E+05 1E+06 1E+07 1E+08
Dynamic viscosity (Pa.s)
Δρ
W 10
W 200
W 1000
V

Pa·s) vs. velocity (m/s) for cylindrical and dike-shaped conduits over the entire range of values for L, $\Delta\rho$, and Q.

For cylindrical conduits with small conduit radii (r = 1 m; Figure 25), magmas with dynamic viscosities of $10^3 - 10^4$ Pa·s have convective velocity scales of ~1 mm/s to ~10 m/s for the entire range of $\Delta\rho$ and Q except for the extreme case of Q = 0.1 m^3/s and $\Delta\rho$ = 10 kg/m^3. Higher viscosity magmas with $\mu > 10^6$ Pa·s have convective velocity scales W < 10^{-4} m/s except for the extreme case of Q = 100 m^3/s and $\Delta\rho >$ 200 kg/m^3. For large conduit radii (r = 50 m; Figure 27), magmas with dynamic viscosities of $10^4 - 10^5$ Pa·s have convective velocity scales of ~1 mm/s to ~1 m/s except for the extreme case of Q = 0.1 m^3/s and $\Delta\rho$ = 10 kg/m^3. Higher viscosity magmas with $\mu > 10^7$ Pa·s have convective velocity scales W < 10^{-4} m/s except for the extreme case of Q = 100 m^3/s and $\Delta\rho >$ 200 kg/m^3. Velocity scale values for dike-shaped conduits are lower than those for cylindrical conduits at the similar values of L, $\Delta\rho$, and Q (Figure 28).

Ascent velocity based on Q and conduit geometry

For a given volumetric flux of the ascending magma (Q in m^3/s) and cross-sectional area of the ascending magma (A in m^2), one can determine the average velocity of the ascending magma (V in m/s) with:

$$V = Q/A \qquad (29)$$

Convection is allowed for flow of magma in conduits in which the average magma ascent velocity (V) is of the same order as the velocity scale (W).

For Re > 1 (inertia-dominated), convection is controlled by conduit size. V is of the same order as W only for cylindrical conduits with radii r < 10 m. Smaller values of magma flux (Q) require smaller conduit radii for convection to occur. For magma flux Q = 0.1 m^3/s, conduit radius must be less than ~1 m for convection to occur (Figure 23). For a dike-shaped conduit with length:width aspect ratio of 100:1, dike widths are constrained to less than ~3 m for convection to occur at a magma flux of Q = 100 m^3/s and less than ~1 m for a magma flux of Q = 1 m^3/s (Figure 24).

For laminar flow conditions (Re < 1, viscous-dominated), convection is controlled by magma viscosity. In cylindrical conduits with small radii (r = 1 m), convection only occurs at low dynamic viscosities, $\mu < \sim 10^{3.5}$ Pa·s (Figure 25). For moderate sized conduits (r = 20 m), convection is possible at dynamic viscosities less than $\sim 10^{5.5}$ Pa·s (Figure 26). For large sized conduits (r = 50 m), convection will occur at dynamic viscosities less than $\sim 10^{6}$ Pa·s (Figure 27). For dike-shaped conduits with fixed length:width aspect ratio of 100:1 and width of 20 m, convection will occur at dynamic viscosities less than $\sim 10^{5.5}$ Pa·s (Figure 28). Higher values of $\Delta\rho$ raise the upper limit of dynamic viscosities for which convection will occur.

Separate two-phase flow and Stokes ascent of bubbles

The Stokes ascent velocity of bubbles in silicate melt (in m/s) is defined by Vergniolle and Jaupart (1986) as:

$$V_{Stokes} = \frac{g \Delta\rho_g d^2}{18\mu} \qquad (30)$$

where d = the bubble diameter (m), g = gravitational acceleration (9.8 m/s^2), $\Delta\rho_g$ = difference in density between gas and silicate liquid (kg/m^3), and μ = dynamic viscosity of silicate melt (Pa·s). As magma ascends, gas bubbles grow in size by the combination of expansion due to pressure decrease, diffusion of volatiles into the bubbles, and coalescence (Sparks, 1978). The large difference in density between gas bubbles and the surrounding silicate melt give the bubbles strong positive buoyancy. The density of gas contained in bubbles is a function of the ambient pressure and can be approximated using the ideal gas law at pressures less than 2000 bar. The ideal gas densities of a hydrous gas phase at 1000 bar and 1 bar are ρ_{gas} = 150 kg/m^3 and 0.2 kg/m^3, respectively. If we assume the silicate liquid has density ρ_{liq} = 2500 kg/m^3, this implies $\Delta\rho_g$ = 2350 – 2500 kg/m^3 for bubbles in the magma at pressures < 1000 bar (or depths < 4 km).

Vergniolle and Jaupart (1986) report that in basaltic magma, dispersed bubbly flow occurs for gas volume fractions less than 20 vol.% and slug flow occurs at gas

volume fractions greater than 20 vol.%. Slug flow involves large bubbles such that separate two-phase flow is more likely. For a closed system, the volume percent of bubbles in the magma is dependent on the pressure and the initial amount of H_2O dissolved in silicate melt. According to the empirical H_2O solubility model of Moore et al. (1998), for typical initial magmatic H_2O contents of 1 to 4 wt.% H_2O, 20 vol.% bubbles is reached at 100 – 750 bar (~0.5 – 3 km depth).

The ascent velocity of bubbles increases with increasing bubble size; however, the viscosity of the surrounding silicate melt hinders ascent of bubbles. Using a wide range of values for the parameters in Equation 30, the range of Stokes ascent velocities of bubbles are explored. Figure 29 shows Stokes bubble ascent velocity for bubbles at 1 bar and 1000 bar ranging in size from d = 1 mm to 1 m rising through silicate melt with viscosity $\mu = 10^0$ to 10^8 Pa·s. The results for V_{Stokes} are less than 10% lower for bubbles at higher pressures (up to 5 kbar) provided the values of other parameters remain the same.

On Figure 29, three separate flow regimes can be defined: explosive ascent, separate two phase flow, and negligible bubble ascent. For very low viscosity and large bubble diameters (d ~ 1 m), the Stokes ascent velocity exceeds 100 m/s. Velocities of this magnitude occur during explosive eruptions and are not realistic for processes at non-explosive, passively degassing volcanoes. At the other end of the spectrum, we define the region of negligible bubble ascent for $V_{Stokes} < 10^{-3}$ m/s. At this rate it would take a bubble ~0.3 years to ascend from a magma body at 1 km depth.

Compared to homogeneous flow of magma in the conduit, separate two-phase flow decreases the gas volume fraction because bubbles rise faster than the surrounding silicate liquid and escape (Vergniolle and Jaupart, 1986). It is difficult, however, to quantitatively assess the effect of separate two phase flow on the gas volume fraction in the magma since we have no data on the bubble size and bubble size distribution at different depths in the conduit. A qualitative assessment of the importance of separate two-phase flow can be made at specific levels in the conduit

Figure 29. Dynamic viscosity of ambient magma (μ in Pa·s) vs. Stokes ascent velocity of bubbles (in m/s) for a range of bubble sizes from diameter d = 1 mm to 1 m. Results are calculated for **a)** 1 bar and **b)** 1000 bar pressures.

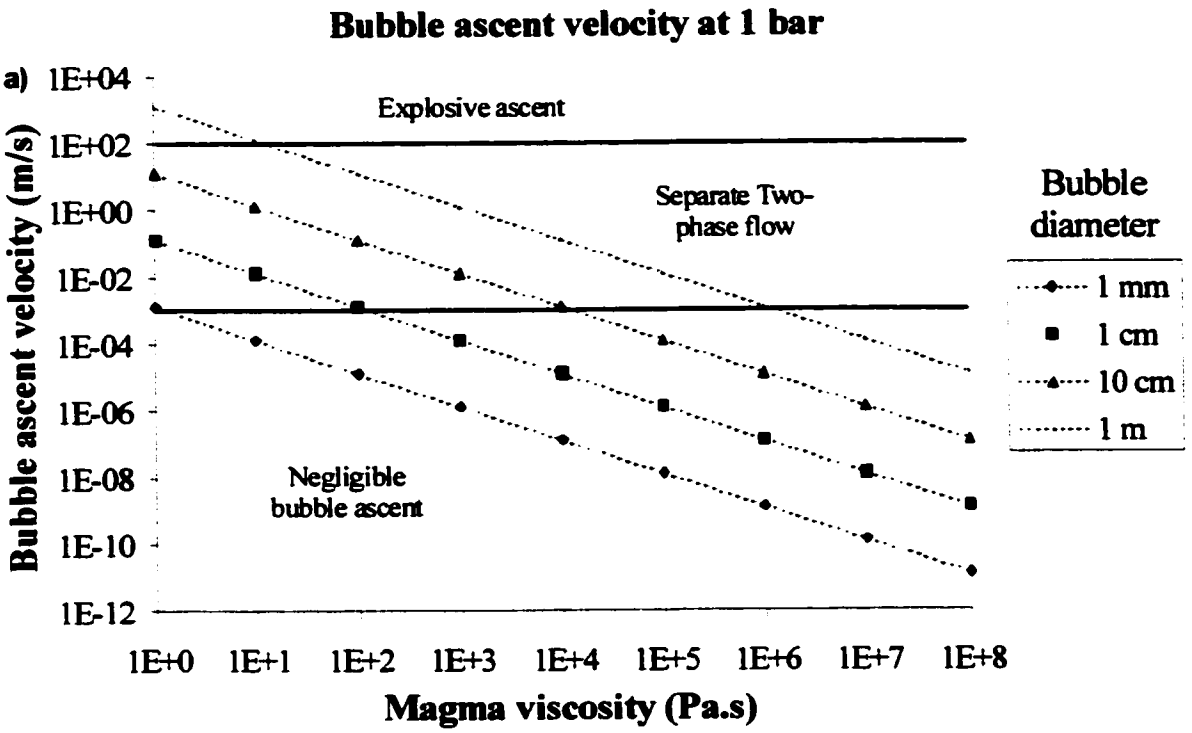
Bubble ascent velocity at 1 bar
a)
Bubble ascent velocity (m/s)
1E+04
1E+02
1E+00
1E-02
1E-04
1E-06
1E-08
1E-10
1E-12
Explosive ascent
Separate Two-phase flow
Negligible bubble ascent
Bubble diameter
1 mm
1 cm
10 cm
1 m
1E+0
1E+1
1E+2
1E+3
1E+4
1E+5
1E+6
1E+7
1E+8
Magma viscosity (Pa.s)

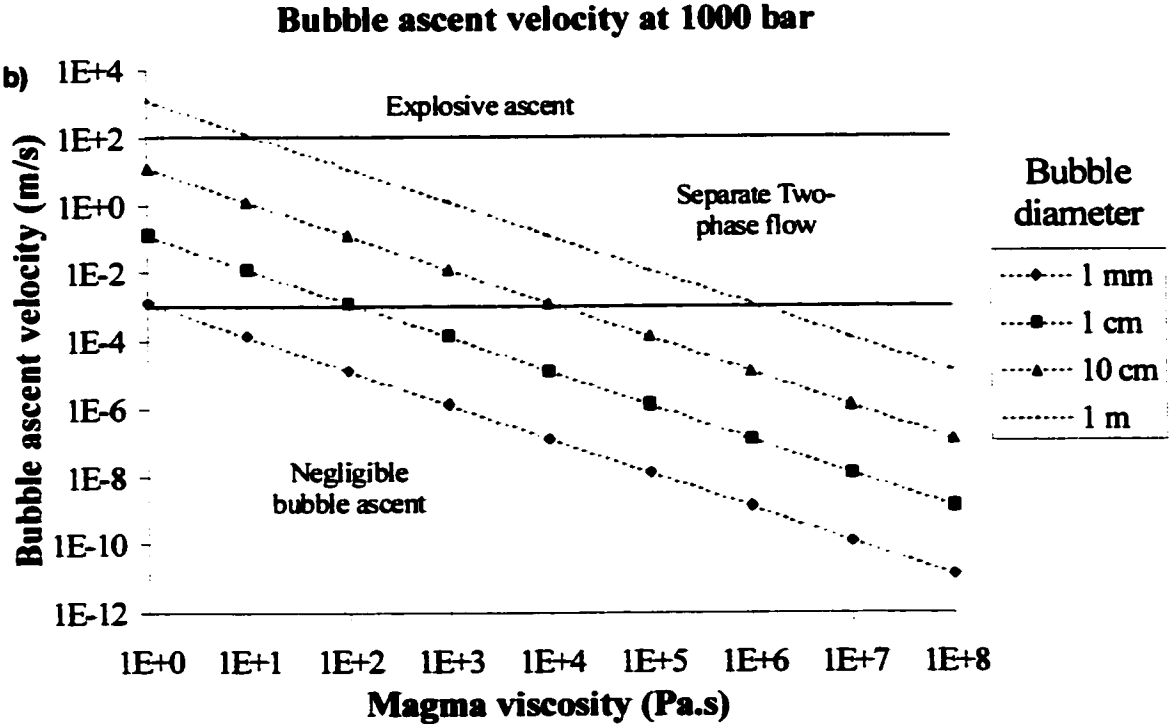
Bubble ascent velocity at 1000 bar
b)
Bubble ascent velocity (m/s)
1E+4
1E+2
1E+0
1E-2
1E-4
1E-6
1E-8
1E-10
1E-12
Explosive ascent
Separate Two-phase flow
Negligible bubble ascent
Bubble diameter
1 mm
1 cm
10 cm
1 m
1E+0
1E+1
1E+2
1E+3
1E+4
1E+5
1E+6
1E+7
1E+8
Magma viscosity (Pa.s)

by comparing convective velocity scale W (Figures 23-28) and V_{Stokes} (Figure 29) for a range of bubble sizes at the values of L, $\Delta\rho$, and Q in question. A quantitative treatment of this subject is beyond the scope of this study.

Application: Case studies of Villarrica (Chile) and Popocatépetl (Mexico)

We apply the quantitative framework outlined above to two passively degassing volcanoes, Villarrica and Popocatépetl, which may have conduit convection as their primary degassing mechanism.

Villarrica volcano

Villarrica is a 2847 m high, basaltic andesite, subduction zone stratovolcano located in the southern Chilean Andes (39.5 °S). This volcano has been characterized by continuous, open-vent, passive degassing from a summit lava lake, with negligible eruption of magmatic material, for the past 17 years. Gas emission measurements of SO_2, HCl, and HF coupled with studies of the dissolved volatile content in glass inclusions in phenocrysts from samples obtained from the lava lake constrain the current average magma degassing rate at Q = 2.2 m^3 of magma per second (see Chapter 3). The initial amount of dissolved H_2O in the Villarrica magma has a minimum of 1 wt.% H_2O (see Chapter 3). Using the fluid dynamic equations of Stevenson and Blake (1998), resulted in conduit radii of R_c = 2.7 m and 2.1 m for the complete convective degassing of magma that initially contained 1 wt.% and 4 wt.% dissolved H_2O, respectively.

For application of the Reynolds number and convective velocity scale analysis, we consider these same two cases: initial dissolved water contents of 1 wt.% and 4 wt.% H_2O. Re and W are calculated at a depth of ~6 km for both cases which corresponds to 0 vol.% bubbles in the magma. For these calculations, magma convection is driven by the density difference between silicate melt rich in dissolved volatiles and degassed magma (Table 38). Re and W are also calculated at depths of

Table 38. Physical parameters for convection in Villarrica magma and results for Reynolds number (Re), velocity scale (W), ascent velocity (V), and buoyancy flux (B) for varying conduit radii (r) and gas volume fractions of 0 and 20 vol.%

Case#1a: Initial dissolved water content 1 wt.% H_2O and 0 vol.% bubbles

						r (m)	B (m^2/s^3)	Re	W (m/s)	V (m/s)
Q =	2.2	m^3/s	μ_a =	18	Pa.s	1	2.8E-1	100	0.7	0.7
$\Delta\rho$ =	100	kg/m^3	μ_d =	1780	Pa.s	5	1.1E-2	300	0.4	3E-2
Bubbles	0	vol.%	ρ_a =	2600	kg/m^3	10	2.8E-3	400	0.3	7E-3
P =	1500	bar	ρ_d =	2700	kg/m^3	20	7.1E-4	700	0.2	2E-3
Depth =	~6	km	η_a =	6.9E-3	m^2/s					
			η_d =	0.66	m^2/s					

Case#1b: Initial dissolved water content 1 wt.% H_2O and 20 vol% bubbles

						r (m)	B (m^2/s^3)	Re	W (m/s)	V (m/s)
Q =	2.2	m^3/s	μ_a =	31	Pa.s	1	2.1E+0	100	1.3	0.7
$\Delta\rho$ =	625	kg/m^3	μ_d =	1780	Pa.s	5	8.3E-2	250	0.7	3E-2
Bubbles	20	vol.%	ρ_a =	2075	kg/m^3	10	2.1E-2	400	0.6	7E-3
P =	100	bar	ρ_d =	2700	kg/m^3	20	5.2E-3	600	0.5	2E-3
Depth =	~0.4	km	η_a =	1.5E-2	m^2/s					
			η_d =	0.66	m^2/s					

Case#2a: Initial dissolved water content 4 wt.% H_2O and 0 vol.% bubbles

						r (m)	B (m^2/s^3)	Re	W (m/s)	V (m/s)
Q =	2.2	m^3/s	μ_a =	0.5	Pa.s	1	7.9E-1	4500	0.9	0.7
$\Delta\rho$ =	280	kg/m^3	μ_d =	1780	Pa.s	5	3.2E-2	13,100	0.5	3E-2
Bubbles	0	vol.%	ρ_a =	2420	kg/m^3	10	7.9E-3	20,800	0.4	7E-3
P =	1500	bar	ρ_d =	2700	kg/m^3	20	2.0E-3	33,100	0.3	2E-3
Depth =	~6	km	η_a =	2.1E-4	m^2/s					
			η_d =	0.66	m^2/s					

Case#2b: Initial dissolved water content 4 wt.% H_2O and 20 vol.% bubbles

						r (m)	B (m^2/s^3)	Re	W (m/s)	V (m/s)
Q =	2.2	m^3/s	μ_a =	2.5	Pa.s	1	2.4E+0	1100	1.3	0.7
$\Delta\rho$ =	700	kg/m^3	μ_d =	1780	Pa.s	5	1.0E-1	3100	0.8	3E-2
Bubbles	20	vol.%	ρ_a =	2004	kg/m^3	10	2.0E-2	5000	0.6	7E-3
P =	750	bar	ρ_d =	2700	kg/m^3	20	6.0E-3	7900	0.5	2E-3
Depth =	~3	km	η_a =	1.3E-3	m^2/s					
			η_d =	0.66	m^2/s					

Q = magma flux, ρ = density, $\Delta\rho = \rho_d - \rho_a$ = density difference between ascending and descending magma, P = pressure

μ = dynamic viscosity, η = kinematic viscosity

Subscripts "a" and "d" denote "ascending" and "descending" magmas

~0.4 km and ~3 km for the 1 wt.% and 4 wt.% H_2O cases, respectively, which correspond to 20 vol.% bubbles for both cases. For these calculations, the presence of bubbles creates a relatively large density difference that drives convection.

Vergniolle and Jaupart (1986) defined dispersed bubbly flow for gas volume fractions less than 20 vol.% and slug flow for gas volume fractions greater than 20 vol.%. Slug flow involves large bubbles, formed by coalescence, which results in high bubble ascent velocities. Dispersed bubbly flow at low gas volume fractions implies smaller bubble diameters. If gas bubbles are sufficiently small (~1 mm diameter) in the dispersed bubbly flow regime then the effects of separate two-phase flow in low-viscosity Villarrica magma (μ = 1 to 30 Pa·s) are small (Figure 29) compared to the ascent velocity of the magma in the conduit (~0.1 to 1 m/s; Table 38). For gas volume fractions greater than 20 vol.% (slug flow), bubbles have likely grown and/or coalesced sufficiently that separate two-phase flow is significant and therefore bulk density of the magma (and Re and W) cannot be predicted with the equations used in this study.

For the 0 vol.% bubbles cases, the density differences are $\Delta\rho$ = 100 kg/m^3 and $\Delta\rho$ = 280 kg/m^3 for the 1 wt.% and 4 wt.% initial dissolved H_2O cases, respectively (Case#1a and 2a, Table 38). For the 20 vol.% bubbles cases, the density differences are $\Delta\rho$ = 625 kg/m^3 and $\Delta\rho$ = 700 kg/m^3 for the 1 wt.% and 4 wt.% initial dissolved H_2O cases, respectively (Case#1b and 2b, Table 38). Based on visual observations in the summit crater of Villarrica, we estimate the radius of the conduit to lie in the range r = 1 to 20 m. We explore this entire range in the present analysis. For the 1 wt.% H_2O and 0 vol.% bubbles example (Case#1a), Re ranges from 100 to 700 and W ranges from 0.7 m/s to 0.2 m/s for r = 1 to 20 m. For the 1 wt.% H_2O and 20 vol.% bubbles example (Case#1b), Re has a similar range but convective velocity scale is higher (W = 1.3 to 0.5 m/s) for r = 1 to 20 m. For the 4 wt.% H_2O and 0 vol.% bubbles example (Case#2a), Re ranges from 4500 to 33,000 and W ranges from 0.9 m/s to 0.3 m/s for r = 1 to 20 m. For the 4 wt.% H_2O and 20 vol.% bubbles example (Case#2b), Re are lower (Re = 1100 to 7900) and convective velocity scale is higher

(W = 1.3 to 0.5 m/s) for r = 1 to 20 m. The urealistically high values of Re (> 10^4; on par with atmospheric turbulence) calculated in Case#2a (4 wt.% dissolved H_2O and 0 vol.% bubbles) for conduit radii $r \geq 5$ m (Table 38) may suggest that lower initial dissolved H_2O contents and/or smaller conduit radii are favored. The large discrepancy (greater than an order of magnitude) between W and V in all cases for conduit radii $r \geq 5$ m (Table 38) imply that smaller conduit radii (r = 1 to 5 m) are more likely. These results are entirely reasonable and consistent with the fluid dynamic calculations shown in Chapter 3. This analysis of Re and W supports the hypothesis that convection of magma in the conduit is a viable magma transport process and degassing mechanism at Villarrica volcano if $r \leq 5$ m.

Popocatépetl volcano

Popocatépetl volcano has degassed a total of ~20 Mt SO_2, accompanied by only minor eruptive activity, since the current phase of activity began in December 1994 (Delgado-Granados et al., 2001). This value compares with the ~17 Mt SO_2 (Gerlach et al., 1996) injected into the stratosphere in a single day during the climactic, highly explosive eruption of Pinatubo (Philippines) on June 15, 1991. Popocatépetl is also one of the largest known natural emitters of SO_2 and CO_2. For the period March 1996 to December 2000, Popocatépetl erupted 3.1 x 10^7 m^3 mixed dacite and basaltic andesite magma (see Chapters 1 & 2). Degassing from this volume of erupted magma accounts for less than 1 wt.% of the observed SO_2 emission. Alternate sources of volatiles such as breakdown of sulfur-bearing magmatic phases, degassing from static unerupted magma, fumarolic remobilization of vapor phase precipitates, and/or assimilation of volatile bearing basement rocks are insufficient to produce the measured volatile output of the volcano. If the only source for the gas emissions is *dissolved* volatiles in the melt phase of magma then, ~2 km^3 of basaltic andesite, ~50 km^3 of dacite, or some mixture of the two with an intermediate volume must *completely* degas to account for the observed gas emissions. If the mixture has an average mafic:silicic mass ratio of 35:65 (see Chapters 1 & 2) then this

intermediate volume is ~6 km^3. Alternatively, complete degassing of ~1 km^3 of mixed magma supplemented with ~9 wt.% separate, pre-existing volatile phase could account for the observed gas emissions (see Chapter 2). Regardless of the source of volatiles, we propose that the mechanism for extracting the volatiles from the magma is conduit convection.

Using the Equations 24-26 and data on the physical properties of magma specific to Popocatépetl (see Chapter 2), we explore the Reynolds number and convective velocity scale for two cases at Popocatépetl. In the first case, ~6 km^3 of magma with no separate, pre-existing volatile phase is completely degassed. In the second case, 1 km^3 of mixed magma with ~9 wt.% separate, pre-existing volatile phase is completely degassed.

For Case #1, the ~6 km^3 of mixed magma is degassed over a period of 4 years and 10 months (1.52×10^8 sec, see Chapter 2) at the rate of $Q = 39.5$ m^3/s. Based on the size of the summit crater of Popocatépetl, we estimate the radius of the conduit to be less than 100 m; we explore the entire range of conduit radii from r = 2 to 100 m. Values for the physical parameters of Popocatépetl magma are shown in Table 39. Deep in the conduit, below the vesiculation level (i.e. > 5 kbar for the estimated ~3 wt.% H_2O and ~3000 ppm CO_2 initially dissolved in the magma at Popocatépetl), magma ascent is driven by the density difference between melt rich in dissolved volatiles and degassed magma. The density difference for Case#1 is $\Delta\rho = 90$ kg/m^3. For r = 5 to 100 m, magma flow is inertia-dominated (Re > 1) and Reynolds number, convective velocity scale, and ascent velocity have the range Re = 1 to 9, W = 1 m/s to 0.4 m/s, and V = 0.5 m/s to 0.001 m/s (Table 39). For this case and r = 2 m, magma flow is viscous dominated (Re < 1) with Re = 0.3, W = 0.6 m/s, and V = 3.1 m/s. In summary, for Case #1, W and V are of the same order, and convection is allowed, for conduit radii $r \leq 10$ m.

For Case#2, the ~9 wt.% separate volatile phase has a mass of ~2.2×10^{11} kg, in addition to the ~1 km^3 of silicate melt plus crystals (~2.4×10^{12} kg with silicate

Table 39. Physical parameters for convection in Popocatépetl magma and results for Reynolds number (Re), velocity scale (W), ascent velocity (V), and buoyancy flux (B) for varying conduit radii (r) and gas volume fractions of 0 and 30 vol.%

Case#1: ~6 km^3 of mixed magma with no separate volatile phase

Q_{degas} =	39.5	m^3/s	μ_a =	10^4	Pa.s	r (m)	B (m^2/s^3)	Re	W (m/s)	V (m/s)
$\Delta\rho$ =	90	kg/m^3	μ_d =	$10^{7.3}$	Pa.s	2	1.1	0.3	0.6	3.1
Bubbles	0	vol.%	ρ_a =	2430	kg/m^3	5	1.8E-1	1	1.0	0.5
P =	5000	bar	ρ_d =	2520	kg/m^3	10	4.6E-2	2	0.8	0.1
Depth =	~20	km	η_a =	4	m^2/s	20	1.1E-2	3	0.6	3E-2
			η_d =	7920	m^2/s	50	1.8E-3	6	0.5	5E-3
						100	4.6E-4	9	0.4	1E-3

Case#1: ~1 km^3 of mixed magma plus ~9 wt.% separate volatile phase

Q_{degas} =	9.4	m^3/s	μ_a =	$10^{3.7}$	Pa.s	r (m)	B (m^2/s^3)	Re	W (m/s)	V (m/s)
$\Delta\rho$ =	670	kg/m^3	μ_d =	$10^{7.3}$	Pa.s	2	2.7	1	1.7	0.7
Bubbles	30	vol.%	ρ_a =	1850	kg/m^3	5	4.2E-1	2	1.3	0.1
P =	5000	bar	ρ_d =	2520	kg/m^3	10	1.1E-1	4	1.0	0.03
Depth =	~20	km	η_a =	3	m^2/s	20	2.7E-2	6	0.8	8E-3
			η_d =	7920	m^2/s	50	4.3E-3	11	0.6	1E-3
						100	1.1E-3	18	0.5	3E-4

density of $\rho = 2400$ kg/m^3). Using the modified Redlich-Kwong equation of state, we predict the water-dominated separate volatile phase has a volume of ~4.3×10^8 m^3 (at 5 kbar, $\rho = 500$ kg/m^3). Thus, the total volume of magma (silicate melt + crystals + separate volatile phase as bubbles) is ~1.4×10^9 m^3 and the separate volatile phase consists of ~30% of this volume as bubbles. For separate two-phase flow to be significant, these bubbles must have a diameter greater than ~10 cm to ascend through Popocatépetl's magma (μ ~10^4 Pa·s) at a rate greater than 10^{-3} m/s. Bubbles of this size are unlikely and we infer that separate two-phase flow is negligible.

Degassing ~1.4×10^9 m^3 of magma over a period of 4 years and 10 months (1.52×10^8 sec, see Chapter 2) would be at an average rate of $Q = 9.4$ m^3/s. We again explore the entire range of conduit radii from $r = 2$ to 100 m. For Case#2, the density difference between magma rich in dissolved volatiles plus bubbles and degassed magma is $\Delta\rho = 670$ kg/m^3. Reynolds number, convective velocity scale, and ascent velocity have the range $Re = 1$ to 18, $W = 1.7$ m/s to 0.5 m/s, and $V = 0.7$ m/s to 0.0003 m/s for $r = 2$ to 100 m. Thus for Case #2, magma flow is inertia-dominated ($Re > 1$) and W and V are of the same order for conduit radii $r \leq 5$ m.

The large discrepancy (greater than an order of magnitude) between W and V in both cases for conduit radii $r > 10$ m (Table 39) imply that smaller conduit radii are more likely. These results are reasonable and consistent with the fluid dynamic calculations shown in Chapter 2 and support the hypothesis that convection of magma in the conduit is a likely degassing mechanism at Popocatépetl volcano regardless of whether the magma does or does not harbor a separate volatile phase.

Conclusions

1) Magma flow in volcanic conduits can be divided into two flow regimes determined by dynamic viscosity. Magmas with $\mu < 10^{2.5}$ are inertia-dominated ($Re > 1$). Magma with $\mu > 10^5$, are viscous-dominated ($Re < 1$). This classification takes into consideration relevant variations in L, $\Delta\rho$, Q, and conduit geometry.

2) Convection is plausible for magma with Re > 1 only in cylindrical conduits with radii less than ~10 m. Low values of Q constrain convection only in small conduits. For convection to occur in dikes, dike width must be less than the radius of a cylindrical conduit for similar values for $\Delta\rho$, and Q.
3) Convection is not possible for magma with Re < 1 and dynamic viscosity $\mu > 10^6$. For magma with dynamic viscosity $\mu < 10^6$ and Re < 1, convection may or may not occur and is a function of L, $\Delta\rho$, Q, and conduit geometry.
4) Convection of magma in the conduit is plausible at Villarrica volcano for conduit radii r = 1 to 5 m and an initial dissolved water content between 1 wt.% and 4 wt.% H_2O.
5) Convection of magma in the conduit is plausible at Popocatépetl volcano for conduit radii r = 2 to 10 m for degassing ~6 km^3 of magma with no separate, pre-existing volatile phase and r = 2 to 5 m for degassing ~1 km^3 of mixed magma with ~9 wt.% separate, pre-existing volatile phase.

CONCLUDING REMARKS

Many volcanoes, with a wide range of magma compositions, have been observed to non-explosively emit large quantities of volatiles over time periods ranging from years to thousands of years with minor to negligible emission of magmatic material. These observations raise two questions: 1) What is/are the source(s) of the emitted volatiles? and 2) What is the mechanism by which the volatiles are able to degas non-explosively? In this dissertation, case-studies of Popocatépetl (Mexico) and Villarrica (Chile) were conducted to answer these questions for two subduction zone volcanoes that span the range of magma compositions from dacite to basaltic andesite. The quantities of magma *erupted* at these two volcanoes as well as alternate sources of volatiles, other than magma, are insufficient to account for the observed gas emission at Popocatépetl and Villarrica. Solutions of analytical equations show that for reasonable rates of magma ascent, convection of *unerupted* magma in the volcanic conduits of these two volcanoes is a mechanism that can supply ample volatile-rich magma to shallow levels where non-explosive degassing takes place. Calculations of the Reynolds number and velocity scale for convection of magma in volcanic conduits provide a test for the plausibility of convection over a wide range of magma viscosities, buoyancy fluxes, conduit sizes, and conduit geometries. Results of these calculations show that convection of magma in the volcanic conduit is permissible at Popocatépetl and Villarrica and is likely a common mechanism to explain long-term, non-explosive "excess degassing" behavior at many volcanoes.

BIBLIOGRAPHY

Aguilera, J.G. and Ordoñez, E., 1895. Expedicion Científica al Popocatépetl. Comision Geológica Mexicana, Mexico, 48 pp.

Allard, P., 1997. Endogenous magma degassing and storage at Mount Etna. Geophysical Research Letters, 24(17): 2219-2222.

Allard, P., Carbonnelle, J., Metrich, N., Loyer, H. and Zettwoog, P., 1994. Sulphur output and magma degassing budget of Stromboli Volcano. Nature, 368: 326-330.

Andersen, D.J., Lindsley, D.H. and Davidson, P.M., 1993. QUILF: A Pascal program to assess equilibria among Fe-Mg-Mn-Ti oxides, pyroxenes, olivine, and quartz. Computers & Geosciences, 19(9): 1333-1350.

Anderson, A.T., 1974. The before-eruption water contents of some high-alumina magmas. Bulletin of Volcanology, 37(4): 530-552.

Anderson, A.T., Jr. et al., 1989. H_2O, CO_2, Cl, and gas in Plinian and ash-flow Bishop rhyolite. Geology, 17(3): 221-225.

Andres, R.J. et al., 1991. Excessive sulfur dioxide emissions from Chilean volcanoes. Journal of Volcanology and Geothermal Research, 46(3-4): 323-329.

Armstrong, J.T., 1984. Quantitative analysis of silicate and oxide minerals: A reevaluation of ZAF corrections and proposal for new Bence-Albee coefficients. In: A.D. Romig Jr. and J.I. Goldstein (Editors), Microbeam Analysis. San Francisco Press, San Francisco, pp. 208-212.

Athanasopoulos, P., 1997. The origin and ascent history of the 1996 dacitic dome, Volcán Popocatépetl , Mexico. Bachelor's Thesis, University of Manitoba, Winnipeg, Canada, 105 pp.

Atl, D., 1939. Volcanes de Mexico, 1. Editorial Polis, Mexico, 1-20 pp.

Bacon, C.R. and Hirschmann, M.M., 1988. Mg/ Mn partitioning as a test for equilibrium between coexisting Fe-Ti oxides. American Mineralogist, 73(1-2): 57-61.

Bergantz, G. and Breidenthal, R., 2001. Non-stationary entrainment and tunneling eruptions: A dynamic link between eruption processes and magma mixing. Geophysical Research Letters, 28(16): 3075-3078.

Bird, R.B., Stewart, W.E. and Lightfoot, E.N., 1960. Transport Phenomena. John Wiley & Sons, New York, 780 pp.

Blatter, D. and Carmichael, I., 1998. Plagioclase-free andesites from Zitacuaro (Michoacan), Mexico: petrology and experimental constraints. Contributions to Mineralogy and Petrology, 132: 121-138.

Boudal, C. and Robin, C., 1988. Relations entre dynamismes éruptifs et réalimentations magmatiques d'origine profonde au Popocatépetl. Canadian Journal of Earth Sciences, 25: 955-971.

Boudal, C. and Robin, C., 1989. Volcán Popocatépetl: Recent eruptive history and potential hazards and risks in future eruptions. In: J.H. Latter (Editor), Volcanic Hazards. IAVCEI Proceedings in Volcanology. Springer-Verlag, Berlin, pp. 110-128.

Bruno, N., Caltabiano, T. and Romano, R., 1999. SO_2 emissions at Mt Etna with particular reference to the period 1993-1995. Bulletin of Volcanology, 60(6): 405-411.

Burton, M.R., Oppenheimer, C., Horrocks, L.A. and Francis, P.W., 2000. Remote sensing of CO_2 and H_2O emission rates from Masaya volcano, Nicaragua. Geology, 28(10): 915-918.

Cabral-Cano, E., Meertens, C. and Correa-Mora, F., 1999. Surface deformation on active volcanoes in central Mexico. Abstract, AGU Fall meeting, San Francisco, CA.

Camacho, H., 1925a. Apuntes acerca de la actividad actual del Popocatépetl en relacion con la sismologia. Anales del Instituto Geológico de Mexico, Tomo II(1, 2, & 3): 38-60.

Camacho, H., 1925b. Resultado de la visita al crater del Popocatépetl el 9 de Marzo de 1922. Anales del Instituto Geológico de Mexico, Tomo II(1, 2, & 3): 64-67.

Cantagrel, J.M., Gourgaud, A. and Robin, C., 1984. Repetitive mixing events and Holocene pyroclastic activity at Pico de Orizaba and Popocatépetl (Mexico). Bulletin of Volcanology, 47-4(1): 735-748.

Carmichael, I.S.E., 1991. The redox states of basic and silicic magmas: a reflection of their source regions? Contributions to Mineralogy and Petrology, 106: 129-141.

Carmichael, I.S.E. and Ghiorso, M.S., 1986. Oxidation-reduction relations in basic magma: a case for homogeneous equilibria. Earth and Planetary Science Letters, 78: 200-210.

Carroll, M., R. and Rutherford, M., J., 1988. Sulfur speciation in hydrous experimental glasses of varying oxidation state; results from measured wavelength shifts of sulfur X-rays. American Mineralogist, 73(7-8): 845-849.

Carroll, M.R. and Rutherford, M.J., 1985. Sulfide and sulfate saturation in hydrous silicate melts. Journal of Geophysical Research, 90: Supplement C601-C612.

CENAPRED-UNAM, 1995. Volcán Popocatépetl: estudios realizados durante la crisis de 1994-1995. Centro Nacional de Prevencion de Desastres, Mexico City, 339 pp.

Clavero, J.R. and Moreno, H., 1994. Ignimbritas Lican y Pucon: evidencias de erupciones explosivas andesitico-basalticas postglaciales del Volcan Villarrica, Andes del Sur., Septimo Congreso Geologico Chileno, Universidad de Concepcion, Concepcion, Chile, pp. 250-254.

Clavero-Ribes, J.E., 1996. Ignimbritas andesitico-basalticas postglaciales del Volcán Villarrica, Andes del Sur (39° 25' S). Magister en Ciencias Thesis, Universidad de Chile, Santiago de Chile, 112 pp.

Clynne, M.A. and Borg, L.E., 1997. Olivine and chromian spinel in primitive calc-alkaline and tholeiitic lavas from the southernmost Cascade Range, California; a reflection of relative fertility of the source. The Canadian Mineralogist, 35: 453-472.

De la Cruz-Reyna, S., Quezada, J.L., Peña, C., Zepeda, O. and Sánchez, T., 1995. Historia de la Actividad Reciente del Popocatépetl (1354 - 1995), Volcán Popocatépetl estudios realizados durante la crisis de 1994 - 1995. CENAPRED - UNAM, Mexico City, pp. 3-22.

De la Cruz-Reyna, S. and Siebe, C., 1997. The giant Popocatépetl stirs. Nature, 388: 227.

Deardorff, J.W., 1970. Convective velocity and temperature scales for the unstable planetary boundary layer and for Rayleigh convection. Journal of the Atmospheric Sciences, 27: 1211-1213.

Delgado, H. and Cárdenas-G, L., 1997. Passive degassing at Volcán Popocatépetl (México): 2.6 x 10^6 tons of SO_2 released in 617 days of activity. Abstract, IAVCEI, Puerto Vallarta, México, pp. 49.

Delgado, H. et al., 1998. CO_2 flux measurements at Popocatépetl volcano: II. Magnitude of emissions and significance. Abstract, American Geophysical Union, San Francisco, CA, pp. F926.

Delgado-Granados, H., Cárdenas-Gonzáles, L. and Piedad-Sánchez, N., 2001. Sulfur dioxide emissions from Popocatépetl volcano (Mexico): case study of a high-emission rate, passively degassing erupting volcano. Journal of Volcanology and Geothermal Research, 108(1-4): 107-120.

Devine, J.D., Gardner, J.E., Brack, H.P., Layne, G.D. and Rutherford, M.J., 1995. Comparison of microanalytical methods for estimating H_2O contents of silicic volcanic glasses. American Mineralogist, 80: 319-328.

Dixon, J.E., Clague, D.A. and Stolper, E.M., 1991. Degassing history of water, sulfur, and carbon in submarine lavas from Kilauea Volcano, Hawaii. Journal of Geology, 99(3): 371-394.

Druitt, T.H. and Bacon, C.R., 1989. Petrology of the zoned calcalkaline magma chamber of Mount Mazama, Crater Lake, Oregon. Contributions to Mineralogy and Petrology, 101(2): 245-259.

Eichelberger, J.C., Carrigan, C.R., Westrich, H.R. and Price, R.H., 1986. Non-explosive silicic volcanism. Nature, 323(6089): 598-602.

Evans, B.W., Scaillet, B. and Kuehner, S.M., 2001a. Iron-Titanium Oxide Thermobarometry at High Oxygen Fugacity. Abstract, Geological Society of America, Boston, MA.

Evans, W.C. et al., 2001b. High CO_2 emissions through porous media; transport mechanisms and implications for flux measurement and fractionation. Chemical Geology, 177(1-2): 15-29.

Fischer, T.P. et al., 1994. Correlations between SO_2 flux and long-period seismicity at Galeras Volcano. Nature (London), 368(6467): 135-137.

Francis, P.W., Burton, M.R. and Oppenheimer, C., 1998. Remote measurements of volcanic gas compositions by solar occultation spectroscopy. Nature, 396: 567-570.

Friedlaender, I., 1921. La Erupcion del Popocatépetl. Societe Scientifique "Antonio Alzate" - Memoires, Tomo 40: 219-229.

Frost, B.R., 1991. Introduction to oxygen fugacity and its petrologic importance. In: D.H. Lindsley (Editor), Oxide minerals: petrologic and magnetic significance. Reviews of Mineralogy, pp. 1-9.

Fuentealba, G., 1984. Informe preliminar de la ultima erupcion del Volcan Villarrica (Octubre 1984 - Enero 1985). Revista Frontera, 3: 45-50.

Garcia, M.O. and Jacobson, S.S., 1979. Crystal Clots, Amphibole Fractionation, and the Evolution of Calc-Alkaline Magmas. Contributions to Mineralogy and Petrology, 69: 319-327.

Gerlach, T.M. et al., 1997. Application of the LI-COR CO_2 analyzer to volcanic plumes; a case study, Volcan Popocatepetl, Mexico, June 7 and 10, 1995. Journal of Geophysical Research, 102(4): 8005-8019.

Gerlach, T.M. and McGee, K.A., 1994. Total sulfur dioxide emissions and pre-eruption vapor-saturated magma at Mount St. Helens. Geophysical Research Letters, 21(25): 2833-2836.

Gerlach, T.M. et al., 1994. Vapor saturation and accumulation in magmas of the 1989-1990 eruption of Redoubt Volcano, Alaska. Journal of Volcanology and Geothermal Research, 62(1-4): 317-337.

Gerlach, T.M., Westrich, H.R. and Symonds, R.B., 1996. Preeruption vapor in magma of the climactic Mount Pinatubo eruption: Source of the giant stratospheric sulfur dioxide cloud. In: C.G. Newhall and R.S. Punongbayan (Editors), Fire and Mud: Eruptions and Lahars of Mount Pinatubo, Philippines. PHIVOLCS, Quezon City and University of Washington Press, Seattle, pp. 415-433.

Ghiorso, M.S., 1999. On the stability relations of hydrous minerals in water-undersaturated magmas. American Mineralogist, 84: 1506-1511.

Ghiorso, M.S. and Sack, R.O., 1991. Fe-Ti oxide geothermometry; thermodynamic formulation and the estimation of intensive variables in silicic magmas. Contributions to Mineralogy and Petrology, 108(4): 485-510.

Ghiorso, M.S. and Sack, R.O., 1995. Chemical Mass Transfer in Magmatic Processes. IV. A Revised and Internally Consistent Thermodynamic Model for the Interpolation and Extrapolation of Liquid-Solid Equilibria in Magmatic Systems at Elevated Temperatures and Pressures. Contributions to Mineralogy and Petrology, 119: 197-212.

Giggenbach, W.F., 1996. Chemical composition of volcanic gases. In: R. Scarpa and I. Tilling Robert (Editors), Monitoring and mitigation of volcano hazards. Springer-Verlag, Berlin, pp. 221-256.

Giordano, D. and Dingwell, D.B., 2003. Viscosity of hydrous Etna basalt: implications for Plinian-style basaltic eruptions. Bulletin of Volcanology, 65: 8-14.

Goff, F. et al., 1998. Geochemical surveillance of magmatic volatiles at Popocatepetl Volcano, Mexico. Geological Society of America Bulletin, 110(6): 695-710.

Goff, F. et al., 2001. Passive infrared remote sensing evidence for large, intermittent CO_2 emissions at Popocatépetl volcano, Mexico. Chemical Geology, 177: 133-156.

GVN, 1992. Spatter ejected from small summit vent; strong fumarolic activity. Global Volcanism Network Bulletin, 17(11).

GVN, 1995. Tremor, mild explosions, and a new pyroclastic cone. Global Volcanism Network Bulletin, 20(4).

GVN, 1996. Popocatépetl (México): Continued ash emissions; new lava dome and lava flows in summit crater. Global Volcanism Network Bulletin, 21(3).

GVN, 1999. Three years of seasonal fluctuations in lava pond height. Global Volcanism Network Bulletin, 24(3).

Harris, A.J.L., Flynn, L.P., Rothery, D.A., Oppenheimer, C. and Sherman, S.B., 1999. Mass flux measurements at active lava lakes: Implications for magma recycling. Journal of Geophysical Research Solid Earth, 104(B4): 7117-7136.

Harris, A.J.L. and Stevenson, D.S., 1997. Magma budgets and steady-state activity of Vulcano and Stromboli. Geophysical Research Letters, 24(9): 1043-1046.

Hauri, E. et al., 2002. SIMS analysis of volatiles in silicate glasses 1. Calibration, matrix effects and comparisons with FTIR. Chemical Geology, 183: 99-114.

Hess, K.-U. and Dingwell, D.B., 1996. Viscosities of hydrous leucogranitic melts: A non-Arrhenian model. American Mineralogist, 81: 1297-1300.

Hickey-Vargas, R., Moreno-Roa, H., Lopez-Escobar, L. and Frey, F.A., 1989. Geochemical variations in Andean basaltic and silicic lavas from the Villarrica-Lanin volcanic chain (39.5 °S): an evaluation of source heterogeneity, fractional crystallization and crustal assimilation. Contributions to Mineralogy and Petrology, 103: 361-386.

Hickey-Vargas, R. et al., 2002. Multiple subduction components in the mantle wedge: Evidence from eruptive centers in the Central Southern volcanic zone, Chile. Geology, 30(3): 199-202.

Holland, T. and Blundy, J., 1994. Non-ideal interactions in calcic amphiboles and their bearing on amphibole-plagioclase thermometry. Contributions to Mineralogy and Petrology, 116: 433-447.

Imai, A., Listanco, E.L. and Fujii, T., 1993. Petrologic and sulfur isotopic significance of highly oxidized and sulfur-rich magma of Mt. Pinatubo, Philippines. Geology, 21: 699-702.

Jaupart, C. and Allègre, C.J., 1991. Gas content, eruption rate and instabilities of eruption regime in silicic volcanoes. Earth and Planetary Science Letters, 102(3-4): 413-429.

Jellinek, A.M., Kerr, R.C. and Griffiths, R.W., 1999. Mixing and compositional stratification produced by natural convection 1. Experiments and their application to Earth's core and mantle. Journal of Geophysical Research, 104(B4): 7183-7201.

Johnson, M.C. and Rutherford, M.J., 1989. Experimental calibration of the aluminum-in-hornblende geobarometer with application to Long Valley Caldera (California) volcanic rocks. Geology, 17(9): 837-841.

Kazahaya, K., Shinohara, H. and Saito, G., 1994. Excessive degassing of Izu-Oshima volcano; magma convection in a conduit. Bulletin of Volcanology, 56(3): 207-216.

Kazahaya, K., Shinohara, H. and Saito, G., 2002. Degassing process of Satsuma-Iwojima volcano, Japan: Supply of volatile components from a deep magma chamber. Earth Planets Space, 54: 327-335.

Klug, C. and Cashman, K.V., 1996. Permeability development in vesiculating magmas; implications for fragmentation. Bulletin of Volcanology, 58(2-3): 87-100.

Kolisnik, A.M.E., 1990. Phenocryst Zoning and Heterogeneity in Andesites and Dacites of Volcán Popocatépetl, Mexico. Master's Thesis, Queen's University, Kingston, Ontario, Canada, 247 pp.

Koyaguchi, T. and Blake, S., 1989. The dynamics of magma mixing in a rising magma batch. Bulletin of Volcanology, 52: 127-137.

Kress, V.C., 1997. Thermochemistry of sulfide liquids. I. the system O-S-Fe at 1 bar. Contributions to Mineralogy and Petrology, 127: 176-186.

Kress, V.C., 2002. Thermochemistry of sulfide liquids III. Ni-bearing liquids at one bar. Contributions to Mineralogy and Petrology, in press.

Kress, V.C. and Carmichael, I.S.E., 1991. The compressibility of silicate liquids containing Fe_2O_3 and the effect of composition, temperature, oxygen fugacity and pressure on their redox states. Contributions to Mineralogy and Petrology, 108: 82-92.

Kress, V.C. and Ghiorso, M.S., 2001. Thermodynamic examination of the post-entrapment crystallization process in igneous melt inclusions. Abstract, AGU Fall meeting. EOS, San Francisco, pp. F1348.

Lange, R.A., 1994. The effect of H_2O, CO_2 and F on the density and viscosity of silicate melts. In: M.R. Carroll and J.R. Holloway (Editors), Volatiles in Magmas. Reviews in Mineralogy, pp. 331-369.

Larocque, A.C.L., Stimac, J.A., Keith, J.D. and Huminicki, M.A.E., 2000. Evidence for open-system behavior in immiscible Fe-S-O liquids in silicate magmas: implications for contributions of metals and sulfur to ore-forming fluids. The Canadian Mineralogist, 38: 1233-1249.

Larocque, A.C.L., Stimac, J.A. and Siebe, C., 1998. Metal-residence sites in lavas and tuffs from Volcán Popocatépetl, Mexico: implications for metal mobility in the environment. Environmental Geology, 33(2/3): 197-208.

Lattard, D., Käsmann, M., Fleischhammer, M. and Höltzen, H., 2001. Towards a Better Calibration of the Titanomagnetite-Ilmenite Thermo-Oxybarometer: New Experimental Results in the Fe-Ti-O System at 1 bar and 1000-1300 °C. Abstract, European Union of Geosciences XI meeting, Strasbourg, France, pp. 585.

LeBas, M.J., LeMaitre, R.W., Streckeisen, A.L. and Zanettin, B., 1986. A chemical classification of volcanic rocks based on the total alkali-silica diagram. Journal of Petrology, 27: 745-750.

Lejeune, A.-M. and Richet, P., 1995. Rheology of crystal-bearing silicate melts; an experimental study at high viscosities. Journal of Geophysical Research, 100(3): 4215-4229.

Lindsley, D.H. and Andersen, D.J., 1983. A two pyroxene thermometer. Journal of Geophysical Research, 88 (Supplement): A887-A906.

Lopez-Escobar, L., Frey, F.A. and Vergara, M., 1977. Andesites and high alumina basalts from the central-south Chile High Andes: geochemical evidence bearing on their petrogenesis. Contributions to Mineralogy and Petrology, 63: 199-228.

Lowenstern, J., Mahood, G., Rivers, M. and Sutton, S., 1991. Evidence for extreme partitioning of copper into a magmatic vapor phase. Science, 252: 1405-1409.

Lowenstern, J.B., 1993. Evidence for a copper-bearing fluid in magma erupted at the Valley of Ten Thousand Smokes, Alaska. Contributions to Mineralogy and Petrology, 114(3): 409-421.

Luhr, J.F., 1990. Experimental Phase Relations of Water- and Sulfur-Saturated Arc Magmas and the 1982 Eruptions of El Chichon Volcano. Journal of Petrology, 31(5): 1071-1114.

Luhr, J.F. and Carmichael, I.S.E., 1985. Jorullo Volcano, Michoacan, Mexico (1759-1774); the earliest stages of fractionation in calc-alkaline magmas. Contributions to Mineralogy and Petrology, 90(2-3): 142-161.

Luhr, J.F., Carmichael, I.S.E. and Varekamp, J.C., 1984. The 1982 eruptions of El Chichon volcano, Chiapas, Mexico: Mineralogy and petrology of the anhydrite-bearing pumices. Journal of Volcanology and Geothermal Research, 23: 69-108.

Mandeville, C. et al., 2001. Sulfur and hydrogen isotopic evidence for open-system degassing during the climactic and pre-climactic eruptions of Mount Mazama, Crater Lake, Oregon. Abstract, AGU Spring meeting, Boston, MA.

Mandeville, C.W., Carey, S. and Sigurdsson, H., 1996. Magma mixing, fractional crystallization and volatile degassing during the 1883 eruption of Krakatau Volcano, Indonesia. Journal of Volcanology and Geothermal Research, 74(3-4): 243-274.

Mandeville, C.W. et al., 1998. Open-system degassing of sulfur from Krakatau 1883 magma. Earth and Planetary Science Letters, 160(3-4): 709-722.

Manga, M., Castro, J., Cashman, K.V. and Loewenberg, M., 1998. Rheology of bubble-bearing magmas. Journal of Volcanology and Geothermal Research, 87(1-4): 15-28.

Martin-Del Pozzo, A.L. et al., 1995. La Emision de cenizas y variaciones geoquimicas durante Diciembre-Marzo en el Volcán Popocatépetl, Volcán Popocatépetl estudios realizados durante la crisis de 1994 - 1995. CENAPRED - UNAM, Mexico City, pp. 285-294.

McKibben, M.A., Eldridge, C.S. and Reyes, A.G., 1996. Sulfur Isotopic Systematics of the June 1991 Mount Pinatubo Eruptions: A SHRIMP Ion Microprobe Study. In: C.G. Newhall and R.S. Punongbayan (Editors), Fire and Mud:

Eruptions and Lahars of Mount Pinatubo, Philippines. PHIVOLCS, Quezon City and University of Washington Press, Seattle, pp. 825-843.

Métrich, N. and Clocchiatti, R., 1996. Sulfur abundance and its speciation in oxidized alkaline melts. Geochimica et Cosmochimica Acta, 60(21): 4151-4160.

Moore, G. and Carmichael, I.S.E., 1998. The hydrous phase equilibria (to 3 kbar) of an andesite and basaltic andesite from western Mexico: constraints on water content and conditions of phenocryst growth. Contributions to Mineralogy and Petrology, 130: 304-319.

Moore, G., Vennemann, T. and Carmichael, I.S.E., 1998. An empirical model for the solubility of H_2O in magmas to 3 kilobars. American Mineralogist, 83: 36-42.

Moreno, H., 1994. Field guide: The Holocene Southern Andes volcanoes between 37° and 39.5° S, Chile, Septimo Congreso Geologico Chileno, pp. 22.

Moreno, H., Clavero, J. and Lara, L., 1994a. Actividad explosiva postglacial del Volcan Villarrica, Andes del Sur, Septimo Congreso Geologico Chileno, Universidad de Concepcion, Concepcion, Chile, pp. 329-333.

Moreno, H., Lopez-Escobar, L. and Cembrano, J., 1994b. The Villarrica-Quetrupillan-Lanin volcanic chain: a review and probable significance in the Southern Andes, Chile, Septimo Congreso Geologico Chileno, Universidad de Concepcion, Concepcion, Chile, pp. 339-341.

Munson, B.R., Young, D.F. and Okiishi, T.H., 1998. Fundamentals of Fluid Mechanics. John Wiley & Sons, New York, 877 pp.

Murphy, M.D., Sparks, R.S.J., Barclay, J., Carroll, M.R. and Brewer, T.S., 2000. Remobilization of Andesite Magma by Intrusion of Mafic Magma at the Soufriere Hills Volcano, Montserrat, West Indies. Journal of Petrology, 41(1): 21-42.

Nakada, S. and Motomura, Y., 1999. Petrology of the 1991-1995 eruption at Unzen: effusion pulsation and groundmass crystallization. Journal of Volcanology and Geothermal Research, 89(1-4): 173-196.

Nakada, S., Shimizu, H. and Ohta, K., 1999. Overview of the 1990-1995 eruption at Unzen Volcano. Journal of Volcanology and Geothermal Research, 89(1-4): 1-22.

Newman, S., Epstein, S. and Stolper, E., 1988. Water, carbon dioxide, and hydrogen isotopes in glasses from the ca. 1340 A.D. eruption of the Mono Craters,

California; constraints on degassing phenomena and initial volatile content. Journal of Volcanology and Geothermal Research, 35(1-2): 75-96.

Newman, S. and Lowenstern, J.B., 2002. VolatileCalc: a silicate melt-H_2O-CO_2 solution model written in Visual Basic for excel. Computers & Geosciences, 28: 597-604.

Nixon, G.T., 1988a. Petrology of the Younger Andesites and Dacites of Iztaccihuatl Volcano, Mexico: I. Disequilibrium Phenocryst Assemblages as Indicators of Magma Chamber Processes. Journal of Petrology, 29(2): 213-264.

Nixon, G.T., 1988b. Petrology of the Younger Andesites and Dacites of Iztaccihuatl Volcano, Mexico: II. Chemical Stratigraphy, Magma Mixing, and the Composition of the Basaltic Magma Influx. Journal of Petrology, 29(2): 265-303.

Noguchi, K. and Kamiya, H., 1963. Prediction of volcanic eruption by measuring the chemical composition and amounts of gases. Bulletin Volcanologique: 367-378.

Ochs, F.A., III and Lange, R.A., 1997. The partial molar volume, thermal expansivity, and compressibility of H (sub 2) O in NaAlSi (sub 3) O (sub 8) liquid; new measurements and an internally consistent model. Contributions to Mineralogy and Petrology, 129(2-3): 155-165.

Ohmoto, H. and Rye, R.O., 1979. Isotopes of sulfur and carbon. In: H.L. Barnes (Editor), Geochemistry of hydrothermal ore deposits. Wiley, pp. 509-567.

Okada, Y., 1992. Internal Deformation due to shear and tensile faults in a half-space. Bulletin of the Seismological Society of America, 82: 1018-1049.

Panfil, M.S., Gardner, T.W. and Hirth, K.G., 1999. Late Holocene stratigraphy of the Tetimpa archaeological sites, northeast flank of Popocatepetl Volcano, central Mexico. Geological Society of America Bulletin, 111(2): 204-218.

Paris, E., Giuli, G., Carroll, M.R. and Davoli, I., 2001. The valence and speciation of sulfur in glasses by X-ray absorption spectroscopy. The Canadian Mineralogist, 39: 331-339.

Pennisi, M. and LeCloarec, M., 1998. Variations in Cl, F and S in Mt Etna's plume (Italy) between 1992 and 1995. Journal of Geophysical Research, 103: 5061-5066.

Petit-Breuilh, M.E., 1994. Contribucion al conocimiento de la cronologia eruptiva historica del Volcan Villarrica, 1558-1985. Revista Frontera, 13: 71-99.

Piccoli, P. and Candela, P., 1994. Apatite in felsic rocks: A model for the estimation of initial halogen concentrations in the Bishop Tuff (Long Valley) and Tuolomne Intrusive Suite (Sierra Nevada Batholith) magmas. American Journal of Science, 294: 92-135.

Quintero, R.M., 1925. Estudio microscopio de las arenas volcanicas del Popocatépetl. Anales del Instituto Geologico de Mexico, Tomo II(1, 2, & 3): 61-63.

Richet, P., Lejeune Anne, M., Holtz, F. and Roux, J., 1996. Water and the viscosity of andesite melts. Chemical Geology, 128(1-4): 185-197.

Robie, R.A. and Hemingway, B.S., 1995. Thermodynamic properties of minerals and related substances at 298.15K and 1 bar (10^5 Pascals) pressure and at higher temperatures. U.S. Geological Survey Bulletin: 1-461.

Robin, C., 1984. Le Volcan Popocatépetl (Mexique): structure, evolution pétrologique et risques. Bulletin Volcanologique, 47(1): 1-23.

Robin, C. and Boudal, C., 1987. A gigantic Bezymianny-type event at the beginning of modern Volcán Popocatépetl. Journal of Volcanology and Geothermal Research, 31: 115-130.

Rose, W.I., Jr., Stoiber Richard, E. and Malinconico, L.L., 1982. Eruptive gas compositions and fluxes of explosive volcanoes; budget of S and Cl emitted from Fuego Volcano, Guatemala. In: R.S. Thorpe (Editor), Andesites; orogenic andesites and related rocks. John Wiley & Sons, pp. 669-676.

Rutherford, M.J. and Devine, J.D., 1988. The May 18, 1980, eruption of Mount St. Helens; 3, Stability and chemistry of amphibole in the magma chamber. Journal of Geophysical Research, 93(10): 11,949-11,959.

Rutherford, M.J. and Hill, P.M., 1993. Magma ascent rates from amphibole breakdown; an experimental study applied to the 1980-1986 Mount St. Helens eruptions. Journal of Geophysical Research, B, Solid Earth and Planets, 98(11): 19,667-19,685.

Rutherford, M.J., Sigurdsson, H., Carey, S. and Davis, A., 1985. The May 18, 1980, eruption of Mount St. Helens; 1, Melt composition and experimental phase equilibria. Journal of Geophysical Research, 90(4): 2929-2947.

Saito, G., Kazahaya, K., Shinohara, H., Stimac, J. and Kawanabe, Y., 2001. Variation of volatile concentration in a magma system of Satsuma-Iwojima volcano deduced from melt inclusion analyses. Journal of Volcanology and Geothermal Research, 108(1-4): 11-31.

Sato, H., Nakada, S., Fujii, T., Nakamura, M. and Suzuki Kamata, K., 1999. Groundmass pargasite in the 1991-1995 dacite of Unzen volcano: phase stability experiments and volcanological implications. Journal of Volcanology and Geothermal Research, 89(1-4): 197-212.

Sato, M., 1978. Oxygen fugacity of basaltic magmas and the role of gas-forming elements. Geophysical Research Letters, 6: 447-449.

Scaillet, B., Clemente, B., Evans, B.W. and Pichavant, M., 1998. Redox control of sulfur degassing in silicic magmas. Journal of Geophysical Research Solid Earth, 103(B10): 23937-23949.

Shaw, H.R., 1972. Viscosities of magmatic silicate liquids; an empirical method of prediction. American Journal of Science, 272(9): 870-893.

Shinohara, H., Kazahaya, K. and Lowenstern, J.B., 1995. Volatile transport in a convecting magma column; implications for porphyry Mo mineralization. Geology, 23(12): 1091-1094.

Siebe, C., Abrams, M., Macías, J.L. and Obenholzner, J., 1996a. Repeated volcanic disasters in Prehispanic time at Popocatépetl, central Mexico: Past key to the future? Geology, 24(5): 399-402.

Siebe, C., Macías Vázquez, J.L., Abrams, M. and Obenholzner, J., 1996b. La destrucción de Cacaxtla y Cholula: un suceso en la historia eruptiva del Popocatépetl. Ciencias, 41: 36-45.

Sigmarsson, O., Chmeleff, J., Morris, J. and Lopez-Escobar, L., 2002. Origin of ^{226}Ra-^{230}Th disequilibria in arc lavas from southern Chile and implications for magma transfer time. Earth and Planetary Science Letters, 196: 189-196.

Sigurdsson, H., Carey, S., Palais, J.M., Devine, J. and Williams, S.N., 1990. Pre-eruption compositional gradients and mixing of andesite and dacite magma erupted from Nevado del Ruiz Volcano, Colombia in 1985. Journal of Volcanology and Geothermal Research, 41(1-4): 127-151.

Simakin, A. and Botcharnikov, R., 2001. Degassing of stratified magma by compositional convection. Journal of Volcanology and Geothermal Research, 105: 207-224.

Simkin, T. and Siebert, L., 1994. Volcanoes of the World. Geoscience Press, Inc., Tucson, Arizona, 349 pp.

Sparks, R.S.J., 1978. The dynamics of bubble formation and growth in magmas: a review and analysis. Journal of Volcanology and Geothermal Research, 3: 1-37.

Sparks, R.S.J. et al., 1998. Magma production and growth of the lava dome of the Soufriere Hills Volcano, Montserrat, West Indies: November 1995 to December 1997. Geophysical Research Letters, 25(18): 3421-3424.

Spera, F.J., 2000. Physical properties of magmas. In: H. Sigurdsson (Editor), Encyclopedia of Volcanoes. Academic Press, San Diego, pp. 171-190.

Stein, D. and Spera, F., 2002. Shear viscosity of rhyolite-vapor emulsions at magmatic temperatures by concentric cylinder rheometry. Journal of Volcanology and Geothermal Research, 113: 243-258.

Stevenson, D.S. and Blake, S., 1998. Modelling the dynamics and thermodynamics of volcanic degassing. Bulletin of Volcanology, 60(4): 307-317.

Stimac, J.A., Siebe, C. and Schaaf, P., 1997. Magmatic processes at Popocatépetl, Mexico. Abstract, IAVCEI, Puerto Vallarta, Mexico.

Stoiber, R.E. and Jepsen, A., 1973. Sulfur dioxide contributions to the atmosphere by volcanoes. Science, 182: 577-578.

Stoiber, R.E., Malinconico, L.L. and Williams, S.N., 1983. Use of the correlation spectrometer at volcanoes. In: H. Tazieff and J.C. Sabroux (Editors), Forecasting Volcanic Events. Elsevier, New York, pp. 425-444.

Stoiber, R.E., Williams, S.N. and Huebert, B.J., 1986. Sulfur and halogen gases at Masaya caldera complex, Nicaragua: total flux and variations with time. Journal of Geophysical Research, 91(B12): 12215-12231.

Stormer, J.C., Jr., 1983. The effects of recalculation on estimates of temperature and oxygen fugacity from analyses of multicomponent iron-titanium oxides. American Mineralogist, 68(5-6): 586-594.

Straub, S.M. and Martin-Del Pozzo, A.L., 2001. The significance of phenocryst diversity in tephra from recent eruptions at Popocatépetl volcano (central Mexico). Contributions to Mineralogy and Petrology, 140: 487-510.

Swanson, D.A. and Holcomb, R.T., 1990. Regularities in growth of the Mount St. Helens dacite dome 1980-1986. In: H. Fink Jonathan (Editor), Lava flows and domes; emplacement mechanisms and hazard implications. IAVCEI Proceedings in Volcanology. Springer-Verlag, Berlin, pp. 3-23.

Taylor, B.E., 1986. Magmatic Volatiles: Isotopic Variation of C, H, and S. In: J.W. Valley, H.P. Taylor and J.R. O'Neil (Editors), Stable Isotopes in High Temperature and Geological Processes. Reviews in Mineralogy. BookCrafters, Inc., Chelsea, Michigan, pp. 185-225.

Thordarson, T., Self, S., Oskarsson, N. and Hulsebosch, T., 1996. Sulfur, chlorine, and fluorine degassing and atmospheric loading by the 1783-1784 AD Laki (Skaftar Fires) eruption in Iceland. Bulletin of Volcanology, 58(2-3): 205-225.

Tormey, D.R., Hickey-Vargas, R., Frey, F.A. and Lopez-Escobar, L., 1991. Recent lavas from the Andean front (33° to 42° S): interpretations of along-arc compositional variations. In: R.S. Harmon and C.W. Rapela (Editors), Andean magmatism and its tectonic setting. Geological Society of America Special Paper, pp. 57-77.

Turcotte, D.L. and Schubert, G., 1982. Geodynamics, Applications of continuum physics to geological problems. John Wiley & Sons, New York, 450 pp.

Vergniolle, S. and Jaupart, C., 1986. Separated two-phase flow and basaltic eruptions. Journal of Geophysical Research, B, Solid Earth and Planets, 91(12): 12,842-12,860.

Waitz, P., 1921. Popocatépetl again in activity. American Journal of Science, Fifth Series, Vol. 1(1): 81-87.

Wallace, P.J., 2001. Volcanic SO_2 emissions and the abundance and distribution of exsolved gas in magma bodies. Journal of Volcanology and Geothermal Research, 108: 85-106.

Wallace, P.J., Anderson, A.T., Jr. and Davis, A.M., 1995. Quantification of pre-eruptive exsolved gas contents in silicic magmas. Nature, 377(6550): 612-616.

Wallace, P.J. and Carmichael, I.S.E., 1994. S speciation in submarine basaltic glasses as determined by measurements of S K-alpha X-ray wavelength shifts. American Mineralogist, 79: 161-167.

Wallace, P.J. and Carmichael, I.S.E., 1999. Quaternary volcanism near the Valley of Mexico: implications for subduction zone magmatism and the effects of crustal thickness variations on primitive magma compositions. Contributions to Mineralogy and Petrology, 135: 291-314.

Wallace, P.J. and Gerlach, T.M., 1994. Magmatic vapor source for sulfur dioxide released during volcanic eruptions; evidence from Mount Pinatubo. Science, 265(5171): 497-499.

Webster, J., Kinzler, R. and Mathez, E., 1999. Chloride and water solubility in basalt and andesite melts and implications for magmatic degassing. Geochimica et Cosmochimica Acta, 63(5): 729-738.

Wendlandt, R., 1982. Sulfide saturation of basalt and andesite melts at high pressures and temperatures. American Mineralogist, 67(1-2): 170-174.

Wessel, P. and Smith, W.H.F., 1991. Free software helps map and display data. EOS Trans. AGU, 72: 441.

Westrich, H.R. and Gerlach, T.M., 1992. Magmatic gas source for the stratospheric SO_2 cloud from the June 15, 1991, eruption of Mount Pinatubo. Geology, 20(10): 867-870.

Wilcox, R.E., 1954. Petrology of Paricutin Volcano, Mexico. U.S. Geological Survey Bulletin, 965-C: 281-349.

Witter, J.B., 1997. Volatile Emissions and Potential Climatic Impact of the Great Kuwae (Vanuatu) Eruption of ~1452-3 A.D. Master's Thesis, University of Hawaii at Manoa, Honolulu, Hawaii, 135 pp.

Zreda-Gostynska, G., Kyle, P.R. and Finnegan, D.L., 1993. Chlorine, fluorine, and sulfur emissions from Mount Erebus, Antarctica and estimated contributions to the Antarctic atmosphere. Geophysical Research Letters, 20(18): 1959-1962.

Appendix A:

A simplified empirical method for high-quality electron microprobe analysis of fluorine in Fe-bearing minerals and glasses

Introduction

Fluorine is commonly found dissolved in the silicate glass phase of volcanic rocks with concentrations from a few hundred to several thousand ppm (Michael and Schilling, 1989; Dunbar and Hervig, 1992a; Dunbar and Hervig, 1992b; Signorelli et al., 1999b; Signorelli et al., 2001). It is also the fifth most abundant component of gases liberated from active volcanoes (following H_2O, CO_2, S-gases, and Cl). Fluorine is also an important volatile element in common igneous and metamorphic minerals such as amphibole, mica, and apatite (Deer et al., 1992) and it may be present in trace amounts in the nominally anhydrous minerals olivine and pyroxene (Hazen et al., 1997; Hoskin, 1999). The precise and accurate determination of F at low levels of detection (tens of ppm) in minerals and silicate glass is important for determining the systematics of F in volcanic systems and the reservoirs of F in the mantle. For example, high-quality analysis of F on the micron scale would be an improvement over bulk analysis of mineral and glass separates in order to determine partition coefficients between the rims of F-bearing minerals and their coexisting silicate liquids (Métrich, 1990). In addition, a comparison of F contents in glass inclusions in phenocrysts and coexisting matrix glasses can assess the extent of F degassing to the atmosphere during volcanic eruptions (Devine et al., 1984). The determination of F in mantle olivine and pyroxene could test the hypothesis that these phases are a significant mantle reservoir for F in addition to H_2O (Bell and Rossman, 1992). The development of a simple, versatile, and high-quality method for analyzing F with the electron microprobe (EMP) would be useful considering the ubiquity of these instruments worldwide.

Analysis of fluorine in Fe-bearing minerals and glasses is not routine in most electron microprobe labs (unlike other volatile elements S and Cl) for a variety of reasons. Conventional TAP diffraction crystals have low count rates for F Kα X-rays resulting in high minimum detection limits and large errors based on counting statistics (Potts and Tindle, 1989). Utilizing a TAP crystal with a high beam current and/or long count time, in order to reduce the minimum detection limits of F, can be problematic due to potential sample damage by the electron beam, including volatile loss. Synthetic multi-layered diffraction crystals (SiW; termed LDE1 by JEOL and PCO by Cameca) that are customized for the diffraction of light element X-rays provide much higher count rates. However, an overlap of the F Kα peak onto the "shoulder" of the Fe $L\alpha_1$ peak makes analyzing F in Fe-bearing minerals and glasses difficult when using SiW (Potts and Tindle, 1989).

In order to overcome these analytical challenges, we developed an electron microprobe method of F analysis using a synthetic multi-layer diffraction crystal that corrects for the presence of Fe using a simple empirical model. We optimized analytical conditions to achieve very low detection limits (~35 ppm) at high precision (~5% relative at ~1000 ppm F) and high spatial resolution (5 μm beam diameter) while minimizing beam damage and/or volatile mobility in sensitive materials such as silicate glass.

Other EMP methods for F analysis

A variety of analytical methods to determine F concentration by electron microprobe are recorded in the literature. Several workers have analyzed F in glass inclusions trapped in phenocrysts and matrix glasses in tephra using a TAP crystal and relatively standard microprobe analytical conditions: 15 kV accelerating voltage, 10 – 25 nA beam current, 1 – 10 μm beam diameter, and 40 – 200 second peak count time (Devine et al., 1984; Palais and Sigurdsson, 1989; Signorelli et al., 1999a; 1999b; 2001). Minimum detection limits (MDL) of ~300 – 2000 ppm F and precisions of 5 – 25% were reported.

Lowenstern et al. (1994) analyzed F in rhyolitic glass inclusions in quartz crystals using a 30 nA beam current, 20 μm beam diameter, 30 second peak count time, and an LDE1 diffraction crystal. They report a 2σ counting uncertainty of 100 ppm F at a concentration of 3720 ppm F and MDL of 370 ppm F. Repeat analyses on one glass inclusion gave a 2σ variation of +/- 440 ppm F. Lowenstern et al. (1994) analyzed the same glass inclusions for F by Secondary Ion Mass Spectrometry (SIMS). On average, F-analyses by EMP are 20% lower than the SIMS analyses, which is greater than the 2σ errors of the two methods based on counting statistics. It is possible that the F analyses by EMP are underestimates due to a background position placed near the Fe $L\alpha_1$ peak.

Michael and Schilling (1989) analyzed F in submarine MORB glasses using a TAP crystal, 8 kV accelerating voltage, 100 nA, and a raster area of 50 μm x 30 μm to minimize damage to the glass. Counts were collected for 500 seconds on the peak position and 250 seconds each on two symmetrically offset background positions. They report precision (2σ) of 30 ppm F based on counting statistics and reproducibility of ~40 ppm F at a concentration of 250 ppm F. This method reproduces the F concentration within 2σ in three out of four standards analyzed by the ion selective electrode method (Schilling et al., 1980).

Thordarson et al. (1996) analyzed F in basaltic glass inclusions in olivine and co-existing matrix glasses using a PC0 diffraction crystal, 15 kV accelerating voltage, 80 nA beam current, 10 μm beam diameter, and 400 second peak count time. Thordarson et al. (1996) also utilized the CSIRO-trace routine of Robinson and Graham (1992), an iterative method that blanks the beam every 10 seconds. Precision (2σ) of 90 ppm F based on counting statistics is reported. Although they make no mention of addressing the problem of Fe peak overlap in their EMP method, their method reproduces the F concentrations determined by Michael and Schilling (1989) using a TAP crystal on the same standard material.

Métrich et al. (2001) analyzed F in Fe-bearing basalt glasses using analytical conditions of 10 kV accelerating voltage, 15 μm beam diameter, and 40-80 nA beam

current. They reduced their analytical error by counting F on two TAP crystals simultaneously. They report a MDL of 210 ppm F with 11% relative error for 900 ppm F with a 400 second total (peak and background) count time (Nicole Métrich, pers. comm. 2002).

Donovan et al. (1993) developed an iterative, theoretical model for correcting spectral interferences on the electron microprobe that is applicable to the analysis of F in Fe-bearing minerals and glasses. However, we found their method to be insensitive for the analysis of F concentrations less than several hundred ppm due to the inherent Poisson variability of X-ray counts on the interference standard.

Todd (1996) outlined an electron microprobe method for analyzing F in Fe-bearing minerals using a PC0 diffraction crystal. He reports that a linear relationship exists between wt% FeO and apparent wt% F in F-free standards such as olivines, pyroxenes, and oxides: apparent wt% F = 0.0167 + 0.00619*FeO wt%. In this method, the F correction equation is applied following the matrix correction algorithm.

While our method builds on the work of Todd (1996) and Thordarson et al. (1996), it differs in that we have created an F-correction equation that is an internal part of the analytical routine that can be easily implemented on any microprobe and solves both problems of beam heating and peak overlaps.

Analytical Method

The F analysis method presented here was developed on a 4-spectrometer JEOL 733 Superprobe with Geller automation at the University of Washington. The method consists of two parts. First, we describe an improved iterative routine that attains high precision and low detection limits while minimizing beam damage and volatile mobility. Second, we present an empirical correction scheme for Fe $L\alpha_1$ peak interference on the F $K\alpha$ peak.

Analytical conditions are as follows: LDE1 diffraction crystal, 10 kV accelerating voltage, 180 nA beam current, 5 μm beam diameter, and 400 second

total peak count time. An accelerating voltage of 10 kV improves the efficiency of F X-ray production and reduces the size of the analytical volume (critical for the analysis of small glass inclusions) while the high beam current of 180 nA produces high count rates. A defocused beam with diameter of 5 μm was used, which reduces sample heating by a factor of 5 according to the equation of Castaing (1951), yet it provides good spatial resolution for assessing F-zonation in minerals and for the analysis of small (>10 μm) glass inclusions contained in phenocrysts. Note that a rastered beam should never be used for analysis as not all portions of the rastered area experience the same dwell time.

In addition to a defocused beam, volatile loss during the analysis due to the very high beam current is further minimized by using an iterative scheme that blanks the electron beam for 10 seconds after each 10 second counting interval, allowing the sample to cool. The total number of peak and background counts is the summation of forty successive iterations for a total peak and background counting time of 400 seconds. We conducted a test of volatile mobility under the electron beam and found X-ray count rates for F remain stable during the entire period of analysis. Our method is a modified version of the routine originally developed by T. Thordarson at the University of Hawaii (see Thordarson et al., 1996).

The ideal F-peak position on our LDE1 diffraction crystal is at an L-value of 83.60 mm (0.29857 sinθ units). We chose only one background position, at 85.60 mm (0.30571 sinθ units), to avoid the nearby peaks Al $K\alpha_2$ and Mg $K\alpha_2$ (Figure 30). Fluorine was calibrated on an Fe-free synthetic F-phlogopite standard (9.02 wt% F) prior to each analytical session. Accuracy of the technique was tested using NIST glass standards SRM610 and SRM620; NMNH glass standard A99; and glass standards KE12, KE3, CFA47 (provided by N. Métrich). These glass standards have F-contents ranging from zero to 4700 ppm. The technique was tested further on internal mineral standards Biotite1, Biotite23a, Biotite27, Mason Biotite, Glaucophane, and Muscovite-M (300 – 6600 ppm F; Table 40).

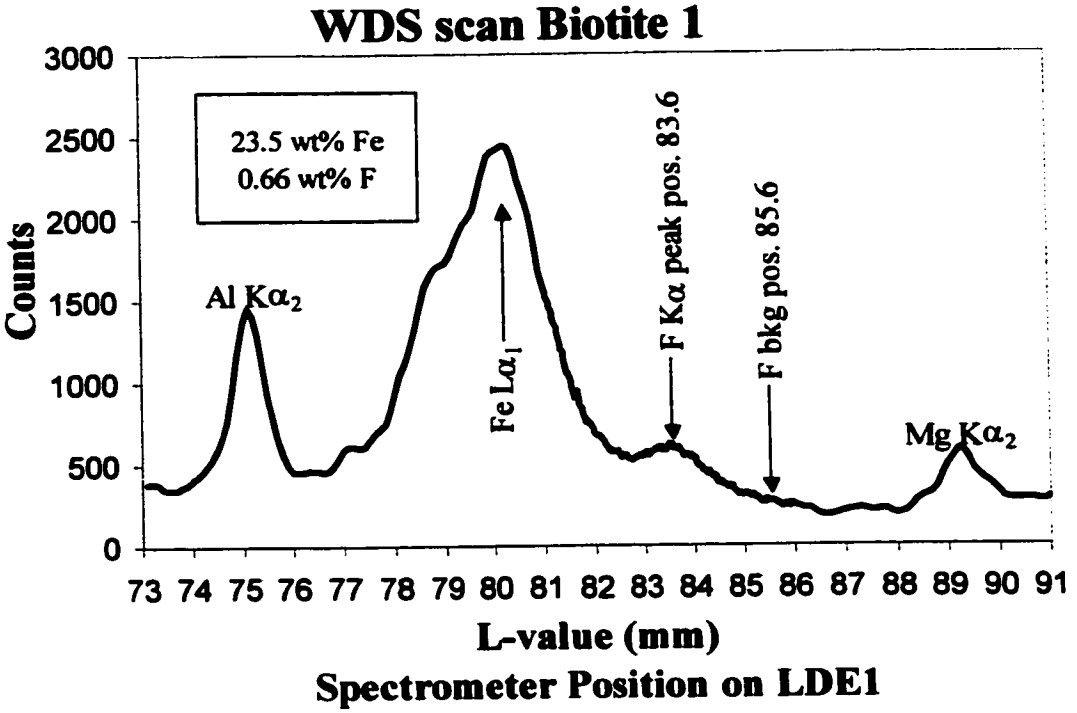

Figure 30. Wavelength scan of the LDE1 diffraction crystal in the region of the F Kα peak for the mineral standard Biotite 1 (which contains 23.5 wt% Fe and 6600 ppm F). Peaks for Al $K\alpha_2$, Fe $L\alpha_1$, F Kα, and Mg $K\alpha_2$ lines are shown. The chosen F background position is also shown. Note the position of the F Kα peak on the "shoulder" of the Fe $L\alpha_1$ peak.

Table 40. Accepted Fe and F contents of mineral and glass standards used in this study.

Glass Standard	Fe (wt.%)	F (ppm)	2σ
A99[a]	10.34	765	±144
KE12[b]	6.50	4000	±240
KE12[c]	6.50	4338	±1096
KE12[d]	6.50	4400	n.r.
KE3[e]	5.68	4700	n.r.
CFA47[b]	2.06	2000	±120
CFA47[f]	2.06	2500	±1200
NIST SRM 610[g]	0.05	295	±32
NIST SRM 620	0.03	0	n.r.

Mineral Standard*	Fe (wt.%)	F (ppm)	2σ**
Biotite 1[h]	23.46	6600	n.r.
Biotite 23a[i]	20.93	3600	n.r.
Biotite 27[j]	16.91	5100	n.r.
Mason Biotite[k]	14.52	2100	n.r.
Glaucophane[l]	9.61	300	n.r.
Muscovite-M[m]	3.96	1000	n.r.

2σ = error on the F-analysis; EMP = electron microprobe
SIMS = secondary ion mass spectrometry; ISE = ion selective electrode
[a] EMP analyses reported in Thordarson et al. (1996)
[b] ISE analyses reported in Mosbah et al. (1991)
[c] EMP analyses reported in Palais and Sigurdsson (1989)
[d] accepted value reported in Palais and Sigurdsson (1989)
[e] accepted value reported in Mosbah et al. (1991)
[f] EMP analyses reported in Signorelli et al. (1999b)
[g] SIMS analyses reported in Hoskin (1999)
[h] Wet chemistry, I. Carmichael, UC Berkeley
[i] Geological Survey of Canada
[j] Rimsaite (1964)
[k] Mason (1962)
[l] Borg (1967)
[m] Evans (1965)
* all analyses of F in mineral standards conducted by classical wet chemistry methods
** An error of ±1000 ppm F is assumed for the wet chemical method
n.r. = not reported

Average analytical errors (2σ) based on counting statistics are 13% at 300 ppm F and 1.8% at 2500 ppm F as determined from the following equations:

$$\%\,\sigma = \frac{\sqrt{N_{peak} + N_{bkg\,calc}}}{\left(N_{peak} - N_{bkg\,calc}\right)} \tag{31}$$

$$\%\ \text{relative error}\ (2\sigma) = 2\sqrt{\%\,\sigma_{unk}^2 + \%\,\sigma_{std}^2}$$

where N_{peak} = total counts at the F peak position and $N_{bkg\,calc}$ = total counts at the F background position corrected for sloping interference from the Fe $L\alpha_1$ line (explained below).

Minimum detection limits are calculated using the method of Reed (1975):

$$\text{Minimum Detection Limit} = \frac{4C_b}{\sqrt{N_{peak} + N_{bkg\,calc}}} \tag{32}$$

$$C_b = C_{std}\left(\frac{I_{bkg}}{I_{std}}\right)$$

where C_b = the "apparent concentration" of the background, C_{std} = the concentration of F in the standard, I_{std} = the total F peak intensity of the standard, and I_{bkg} = intensity of the background in the unknown. We obtain a minimum detection limit of 35 ppm F using this relationship.

The major challenge for accurate analysis of F is correcting the spectral interference between the F Kα peak and the Fe $L\alpha_1$ line (Figure 30). To overcome this problem we first measured the number of counts derived from Fe at the F Kα peak position on a variety of F-free standards containing 0-30 wt% Fe (Figure 31). Background counts were collected on only one side of the F Kα peak, away from Fe interference. The slope of the "shoulder" of the Fe $L\alpha_1$ peak increases with increasing Fe-concentration in the F-free standards (Figure 31). We calculated the following correction factor (C_F) to correct for the presence of the "shoulder" of the Fe $L\alpha_1$ peak that lies under the F peak position:

$$C_F = N_{F\text{-}peak} / N_{F\text{-}bkg} \tag{33}$$

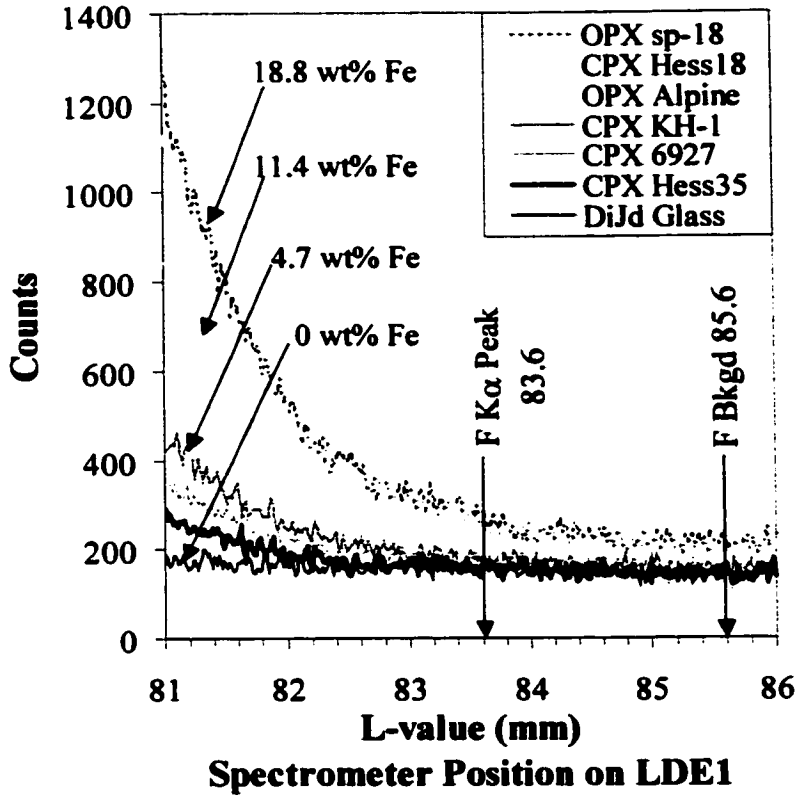

Figure 31. Wavelength scans of the LDE1 diffraction crystal in the region of the F Kα peak for a variety of F-free standards of varying Fe content. Wavelength scans are superimposed to show the increase in slope of the "shoulder" of the Fe $L\alpha_1$ peak with increasing Fe content. The F Kα peak position and F background position are shown. The Fe $L\alpha_1$ peak position is off the left side of the chart at an L-value of 80.2 mm. For clarity, not all Fe concentrations are indicated. These are: CPX Hess 35, 2.22 wt% Fe; CPX 6927, 2.95 wt% Fe; and CPX Hess 18, 18.65 wt% Fe. Curve for Olivine YS-15 (29.77 wt% Fe) not shown.

where $N_{F\text{-}peak}$ = number of counts at the F peak position on F-free phases and $N_{F\text{-}bkg}$ = number of counts at the F background position (Figure 32). The correction factor C_F is the fractional amount that the X-ray counts at the F Kα peak position exceed X-ray counts at the F background position in F-free standards as a result of the Fe $L\alpha_1$ "shoulder." Our measurements of $N_{F\text{-}peak}$ and $N_{F\text{-}bkg}$ show that, within analytical error, the C_F varies linearly with Fe content (Figure 33). Even for solids that contain 0 wt% Fe, the $C_F \sim 1.1$. This is due to the natural slope of the background "Bremsstrahlung" radiation between the F peak ($N_{F\text{-}peak}$) and background ($N_{F\text{-}bkg}$) spectrometer positions using the LDE1 diffraction crystal.

Based upon our determinations of the C_F for a variety of F-free, Fe-bearing standards we derived a linear least squares equation for the best-fit line that relates C_F to Fe-content (Figure 33):

$$C_F = 0.0085 * \text{Fe wt\%} + 1.1108 \quad (34)$$

If the Fe-content of a sample under analysis is known, the number of Fe background counts at the F peak position ($N_{F\text{-}peak}$) can be calculated by simply multiplying the intensity measured at the background position ($N_{F\text{-}bkg}$) by C_F (Figure 32):

$$N_{F\text{-}peak} = N_{F\text{-}bkg} * C_F = N_{bkg\ calc} \quad (35)$$

This calculated background intensity at the F peak position is subsequently referred to as $N_{bkg\ calc}$.

For the analysis of phases that contain both F and Fe, the number of counts at the F peak (N_{peak}) and background ($N_{F\text{-}bkg}$) positions are measured (Figure 32). The background intensity at the F peak position ($N_{bkg\ calc}$) is calculated using Equations (34) and (35) and the known Fe-content of the phase under analysis. The net F peak intensity is calculated from the difference between the total counts at the F peak location (N_{peak}) and the calculated F background counts ($N_{bkg\ calc}$; see Figure 32). In our study, the resulting net F intensity was then inserted into a table with known

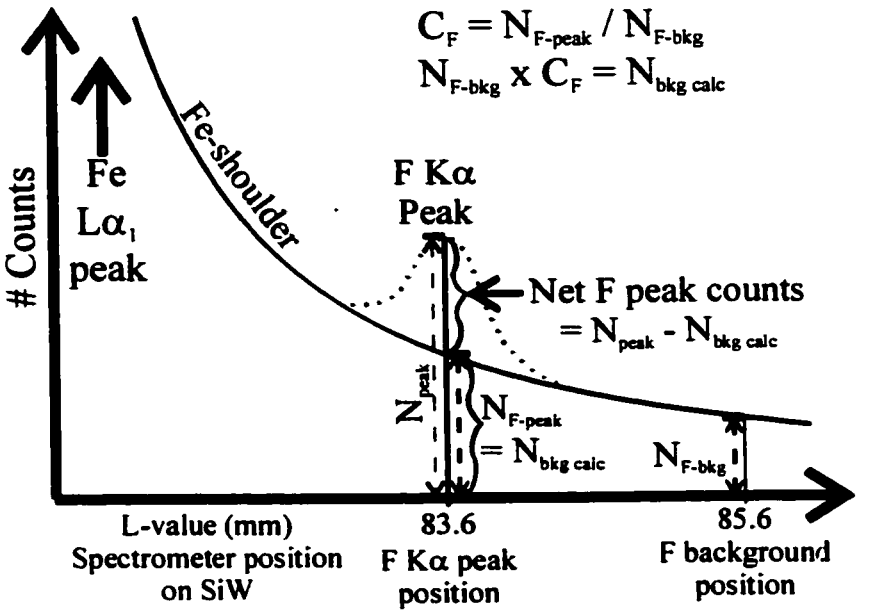

Figure 32. A schematic diagram showing a wavelength scan of the LDE1 diffraction crystal in the region of F Kα peak illustrating our method of determining the contribution of X-ray counts at the F peak position due to the Fe $L\alpha_1$ peak. The "shoulder" of the Fe $L\alpha_1$ peak is shown as a solid sloping line. The F Kα peak is shown as a dotted line. The number of counts at the F background position ($N_{F\text{-}bkg}$) and the number of counts at the F Kα peak position ($N_{F\text{-}peak}$) due to the Fe $L\alpha_1$ "shoulder" are measured on F-free standards. The value of the correction factor C_F is calculated from the ratio of $N_{F\text{-}peak}$: $N_{F\text{-}bkg}$.

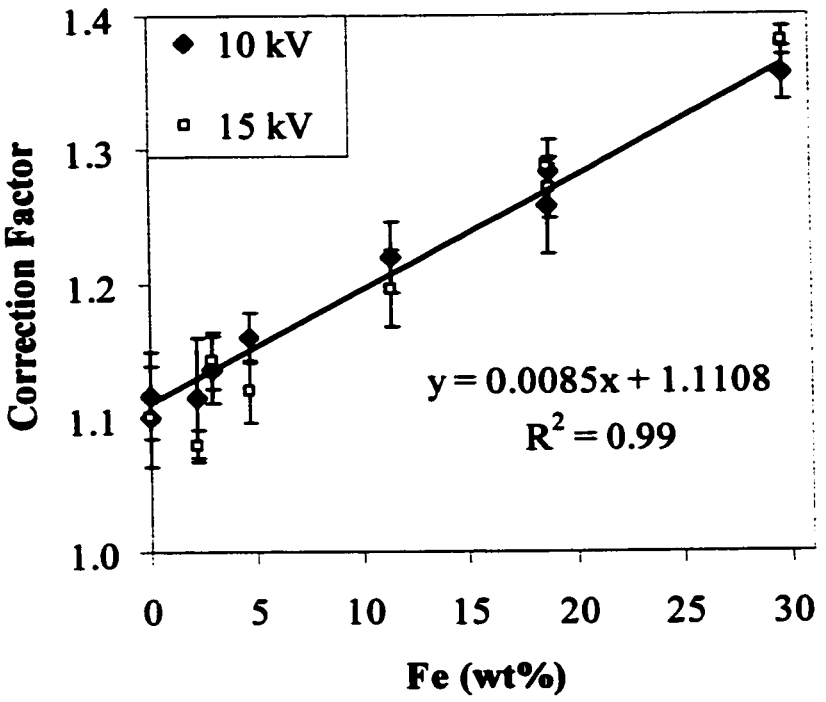

Figure 33. Plot of Fe-content in F-free standards vs. correction factor, C_F. The correction factor was calculated using nine F-free standards with varying Fe content from the following formula: $C_F = N_{F\text{-}peak} / N_{F\text{-}bkg}$, where $N_{F\text{-}peak}$ = number of counts at the F Kα peak position and $N_{F\text{-}bkg}$ = number of counts at the F background position (see Figure 32). For each standard we collected counts at 10 kV (*filled diamonds*) on the peak and background positions five times for 30 seconds each time and averaged the results. This process was repeated for each standard at 15 kV (*open squares*) for comparison. Error bars are 2σ standard deviations. Agreement between analyses done at 10 kV and 15 kV are within error. The solid line represents the linear least squares regression for the 10 kV analyses. The equation for this line and R^2 statistic are shown.

major element concentrations of the glass and mineral standards and the matrix corrections calculated via the method of Armstrong (1984).

For analyzing F in Fe-bearing unknowns (e.g. glass inclusions, matrix glass, minerals), the net F intensity can be inserted into a table with major element data for the unknown that were collected previously (under different analytical conditions). The fluorine data are reprocessed with the major element data and the appropriate matrix corrections are applied. If one chooses to determine all elements, including F, simultaneously (under the same analytical conditions) then C_F can be determined during analysis by estimating the Fe wt% via the relationship:

$$C^{Fe}_{unk} = C^{Fe}_{std} \frac{I^{Fe}_{unk}}{I^{Fe}_{std}} \qquad (36)$$

where C^{Fe}_{unk} = the concentration of iron in the unknown, C^{Fe}_{std} = the concentration of iron in the standard, I^{Fe}_{unk} = intensity of iron in the unknown, and I^{Fe}_{std} = intensity of iron in the standard. The net F intensity can then be calculated and matrix corrections applied to all elements simultaneously.

Results

We analyzed several mineral and glass standards with known F contents that range from a zero to several thousand ppm F. As a test of the quality of our Fe-correction scheme we analyzed F in mineral standards that contain both Fe and F with TAP and LDE1 diffraction crystals simultaneously (Figure 34; Table 41). Although the analyses with TAP are less precise than LDE1, we would expect the results using the two different diffraction crystals to overlap if our correction scheme is accurate. Agreement between the results obtained with the two diffraction crystals is very good. Since there are no spectral interferences when analyzing F with the TAP crystal, this suggests that the correction scheme presented here adequately corrects for overlap of the F Kα peak on the "shoulder" of the Fe $L\alpha_1$ peak.

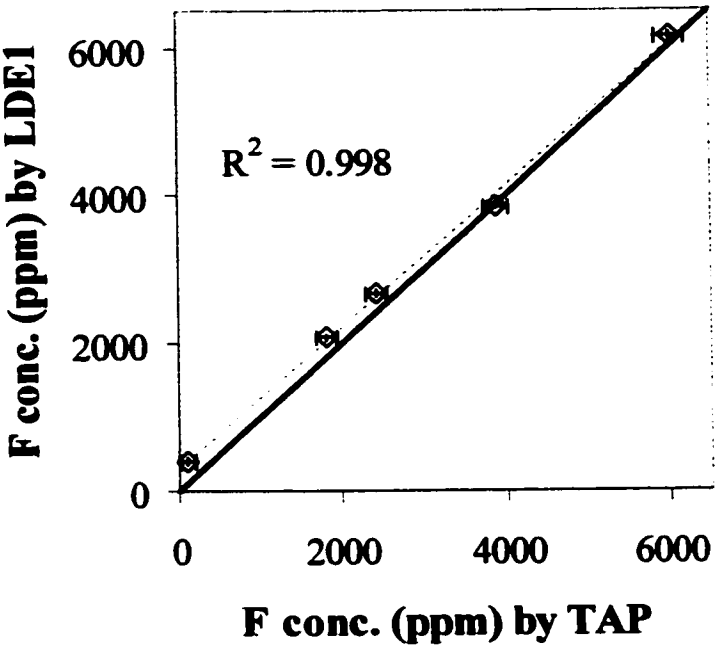

Figure 34. Comparison of EMP analysis of fluorine in mineral standards using different diffraction crystals. EMP analysis of the same spot by TAP and LDE1 conducted simultaneously under identical analytical conditions (described in the text). Each data point represents one analysis. Heavy solid line is the 1:1 line. Two-sigma error based on counting statistics is shown. Light dashed line is the linear least squares regression through the data with R^2 statistic shown.

Table 41. Comparison of EMP analysis of fluorine in mineral standards using different diffraction crystals. EMP analysis by TAP and LDE1 conducted simultaneously under identical analytical conditions.

	LDE1			TAP			Accepted
Sample	F (ppm)	2σ	MDL	F (ppm)	2σ	MDL	F (ppm)
Glaucophane	**399**	44	37	**107**	87	82	**300**
Muscovite-M	**2076**	42	35	**1801**	126	82	**1000**
Mason Biotite	**2520**	48	39	**2424**	121	92	**2100**
Biotite 23a	**3804**	53	42	**3868**	155	96	**3600**
Biotite 27	**6150**	62	44	**6005**	180	95	**5100**
Biotite 1	**6602**	59	45	**n/a**	n/a	n/a	**6600**

2σ = error based on counting statistics
MDL = minimum detection limit
n/a = not analyzed

A comparison between the F-content determined in mineral and glass standards using the LDE1 diffraction crystal and the accepted F-content is shown in Figure 35 and Tables 41 & 42. Agreement is quite good between accepted and measured values, especially since the composition of the majority of the mineral standards were determined by wet chemistry which, because this is a bulk analytical method, will average any chemical inhomogeneities present in the sample. We estimate the analytical errors in the wet chemical analysis to be ±0.1 wt% (Bernard Evans, pers. comm. 2002).

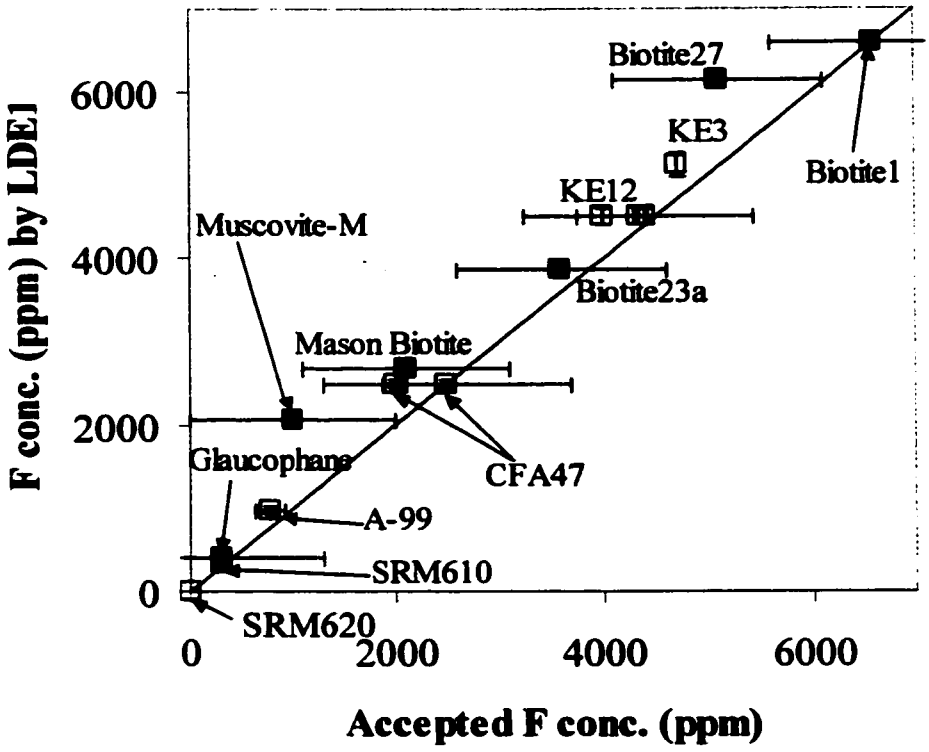

Figure 35. Comparison of accepted and measured fluorine concentration in mineral (*filled squares*) and glass standards (*open squares*). Fluorine measured by EMP using an LDE1 diffraction crystal and analytical conditions described in the text. Heavy solid line is the 1:1 line. Two-sigma errors based on counting statistics for the EMP analysis are the same size or smaller than the symbols for mineral analyses and are shown for glass standard analyses. Analytical errors on the accepted values of the mineral standards are estimated to be ±1000 ppm F. Error bars on the accepted values of the glass standards show the two-sigma error based on counting statistics or the two-sigma variation on multiple analyses on a single standard, whichever is greater. The accepted value of the glass standard A-99 is dubious since it is based on electron microprobe analyses using a multi-layer diffraction crystal. Whether or not a correction for spectral interference between F and Fe was undertaken to determine the accepted value is unknown. The analytical method used to determine the accepted value of glass standard KE3 is also unknown, as are the errors associated with that analysis.

Table 42. Analyses of F in glass standards using LDE1 diffraction crystal

Standard	F conc.	2σ Var.	2σ Err	MDL	n
KE3	5130	138	51	37	2
KE12	4513	88	50	36	2
CFA47	2483	32	45	33	2
A-99	976	8	45	36	2
NBS610	336	24	42	31	3
NBS620	0	0	n/a	30	4

All analyses made with the LDE1 synthetic multi-layer diffraction crystal
All results reported as ppm.
n = number of analyses
conc. = concentration
2σ Var. = two-sigma variation in the multiple analyses of a single standard
2σ Err = two-sigma error based on counting statistics
MDL = minimum detection limit

References

Armstrong, J.T., 1984. Quantitative analysis of silicate and oxide minerals: A reevaluation of ZAF corrections and proposal for new Bence-Albee coefficients. In: A.D. Romig Jr. and J.I. Goldstein (Editors), Microbeam Analysis. San Francisco Press, San Francisco, pp. 208-212.

Bell, D.R. and Rossman, G.R., 1992. Water in Earth's Mantle: The role of nominally anhydrous minerals. Science, 255: 1391-1397.

Castaing, R., 1951. Application des sondes éléctroniques à une méthode d'analyse ponctuelle chimique et cristallographique. Ph.D. Thesis, University of Paris.

Deer, W.A., Howie, R.A. and Zussman, J., 1992. An Introduction to the Rock-Forming Minerals. Longman Scientific & Technical, Essex, England, 696 pp.

Devine, J.D., Sigurdsson, H., Davis, A.N. and Self, S., 1984. Estimates of sulfur and chlorine yield to the atmosphere from volcanic eruptions and potential climatic effects. Journal of Geophysical Research, 89(7): 6309-6325.

Donovan, J.J., Snyder, D.A. and Rivers, M.L., 1993. An improved interference correction for trace element analysis. Microbeam Analysis, 2: 23-28.

Dunbar, N.W. and Hervig, R.L., 1992a. Petrogenesis and volatile stratigraphy of the Bishop Tuff; evidence from melt inclusion analysis. Journal of Geophysical Research, B, Solid Earth and Planets, 97(11): 15,129-15,150.

Dunbar, N.W. and Hervig, R.L., 1992b. Volatile and trace element composition of melt inclusions from the lower Bandelier Tuff; implications for magma chamber processes and eruptive style. Journal of Geophysical Research, 97(11): 15,151-15,170.

Hazen, R.M., Yang, H., Prewitt, C.T. and Gasparik, T., 1997. Crystal chemistry of superfluorous phase B ($Mg_{10}Si_3O_{14}F_4$): Implications for the role of fluorine in the mantle. American Mineralogist, 82: 647-650.

Hoskin, P.W.O., 1999. SIMS Determination of $\mu g\ g^{-1}$ level fluorine in geological samples and its concentration in NIST SRM 610. Geostandards Newsletter, 23(1): 69-76.

Lowenstern, J.B., Bacon, C.R., Calk, L.C., Hervig, R.L. and Aines, R.D., 1994. Major-element, trace-element, and volatile concentrations in silicate melt inclusions from the tuff of Pine Grove, Wah Wah Mountains, Utah. U.S. Geological Survey, Open-file Report, 94-242: 1-20.

Métrich, N., 1990. Chlorine and fluorine in tholeiitic and alkaline lavas of Etna (Sicily). Journal of Volcanology and Geothermal Research, 40: 133-148.

Métrich, N., Bertagnini, A., Landi, P. and Rosi, M., 2001. Crystallization Driven by Decompression and Water Loss at Stromboli Volcano (Aoelian Islands, Italy). Journal of Petrology, 42(8): 1471-1490.

Michael, P.J. and Schilling, J.-G., 1989. Chlorine in mid-ocean ridge magmas: Evidence for assimilation of seawater-influenced components. Geochimica et Cosmochimica Acta, 53: 3131-3143.

Palais, J.M. and Sigurdsson, H., 1989. Petrologic evidence of volatile emissions from major historic and pre-historic volcanic eruptions. In: A. Berger, R.E. Dickinson and J.W. Kidson (Editors), Understanding Climate Change, Geophysical Monograph 52. IUGG and AGU, Washington, D.C., pp. 31-53.

Potts, P.J. and Tindle, A.G., 1989. Analytical characteristics of a multilayer dispersion element (2d=60 Å) in the determination of fluorine in minerals by electron microprobe. Mineralogical Magazine, 53: 357-362.

Reed, S.J.B., 1975. Principles of X-ray generation and quantitative analyses with the electron microprobe. In: C.A. Anderson (Editor), Microprobe Analysis, pp. 53-81.

Robinson, B.W. and Graham, J., 1992. Advances in electron microprobe trace-element analysis. Journal of Computer-Assisted Microscopy, 4(3): 263-265.

Schilling, J.-G., Bergeron, M.B. and Evans, R., 1980. Halogens in the mantle beneath the North Atlantic. Philosophical Transactions of the Royal Society of London, Series A, 297(1431): 147-178.

Signorelli, S., Vaggelli, G., Francalanci, L. and Rosi, M., 1999a. Origin of magmas feeding the Plinian phase of the Campanian Ignimbrite eruption, Phlegrean Fields (Italy): constraints based on matrix-glass and glass-inclusion compositions. Journal of Volcanology and Geothermal Research, 91: 199-220.

Signorelli, S., Vaggelli, G. and Romano, C., 1999b. Pre-eruptive volatile (H_2O, F, Cl, and S) contents of phonolitic magmas feeding the 3550-year old Avellino eruption from Vesuvius, southern Italy. Journal of Volcanology and Geothermal Research, 93: 237-256.

Signorelli, S., Vaggelli, G., Romano, C. and Carroll, M.R., 2001. Volatile element zonation in Campanian ignimbrite magmas (Phlegrean Fields, Italy): evidence from the study of glass inclusions and matrix glasses. Contributions to Mineralogy and Petrology, 140: 543-553.

Thordarson, T., Self, S., Oskarsson, N. and Hulsebosch, T., 1996. Sulfur, chlorine, and fluorine degassing and atmospheric loading by the 1783-1784 AD Laki (Skaftar Fires) eruption in Iceland. Bulletin of Volcanology, 58(2-3): 205-225.

Todd, C.S., 1996. Fluorine analysis by electron microprobe: correction for iron interference. Abstract, GSA Annual Meeting, Denver, CO, pp. A-212.

Appendix B:

Additional petrographic and petrologic information for Popocatépetl volcano

Rock Descriptions

Rock samples used in this study were obtained from various small explosive events in 1997 and 1998. All samples are vesicular or were emplaced hot as evidenced by nearby burnt vegetation or melted equipment. All samples represent juvenile magma. We focused our efforts on pumiceous samples from the eruption of June 30, 1997 and dome blocks from the eruption of January 1, 1998. Petrographic studies were also undertaken on samples from other small explosive events in December 1997 and January, March, and April 1998.

One suite of samples was derived from the moderately explosive eruption of June 30, 1997. The sampled eruption products include volumetrically dominant, dark-gray andesite pumice and subordinate, white dacite pumice. Some clasts are banded. The eruption had two pulses and lasted a total of ~3½ hours. The eruption column rose to a height of at least 13 km above sea level and showered ash on Mexico City. It was one of the most powerful eruptive events at Popocatépetl since 1994 (GVN, 1997b).

A second suite of samples was derived from a smaller eruption on January 1, 1998. This eruption produced a crystal-rich, poorly vesicular, gray dacite containing volumetrically minor, deformed blebs of darker material. The maximum intensity of the eruption lasted ~1½ minutes and the eruption plume reached ~5 km above the crater (GVN, 1997a).

The various samples of ballistic ejecta from dome explosions in December 1997 to April 1998 are all light to dark gray, dense, crystal-rich lava. Some samples are micro-vesicular while others show subtle bands of lighter and darker material.

Petrography and igneous textures

Orthopyroxene rims on Cr-spinel-bearing olivine are rare and narrow in our samples from the June 30, 1997 eruption. Orthopyroxene rims are more common and better-developed on olivines in samples from the January 1, 1998 dome explosion event and the December 1997 to April 1998 dome rocks. Straub & Martin-Del Pozzo (2001) also reported orthopyroxene rims on olivine whereas Kolisnik (1990) found abundant and well developed orthopyroxene reaction rims on olivine in Quaternary Popocatépetl lavas. The higher abundance of orthopyroxene rims in the dense lavas and dome rocks probably reflects longer cooling times, compared to the more rapidly quenched pumices erupted on June 30, 1997. Orthopyroxene rims are not found on olivine microphenocrysts.

Anhedral Fe-Ti oxides commonly occur as 5-100 μm inclusions in clinopyroxene, orthopyroxene and, less commonly, plagioclase phenocrysts. Titanomagnetite and ilmenite occur as microphenocrysts (up to 250 μm in diameter) and as microlites (< 10 μm in diameter) in the groundmass. Rare Fe-Ti oxide grains contain glass inclusions up to 30 μm in size. Titanomagnetite and ilmenite occur separately as well as in intimate contact. Exsolution of titanomagnetite in ilmenite or vice versa has not been observed.

Orthopyroxene and clinopyroxene are common as phenocrysts in all samples and reach up to 1 mm in length. Clinopyroxene phenocrysts are generally euhedral to subhedral. Most orthopyroxene phenocrysts are subhedral; however, some appear reacted and embayed. Both clinopyroxene and orthopyroxene phenocrysts contain abundant glass inclusions ~5-50 μm in diameter. Rare, globular, sulfide inclusions ~5-15 μm in size and lath-shaped apatite 10-50 μm long also occur as inclusions in pyroxene. Microphenocrysts of clinopyroxene and orthopyroxene (30-300 μm) are common, frequently have octagonal or lath shaped cross-section, and rarely contain melt or mineral inclusions.

Plagioclase is by far the most abundant phenocryst in the recent Popocatépetl samples reaching up to 2 mm in size. Many are rich in glass inclusions and concentric

bands of glass inclusions in plagioclase are common. Complex, oscillatory zonation as well as subhedral or embayed plagioclase crystals are common. Many plagioclase grains have sieve-textured cores and/or evidence of mineral dissolution followed by re-growth. In contrast, other plagioclase grains are relatively pristine, euhedral and/or inclusion free. Microphenocrysts of plagioclase (30-300 μm) are common and frequently occur as euhedral laths.

The felty textured groundmass in dark-colored pumiceous hand samples is dominated by randomly oriented plagioclase and Fe-Ti oxide microlites. Some of the plagioclase microlites are lath-shaped while others are hopper-shaped. Very little dark-colored, quenched glass is present. Some areas of the matrix in the dark-colored pumiceous hand samples have partially aligned lath-shaped plagioclase microphenocrysts and microlites that show a pilotaxitic texture. In light-colored pumiceous hand samples, groundmass is composed of abundant, colorless, microlite-poor glass with a vesicular hyalopilitic texture.

Nearly all samples contain crystal clots of clinopyroxene + orthopyroxene + Fe-Ti oxides or plagioclase + clinopyroxene + orthopyroxene + Fe-Ti oxides. They usually occur as one glomerocryst per thin section. Pyroxene dominated glomerocrysts often have a granular texture. However, glomerocrysts that contain plagioclase exhibit hypidiomorphic granular texture.

The mineralogy of the dome explosion samples of December 1997 and January, March, and April 1998 is identical to the mineralogy of the more pumiceous samples of the June 30, 1997 eruption. However, texturally, the matrix in the dome samples is generally coarser grained, with a smaller proportion of interstitial glass. In addition, textural variations, such as color banding (reflecting regions of microlite-rich vs. microlite-free matrix) are less pronounced and subtler in the dome samples compared to the more dramatically banded pumice samples.

Modes and Mineral Chemistry

Modal analyses were performed by point counting ~1300 points per thin section (Table 4). Hand samples that are darker in color generally have a higher proportion of olivine. White pumice from the June 30, 1997 eruption is rich in plagioclase and pyroxene phenocrysts, but is poor in olivine phenocrysts and plagioclase microlites. In contrast, brown pumice ejected in the June 30, 1997 eruption is richer in olivine, has abundant plagioclase microlites (~35 vol.%) and is poorer in pyroxene and plagioclase phenocrysts than their white pumice counterparts. Vesicular dome rocks ejected on January 1, 1998 have modal proportions that are similar to the white pumice of June 30, 1997 (rich in plagioclase and pyroxene phenocrysts and poor in olivine phenocrysts and plagioclase microlites). However, the January 1, 1998 dome rocks are richer in total phenocrysts (~60 vol.%) than the June 30, 1997 white pumices (~30-40 vol.%). The brown pumice from June 30, 1997 has the lowest proportion of phenocrysts (<20 vol.%). Modal analysis of juvenile rocks by Athanasopoulos (1997) from the first magmatic material effused in March-April 1996 are shown in Table 4 for comparison.

Olivine

Cores and rims of twenty-two olivine xenocrysts were analyzed by EPMA along with an additional eleven core analyses of olivine microphenocrysts (Table 5). The total range of olivine compositions presented in this study are very similar to those reported for Popocatépetl's Quaternary lavas (Kolisnik, 1990). Our results show a slightly broader range in Fo than the recent eruptives studied by Straub & Martin-Del Pozzo (2001) and are comparable with the olivine from the March 1996 dome (Athanasopoulos, 1997).

Clynne & Borg (1997) distinguished between high-alumina olivine tholeiites, calc-alkaline basalts, and mafic andesites from the Lassen Peak region on a plot of Fo vs. CaO content in olivine (their Figure 2B). Glass inclusion-free olivine xenocrysts from Popocatépetl plot within the field of calc-alkaline mafic andesites but outside

the fields for calc-alkaline basalts and high-alumina olivine tholeiites. In contrast, glass inclusion-bearing olivine microphenocrysts from Popocatépetl plot outside of the three fields in a region of lower Fo-content.

Chromian spinel

Twenty-two analyses of chromian spinel were conducted by EPMA (Table 43). Chromian spinel core compositions are rich in Cr, Al, and Mg. Chromian spinel rims, however, that are in contact with silicate melt have a much higher content of Fe^{+2}, Fe^{+3} and Ti (all analyses recalculated according to Stormer (1983)).

Clynne & Borg (1997) distinguished rock types in the Lassen Peak area using chromian spinel compositions on the plot Mg# (= Mg/Mg+Fe^{+2}) vs. Cr# (= Cr/Cr+Al) (their Figure 6). With this diagram, chromian spinel in mafic volcanic rocks from the Lassen region, Jorullo basalt to basaltic andesites (Luhr and Carmichael, 1985), and MORB lavas from the Lamont seamount chain (Allan *et al.*, 1989) can be compared with those of Popocatépetl. Popocatépetl chromian spinel plot primarily within the fields of calc-alkaline mafic andesite from the Lassen region and Jorullo basalt to basaltic andesite. The relatively high Cr content may reflect a rather primitive source region for Popocatépetl's mafic input. Our analyses of Cr-spinel are similar to those presented in Straub & Martin-Del Pozzo (2001) for recent Popocatépetl eruptives.

Fe-Ti oxides

Twenty grains of titanomagnetite and twenty grains of ilmenite were analyzed by EPMA (Table 44). Titanomagnetite and ilmenite compositions have the range X_{Usp} = 0.29 to 0.48 and X_{Ilm} = 0.65 to 0.85, respectively (all analyses recalculated according to Stormer (1983)). The compositional range of Popocatépetl Fe-Ti oxides is broadly similar to those found in pumices from the 2.2 ka eruption of Mount Rainier (Venezky and Rutherford, 1997). Compared to 1991 Unzen Fe-Ti oxides, Popocatépetl titanomagnetites have somewhat higher X_{Usp} while ilmenites have lower X_{Ilm} (Venezky and Rutherford, 1999).

Table 43. Cr-spinel EPMA analyses (in wt.%) recalculated according to Stormer (1983)

	chr36ats5*	chr36bts5	chr37ats5	chr37bts5*	chr37cts5	chr32ats5*	chr32bts5	chr20ats2*	chr20bts2	chr22ats2	chr22bts2
Cr_2O_3	24.5	45.2	39.4	17.4	40.5	38.2	43.5	25.7	40.1	41.3	42.4
SiO_2	0.00	0.00	0.00	0.00	0.00	0.00	0.00	0.00	0.00	0.00	0.00
TiO_2	4.75	0.58	0.77	6.18	0.82	2.43	0.73	5.39	0.94	0.87	0.76
Al_2O_3	9.34	18.0	16.5	3.50	19.2	11.2	18.9	4.17	19.4	16.5	18.4
FeO	24.0	14.1	25.9	32.4	15.6	23.3	14.6	31.2	16.3	23.9	15.4
Fe_2O_3	27.3	7.56	10.5	36.6	9.93	16.2	7.75	28.6	10.3	9.14	9.08
MnO	0.37	0.27	0.50	0.49	0.33	0.39	0.30	0.41	0.27	0.43	0.29
MgO	8.20	13.4	5.64	3.06	12.7	7.66	13.2	3.50	12.5	7.02	12.7
CaO	0.05	0.01	0.03	0.05	0.03	0.09	0.01	0.06	0.04	0.05	0.02
NiO	0.19	0.26	0.08	0.06	0.20	0.20	0.25	0.11	0.13	0.08	0.20
Total	98.7	99.4	99.4	99.7	99.2	99.6	99.3	99.1	100.0	99.3	99.2

	chr24ats2	chr25ats2*	chr4ts1	chr3ats1	chr3bts1	chr6ts1	chr5ts1	chr6ts5	chr7ts5	chr1core	chr1rim*
Cr_2O_3	41.8	34.1	44.0	42.8	43.8	42.7	42.2	45.4	45.2	40.5	18.7
SiO_2	0.00	0.00	0.00	0.00	0.00	0.00	0.02	0.01	0.02	0.06	0.15
TiO_2	0.87	3.10	0.66	0.80	0.65	0.73	0.85	0.59	0.55	1.03	7.43
Al_2O_3	15.2	6.68	17.7	15.8	17.9	16.5	15.9	17.1	17.2	15.1	5.55
FeO	22.0	29.0	12.6	19.1	14.9	17.3	18.6	14.3	14.4	23.3	30.4
Fe_2O_3	10.8	22.1	8.77	10.3	8.86	10.2	10.2	7.95	7.84	11.4	30.5
MnO	0.38	0.43	0.23	0.33	0.30	0.31	0.33	0.29	0.31	0.42	0.42
MgO	8.19	3.93	14.3	10.1	13.0	11.3	10.4	13.2	13.0	7.47	5.55
CaO	0.01	0.05	0.01	0.05	0.02	0.04	0.02	0.00	0.02	n.d.	n.d.
NiO	0.13	0.05	0.26	0.08	0.17	0.16	0.11	0.25	0.23	n.d.	n.d.
Total	99.4	99.5	98.5	99.3	99.6	99.2	98.7	99.0	98.8	99.3	98.7

* Cr-spinel grain on edge of olivine, exposed to silicate melt with reacted Cr-spinel rim

Table 44. EPMA analyses of titanomagnetite and ilmenite (in wt.%)

Titanomagnetite

Label	SiO_2	TiO_2	Al_2O_3	Cr_2O_3	FeO	Fe_2O_3	MnO	MgO	CaO	NiO	Total	X_{Usp}
mgt1ts2	0.12	15.0	1.72	0.27	40.7	38.5	0.43	2.89	n.d.	n.d.	99.7	0.428
mgt2ts2	0.10	15.5	1.80	0.24	41.2	37.6	0.44	2.85	n.d.	n.d.	99.7	0.443
mgt3ts2	0.11	15.6	1.82	0.33	41.3	37.4	0.46	2.80	n.d.	n.d.	99.9	0.446
mgt5ts1	0.18	11.7	2.14	0.32	36.9	44.3	0.32	3.30	0.23	0.08	99.5	0.332
mgt6ts1	0.11	11.4	1.60	0.37	37.9	45.4	0.39	2.44	0.08	0.03	99.7	0.324
mgt6ats1	0.09	10.6	1.77	0.41	37.0	47.1	0.38	2.47	0.07	0.04	99.9	0.299
mgt7ts1	0.12	10.4	1.83	0.20	35.8	47.4	0.38	3.24	0.07	0.05	99.6	0.289
mgt8ts2	0.11	15.0	1.67	0.11	41.0	38.1	0.45	2.73	0.10	0.01	99.3	0.435
mgt10ts5	0.13	16.0	1.50	0.20	43.6	35.3	0.42	1.82	0.08	0.04	99.1	0.483
mgt11ts5	0.09	11.7	1.76	0.31	38.5	44.6	0.37	2.34	0.01	0.00	99.7	0.337
mgt12ts6	0.07	13.8	2.44	1.00	39.7	39.2	0.32	2.86	0.10	0.06	99.6	0.415
mgt13ts6	0.07	10.9	1.61	0.25	37.8	46.2	0.40	2.24	0.02	0.06	99.5	0.315
mgt14ts5	0.20	14.8	1.61	0.17	41.7	38.0	0.41	2.28	0.11	0.00	99.3	0.437
mgt21ts1	0.10	12.1	2.60	0.25	37.1	43.6	0.35	3.51	0.06	0.06	99.7	0.343
mgt21ats1	0.11	12.6	2.29	0.40	37.3	42.8	0.39	3.62	0.08	0.09	99.7	0.355
mgt22ts1	0.15	14.3	1.94	0.24	39.8	39.3	0.34	3.09	0.13	0.05	99.4	0.412
mgt22ats1	0.46	12.2	2.38	0.33	38.2	42.2	0.36	3.11	0.10	0.08	99.5	0.359
mgt23ts2	0.08	14.1	1.72	0.13	40.0	40.3	0.37	2.73	0.08	0.04	99.6	0.402
mgt23bts2	0.09	14.0	1.74	0.13	39.9	40.7	0.37	2.67	0.09	0.07	99.7	0.397
mgt24ts2	0.18	14.7	1.72	0.06	40.8	38.4	0.42	2.82	0.11	0.00	99.1	0.429
mgt24ats2	0.12	15.2	1.79	0.09	41.3	37.4	0.44	2.74	0.06	0.05	99.2	0.445
mgt25ts5	0.11	12.2	1.88	0.20	38.7	43.7	0.41	2.38	0.12	0.04	99.6	0.351
mgt26ts5	0.11	13.0	1.76	0.38	39.7	42.1	0.39	2.27	0.07	0.06	99.8	0.376
mgt26ats5	0.11	12.7	1.60	0.39	39.3	42.4	0.42	2.43	0.05	0.01	99.3	0.370
mgt28ts5	0.11	13.5	1.74	0.15	40.2	41.1	0.42	2.25	0.07	0.06	99.6	0.392
mgt29ts6	0.12	12.9	1.89	0.15	39.5	42.0	0.42	2.39	0.10	0.04	99.4	0.376

Table 44. Continued

Ilmenite

Label	SiO_2	TiO_2	Al_2O_3	Cr_2O_3	FeO	Fe_2O_3	MnO	MgO	CaO	NiO	Total	X_{Ilm}
ilm1ts2	0.07	43.2	0.27	0.04	32.7	19.0	0.41	3.58	n.d.	n.d.	99.3	0.807
ilm2ts2	0.03	44.0	0.27	0.08	32.7	19.1	0.42	3.54	n.d.	n.d.	100.2	0.807
ilm5ts1	0.15	39.4	0.41	0.06	28.7	25.5	0.29	4.02	0.13	0.01	98.7	0.738
ilm6ts1	0.02	34.5	0.30	0.13	27.2	34.5	0.22	2.33	0.02	0.01	99.3	0.654
ilm6(r)ts1	0.02	35.7	0.30	0.11	27.6	33.1	0.26	2.54	0.03	0.02	99.7	0.667
ilm7ts1	0.04	35.2	0.37	0.09	26.7	33.5	0.25	2.92	0.05	0.02	99.2	0.661
ilm8ts2	0.05	42.9	0.28	0.06	32.0	20.1	0.39	3.60	0.15	0.04	99.5	0.796
ilm10ts5	0.08	40.3	0.43	0.06	31.7	23.7	0.45	2.54	0.09	0.01	99.4	0.762
ilm11ts5	0.02	37.2	0.34	0.09	28.8	29.9	0.31	2.69	0.01	0.03	99.4	0.699
ilm12ts6	0.02	43.9	0.31	0.21	32.1	18.3	0.32	4.09	0.07	0.04	99.4	0.813
ilm13ts6	0.02	35.4	0.34	0.05	27.7	33.3	0.25	2.38	0.02	0.01	99.5	0.666
ilm14ts5	0.06	39.9	0.32	0.06	32.0	24.1	0.31	2.28	0.08	0.04	99.1	0.759
ilm21ts1	0.05	39.8	0.40	0.07	27.3	27.6	0.33	4.49	0.06	0.05	100.1	0.715
ilm22ts1	0.04	42.6	0.35	0.05	30.4	22.5	0.36	4.04	0.07	0.02	100.4	0.770
ilm23ts2	0.06	37.1	0.35	0.07	28.4	30.8	0.21	2.75	0.02	0.01	99.7	0.691
ilm24ts2	0.10	42.9	0.30	0.05	32.4	19.5	0.41	3.52	0.11	0.01	99.3	0.802
ilm25ts5	0.18	39.5	0.86	0.05	30.6	24.8	0.34	2.87	0.08	0.03	99.3	0.749
ilm26ts5	0.28	41.2	0.29	0.08	31.2	22.9	0.42	3.19	0.21	0.01	99.7	0.768
ilm27ts5	0.05	44.7	0.19	0.00	35.4	15.5	0.44	2.61	0.30	0.00	99.2	0.845
ilm28ts5	0.04	35.0	0.32	0.33	27.8	33.9	0.14	2.12	0.01	0.08	99.7	0.661
ilm29ts6	0.05	38.7	0.35	0.08	29.7	27.3	0.34	2.76	0.14	0.07	99.5	0.725

X_{Usp} and X_{Ilm} calculated according to Stormer (1983)

Pyroxene

Twenty-four core and twenty-three rim analyses of orthopyroxene were performed by EPMA along with eleven additional analyses of orthopyroxene host mineral near glass inclusions. Three analyses were obtained of an orthopyroxene host near a sulfide inclusion. Twenty-three core and twenty-one rim EPMA analyses of clinopyroxene were performed along with twenty-three additional analyses of clinopyroxene host mineral near glass inclusions. Analyses of pyroxene cores and rims are shown in Table 6. Pyroxene core compositions occur as high-Mg# and low-Mg# phases (Mg# = $Mg/Mg+Fe^{+2}$). A few pyroxene grains do not fit into the high- or low-Mg# groupings. Two pyroxenes have intermediate compositions. One clinopyroxene is interpreted to be a xenocryst due to anomalously high Al_2O_3 content. One orthopyroxene is interpreted to be a xenocryst due to anomalously high Cr_2O_3 content and low Mg#.

Pyroxenes are characterized by broad, compositionally uniform cores with or without narrow, zoned rims. We interpret the pyroxene core compositions as an indication of the origin of the pyroxene. Compositional variations in the pyroxene rims are interpreted to result from magma mixing. High- and low-Mg# clinopyroxene cores are augite with compositions $En_{47-49}Fs_{8-10}Wo_{42-44}$ (Mg# 83-86 and Cr_2O_3 0.2-0.7 wt.%) and $En_{40-44}Fs_{13-18}Wo_{40-45}$ (Mg# 70-78 and $Cr_2O_3 < 0.3$ wt.%), respectively. High-Mg# orthopyroxene cores are bronzite with composition $En_{82-83}Fs_{14-15}Wo_{2-4}$ (Mg# 84-85 and Cr_2O_3 0.1-0.4 wt.%). Low-Mg# orthopyroxene cores are hypersthene with composition $En_{61-69}Fs_{29-35}Wo_{2-3}$ (Mg# 63-72 and $Cr_2O_3 < 0.15$ wt.%). EPMA analyses of pyroxene in recent Popocatépetl eruptives by Athansopoulous (1997) and Straub & Martin-Del Pozzo (2001) cover the same compositional range as the analyses presented here. However, the high-Mg# orthopyroxenes in their studies occur as mantles around olivine. This is in contrast to the high-Mg# orthopyroxene *phenocrysts* presented in this study. Kolisnik (1990) also found high- and low-Mg# populations of clino- and orthopyroxene phenocrysts in her study of Quaternary lavas

of the Popocatépetl edifice that cover the same compositional range as those presented here.

Core-to-rim zonation in pyroxene is highly variable. High-Mg# pyroxene are generally normally zoned (up to $\Delta En = 21$ mol%) while low-Mg# pyroxene are predominantly reversely zoned (up to $\Delta En = 15$ mol%). Many pyroxene grains, however, are unzoned or have weak normal to reverse zoning ($\Delta En < 3$ mol%). Zonation variations in pyroxene are similar in magnitude to that found in studies by Kolisnik (1990), Athanasopoulous (1997), and Straub & Martin-Del Pozzo (2001).

Plagioclase

Twenty-four plagioclase core and twenty plagioclase rim analyses were performed by EPMA (Table 45). Plagioclase phenocryst core compositions cover the range An_{28-61}. Rim compositions cover a similar range. Zonation is dominantly reverse (up to $\Delta An = 20$ mol %) but some phenocrysts are normally zoned (up to $\Delta An = 5$ mol%). Petrographic observations discussed previously (oscillatory zonation and dissolution surfaces) suggest that zoning patterns in plagioclase are much more complex than the zoning patterns revealed by individual core and rim EPMA analyses. It is apparent that there is no correlation between plagioclase composition and phenocryst texture. In addition, plagioclase compositions do not fall into two clearly defined compositional groups, as do the pyroxenes.

Our plagioclase data is similar to that found by Straub & Martin-Del Pozzo (2001) for other recent Popocatépetl eruptives. In an exhaustive study of plagioclase zonation in Quaternary lavas from Popocatépetl, Kolisnik (1990) found plagioclase phenocrysts with a broader compositional range (An_{21-71}) characterized by complex discontinuous zoning patterns. She also inferred repetitive dissolution and renewed growth. The extremely heterogeneous plagioclase crystal populations had little correlation of zoning between coexisting grains with calcic excursions in An content of up to 37 mol%.

Table 45. EPMA analyses of plagioclase (in wt.%)

Label	SiO_2	Al_2O_3	MgO	FeO	CaO	Na_2O	K_2O	Total
plag5corets1	51.9	30.0	0.05	0.44	12.5	4.38	0.17	99.4
plag5rimts1	53.0	29.2	0.03	0.51	12.1	4.77	0.19	99.8
plag10corets1	60.3	23.6	0.02	0.42	5.81	7.68	0.70	98.6
plag10rimts1	58.0	25.1	0.01	0.38	7.37	7.31	0.46	98.6
plag11corets1	53.9	28.3	0.03	0.33	10.7	5.45	0.31	99.0
plag11rimts1	52.3	29.2	0.25	0.69	12.6	4.21	0.14	99.3
plag12corets1	58.0	26.0	0.03	0.42	8.21	6.55	0.49	99.7
plag12rimts1	56.5	26.9	0.04	0.45	9.20	6.37	0.34	99.9
plag16rimts1	53.2	28.6	0.12	0.61	11.4	4.87	0.16	99.0
plag18corets1	58.3	25.0	0.04	0.45	7.41	6.97	0.67	98.8
plag18rimts1	53.1	28.6	0.10	0.61	11.4	4.96	0.21	98.9
plag3corets2	58.7	24.6	0.03	0.41	6.64	7.42	0.63	98.4
plag3rimts2	54.4	28.0	0.02	0.51	10.1	5.59	0.32	99.0
plag4corets2	53.8	28.2	0.09	0.81	11.4	4.47	0.47	99.3
plag4rimts2	51.9	29.3	0.10	0.56	12.3	4.51	0.15	98.8
plag5corets2	55.9	26.6	0.02	0.41	8.63	6.48	0.40	98.4
plag5rimts2	57.4	26.3	0.03	0.53	8.41	6.65	0.41	99.7
plag6corets2	56.3	26.3	0.05	0.34	8.60	6.31	0.42	98.3
plag6rimts2	55.4	27.3	0.04	0.44	9.85	5.86	0.31	99.2
plag7corets2	55.4	26.8	0.02	0.43	8.94	6.32	0.33	98.2
plag7rimts2	56.7	26.5	0.03	0.44	8.90	6.62	0.36	99.5
plag8corets2	54.7	27.9	0.02	0.40	10.3	5.70	0.25	99.2
plag8rimts2	52.6	28.6	0.05	0.46	11.4	5.02	0.23	98.3
plag9corets2	57.2	25.9	0.05	0.47	8.11	6.72	0.39	98.8
plag9rimts2	53.9	27.7	0.09	0.73	10.9	4.96	0.39	98.6
plag2corets2	55.0	27.3	0.03	0.39	9.30	6.01	0.34	98.4
plag2rimts2	56.9	26.0	0.02	0.46	8.52	6.55	0.34	98.9
plag21corets5	57.9	25.9	0.03	0.43	8.06	6.74	0.55	99.6
plag21rimts5	55.4	28.0	0.01	0.42	10.5	5.59	0.31	100.2
plag22rimts5	55.4	26.9	0.02	0.42	9.13	6.15	0.40	98.4
plag23corets5	53.9	28.1	0.00	0.30	10.3	5.64	0.37	98.5
plag26corets5	59.6	23.8	0.02	0.39	5.94	7.75	0.83	98.4
plag27corets5	53.9	28.6	0.01	0.36	10.7	5.22	0.26	99.0
plag30corets5	57.3	26.5	0.03	0.46	8.27	6.51	0.47	99.5
plag31corets6	57.6	26.7	0.03	0.41	8.79	6.45	0.38	100.3
plag31rimts6	52.7	28.6	0.10	0.66	11.7	4.82	0.21	98.7
plag32corets6	55.5	27.6	0.02	0.37	9.79	5.97	0.36	99.6
plag33corets6	55.0	27.2	0.03	0.39	9.71	5.93	0.35	98.6
plag34rimts6	55.6	27.2	0.03	0.47	9.52	6.00	0.37	99.2
plag35corets6	58.4	25.9	0.04	0.44	8.07	6.90	0.42	100.1
plag35rimts6	59.5	25.0	0.09	0.51	7.03	7.29	0.54	100.0
plag36corets6	60.3	24.7	0.03	0.38	6.63	7.66	0.66	100.4
plag36rimts6	55.3	27.4	0.00	0.45	9.69	6.00	0.35	99.2
plag37corets6	58.8	25.2	0.03	0.37	7.49	7.01	0.55	99.4

Hornblende

Seventeen major element analyses of hornblende were performed by EPMA. Of these, seven were also analyzed for volatile elements S, Cl, and F (Table 7). Utilizing the amphibole nomenclature scheme of Leake *et al.* (1997) and depending on how they are recalculated, Popocatépetl hornblende can be classified as the calcic amphiboles tschermakite, pargasite, or magnesiohastingsite. The low Na-content and high Ca-content of Popocatépetl hornblende places them in the calcic group like many amphiboles found in subduction zone magmas. The (Na+K) content in the A-site differentiates the nomenclature between tschermakite and pargasite/magnesiohastingsite at $(Na+K)_A=0.5$. Popocatépetl hornblende has $(Na+K)_A \sim 0.5$. The relative proportions of Al^{VI} and Fe^{3+} distinguish pargasite and magnesiohastingsite. Ferric-ferrous recalculation schemes for amphibole generally produce large errors making exact classification difficult. As a result of these considerations we choose to refer to the Popocatépetl amphiboles under scrutiny with the more generic name "hornblende." What is important to note, however, is that despite the difficulty in nomenclature, Popocatépetl hornblende has a restricted compositional range. EPMA analyses of hornblende rims in contact with silicate melt were not possible due to the ubiquitous presence of breakdown rims on hornblende.

Recalculating hornblende EPMA analyses on the basis of 23 oxygens and utilizing the ferric-ferrous scheme of Holland & Blundy (1994) gives the following average chemical formula:

$$(Na_{0.4}K_{0.1})(Ca_{1.7}Na_{0.3})(Ti_{0.2}Al^{VI}_{0.3}Fe^{+3}_{0.7}Fe^{+2}_{0.8}Mn_{0.02}Mg_{3.0})(Si_{6.3}Al^{IV}_{1.7})O_{22}(F_{0.2}Cl_{0.004}OH_{1.8})$$

Compositionally, our data compares well with the hornblende data of Athanasopoulos (1997) from Popocatépetl's March 1996 dome.

Apatite

Popocatépetl apatite is classified as fluorapatite (Table 46). Systematic zonation of F, Cl, S, Si, Na, Mn, Fe, Mg and Sr in apatite was not found. Recalculating apatite EPMA analyses on the basis of 13 (O, OH, F, Cl) gives the following chemical formula:

$$(Ca_{5.01}Mg_{0.04}Fe_{0.03}Mn_{0.005}Sr_{0.002}Na_{0.03})(P_{0.97}Si_{0.01}S_{0.01}O_4)_3(OH_{0.17}F_{0.76}Cl_{0.07})$$

Our analyses are similar to those of other volcanic apatites (Peng *et al.*, 1997).

Table 46. EPMA analyses of apatite (in wt.%)

Label	CaO	MgO	FeO	MnO	SrO	Na_2O	P_2O_5	SiO_2	SO_3	Cl	F	OH*	Total
apatite1ts6 A (core)	54.4	0.29	0.37	0.06	0.03	0.19	39.8	0.33	0.50	0.53	2.80	0.61	99.8
apatite1ts6 B	54.0	0.29	0.52	0.03	0.11	0.22	39.5	0.33	0.54	0.52	2.66	0.74	99.4
apatite1ts6 C	54.4	0.30	0.50	0.08	0.11	0.22	39.5	0.29	0.52	0.52	2.71	0.69	99.9
apatite1ts6 D	54.0	0.30	0.41	0.06	0.07	0.20	40.1	0.26	0.49	0.50	2.69	0.72	99.7
apatite1ts6 E	53.7	0.27	0.43	0.08	0.00	0.21	38.9	0.26	0.47	0.48	2.75	0.68	98.3
apatite1ts6 F	54.0	0.28	0.39	0.08	0.06	0.22	39.8	0.26	0.46	0.42	2.81	0.66	99.4
apatite1ts6 G	54.4	0.27	0.51	0.08	0.22	0.21	39.9	0.25	0.45	0.46	2.94	0.51	100.2
apatite1ts6 H (rim)	54.1	0.28	0.39	0.06	0.10	0.20	40.5	0.27	0.49	0.53	2.99	0.43	100.3

* OH content is calculated using the following equation from Piccoli and Candela (1994)
wt.% OH = 3.384*(1-(wt.% F/3.767)-(wt.% Cl/6.809))
Assumes perfect stoichiometry

References

Allan, J.F., Sack, R.O. and Batiza, R., 1989. Cr-rich spinels as petrogenetic indicators; MORB-type lavas from the Lamont seamount chain, eastern Pacific. American Mineralogist, 73(7-8): 741-753.

Athanasopoulos, P., 1997. The origin and ascent history of the 1996 dacitic dome, Volcán Popocatépetl , Mexico. Bachelor's Thesis, University of Manitoba, Winnipeg, Canada, 105 pp.

Clynne, M.A. and Borg, L.E., 1997. Olivine and chromian spinel in primitive calc-alkaline and tholeiitic lavas from the southernmost Cascade Range, California; a reflection of relative fertility of the source. The Canadian Mineralogist, 35: 453-472.

GVN, 1997a. Explosion on 1 January causes fires, ashfall. Global Volcanism Network Bulletin, 22(12).

GVN, 1997b. Largest ash emission of the 1994-97 eruption on 30 June. Global Volcanism Network Bulletin, 22(7).

Holland, T. and Blundy, J., 1994. Non-ideal interactions in calcic amphiboles and their bearing on amphibole-plagioclase thermometry. Contributions to Mineralogy and Petrology, 116: 433-447.

Kolisnik, A.M.E., 1990. Phenocryst Zoning and Heterogeneity in Andesites and Dacites of Volcán Popocatépetl, Mexico. Master's Thesis, Queen's University, Kingston, Ontario, Canada, 247 pp.

Leake, B.E. et al., 1997. Nomenclature of amphiboles: Report of the Subcommittee on Amphiboles of the International Mineralogical Association, Commission on New Minerals and Mineral Names. American Mineralogist, 82(9-10): 1019-1037.

Luhr, J.F. and Carmichael, I.S.E., 1985. Jorullo Volcano, Michoacan, Mexico (1759-1774); the earliest stages of fractionation in calc-alkaline magmas. Contributions to Mineralogy and Petrology, 90(2-3): 142-161.

Peng, G., Luhr, J.F. and McGee, J.J., 1997. Factors controlling sulfur concentrations in volcanic apatite. American Mineralogist, 82: 1210-1224.

Stormer, J.C., Jr., 1983. The effects of recalculation on estimates of temperature and oxygen fugacity from analyses of multicomponent iron-titanium oxides. American Mineralogist, 68(5-6): 586-594.

Straub, S.M. and Martin-Del Pozzo, A.L., 2001. The significance of phenocryst diversity in tephra from recent eruptions at Popocatépetl volcano (central Mexico). Contributions to Mineralogy and Petrology, 140: 487-510.

Venezky, D.Y. and Rutherford, M.J., 1997. Preeruption conditions and timing of dacite-andesite magma mixing in the 2.2 ka eruption at Mount Rainier. Journal of Geophysical Research, 102(B9): 20,069-20,086.

Venezky, D.Y. and Rutherford, M.J., 1999. Petrology and Fe-Ti oxide reequilibration of the 1991 Mount Unzen mixed magma. Journal of Volcanology and Geothermal Research, 89(1-4): 213-230.

Vita

Jeffrey Bruce Witter

1992 A.B. Occidental College, Geophysics

1997 M.S. University of Hawaii, Geology and Geophysics

2003 Ph.D. University of Washington, Earth and Space Sciences